INNOVATIVE BIOMEDICAL APPLICATIONS USING HYBRID NANOPARTICLES

Jason Sung Kim

A dissertation submitted to the faculty of the University of North Carolina at Chapel Hill in partial fulfillment of the requirements for the degree of Doctor of Philosophy in the Department of Chemistry.

Chapel Hill
2008

Approved by:

Professor Wenbin Lin

Professor Cynthia K. Schauer

Professor Holden H. Thorp

Professor Rihe Liu

Professor Teresa K. Tarrant

ABSTRACT

JASON SUNG KIM: Innovative Biomedical Applications Using Hybrid Nanoparticles
(Under the direction of Wenbin Lin)

Nanoparticle and metal-chelate technologies can be combined to create innovative hybrid materials with versatile functions for research and clinical purposes. This dissertation addresses the novel use of hybrid inorganic/organic nanoparticles in biomedical applications, including early detection of autoimmune disease and cancer as well as purification of therapeutic proteins. In an *in vivo* animal model of rheumatoid arthritis (RA), fluorescent nanoparticles coated with a magnetic resonance imaging (MRI) contrast enhancing metal-chelate are used for cell specific trafficking of monocytes, which correlate with disease activity. Metal-chelate derivatized magnetic nanoparticles isolate tagged proteins, potential cancer therapeutics, from impurities generated from bacterial and mammalian cell expression systems. The novel applications of hybrid magnetic nanoparticles pursued in this dissertation have the ability to translate into new and more sensitive strategies to treat patients with chronic disease.

ACKNOWLEDGEMENTS

The work presented in this thesis would be impossible without the tremendous help and support of many mentors, colleagues, friends, and family members. My advisor, Professor Wenbin Lin, gave me everything he promised when I first arrived in his group, five years ago. Throughout this time, I have never needed to be concerned about work space, funding, or extended time without intellectual advice--allowing me to focus a variety of interesting projects within his research program. I can only hope to have absorbed a fraction of his boundless energy, contagious intensity, and highly critical eye for science. His presence has made me a stronger, more confident person both inside and outside of the laboratory. Early on, I was allowed to have an incredible range of freedom to pursue diverse research that my peers my find unimaginable. The many collaborations that I have been asked to pursue has been the most valuable, gratifying experiences that Wenbin has given to me.

The many people that I have met while roaming the laboratories of the UNC campus have been incredible. Professor Rihe Liu has been so generous with his time and resources, always being available for discussions and giving me free reign over anything in his lab. He has told me on multiple occasions to consider myself a part of his group, and I have always felt fully accepted. Alex Valencia and Biao Dong have always welcomed me, and taught me how to make publishable SDS-PAGE gels, of which I have now run seemingly hundreds. Alex, especially, has always had time for me and my questions about science and career.

The rest of the group has also been great friends to me, especially Steve Cotton, Christian Bailey, Jim Aloor, and Harsha Kulkarni.

During my time at the Pharmacy School, I became roped into attending weekly Journal Club, where I became lucky enough to be exposed to new research and fantastic people. Professor Moo Cho opened up his lab to me, allowing me to use and borrow anything I needed. He has also been a great mentor to a young Korean-American scientist, which is not easily found in Chapel Hill, North Carolina. I really appreciate the members of his lab: John Ahn, Jin Lee, and Roland Cheung; as well the other Journal Club members of Professor Leaf Huang's lab.

In a later collaboration, I met Professor Teresa Tarrant at the School of Medicine to embark on my first experience with disease models and animal work. Years ago I would have never fathomed being able to do this type of work, but Terri patiently taught me the necessary techniques and theory that one could ask for--short of taking a full courseload. Again, I was given all lab space and supply I desired, as well as the kind support of her lab members. Terri has incredible work-life balance, of which I hope to mimic one day. She has helped me with many skills that average scientists are not usually proficient; but mostly, Terri has been a caring mentor and friend.

The actual data of this thesis would not exist without Kathryn Taylor and BJ Rieter. I appreciate Kathryn's quiet efficiency, as she always returns results of submitted samples quickly and mistake-free. Though she is soft-spoken, her words are always precise, clear, and meaningful. BJ has always been at the root of my work, providing valuable materials for which I was able to explore interesting applications.

Professor Hongyu An and Dr. Yonglong Hong of Weili Lin's lab in the Department of Radiology were obviously instrumental in any MRI imaging. Hongyu was always helpful and responsive to my naïve questions. Yonglong and I spent many hours and days together troubleshooting and optimizing the scanning of the poor, little, arthritis-ridden mice. The many hours logged on the confocal microscopes would be much longer without the help of the staff at the Michael Hooker Microscopy Facility and Microscopy Services Facility.

My closest friends in the Lin group, Nick Zafiropoulos and David Mihalcik, I will always be thankful for the intellectual and emotional support. There is no way that I could have survived without the almost daily lunches (along with Dana), the jokes, and all the good times. Nick may be one of the most intelligent people I know, and I have fed off of his steady work ethic and discipline. Dave has always been a great friend to me: cheering me up during rough patches, ready to move furniture at the drop of a hat, and cross-checking 7-footers. I am sorry for exposing your embarrassing secrets from ratemyprofessors.com.

I also want to thank Jason Lee for his friendship, support, and trailblazing the path to North Carolina for the SHHS crew. I have always been welcomed freely into his home and have spent numerous hours at his house thinking about anything besides chemistry. But, my other close friends from high school and college have always helped and supported me: Karen Cheng, Amit Pandhi, Herman Wang, Karen Chau, Rohit Wanchoo, and Farhana Haque. Without my friends' visions for something greater, I think I would be doing dull work in the suburbs of Orange County.

When I first arrived in the Lin group, I was helped to acclimate to my new life by Suk Joong Lee, Banu Kesanli, Helen Ngo and Dr. Hu. Leading up to UNC, I was helped by the folks at my previous schools. Professor Fred Hawthorne first encouraged me to pursue

graduate school, and for that I am always grateful. Professor Mark Lee, who I helped as an undergraduate at UCLA, first introduced me to the "glamorous" life of a graduate student. Fortunately, I was not scared away. I also cherish my times with my many friends from the de Lijser group at CSUF.

Finally, I want to thank my family. My parents have always helped me emotionally and financially, though they may not understand what it is that I do. They have given me tenacity and strength, and I hope I can live up to their ideals of a son. Myron, my brother and best friend since he was born, understands me like no one can or ever will.

TABLE OF CONTENTS

Page

LIST OF TABLES

Table

LIST OF FIGURES

Figures

ABBREVIATIONS

3.0T	3.0 Tesla
4.7T	4.7 Tesla
9.4T	9.4 Tesla
$\alpha\nu\beta3$	vitronectin receptor
ATCC	American type culture collection
B220	B-cell antibody (CD45R)
Balb/c	highly inbred, common mouse strain
Bis-Ni-NTA	bivalent nitrilotriacetate chelated Ni (II)
BET	Brunauer, Emmett, Teller
bFGF	basic fibroblast growth factor
Bn	benzyl
BSA	bovine serum albumin
CD3	cluster of differentiation-3, T-cell antibody
cDNA	complementary DNA
CE-MRI	contrast enhanced magnetic resonance imaging
CIA	collagen induced arthritis
CLIO	cross-linked iron oxide
C-PAE	cow pulmonary artery endothelial
CR	conventional radiography
Csp	caspase
CT	computed tomography

Cu(II)	Copper (II) ion
DA	dopamine
DBA-1J	inbred mouse strain widely used for CIA
DCC	dicyclohexylcarbodiimide
DCP	direct current plasma
DIC	differential interference contrast
dH_2O	distilled water
DL	direct lysate
DLAM	Division of Laboratory Animal Medicine
DMEM	Dulbecco's minimal essential media
DMF	dimethylformamide
DMSO	dimethylsulfoxide
DNA	deoxyribonucleic acid
DOTA	tetraazacyclododecanetetraacetic acid
DsRed	*Discosoma sp.* red fluorescent protein
DTPA	diethylenetriaminepentaacetic acid
DTPA-BMA	bis-[2-(carboxymethylmethylcarbamoylmethylamino)ethyl] amino acetic acid
DTTA	diethylenetrimaine tetraacetate
E1	elution 1
E2	elution 2
ECM	extracellular matrix
EMEM	Eagle's minimal essential media
EndoGluC	C-terminal glutamic acid specific endoproteinase

ESI-MS	electrospray ionization mass spectroscopy
^{19}F	fluorine isotope of 19 atomic mass units
FBS	fetal bovine serum
FITC	fluorescein isocyanate
FLASH	fast low angle shot
FOV	field of view
FS	forward scattered
FT	flow through
Gd	gadolinium
Gd(III)	gadolinium (III) ion
Gd-DTPA	gadolinium diethylenetriaminepentaacetic acid
GFP	green fluorescent protein
GMAP-210	Golgi-associated microtubule-binding protein
GRAS	generally regarded as safe
^{1}H	hydrogen isotope of 1 atomic mass unit
H&E	hematoxylin and eosin
HBSS	Hanks' balanced buffered saline solution
HEK 293T	human embryonic kidney
HEPES	4-(2-hydroxyehtyl-1-piperazineethanesulfonic acid
His×2	bishistidine tag
His×6	hexahistidine tag
HOBt	*N*-Hydroxybenzotriazole
HPDO3A	1,4,7,10-tetraazacyclododecane-1-hydroxypropyl-4,7,10-trisacetic acid

HT-29	human colon carcinoma
ICPES	inductively coupled plasma atomic emission spectroscopy
IDV	intensity density value
IMAC	immobilized metal affinity chromatography
IL-6	interleukin-6
LADMAC	mouse bone marrow producing colony stimulation factor
LB	Langmuir-Blodgett
LbL	layer-by-layer
JRA	juvenile rheumatoid arthritis
K_7RGD	(lysine)$_7$-arginine-glycine-aspartic acid
K_7GRD	(lysine)$_7$-glycine-arginine-aspartic acid
MALDI-MS	matrix assisted laser desorption/ionization mass spectrometry
MNP	multimodal nanoparticle
MOMA-2	monocyte/macrophage antibody-2
MRI	magnetic resonance imaging
MR	magnetic resonance
MTS	3-(4,5-dimethylthiazol-2-yl)-5-(3-carboxymethoxyphenyl)-2-(4-sulfophenyl)-2H-tetrazolium salt
NHS	*N*-hydroxysuccinimide
Ni(II)	Nickel (II) ion
Ni-NTA	nitrilotriacetate chelated nickel (II)
NMR	nuclear magnetic resonance
NTA	nitrilotriacetic acid
OCT	optimum cutting temperature

PBS	phosphate buffered saline
PCR	polymerase chain reaction
PE	phycoerythrin
PEG	polyethylene glycol
PET	positron-emission tomography
PSS	polystyrene sulfonate
PXRD	powder X-ray diffraction
r1	longitudinal relaxation rate
r2	transverse relaxation rate
RA	rheumatoid arthritis
RARE	rapid acquisition relaxation enhanced
RES	reticuloendothelial system
RF	rheumatoid factor
RGD	arginine-glycine-aspartic acid
rmES	recombinant Endostatin
ROI	region of interest
RPM	revolution per minute
$Ru(bpy)_3Cl_2$	ruthenium (III) trisbipyridine dichloride
SDS-PAGE	sodium dodecyl sulfate polyacrylamide gel electrophoresis
SEM	scanning electron microscopy
SiO_2	silica
SPECT	single positron-emission coupled tomography
SPIO	superparamagnetic iron oxide

SS	side scattered
T1	longitudinal relaxation time
T2	transverse relaxation time
tBOC	tert-butyl carbonate
TE	echo time
TEA	triethylamine
TEM	transmission electron microscopy
TFA	trifluoroacetic acid
TGA	thermogravimetric analysis
TLC	thin layer chromatography
TMV	tobacco mosaic virus
TNF-α	tumor necrosis factor-α
TNT	*in vitro* transcription/translation
TR	repetition time
UGT	UDP glycoslytransferase
USPIO	ultrasmall superparamagnetic iron oxide
Ub	ubiquitin
UCH-L1	ubiquitin C-terminal hydrolase L-1
UTR	untranslated region
UV	ultraviolet
VCAM-1	vascular cell adhesion molecule-1
VEGF	vascular endothelial growth factor
W1	wash 1

W2	wash 2
W3	wash 3
XRD	X-ray diffraction
Zn(II)	zinc (II) ion

CHAPTER 1

HYBRID NANOMATERIALS FOR BIOMEDICAL APPLICTIONS: FUNDAMENTALS, STRATEGIES, AND HISTORICAL OVERVIEW

1.1 Introduction to hybrid nanomaterials

Inorganic nanostructures such as II-VI semiconducting quantum dots and superparamagnetic Spinel ferrite nanoparticles have attracted great interest from the scientific, engineering, and medical communities because of their strongly size- and shape-dependent physical properties.[1-5] The past two decades of intensive research has led to numerous highly reliable and reproducible synthetic methodologies for inorganic nanostructures with well-defined and nearly identical properties such as size, shape, composition, crystal structure and surface properties. The field of organic polymer colloidal particles is even more mature,[6-12] as evidenced by the commercial availability of numerous polymeric nanoparticles. Reverse microemulsion polymerization and precipitation polymerization have, for example, allowed the synthesis of many monodisperse polymeric colloidal particles. In contrast to the inorganic nanostructures and polymer colloidal particles, relatively little has been done on organic/inorganic hybrid nanomaterials.

By merging the unique attributes of both soft organic and hard inorganic components, organic/inorganic hybrid nanomaterials offer many interesting characteristics that do not exist in either inorganic nanostructures or polymer colloidal particles alone. They can not only possess some of the unique properties of inorganic nanostructures as a result of the size-

dependent behaviors but also allow synthetic manipulations of the organic components with a molecular precision. The modular synthetic procedures for organic/inorganic hybrid nanomaterials further allow systematic fine-tuning of their properties for specific applications. Indeed, such an amalgam of hybrid materials and nanotechnology has already opened the door for a wide range of applications across multiple fields of science, engineering, and medicine. For example, the synergistic interactions between adsorbed ruthenium complex antenna and titania nanoparticles have led to the design of Grätzel solar cells that have the potential to revolutionize solar energy utilization.[13-16] In heterogenous asymmetric catalysis, Lin *et al.* has developed a magnetically recoverable iron oxide hybrid nanoparticle-supported chiral ruthenium (II) catalyst for the synthesis of chiral secondary alcohols.[17] The applications of organic/inorganic hybrid nanomaterials in other fields (such as biological sensing, biomedical imaging, and catalysis) have also been recently demonstrated.[18-22] This chapter surveys some of the latest developments in the design and applications of hybrid nanomaterials in the biomedical and biological fields.

1.2 Hybrid nanomaterials as MRI contrast agents

Magnetic resonance imaging (MRI) is a diagnostic tool that relies on the same mechanism as the commonly used nuclear magnetic resonance (NMR). Based on the differentiated water proton signals, MRI provides images of anatomical structures and other physiological environments with an excellent spatial resolution.[23] A patient is placed within a homogenous, static magnetic field $\boldsymbol{B_0}$ of an MR scanner to resonate nuclear spins at a determined frequency. The hydrogen nuclei of water protons precess at the Larmor frequency (ω_L) around and directed relative to $\boldsymbol{B_0}$ **(Figure 1.1)**. Possessing a ½ spin, the

hydrogen nuclei have two quantum mechanically allowed directions that correspond to the energy levels of the nuclei. A radiofrequency pulse ($\boldsymbol{B_1}$) sequence, perpendicular to $\boldsymbol{B_0}$, is used to excite the proton spins, which changes the net magnetization ($\boldsymbol{M}$). The Boltzmann distribution shows that slightly more spins occupy the lower energy state (spin up) than the higher energy state (spin down), ultimately leading to the vector $\boldsymbol{M}$.[24] As the spins relax back to their original thermal equilibrium, the electromagnetic signals are recorded and transformed to three dimensional images.

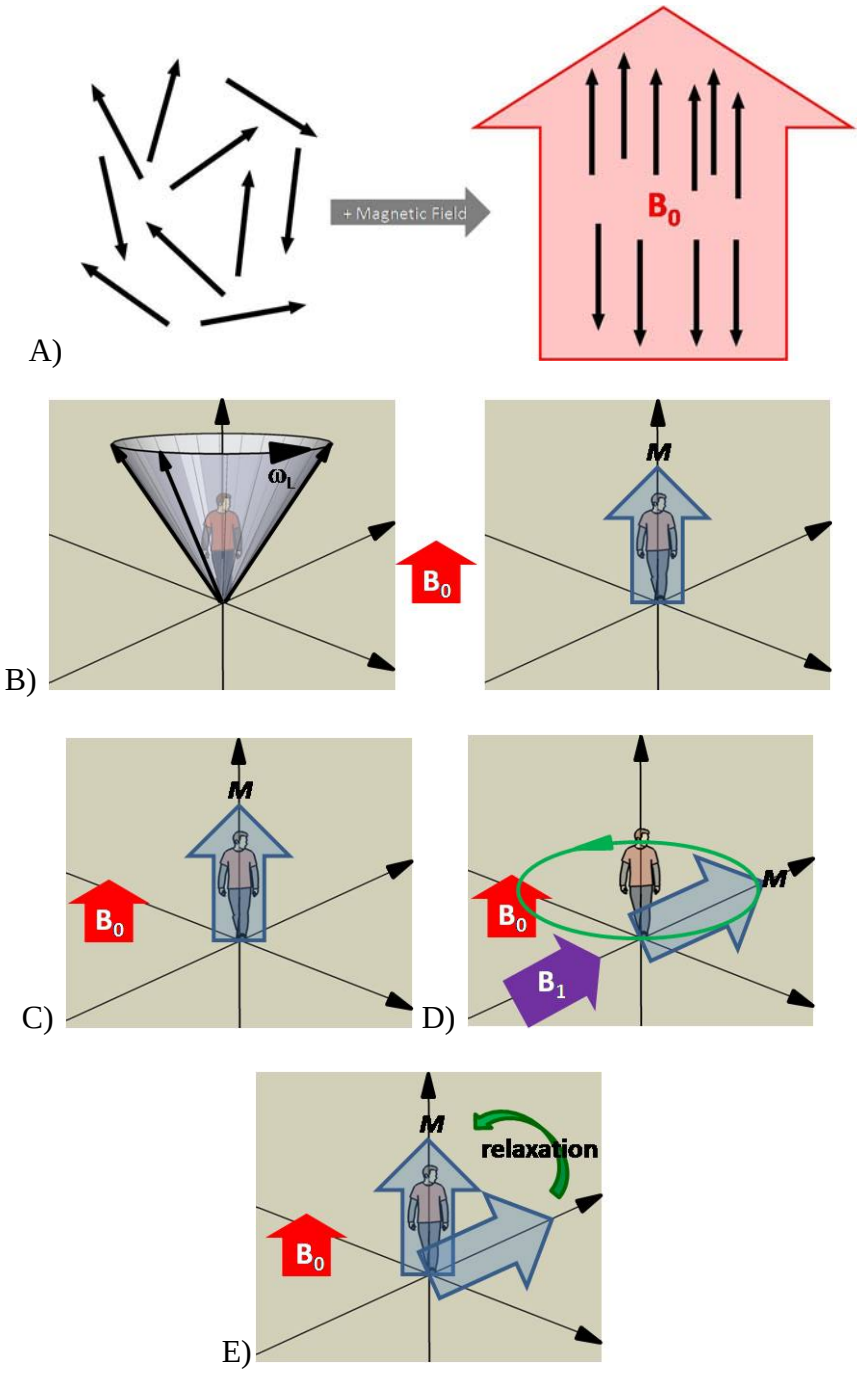

Figure 1.1 Schematic representation of hydrogen nuclei before and after placement within a magnetic field $\boldsymbol{B_0}$. A) Nuclei are randomly oriented until application of magnetic field induces alignment. B) The hydrogen nuclei precess around $\boldsymbol{B_0}$ at the Larmor frequency, ω_L, the net magnetization vector $\boldsymbol{M}$ is a result of more spins occupying the lower energy state (spin up). C) The net magnetization before electromagnetic radiofrequency pulse. D) The radiofrequency pulse generates a magnetic field $\boldsymbol{B_1}$ that causes **M** to flip perpendicular to $\boldsymbol{B_0}$, while revolving around the $\boldsymbol{B_0}$-axis. E) The removal of the radiofrequency pulse allows the relaxation of **M** to the original state.

MR image contrasts result from the inherently variable levels of water present in different tissues and water environments. For example, the higher water content of the brain leads to differences in MR contrast compared to muscle tissue of lower water content. The longitudinal relaxation time constant (*T1*) and the transverse relaxation time constant (*T2*) of the proton spins are the most significant factors that determine the proton signal intensity from a particular tissue. *T1* describes the spin-lattice relaxation of **M** returning to equilibrium after $\boldsymbol{B_1}$ is removed. Here, random motion of lattice molecules fluctuates at the Larmor frequency to increase relaxation to the lower energy state. *T2* describes the spin-spin relaxation returning to zero as random motion of molecules resonating at the same frequency leads to reduction of phase coherence.

Further, longitudinal relaxation rate can be enhanced by the addition of a paramagnetic metal and is described by,

$$R_1^{obs} = R_{1p}^{is} + R_{1p}^{os} + R_1^{w}.$$

R_{1p}^{is} represents the contribution due to exchange of water molecules coordinating to the inner sphere of the metal ion, while R_{1p}^{os} represents the contribution due to water diffusion into to outer sphere of the metal ion. These contributions are added to the water relaxation rate in the absence of the paramagnetic metal, R_1^{w}, to determine the observed longitudinal relaxation rate R_1^{obs}. **Figure 1.2** schematically represents the two relaxation mechanisms. The equation,

$$R_{1p}^{is} = \frac{(c \times q)}{55.6} \times \frac{1}{(T^{H}_{1M} + \tau_m)}$$

describes the inner sphere relaxation rate. The molar concentration of the paramagnetic metal ion is c. The number of water molecules coordinated to the metal ion is q, with τ_m as the mean residence lifetime. T^{H}_{1M} is the longitudinal relaxation time of each coordinated water molecule which is described in clinical settings as,

$$T^{H}_{1M} = \frac{(2\ \gamma_1^2 g^2 \mu_B^2)}{(15\ r_{GdH}^6)} \quad S(S+1) \quad \frac{[(7\ \tau_{c2})}{[(1 + \omega_S^2 \tau_{c2}^3)} + \frac{(3\ \tau_{c1})]}{(1 + \omega_I^2\ \tau_{c1}^2)]}.$$

Here, $\gamma_1$is the nuclear gyromagnetic factor, g is the electron g-factor, μ_B is the Bohr magneton, r_{GdH} is the electron spin-proton distance, S is the spin of the paramagnetic ion, ω_S is the electron Larmor frequency, ω_I is the nuclear Larmor frequency, and τ_c is the correlation time. The correlation time is described by,

$$\frac{1}{\tau_c} = \frac{1}{\tau_m} + \frac{1}{\tau_r} + \frac{1}{\tau_c^i} \quad ; i = 1,2$$

where τ_m is the water proton mean residence time, τ_r is the reorientational correlation time, τ_c^1 is the longitudinal electron spin relaxation time, and τ_c^2 is transverse electron spin relaxation time. Many groups have attempted to alter relaxivities by adjusting parameters, such as q, τ_m , τ_r, and r_{GdH}.[25, 26]

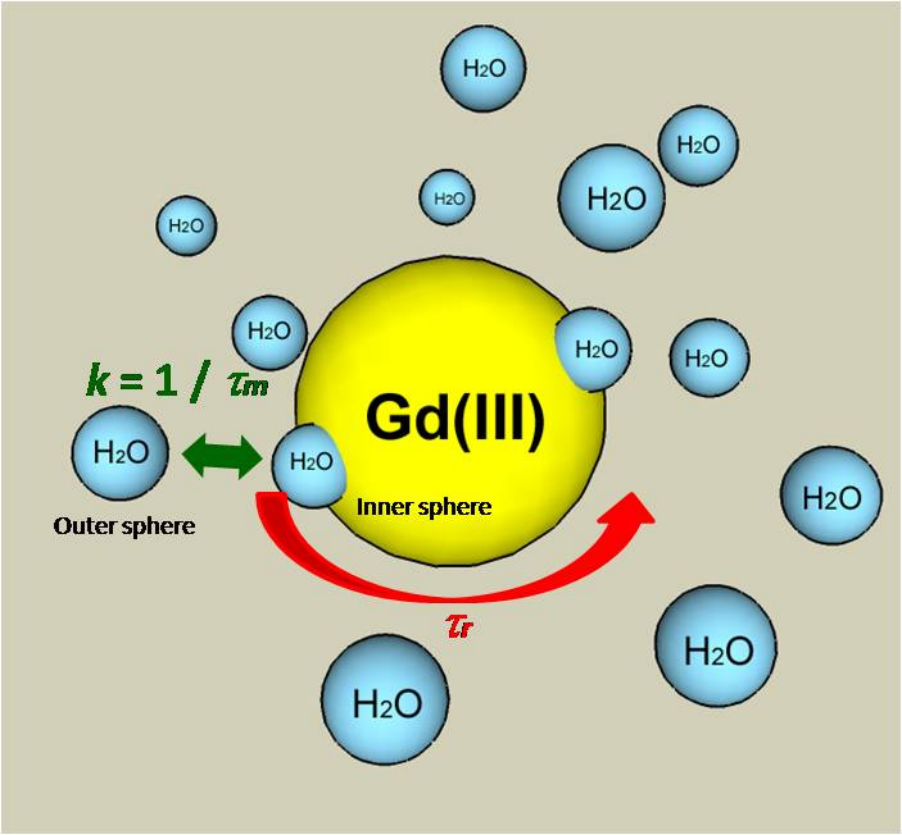

Figure 1.2 Schematic representation of paramagnetic Gd(III) interaction with water molecules and some of the main parameters affecting relaxation.

By administering contrast agents, the *T1* and *T2* parameters can be manipulated to gain greater image contrast of specific tissues. This is particularly important when imaging diseases where the abnormal disease tissue has similar water content to the normal tissue. Highly paramagnetic Gd(III)-chelates have been used to enhance water proton longitudinal relaxation, which results in increased (hyper-intense) MR signals. Approximately half of clinical MR images are performed with the aid of Gd(III)-chelate contrast agents to detect conditions such as organ perfusion, blood/brain barrier abnormalities, and aberrant kidney

function.[27] Alternatively, a contrast agent can be used to enhance water transverse relaxation, leading to reduced (hypo-intense) MR signals.

MRI is intrinsically much less sensitive than other imaging techniques such as positron-emission tomography (PET) or single photon-emission computed tomography (SPECT). As a result, it remains a great challenge to develop MR contrast agents that specifically target the diseased tissues. The advances in molecular and cell biology have uncovered a large number of biomarkers that are overexpressed on cell surfaces of a number of diseases. A straightforward strategy is to selectively and specifically delivering imaging contrast agents by conjugation to affinity molecules to the biomarkers. Such an approach has been successfully used to design target-specific PET and SPECT contrast agents by tagging radionuclides or their complexes with antibodies or other cell-targeting molecules.[28-33] However, Gd(III)-chelates at sub-mM concentrations are needed to provide sufficient MR image contrasts. This concentration is several orders of magnitude higher than that of overexpressed biomarkers.[34] There is thus a urgent need of synthetic strategies that allow for the delivery of a very large payload of Gd(III) chelates with each cell-targeting molecule.

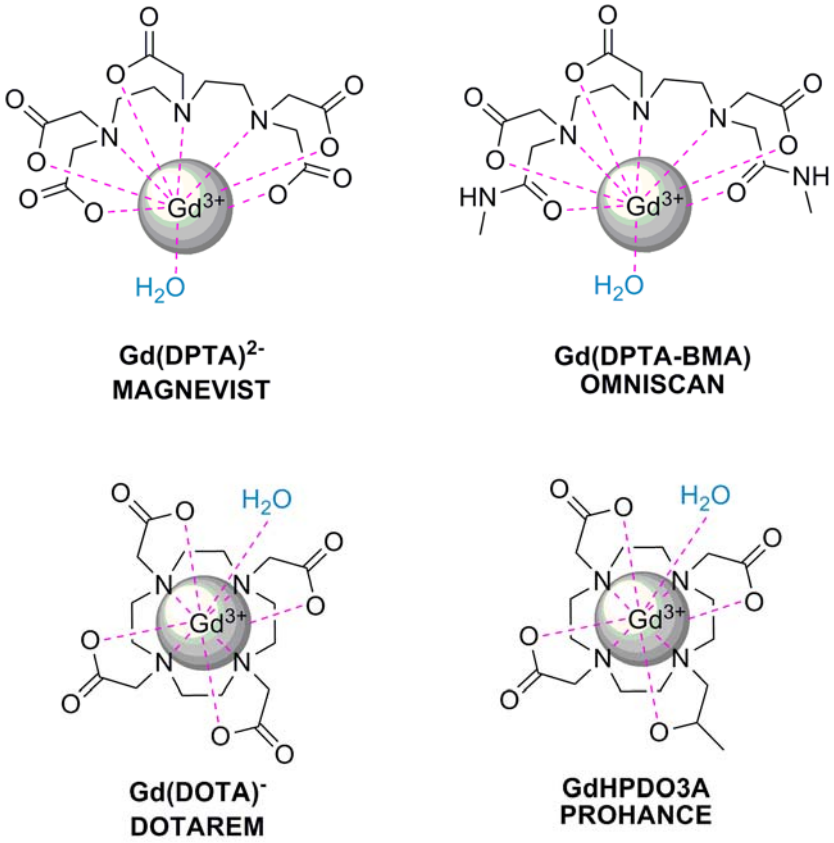

Figure 1.3 Examples of low molecular weight Gd(III) complexes clinically used for contrast-enhanced MRI.

Nanometer-scale materials have the ability to carry high payloads while maintaining the ability to move through physiological systems. For MRI contrast enhancement, these materials continue to require paramagnetic metals ions such as Gd(III), necessitating the development of hybrid cargo platforms. The many nanomaterial strategies – including superparamagnetic iron oxide, microemulsions, liposomes, and hybrid silica nanoparticles – will be discussed throughout this section.

1.2.1 Superparamagnetic iron oxide nanoparticles

Superparamagnetic iron oxide (SPIO) nanoparticles were initially shown to improve the detection of focal liver lesions over the Gd(III)-DTPA enhanced MRI scans, leading to their FDA approval for clinical use in 1996,[35-37] SPIOs are ferrites composed of γ-Fe_2O_3 and Fe_3O_4 magnetite phases that can be prepared by a variety of methods, [1,38] most commonly by oxidative coprecipitation or thermal decomposition. Superparamagnetic properties of SPIOs allow for zero magnetization in the absence of an external magnetic field and the ability to efficiently relax proton spins for MRI. The highly efficient spin relaxation rates, longitudinal r_1 and transverse r_2, are achieved through the dipole interaction between the surrounding water protons and the high magnetic moment of the superparamagnetic particles.[38] The large magnetization difference between the non-homogeneous distribution of SPIOs gives rise to local field gradients, further enhancing relaxation of proton spins. Superparamagnetic species experience this phenomenon more significantly than individual paramagnetic Gd(III)-complexes, generating large increases in r_2 when moving to increased magnetic fields. At low concentrations, *T1*-effects can be detected, producing signal enhancement (bright images). In general, the *T2*-effects dominate and result in large enhancements of signal void (darkening of images). Higher detection sensitivity has been reported by utilizing sequences designed for *T2*-weighted imaging.[39]

As pioneered by Ralph Weissleder, recent efforts have been focused on developing SPIO/biomolecule conjugates for target-specific MR imaging of cancers and other diseases. In one formulation, superparamagnetic iron oxide nanoparticles were coated with cross-linked dextran, a naturally occurring glucose-based polysaccharide capable of complexing iron metal ions. Several variations of the formulation exist and are called cross-linked iron

oxide (CLIO), ultrasmall superparamagnetic iron oxide (USPIO), Combidex®, or Ferumoxtran in the basic science and clinical literature. Combidex® is composed of materials on the generally regarded as safe (GRAS) list and has received an approvable letter by the FDA (subject to certain conditions). CLIO has been extensively used to image diseases in animals and humans, such as cancers or arthritis, as well as molecular biological processes.

The surface modification with dextran that is crosslinked with epichlorohydrin is of key importance to achieve longer blood circulation times. Further, the dextran can be chemically modified for conjugation of targeting molecules.[40] Often, the dextran coated iron oxide nanoparticles can be used without any further functionalization to show image enhancement of disease states. Due to the dextran stealth capabilities from the reticuloendothelial system (RES), signal void in the circulation can be detected due to the *T2* relaxation of the water protons. Upon capture, the CLIO contrast enhancement can image abnormalities of the RES. Weissleder showed such imaging capabilities in a clinical study of eighty prostate cancer patients[41] as well as other diseases[21, 41-45]. The CLIO was shown to be lymphtrophic and could be effectively used to image nodal abnormalities that were otherwise undetectable.

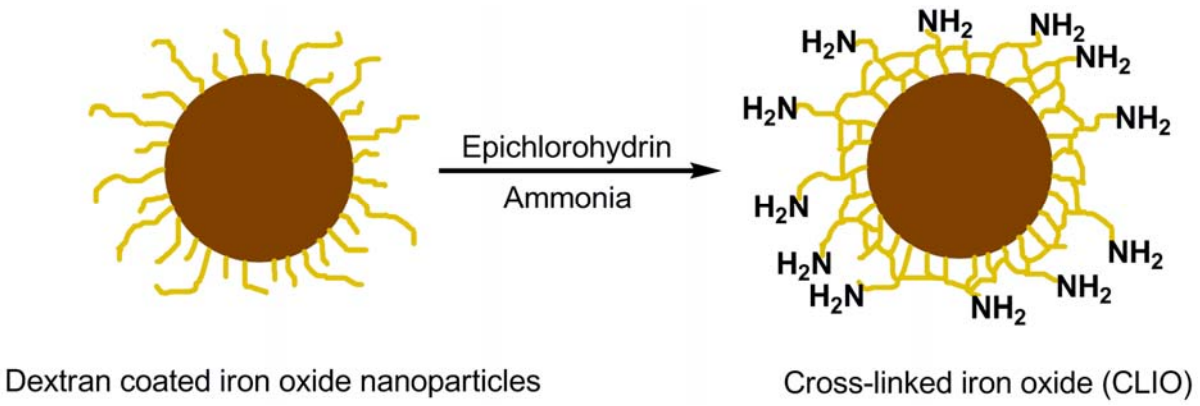

Figure 1.4 Dextran coating of iron oxide nanoparticles are cross-linked by epichlorohydrin and amine terminated by ammonia to form hybrid nanomaterial MRI contrast agents with surface functionalization moieties.

The cellular events involved in inflammation has led to the study of leukocyte action in arthritis[46] and arteriosclerosis[47, 48]. Particularly, monocytes and macrophages have emerged as a highly active set of cells in the inflammatory process. Adoptive transfer studies have been presented as an additional use for CLIO nanoparticles for imaging cellular pathogenesis of autoimmune diseases. Specifically, monocytes and T-cells were loaded *ex vivo* before allowing migration to disease sites.[49-53] CLIO can also be used to detect analyte concentrations within tissue through action as a magnetic switch that can form reversible cluster assemblies. At low glucose concentrations, concavalin-A is multivalently bound by glucose-derivatized CLIO to form larger aggregations that can be detected by *T2* changes.[54] Additional CLIO systems based upon this *T2*-effect magnetic switch concept have been used to detect changes due to enzymatic activity on peptide sequences[20] and oligonucleotides.[55] The dextran coating can be chemically modified and used to conjugate affinity molecules to enable the iron oxide nanoparticles to target and report the presence of disease tissue. Peptides and proteins have been used as functional conjugates with these nanoparticles to image prostate, hepatic, splenic, and glial neoplasia.[41, 43, 56-61] Conjugated to E-selectin or

VCAM-1, CLIO detects endothelium specific proteins to monitor tumor angiogenesis.[40, 62] Apoptotic cells can also be detected when the CLIO particles are functionalized with Annexin V, a calcium dependant protein that has high affinity for the phosphatidylserine apoptosis marker in the cell membrane.[19, 22, 63-66] These recent targeted iron oxide based contrast agents have progressed significantly from the fibrin-targeted CLIO that utilized the high availability of thrombin involved in blood coagulation.[67] Though extensively studied and considered relatively mature, the iron oxide MR contrast agents continue to be the trailblazer in biomedical imaging.

1.2.2 Multimodal perfluorocarbon microemulsion contrast agents

Wickline and Lanza have devoted immense efforts toward preparing MRI contrast agents using oil-in-water microemulsion technology.[68-71] Individual emulsion nanoparticles, approximately 250 nm in diameter, are formed with a perfluorocarbon core surrounded by a monolayer lipid shell. The particles can be synthesized by emulsification of the perfluorodichlorooctane, safflower oil, and glycerin with preformed microemulsions.[70] While stabilizing the nanoparticle, the lipid can also be designed to carry extraordinarily high payloads of metal centers, up to 90,000 Gd(III) chelates per microemulsion nanoparticle. These Gd-containing nanoparticles possess extremely large MR relaxivities on per particle basis,[72] and provide an ideal platform for conjugation to affinity molecules for target-specific imaging of various diseases.

Targeting molecules can also be incorporated into the lipid layer to create a highly modifiable surface capable of directing these particles to specific sites. Ligands for overexpressed disease biomarkers that have been used for this material ranges from small

molecules,[73] integrins,[74-76] fibrin,[77, 78] and antibodies.[79, 80] The targeted derivatives of the perfluorocarbon-lipid nanoparticles were used extensively to image cardiovascular structures and disorders, such as arterosclerosis.[68, 69, 71, 81, 82] Targeted imaging of neovascularization in atherosclerosis could be accomplished through avβ3-integrin modified perfluorocarbon microemulsion nanomaterials.[76, 83] In the past few years, these nanoparticulate MRI contrast agents have been used to detect tumors and angiogenesis.[84-87]

The perfluorocarbon core also allows for the unique capability of an additional MRI probe using the ^{19}F signal. ^{19}F MRI is an advantageous imaging tool because the magnetic resonance sensitivity is nearly as high as ^{1}H (83%), the low abundance of endogenous ^{19}F in biological systems, and the 100% natural abundance of ^{19}F isotope.[88] The perfluorocarbon emulsions encapsulated by lipid-surfactant monolayers have been used to prepare MRI contrast agents with high ^{19}F payloads. The perfluorocarbon-based microemulsion nanoparticles developed by Wickline and Lanza have demonstrated capabilities for target-specific Gd(III) enhanced MR imaging but also shown multimodalities that further expand the utilities of this novel class of nanomaterials in early diagnosis of a variety of diseases.

Figure 1.5 Dual $^{1}H/^{19}F$ MR imaging of thrombus in a human carotid endarterectomy: (a) Optical imaging showing moderate luminal narrowing, several atherosclerotic lesions and areas of calcification, (b) ^{19}F projection image acquired at 4.7T at the same location showing high signal enhancement due to perfluorocarbon nanoparticles, (c) ^{1}H image with false color overlay of quantified ^{19}F image. (Images have been used with permissions from reference [89].)

1.2.3 Liposomes

Liposomes, first discovered over 40 years ago, are vesicles formed from amphiphiles such as phospholipids. The interaction of the amphiphilic molecules with each other and the surrounding environment induces the formation of a lipid bilayer structure that is spherical in shape. Due to their cargo carrying capacity, liposomes have been widely explored for drug delivery. With the ability to encapsulate and protect a variety of therapeutics that may be unstable or poorly soluble in physiological systems, the efficiency of liposomes in drug delivery is believed to result from membrane bilayer fusion with the target cell membrane or via endocytosis. In cell culture, liposomes are actively used and commercially available for transfection of DNA to transform a host cell.

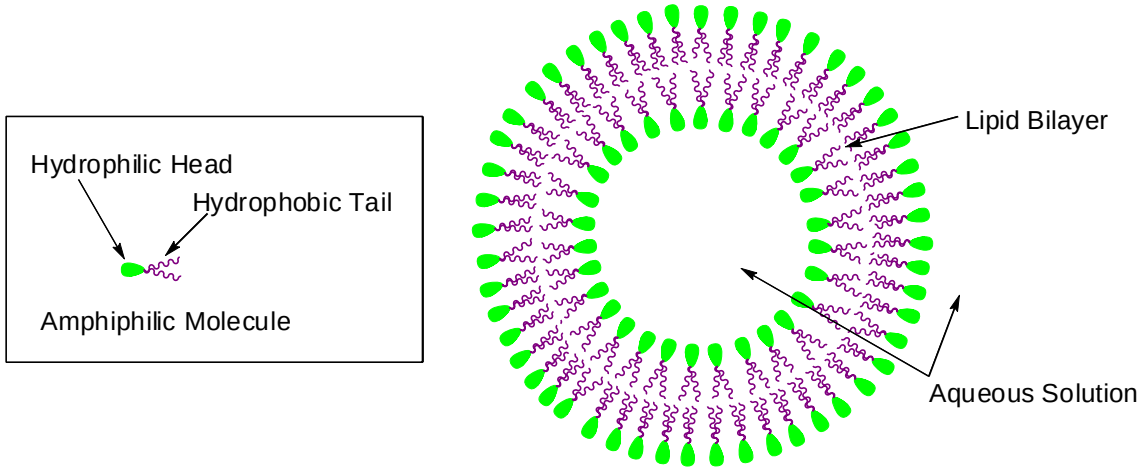

Figure 1.6 Schematic representation of liposome: Self-assembly of amphiphilic molecules in aqueous solution forms a lipid bilayer containing spherical vesicle.

Gadolinium-labeled liposomes[90-96] were prepared by modifying the structure of the amphiphiles. Gd(III) was coordinated to a DTPA chelator incorporated into the hydrophilic head group. The lipid bilayer composition is easily modifiable, as the paramagnetic Gd(III) containing amphipathic molecules could be incorporated into preexisting liposome designs composed of egg lecithin and cholesterol. The first Gd(III)-containing liposomes, tested by imaging the liver and spleen of normal Balb/c mice, were confirmed to be viable as MRI contrast agents. Later formulations were reported to show contrast enhancement of hepatic metastases in rats.[97, 98]

A key advantage of liposomal nanoparticles is the tunable composition of the bilayer structure. Amphiphiles with different unique properties can be used to tune the characteristics and behavior of the liposome. In addition to the incorporation of Gd(III)-based MR contrast agents in the liposome bilayer, they also allow for multimodal imaging by including contrast agents for optical imaging,[99, 100] single-photon emission computed tomography (SPECT),[101-103] and improved *T2*-weighted enhancement.[104]. Another important potential of liposomes lies in the ability to add cell-targeting moieties to the bilayer surface. This is generally accomplished by synthesis of hydrophilic targeting molecules with hydrophilic tails to be incorporated into the bilayer as amphiphiles. A number of target-specific liposome-based contrast agents have already been explored for imaging IGROV-1 xenograft tumors[99] and hepatic metastases[98] in rodents.

1.2.4 Microemulsion-templated wax nanoparticles

Oil-in-water microemulsions have been used as templates to engineer stable emulsifying wax nanoparticles containing gadolinium for potential use as MRI contrast

agents.[105] Using a simple, reproducible technique (**Figure 1.5**) reported by Mumper *et al*. table wax nanoparticles of ~125 nm in diameter were produced. This synthetic procedure is scalable to industrial production levels.[106-108] The wax nanoparticles were first reported as delivery vessels of Gd(III) existing with a variety of hydrophobic ligands, such as acetylacetonate or hexanedione, for potential neutron capture therapy.

To adapt for use as an MRI contrast agent precursor, dimyristoyl phosphoethanolamine diethylene triamine pentaacetate (DTPA) molecules were added during the nanoparticle formation. Preloading the dimyristoyl phosphoethanolamine DTPA with Gd(III) before particle formation could greatly enhance the Gd(III) loading. With recent safety concerns with Gd(III) toward patients prone to renal failure, limiting Gd(III) may be a beneficial strategy. In addition, introduction of Gd(III) after nanoparticle formation would coordinate only surfaced exposed dimyristoyl phosphoethanolamine DTPA with ready access to water, maximizing the efficiency of each metal center to relax water protons.

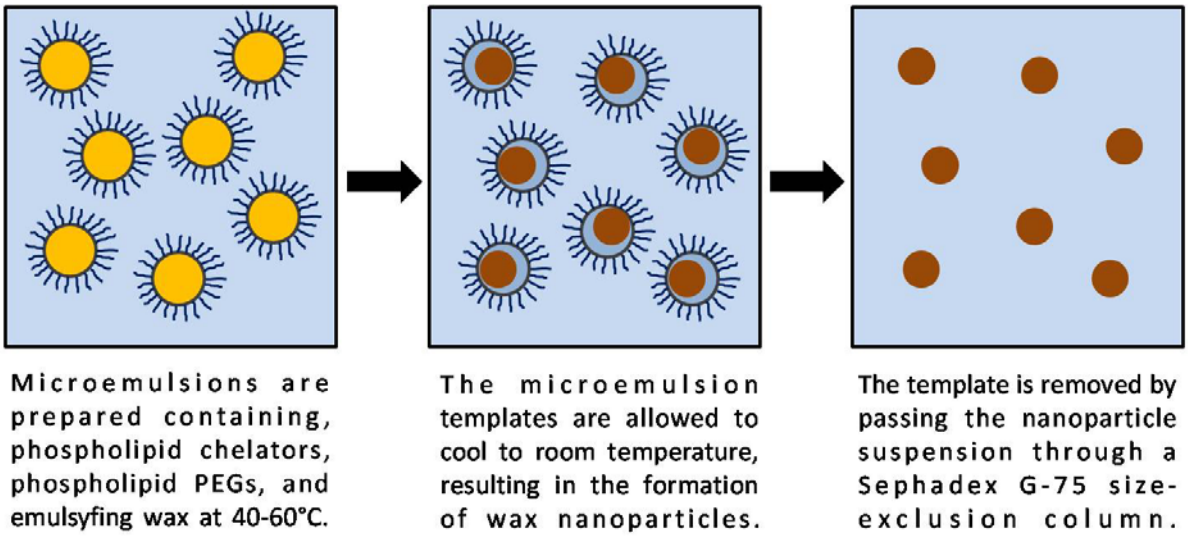

Figure 1.7 Schematic representation of the formation of "wax" nanoparticles by microemulsion template synthesis using variable temperature techniques.

The wax nanoparticles have a payload of approximately 10^5 Gd(III) per nanoparticle, determined through inductively coupled plasma-atomic emission spectroscopy. In a 4.7T MR scanner, relaxivities were determined to be *r1* = 7.1 and *r2* = 13.0 per s^{-1} per mM Gd, suspended in 10% bovine serum. Zn(II) and Cu(II) were used as competing ions for transmetallation kinetics of Gd(III) from the nanoparticles. Kinetic constants of K_1 = 0.033 and K_{-1} = 0.022 h^{-1} with an equilibrium constant of 1.5 and thermodynamic binding constant for Gd(III) to the nanoparticles of ~10^{18} M^{-1} were determined.

Polyethylene glycol (PEG; average MW = 5000) was later incorporated into the Gd(III)-containing wax nanoparticles.[109] The PEG molecules reduce the uptake by the RES system, allowing longer blood circulation times. Using the enhanced permeability and retention (EPR) effect caused by the leaky vasculature of tumors, the PEGylated Gd(III)-containing wax nanoparticles were used for MRI of nude mice bearing A549 lung carcinoma xenografts. Detailed biodistribution profiles and pharmacokinetics reported in these animals, with tumor uptake of Gd(III) consistent with values of *T1* enhancement from MRI.

1.2.5 Hybrid silica nanoparticles

Perfluorocarbon microemulsion, liposomal, and wax nanoparticles described above tend to be larger in size with diameters typically in 125-300 nm. Such particles are useful for intravascular applications but might not efficiently pass through blood vessel for extravascular imaging. The Lin group has sought to develop Gd-containing hybrid nanoparticles that have tunable sizes. Highly robust hybrid multimodal contrast agents have been developed using silica nanoparticles of diameters from 20 to 100 nm. Silica, a network of SiO_2, is often used to develop functional materials by grafting alkylsiloxane-containing

agents. In physiological systems, the material is inert and shows negligible acute toxicity in tissues and cells. The preparation and industrial use of silica particles are well established. Ammonia catalyzed hydrolysis of tetraethylorthosilicate (the so called Stöber synthesis) is a well established route for the production of silica particles.[110, 111]

Previously, the Lin group has designed hybrid silica nanoparticles with potential utility as multimodal imaging agents.[112] Using a well-established water-in-oil reverse microemulsion synthetic procedure, nanoparticles with luminescent $[Ru(bpy)_3]Cl_2$ core and silylated Gd(III) complex surface coatings were prepared for optical and MR imaging. In supplement to a monolayer system of Gd(III) chelate surface coating, a multilayer system was also developed for increased Gd(III) loading. The nanomaterials were extensively characterized by TEM, TGA, DCP, and relaxivity measurements in a clinical MR scanner.

The nanoparticles were further evaluated as multimodal imaging agents with *in vitro* studies using cell viability assays, confocal fluorescence microscopy, flow cytometry, and MRI of cell pellets. The ability to label monocytes was specifically studied, because of these cells' participation in mounting inflammatory responses and adherent phagocytic capacity. Further, the nanomaterials were shown to be robust and resist degradation by the phagocytic monocytes after intracellular uptake. Thus, these hybrid nanomaterials were determined to be attractive for tracking labeled monocytes in *in viv*o disease models of inflammatory arthritis. Chapter 2 describes the efficacy of the monolayer coated nanoparticle for early detection of collagen-induced arthritis in murine mouse models.

In order to design further methods of increasing Gd(III) payloads on the surfaces of hybrid silica nanomaterials, our group devised a polyelectrolyte layer-by-layer self-assembly approach to increase the Gd(III) loading.[113] Unlike the previously described multilayer

system of silylated Gd(III) complexes,[112] this approach maintains water accessibility to the metal centers for efficient water proton relaxation. MR-enhancing Gd(III)-chelate oligomers with a net positive charge were deposited onto the negatively charged surface of the aforementioned silica nanoparticles with a monolayer of Gd(III) complexes. The addition of polyanion layers could be utilized for incorporating additional layers of Gd(III)-chelate oligomer. The alternating, stepwise layer-by-layer deposition of polyanions and polycations produces flexible architectures of macromolecules on nanomaterial surfaces. Further, electrostatics could be used to add cancer targeting peptides to the surface of the nanoparticles. Chapter 3 describes the steps and characterization of these hybrid nanomaterials for increasing MR relaxivities and targeting of cancer cells.

1.3 Hybrid nanomaterials for protein purification

Recent advances in proteomics provide the ability to design and generate many recombinant proteins in cell cultures. A large number of proteins can be produced in large quantities for research and pharmaceutical purposes. The purification of proteins however remains a significant challenge due to the complexities of their isolation from the biological systems. After the protein is produced, release is achieved through cell lysis, which can be accomplished through mechanical disruption, sonication, freeze/thaw, mortar/pestle grinding, detergents, or protease inhibitors. The crude cell lysate mixtures from these processes contain cell debris and/or surfactants. Many techniques have been employed to purify desired proteins, including precipitation, dialysis, gel filtration, ion exchange chromatography, and affinity chromatography.

Affinity chromatography uses specific binding interactions between molecules to purify target proteins. A variety of ligands, ranging from antibodies, proteins (avidin) and protein fragments (Protein A or G), peptides (glutathione), carbohydrates (dextrin), and small molecules (biotin), are available for interaction with the target protein. The ligand of choice may be immobilized onto a solid support to bind the target, allowing impurities to be washed away, before elution of purified protein. Immobilized metal affinity chromatography (IMAC)[114] uses chelated metal ions to biding and purify recombinant fusion proteins.

For IMAC, the desired recombinant protein is designed to include a tag of six or more histidines at the N- or C-terminus (His×6 tag). Histidine contains an imidazole moiety that is able to bind metal ions. To isolate the target protein, the crude cell lysate is passed through resin containing immobilized metal ions. Nickel(II) ions chelated by an organic molecule with three or four binding sites, such as nitrilotriacetic acid (NTA), is a commonly used for resin immobilization.[115] The histidine tag will bind with the chelated metal with greater affinity than untagged impurities. After thorough washing, an imidazole solution is used to release the purified protein from the chelated metal ions.

The resin used in IMAC is a key parameter for the purification of the protein, as the affinity support needs to be chemically modifiable for attachment of protein-binding metal ions and have a high surface area for interaction. Porous gel supports, such as cross-linked agarose or polyacrylamide are widely used, but easily crush under pressure and often necessitate the use of gravity flow columns. Microscale magnetic beads are a convenient support for affinity chromatography. The beads can be quickly immobilized with a magnet, allowing facile manipulation of supernatant washes and elutions. Magnetic nanoparticles

(~10 nm), which are several orders of magnitude smaller than commercially-available magnetic beads (~50 μm), have obvious surface area-to-volume advantages.

Bing Xu and coworkers have shown use of dopamine to design as a robust bifunctional molecule able to anchor chelated nickel(II) ions onto an the iron oxide surface of a cobalt nanoparticle.[116, 117] Dopamine contains a catechol moiety, a bidentate enediol, that is capable of tightly coordinating to transition metal ions. The interaction between the catechol moiety of dopamine and the iron on the surface of the nanoparticle was shown to be stable at high salt concentrations, in the presence of detergents, and in boiling water. These materials could be used to purify highly overexpressed green fluorescent protein (GFP) from *E. coli* cell lysates.

Significant effort has been devoted to gaining better understanding of the interaction between Ni-NTA/His×6 tag to improve the IMAC protein purification process. Using fluorescence anisotropy and fluorescence resonance energy transfer, Ebright *et al.* demonstrated the enhanced binding of the His×6 tag to a bivalent Ni-NTA compared to monovalent Ni-NTA.[118] Piehler *et al.* has continued to examine further affinity enhancements by multivalency of Ni-NTA to His×6 tag.[119, 120] Combining the strong affinity of multivalent Ni-NTA molecules with the increased surface area of superparamagnetic nanoparticles will allow improvement of IMAC protein purification.

The Lin group has designed a new bivalent Ni-NTA molecule with the catechol anchor for binding to iron oxide nanoparticles to create a hybrid system for protein purification.[121] The study showed that the multivalency effect led to enhanced binding of His×6 tagged proteins in native, folded conformations. Recombinant proteins often must be denatured during the IMAC purification process to expose the full His×6 tag from the protein

structure to ensure effective binding. Denaturing proteins can increase the efficiency of purification, but may not yield an active product. Refolding proteins in the test tube cannot accurately mimic the folding conditions within the cell during translation. A large percentage of recombinant proteins remain difficult to purify, hindering research on many important proteins.[122]

This work demonstrates the utility of the multivalency strategy in enhancing the binding of His×6-tagged proteins in their native, folded conformations. Selective purification of His×6-tagged proteins from crude cell lysates was achieved by using the Ni(II)-loaded iron oxide nanoparticles. The present platform is capable of efficient purification of His×6-tagged proteins that are expressed at low levels in mammalian cells. The present hybrid nanomaterial represents a novel nanoparticle-based high-capacity protein purification system with shorter incubation times, proportionally large washes, and significantly smaller elution volumes compared to commercially available microbeads.

1.4 Concluding remarks

We have introduced in this chapter several hybrid nanomaterial systems and their applications in biological applications such as MR image diagnostics and protein purification. In each case, the hybrid material system outperformed the current technology as a result of the unique combination of interesting properties. The success in these areas of research provides a testament to organic/inorganic hybrid nanomaterials's ability to offer many interesting characteristics that do not exist in either inorganic nanostructures or polymer colloidal particles alone. The modular synthetic procedures for organic/inorganic hybrid nanomaterials should allow further fine-tuning of their properties for target

applications. Such an amalgam of molecular chemistry and nanotechnology promises to lead to new hybrid nanomaterials for a wide range of biomedical applications, such as imaging or protein purification, across multiple scientific fields.

1.5 References

1. Gupta, A. K.; Naregalkar, R. R.; Vaidya, V. D.; Gupta, M., Recent advances on surface engineering of magnetic iron oxide nanoparticles and their biomedical applications. *Nanomed* **2007,** 2, (1), 23-39.

2. Sun, S.; Zeng, H., Size-controlled synthesis of magnetite nanoparticles. *J Am Chem Soc* **2002,** 124, (28), 8204-5.

3. So, M. K.; Xu, C.; Loening, A. M.; Gambhir, S. S.; Rao, J., Self-illuminating quantum dot conjugates for in vivo imaging. *Nat Biotechnol* **2006,** 24, (3), 339-43.

4. Jaiswal, J. K.; Mattoussi, H.; Mauro, J. M.; Simon, S. M., Long-term multiple color imaging of live cells using quantum dot bioconjugates. *Nat Biotechnol* **2003,** 21, (1), 47-51.

5. Vdovin, E. E.; Levin, A.; Patane, A.; Eaves, L.; Main, P. C.; Khanin, Y. N.; Dubrovskii, Y. V.; Henini, M.; Hill, G., Imaging the electron wave function in self-assembled quantum dots. *Science* **2000,** 290, (5489), 122-4.

6. Lee, C. C.; MacKay, J. A.; Frechet, J. M.; Szoka, F. C., Designing dendrimers for biological applications. *Nat Biotechnol* **2005,** 23, (12), 1517-26.

7. Hecht, S.; Frechet, J. M., Dendritic Encapsulation of Function: Applying Nature's Site Isolation Principle from Biomimetics to Materials Science. *Angew Chem Int Ed Engl* **2001,** 40, (1), 74-91.

8. Chen, T. J.; Cheng, T. H.; Hung, Y. C.; Lin, K. T.; Liu, G. C.; Wang, Y. M., Targeted folic acid-PEG nanoparticles for noninvasive imaging of folate receptor by MRI. *J Biomed Mater Res A* **2007**.

9. Kunii, R.; Onishi, H.; Machida, Y., Preparation and antitumor characteristics of PLA/(PEG-PPG-PEG) nanoparticles loaded with camptothecin. *Eur J Pharm Biopharm* **2007,** 67, (1), 9-17.

10. Yang, A.; Yang, L.; Liu, W.; Li, Z.; Xu, H.; Yang, X., Tumor necrosis factor alpha blocking peptide loaded PEG-PLGA nanoparticles: preparation and in vitro evaluation. *Int J Pharm* **2007,** 331, (1), 123-32.

11. Cheng, J.; Teply, B. A.; Sherifi, I.; Sung, J.; Luther, G.; Gu, F. X.; Levy-Nissenbaum, E.; Radovic-Moreno, A. F.; Langer, R.; Farokhzad, O. C., Formulation of functionalized PLGA-PEG nanoparticles for in vivo targeted drug delivery. *Biomaterials* **2007,** 28, (5), 869-76.

12. Oyewumi, M. O.; Yokel, R. A.; Jay, M.; Coakley, T.; Mumper, R. J., Comparison of cell uptake, biodistribution and tumor retention of folate-coated and PEG-coated gadolinium nanoparticles in tumor-bearing mice. *J Control Release* **2004,** 95, (3), 613-26.

13. Gratzel, M., Applied physics: Solar cells to dye for. *Nature* **2003,** 421, (6923), 586-7.

14. Wang, P.; Zakeeruddin, S. M.; Exnar, I.; Gratzel, M., High efficiency dye-sensitized nanocrystalline solar cells based on ionic liquid polymer gel electrolyte. *Chem Commun (Camb)* **2002**, (24), 2972-3.

15. Gratzel, M., Photoelectrochemical cells. *Nature* **2001,** 414, (6861), 338-44.

16. Nazeeruddin, M. K.; Pechy, P.; Renouard, T.; Zakeeruddin, S. M.; Humphry-Baker, R.; Comte, P.; Liska, P.; Cevey, L.; Costa, E.; Shklover, V.; Spiccia, L.; Deacon, G. B.; Bignozzi, C. A.; Gratzel, M., Engineering of efficient panchromatic sensitizers for nanocrystalline TiO(2)-based solar cells. *J Am Chem Soc* **2001,** 123, (8), 1613-24.

17. Hu, A.; Yee, G. T.; Lin, W., Magnetically recoverable chiral catalysts immobilized on magnetite nanoparticles for asymmetric hydrogenation of aromatic ketones. *J Am Chem Soc* **2005,** 127, (36), 12486-7.

18. Wu, C. D.; Hu, A.; Zhang, L.; Lin, W., A homochiral porous metal-organic framework for highly enantioselective heterogeneous asymmetric catalysis. *J Am Chem Soc* **2005,** 127, (25), 8940-1.

19. Quinti, L.; Weissleder, R.; Tung, C. H., A fluorescent nanosensor for apoptotic cells. *Nano Lett* **2006,** 6, (3), 488-90.

20. Perez, J. M.; Josephson, L.; O'Loughlin, T.; Hogemann, D.; Weissleder, R., Magnetic relaxation switches capable of sensing molecular interactions. *Nat Biotechnol* **2002,** 20, (8), 816-20.

21. Harisinghani, M. G.; Weissleder, R., Sensitive, noninvasive detection of lymph node metastases. *PLoS Med* **2004,** 1, (3), e66.

22. Weissleder, R., Molecular imaging in cancer. *Science* **2006,** 312, (5777), 1168-71.

23. Sharma, P.; Brown, S.; Walter, G.; Santra, S.; Moudgil, B., Nanoparticles for bioimaging. *Adv Colloid Interface Sci* **2006,** 123-126, 471-85.

24. Merbach, A. E.; Toth, E., *The Chemistry of Contrast Agents in Medical Magnetic Resonance Imaging*. John Wiley & Sons, Ltd.: New York, 2001.

25. Doble, D. M.; Melchior, M.; O'Sullivan, B.; Siering, C.; Xu, J.; Pierre, V. C.; Raymond, K. N., Toward optimized high-relaxivity MRI agents: the effect of ligand basicity on the thermodynamic stability of hexadentate hydroxypyridonate/catecholate gadolinium(III) complexes. *Inorg Chem* **2003,** 42, (16), 4930-7.

26. Aime, S.; Botta, M.; Fasano, M.; Terreno, E., Lanthanide(III) chelates fro NMR biomedical applications. *Chem. Soc. Rev.* **1998,** 27, 19-29.

27. Aime, S.; Botta, M.; Fasano, M.; Terreno, E., Lanthanide(III) chelates for NMR biomedical applications. *Chemical Society Reviews* **1998,** 27, 19-29.

28. Haubner, R.; Weber, W. A.; Beer, A. J.; Vabuliene, E.; Reim, D.; Sarbia, M.; Becker, K. F.; Goebel, M.; Hein, R.; Wester, H. J.; Kessler, H.; Schwaiger, M., Noninvasive visualization of the activated alphavbeta3 integrin in cancer patients by positron emission tomography and [18F]Galacto-RGD. *PLoS Med* **2005,** 2, (3), e70.

29. Larson, S. M., Radioimmunology. Imaging and therapy. *Cancer* **1991,** 67, (4 Suppl), 1253-60.

30. Miller, J. C.; Thrall, J. H., Clinical molecular imaging. *J Am Coll Radiol* **2004,** 1, (1 Suppl), 4-23.

31. Yang, D. J.; Kim, E. E.; Inoue, T., Targeted molecular imaging in oncology. *Ann Nucl Med* **2006,** 20, (1), 1-11.

32. Kung, M. P.; Kung, H. F., Mass effect of injected dose in small rodent imaging by SPECT and PET. *Nucl Med Biol* **2005,** 32, (7), 673-8.

33. Bischof Delaloye, A.; Delaloye, B., Tumor imaging with monoclonal antibodies. *Semin Nucl Med* **1995,** 25, (2), 144-64.

34. Caravan, P.; Ellison, J. J.; McMurry, T. J.; Lauffer, R. B., Gadolinium(III) Chelates as MRI Contrast Agents: Structure, Dynamics, and Applications. *Chem Rev* **1999,** 99, (9), 2293-352.

35. Gupta, H.; Weissleder, R., Targeted contrast agents in MR imaging. *Magn Reson Imaging Clin N Am* **1996,** 4, (1), 171-84.

36. Petersein, J.; Saini, S.; Weissleder, R., Liver. II: Iron oxide-based reticuloendothelial contrast agents for MR imaging. Clinical review. *Magn Reson Imaging Clin N Am* **1996,** 4, (1), 53-60.

37. Stiskal, M.; Schwickert, H. C.; Demsar, F.; Roberts, T. P.; Szolar, D.; Weissleder, R.; Brasch, R. C., Contrast enhancement in experimental radiation-induced liver injury: comparison of hepatocellular and reticuloendothelial particulate contrast agents. *J Magn Reson Imaging* **1996,** 6, (2), 286-90.

38. Corot, C.; Robert, P.; Idee, J. M.; Port, M., Recent advances in iron oxide nanocrystal technology for medical imaging. *Adv Drug Deliv Rev* **2006,** 58, (14), 1471-504.

39. Daldrup-Link, H. E.; Rudelius, M.; Oostendorp, R. A.; Settles, M.; Piontek, G.; Metz, S.; Rosenbrock, H.; Keller, U.; Heinzmann, U.; Rummeny, E. J.; Schlegel, J.; Link, T. M., Targeting of hematopoietic progenitor cells with MR contrast agents. *Radiology* **2003,** 228, (3), 760-7.

40. Kang, H. W.; Josephson, L.; Petrovsky, A.; Weissleder, R.; Bogdanov, A., Jr., Magnetic resonance imaging of inducible E-selectin expression in human endothelial cell culture. *Bioconjug Chem* **2002,** 13, (1), 122-7.

41. Harisinghani, M. G.; Barentsz, J.; Hahn, P. F.; Deserno, W. M.; Tabatabaei, S.; van de Kaa, C. H.; de la Rosette, J.; Weissleder, R., Noninvasive detection of clinically occult lymph-node metastases in prostate cancer. *N Engl J Med* **2003,** 348, (25), 2491-9.

42. Harisinghani, M.; Ross, R. W.; Guimaraes, A. R.; Weissleder, R., Utility of a new bolus-injectable nanoparticle for clinical cancer staging. *Neoplasia* **2007,** 9, (12), 1160-5.

43. Harisinghani, M. G.; Jhaveri, K. S.; Weissleder, R.; Schima, W.; Saini, S.; Hahn, P. F.; Mueller, P. R., MRI contrast agents for evaluating focal hepatic lesions. *Clin Radiol* **2001,** 56, (9), 714-25.

44. Harisinghani, M. G.; Saini, S.; Weissleder, R.; Halpern, E. F.; Schima, W.; Rubin, D. L.; Stillman, A. E.; Sica, G. T.; Small, W. C.; Hahn, P. F., Differentiation of liver hemangiomas from metastases and hepatocellular carcinoma at MR imaging enhanced with blood-pool contrast agent Code-7227. *Radiology* **1997,** 202, (3), 687-91.

45. Harisinghani, M. G.; Saini, S.; Weissleder, R.; Rubin, D.; deLange, E.; Harms, S.; Weinreb, J.; Small, W.; Sukerkar, A.; Brown, J. J.; Zelch, J.; Lucas, M.; Morris, M.; Hahn, P. F., Splenic imaging with ultrasmall superparamagnetic iron oxide ferumoxtran-10 (AMI-7227): preliminary observations. *J Comput Assist Tomogr* **2001,** 25, (5), 770-6.

46. Wunder, A.; Schellenberger, E.; Mahmood, U.; Bogdanov, A., Jr.; Muller-Ladner, U.; Weissleder, R.; Josephson, L., Methotrexate-induced accumulation of fluorescent annexin V in collagen-induced arthritis. *Mol Imaging* **2005,** 4, (1), 1-6.

47. Jaffer, F. A.; Nahrendorf, M.; Sosnovik, D.; Kelly, K. A.; Aikawa, E.; Weissleder, R., Cellular imaging of inflammation in atherosclerosis using magnetofluorescent nanomaterials. *Mol Imaging* **2006,** 5, (2), 85-92.

48. Swirski, F. K.; Pittet, M. J.; Kircher, M. F.; Aikawa, E.; Jaffer, F. A.; Libby, P.; Weissleder, R., Monocyte accumulation in mouse atherogenesis is progressive and proportional to extent of disease. *Proc Natl Acad Sci U S A* **2006,** 103, (27), 10340-5.

49. Kang, H. W.; Torres, D.; Wald, L.; Weissleder, R.; Bogdanov, A. A., Jr., Targeted imaging of human endothelial-specific marker in a model of adoptive cell transfer. *Lab Invest* **2006,** 86, (6), 599-609.

50. Kircher, M. F.; Grimm, J.; Swirski, F. K.; Libby, P.; Gerszten, R. E.; Allport, J. R.; Weissleder, R., Noninvasive In Vivo Imaging of Monocyte Trafficking to Atherosclerotic Lesions. *Circulation* **2008**.

51. Melder, R. J.; Munn, L. L.; Stoll, B. R.; Marecos, E. M.; Baxter, L. T.; Weissleder, R.; Jain, R. K., Systemic distribution and tumor localization of adoptively transferred lymphocytes in mice: comparison with physiologically based pharmacokinetic model. *Neoplasia* **2002,** 4, (1), 3-8.

52. Moore, A.; Sun, P. Z.; Cory, D.; Hogemann, D.; Weissleder, R.; Lipes, M. A., MRI of insulitis in autoimmune diabetes. *Magn Reson Med* **2002,** 47, (4), 751-8.

53. Pittet, M. J.; Grimm, J.; Berger, C. R.; Tamura, T.; Wojtkiewicz, G.; Nahrendorf, M.; Romero, P.; Swirski, F. K.; Weissleder, R., In vivo imaging of T cell delivery to tumors after adoptive transfer therapy. *Proc Natl Acad Sci U S A* **2007,** 104, (30), 12457-61.

54. Sun, E. Y.; Weissleder, R.; Josephson, L., Continuous analyte sensing with magnetic nanoswitches. *Small* **2006,** 2, (10), 1144-7.

55. Perez, J. M.; O'Loughin, T.; Simeone, F. J.; Weissleder, R.; Josephson, L., DNA-based magnetic nanoparticle assembly acts as a magnetic relaxation nanoswitch allowing screening of DNA-cleaving agents. *J Am Chem Soc* **2002,** 124, (12), 2856-7.

56. Funovics, M.; Montet, X.; Reynolds, F.; Weissleder, R.; Josephson, L., Nanoparticles for the optical imaging of tumor E-selectin. *Neoplasia* **2005,** 7, (10), 904-11.

57. Elizondo, G.; Weissleder, R.; Stark, D. D.; Guerra, J.; Garza, J.; Fretz, C. J.; Todd, L. E.; Ferrucci, J. T., Hepatic cirrhosis and hepatitis: MR imaging enhanced with superparamagnetic iron oxide. *Radiology* **1990,** 174, (3 Pt 1), 797-801.

58. Weissleder, R.; Elizondo, G.; Stark, D. D.; Hahn, P. F.; Marfil, J.; Gonzalez, J. F.; Saini, S.; Todd, L. E.; Ferrucci, J. T., The diagnosis of splenic lymphoma by MR imaging: value of superparamagnetic iron oxide. *AJR Am J Roentgenol* **1989,** 152, (1), 175-80.

59. Weissleder, R.; Saini, S.; Stark, D. D.; Wittenberg, J.; Ferrucci, J. T., Dual-contrast MR imaging of liver cancer in rats. *AJR Am J Roentgenol* **1988,** 150, (3), 561-6.

60. Wunderbaldinger, P.; Josephson, L.; Weissleder, R., Tat peptide directs enhanced clearance and hepatic permeability of magnetic nanoparticles. *Bioconjug Chem* **2002,** 13, (2), 264-8.

61. Montet, X.; Montet-Abou, K.; Reynolds, F.; Weissleder, R.; Josephson, L., Nanoparticle imaging of integrins on tumor cells. *Neoplasia* **2006,** 8, (3), 214-22.

62. Kelly, K. A.; Allport, J. R.; Tsourkas, A.; Shinde-Patil, V. R.; Josephson, L.; Weissleder, R., Detection of vascular adhesion molecule-1 expression using a novel multimodal nanoparticle. *Circ Res* **2005,** 96, (3), 327-36.

63. Korngold, E. C.; Jaffer, F. A.; Weissleder, R.; Sosnovik, D. E., Noninvasive imaging of apoptosis in cardiovascular disease. *Heart Fail Rev* **2007**.

64. Schellenberger, E. A.; Hogemann, D.; Josephson, L.; Weissleder, R., Annexin V-CLIO: a nanoparticle for detecting apoptosis by MRI. *Acad Radiol* **2002,** 9 Suppl 2, S310-1.

65. Petrovsky, A.; Schellenberger, E.; Josephson, L.; Weissleder, R.; Bogdanov, A., Jr., Near-infrared fluorescent imaging of tumor apoptosis. *Cancer Res* **2003,** 63, (8), 1936-42.

66. Schellenberger, E. A.; Sosnovik, D.; Weissleder, R.; Josephson, L., Magneto/optical annexin V, a multimodal protein. *Bioconjug Chem* **2004,** 15, (5), 1062-7.

67. Botnar, R. M.; Perez, A. S.; Witte, S.; Wiethoff, A. J.; Laredo, J.; Hamilton, J.; Quist, W.; Parsons, E. C., Jr.; Vaidya, A.; Kolodziej, A.; Barrett, J. A.; Graham, P. B.; Weisskoff, R. M.; Manning, W. J.; Johnstone, M. T., In vivo molecular imaging of acute and subacute thrombosis using a fibrin-binding magnetic resonance imaging contrast agent. *Circulation* **2004,** 109, (16), 2023-9.

68. Wickline, S. A.; Neubauer, A. M.; Winter, P. M.; Caruthers, S. D.; Lanza, G. M., Molecular imaging and therapy of atherosclerosis with targeted nanoparticles. *J Magn Reson Imaging* **2007,** 25, (4), 667-80.

69. Lanza, G.; Winter, P.; Cyrus, T.; Caruthers, S.; Marsh, J.; Hughes, M.; Wickline, S., Nanomedicine opportunities in cardiology. *Ann N Y Acad Sci* **2006,** 1080, 451-65.

70. Lanza, G. M.; Wallace, K. D.; Scott, M. J.; Cacheris, W. P.; Abendschein, D. R.; Christy, D. H.; Sharkey, A. M.; Miller, J. G.; Gaffney, P. J.; Wickline, S. A., A novel site-targeted ultrasonic contrast agent with broad biomedical application. *Circulation* **1996,** 94, (12), 3334-40.

71. Lanza, G. M.; Winter, P. M.; Caruthers, S. D.; Hughes, M. S.; Cyrus, T.; Marsh, J. N.; Neubauer, A. M.; Partlow, K. C.; Wickline, S. A., Nanomedicine opportunities for cardiovascular disease with perfluorocarbon nanoparticles. *Nanomed* **2006,** 1, (3), 321-9.

72. Morawski, A. M.; Winter, P. M.; Crowder, K. C.; Caruthers, S. D.; Fuhrhop, R. W.; Scott, M. J.; Robertson, J. D.; Abendschein, D. R.; Lanza, G. M.; Wickline, S. A., Targeted nanoparticles for quantitative imaging of sparse molecular epitopes with MRI. *Magn Reson Med* **2004,** 51, (3), 480-6.

73. Low, P. S.; Henne, W. A.; Doorneweerd, D. D., Discovery and development of folic-Acid-based receptor targeting for imaging and therapy of cancer and inflammatory diseases. *Acc Chem Res* **2008,** 41, (1), 120-9.

74. Anderson, S. A.; Rader, R. K.; Westlin, W. F.; Null, C.; Jackson, D.; Lanza, G. M.; Wickline, S. A.; Kotyk, J. J., Magnetic resonance contrast enhancement of neovasculature with alpha(v)beta(3)-targeted nanoparticles. *Magn Reson Med* **2000,** 44, (3), 433-9.

75. Cyrus, T.; Abendschein, D. R.; Caruthers, S. D.; Harris, T. D.; Glattauer, V.; Werkmeister, J. A.; Ramshaw, J. A.; Wickline, S. A.; Lanza, G. M., MR three-dimensional molecular imaging of intramural biomarkers with targeted nanoparticles. *J Cardiovasc Magn Reson* **2006,** 8, (3), 535-41.

76. Winter, P. M.; Neubauer, A. M.; Caruthers, S. D.; Harris, T. D.; Robertson, J. D.; Williams, T. A.; Schmieder, A. H.; Hu, G.; Allen, J. S.; Lacy, E. K.; Zhang, H.; Wickline, S. A.; Lanza, G. M., Endothelial alpha(v)beta3 integrin-targeted fumagillin nanoparticles inhibit angiogenesis in atherosclerosis. *Arterioscler Thromb Vasc Biol* **2006,** 26, (9), 2103-9.

77. Marsh, J. N.; Partlow, K. C.; Abendschein, D. R.; Scott, M. J.; Lanza, G. M.; Wickline, S. A., Molecular imaging with targeted perfluorocarbon nanoparticles:

quantification of the concentration dependence of contrast enhancement for binding to sparse cellular epitopes. *Ultrasound Med Biol* **2007,** 33, (6), 950-8.

78. Marsh, J. N.; Senpan, A.; Hu, G.; Scott, M. J.; Gaffney, P. J.; Wickline, S. A.; Lanza, G. M., Fibrin-targeted perfluorocarbon nanoparticles for targeted thrombolysis. *Nanomed* **2007,** 2, (4), 533-43.

79. Mulder, W. J.; Strijkers, G. J.; Griffioen, A. W.; van Bloois, L.; Molema, G.; Storm, G.; Koning, G. A.; Nicolay, K., A liposomal system for contrast-enhanced magnetic resonance imaging of molecular targets. *Bioconjug Chem* **2004,** 15, (4), 799-806.

80. Mulder, W. J.; Strijkers, G. J.; van Tilborg, G. A.; Griffioen, A. W.; Nicolay, K., Lipid-based nanoparticles for contrast-enhanced MRI and molecular imaging. *NMR Biomed* **2006,** 19, (1), 142-64.

81. Cyrus, T.; Lanza, G. M.; Wickline, S. A., Molecular imaging by cardiovascular MR. *J Cardiovasc Magn Reson* **2007,** 9, (6), 827-43.

82. Cyrus, T.; Winter, P. M.; Caruthers, S. D.; Wickline, S. A.; Lanza, G. M., Magnetic resonance nanoparticles for cardiovascular molecular imaging and therapy. *Expert Rev Cardiovasc Ther* **2005,** 3, (4), 705-15.

83. Winter, P. M.; Morawski, A. M.; Caruthers, S. D.; Fuhrhop, R. W.; Zhang, H.; Williams, T. A.; Allen, J. S.; Lacy, E. K.; Robertson, J. D.; Lanza, G. M.; Wickline, S. A., Molecular imaging of angiogenesis in early-stage atherosclerosis with alpha(v)beta3-integrin-targeted nanoparticles. *Circulation* **2003,** 108, (18), 2270-4.

84. Caruthers, S. D.; Wickline, S. A.; Lanza, G. M., Nanotechnological applications in medicine. *Curr Opin Biotechnol* **2007,** 18, (1), 26-30.

85. Hu, G.; Lijowski, M.; Zhang, H.; Partlow, K. C.; Caruthers, S. D.; Kiefer, G.; Gulyas, G.; Athey, P.; Scott, M. J.; Wickline, S. A.; Lanza, G. M., Imaging of Vx-2 rabbit tumors with alpha(nu)beta3-integrin-targeted 111In nanoparticles. *Int J Cancer* **2007,** 120, (9), 1951-7.

86. Schmieder, A. H.; Winter, P. M.; Caruthers, S. D.; Harris, T. D.; Williams, T. A.; Allen, J. S.; Lacy, E. K.; Zhang, H.; Scott, M. J.; Hu, G.; Robertson, J. D.; Wickline, S. A.; Lanza, G. M., Molecular MR imaging of melanoma angiogenesis with alphanubeta3-targeted paramagnetic nanoparticles. *Magn Reson Med* **2005,** 53, (3), 621-7.

87. Winter, P. M.; Caruthers, S. D.; Kassner, A.; Harris, T. D.; Chinen, L. K.; Allen, J. S.; Lacy, E. K.; Zhang, H.; Robertson, J. D.; Wickline, S. A.; Lanza, G. M., Molecular imaging of angiogenesis in nascent Vx-2 rabbit tumors using a novel alpha(nu)beta3-targeted nanoparticle and 1.5 tesla magnetic resonance imaging. *Cancer Res* **2003,** 63, (18), 5838-43.

88. Higuchi, M.; Iwata, N.; Matsuba, Y.; Sato, K.; Sasamoto, K.; Saido, T. C., 19F and 1H MRI detection of amyloid beta plaques in vivo. *Nat Neurosci* **2005,** 8, (4), 527-33.

89. Morawski, A. M.; Winter, P. M.; Yu, X.; Fuhrhop, R. W.; Scott, M. J.; Hockett, F.; Robertson, J. D.; Gaffney, P. J.; Lanza, G. M.; Wickline, S. A., Quantitative "magnetic resonance immunohistochemistry" with ligand-targeted (19)F nanoparticles. *Magn Reson Med* **2004,** 52, (6), 1255-62.

90. Kabalka, G.; Buonocore, E.; Hubner, K.; Moss, T.; Norley, N.; Huang, L., Gadolinium-labeled liposomes: targeted MR contrast agents for the liver and spleen. *Radiology* **1987,** 163, (1), 255-8.

91. Kabalka, G. W.; Buonocore, E.; Hubner, K.; Davis, M.; Huang, L., Gadolinium-labeled liposomes containing paramagnetic amphipathic agents: targeted MRI contrast agents for the liver. *Magn Reson Med* **1988,** 8, (1), 89-95.

92. Kabalka, G. W.; Davis, M. A.; Buonocore, E.; Hubner, K.; Holmberg, E.; Huang, L., Gd-labeled liposomes containing amphipathic agents for magnetic resonance imaging. *Invest Radiol* **1990,** 25 Suppl 1, S63-4.

93. Kabalka, G. W.; Davis, M. A.; Holmberg, E.; Maruyama, K.; Huang, L., Gadolinium-labeled liposomes containing amphiphilic Gd-DTPA derivatives of varying chain length: targeted MRI contrast enhancement agents for the liver. *Magn Reson Imaging* **1991,** 9, (3), 373-7.

94. Kabalka, G. W.; Davis, M. A.; Moss, T. H.; Buonocore, E.; Hubner, K.; Holmberg, E.; Maruyama, K.; Huang, L., Gadolinium-labeled liposomes containing various amphiphilic Gd-DTPA derivatives: targeted MRI contrast enhancement agents for the liver. *Magn Reson Med* **1991,** 19, (2), 406-15.

95. Tilcock, C.; Unger, E.; Cullis, P.; MacDougall, P., Liposomal Gd-DTPA: preparation and characterization of relaxivity. *Radiology* **1989,** 171, (1), 77-80.

96. Unger, E.; Needleman, P.; Cullis, P.; Tilcock, C., Gadolinium-DTPA liposomes as a potential MRI contrast agent. Work in progress. *Invest Radiol* **1988,** 23, (12), 928-32.

97. Unger, E. C.; MacDougall, P.; Cullis, P.; Tilcock, C., Liposomal Gd-DTPA: effect of encapsulation on enhancement of hepatoma model by MRI. *Magn Reson Imaging* **1989,** 7, (4), 417-23.

98. Unger, E. C.; Winokur, T.; MacDougall, P.; Rosenblum, J.; Clair, M.; Gatenby, R.; Tilcock, C., Hepatic metastases: liposomal Gd-DTPA-enhanced MR imaging. *Radiology* **1989,** 171, (1), 81-5.

99. Kamaly, N.; Kalber, T.; Ahmad, A.; Oliver, M. H.; So, P. W.; Herlihy, A. H.; Bell, J. D.; Jorgensen, M. R.; Miller, A. D., Bimodal Paramagnetic and Fluorescent Liposomes for Cellular and Tumor Magnetic Resonance Imaging. *Bioconjug Chem* **2008,** 19, (1), 118-129.

100. Tan, W. B.; Zhang, Y., Multi-functional chitosan nanoparticles encapsulating quantum dots and Gd-DTPA as imaging probes for bio-applications. *J Nanosci Nanotechnol* **2007,** 7, (7), 2389-93.

101. Zielhuis, S. W.; Seppenwoolde, J. H.; Mateus, V. A.; Bakker, C. J.; Krijger, G. C.; Storm, G.; Zonnenberg, B. A.; van het Schip, A. D.; Koning, G. A.; Nijsen, J. F., Lanthanide-loaded liposomes for multimodality imaging and therapy. *Cancer Biother Radiopharm* **2006,** 21, (5), 520-7.

102. Zheng, J.; Liu, J.; Dunne, M.; Jaffray, D. A.; Allen, C., In vivo performance of a liposomal vascular contrast agent for CT and MR-based image guidance applications. *Pharm Res* **2007,** 24, (6), 1193-201.

103. Zheng, J.; Perkins, G.; Kirilova, A.; Allen, C.; Jaffray, D. A., Multimodal contrast agent for combined computed tomography and magnetic resonance imaging applications. *Invest Radiol* **2006,** 41, (3), 339-48.

104. De Cuyper, M.; Soenen, S. J.; Coenegrachts, K.; Beek, L. T., Surface functionalization of magnetoliposomes in view of improving iron oxide-based magnetic resonance imaging contrast agents: anchoring of gadolinium ions to a lipophilic chelate. *Anal Biochem* **2007,** 367, (2), 266-73.

105. Zhu, D.; White, R. D.; Hardy, P. A.; Weerapreeyakul, N.; Sutthanut, K.; Jay, M., Biocompatible nanotemplate-engineered nanoparticles containing gadolinium: stability and relaxivity of a potential MRI contrast agent. *J Nanosci Nanotechnol* **2006,** 6, (4), 996-1003.

106. Oyewumi, M. O.; Mumper, R. J., Engineering tumor-targeted gadolinium hexanedione nanoparticles for potential application in neutron capture therapy. *Bioconjug Chem* **2002,** 13, (6), 1328-35.

107. Oyewumi, M. O.; Mumper, R. J., Gadolinium-loaded nanoparticles engineered from microemulsion templates. *Drug Dev Ind Pharm* **2002,** 28, (3), 317-28.

108. Oyewumi, M. O.; Mumper, R. J., Influence of formulation parameters on gadolinium entrapment and tumor cell uptake using folate-coated nanoparticles. *Int J Pharm* **2003,** 251, (1-2), 85-97.

109. Zhu, D.; Lu, X.; Hardy, P. A.; Leggas, M.; Jay, M., Nanotemplate-Engineered Nanoparticles Containing Gadolinium for Magnetic Resonance Imaging of Tumors. *Invest Radiol* **2008,** 43, (2), 129-140.

110. Matteson, M. J.; Stober, W., The generation of aerosols from various electrolyte solutions. *J Colloid Interface Sci* **1967,** 23, (2), 203-14.

111. Flachsbart, H.; Stober, W., Preparation of radioactively labeled monodisperse silica spheres of colloidal size. *J Colloid Interface Sci* **1969,** 30, (4), 568-73.

112. Rieter, W. J.; Kim, J. S.; Taylor, K. M.; An, H.; Lin, W.; Tarrant, T.; Lin, W., Hybrid silica nanoparticles for multimodal imaging. *Angew Chem Int Ed Engl* **2007,** 46, (20), 3680-2.

113. Kim, J. S.; Rieter, W. J.; Taylor, K. M.; An, H.; Lin, W.; Lin, W., Self-assembled hybrid nanoparticles for cancer-specific multimodal imaging. *J Am Chem Soc* **2007,** 129, (29), 8962-3.

114. Garrett, R.; Grisham, C. M., *Biochemistry*. 3rd ed.; Thomson Brooks/Cole: Belmont, CA, 2005; p 1 v. (various pagings).

115. Hochuli, E.; Dobeli, H.; Schacher, A., New metal chelate adsorbent selective for proteins and peptides containing neighbouring histidine residues. *J Chromatogr* **1987,** 411, 177-84.

116. Xu, C.; Xu, K.; Gu, H.; Zheng, R.; Liu, H.; Zhang, X.; Guo, Z.; Xu, B., Dopamine as a robust anchor to immobilize functional molecules on the iron oxide shell of magnetic nanoparticles. *J Am Chem Soc* **2004,** 126, (32), 9938-9.

117. Xu, C.; Xu, K.; Gu, H.; Zhong, X.; Guo, Z.; Zheng, R.; Zhang, X.; Xu, B., Nitrilotriacetic acid-modified magnetic nanoparticles as a general agent to bind histidine-tagged proteins. *J Am Chem Soc* **2004,** 126, (11), 3392-3.

118. Kapanidis, A. N.; Ebright, Y. W.; Ebright, R. H., Site-specific incorporation of fluorescent probes into protein: hexahistidine-tag-mediated fluorescent labeling with (Ni(2+):nitrilotriacetic Acid (n)-fluorochrome conjugates. *J Am Chem Soc* **2001,** 123, (48), 12123-5.

119. Lata, S.; Reichel, A.; Brock, R.; Tampe, R.; Piehler, J., High-affinity adaptors for switchable recognition of histidine-tagged proteins. *J Am Chem Soc* **2005,** 127, (29), 10205-15.

120. Lata, S.; Gavutis, M.; Tampe, R.; Piehler, J., Specific and stable fluorescence labeling of histidine-tagged proteins for dissecting multi-protein complex formation. *J Am Chem Soc* **2006,** 128, (7), 2365-72.

121. Kim, J. S.; Valencia, C. A.; Liu, R.; Lin, W., Highly-efficient purification of native polyhistidine-tagged proteins by multivalent NTA-modified magnetic nanoparticles. *Bioconjug Chem* **2007,** 18, (2), 333-41.

122. Braun, P.; Hu, Y.; Shen, B.; Halleck, A.; Koundinya, M.; Harlow, E.; LaBaer, J., Proteome-scale purification of human proteins from bacteria. *Proc Natl Acad Sci U S A* **2002,** 99, (5), 2654-9.

CHAPTER 2

MULTIMODAL NANOPARTICLE CONTRAST AGENTS FOR TARGETED MONOCYTE IMAGING OF SYNOVIAL INFILTRATION IN INFLAMMATORY ARTHRITIS DISEASE MODELS

2.1 Introduction

Rheumatoid arthritis (RA) is a chronic inflammatory autoimmune disease characterized by progressive damage of joints. Affecting 1-2% of the worldwide population, disease onset can occur at any age of adulthood (25-50), and has a three times greater incidence in women.[1] As one of the most common immune-mediated inflammatory disease, the aberrant immune system causes swelling, pain, and stiffness of the joint as well as destruction and deformity of the cartilage, bone, and ligaments. Thus, RA results in diminished quality of life and has been linked to increased risk of myocardial infarction, lymphoma, osteoporosis, and reduction of life expectancy.[2-4] Events that initiate disease are unclear, though the presence and activation of T-cells, B-cells, and macrophages in the inflamed joint is generally accepted. While a cure does not exist, the early treatment of RA using existing disease modifying and anti-inflammatory therapies (i.e. Rituxan®, Enbrel®, Humira®) can prevent irreversible joint damage, a primary cause of the associated chronic pain.

Diagnosis of RA is largely dependent on clinical criteria established by the American Rheumatism Association in 1987. Four symptoms must be present for at least six weeks: early morning joint stiffness; polyarticular inflammation; swelling of proximal

interphalangeal, metacarpophalangeal, or wrist joints; and symmetric swelling.[5] Serologic tests, such as measurement of rheumatoid factor (RF) and anti-cyclic citrullinated peptides, can also be used to help confirm diagnosis but cannot act as stand-alone assays. Seronegative RF appears in approximately 20% of RA patients and can also be positive in other diseases.[6] For the research and treatment of RA, the ability to noninvasively characterize early inflammatory events within the joints remains a significant challenge.

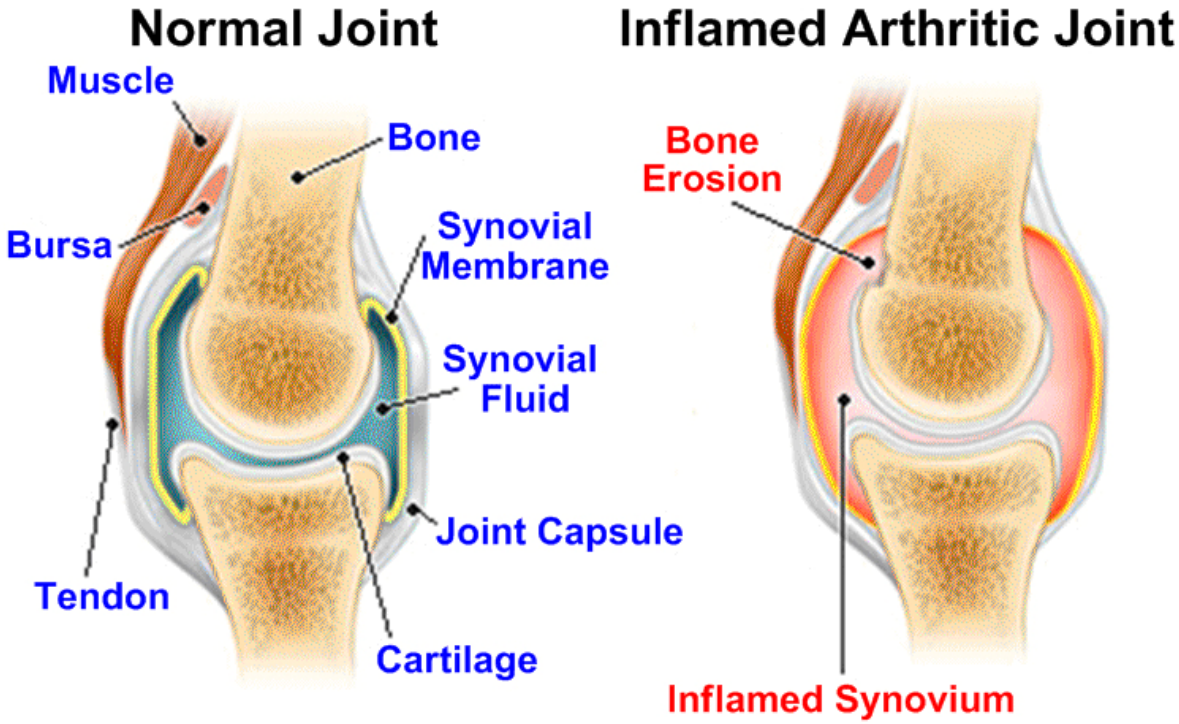

Figure 2.1 Diagram of normal joint compared to inflamed joint found in rheumatoid arthritis. (Adapted from reference [7].)

Conventional radiography (CR or X-ray) remains the standard diagnostic, but ultrasound, computed tomography (CT), and MRI are gaining popularity.[8] X-rays pass through soft tissues but are absorbed or scattered by denser bones, providing high quality images of bony structure. In 2005, a long term comparison study of individual imaging modalities for rheumatoid arthritis was published, establishing the superiority of MRI over

CR.[9] In this study, bone erosions could be detected 7 years sooner by MRI compared to CR. Inherently dependent on water distribution, MRI allows detection of early soft tissue changes, such as tissue inflammation, edema formation, and cartilage damage.[10-14] These soft tissue changes occur earlier in disease progression than bone erosions, thus provide a more effective measure of response to treatment.[15, 16]

A. 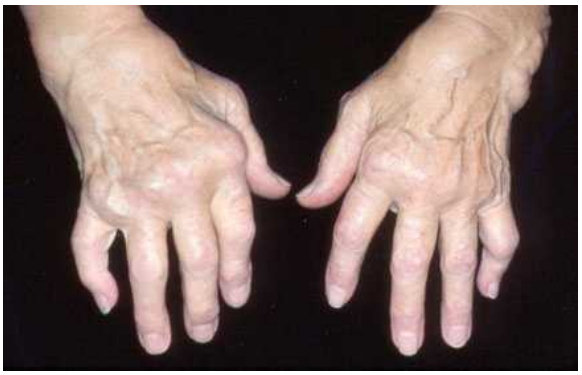 B. 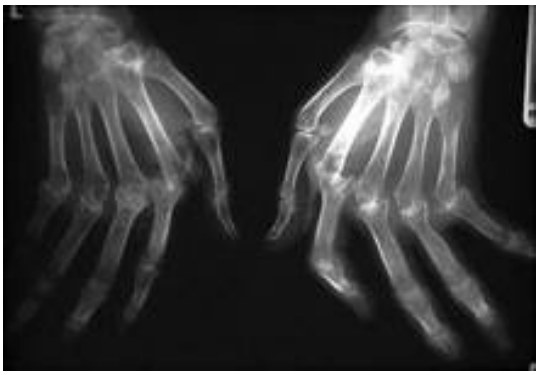

Figure 2.2 Hands of rheumatoid arthritis patient imaged A) visually and B) conventional radiography (X-Ray) showing bone damage detail but little soft tissue information.[17]

While much more sensitive, MRI is often limited to structural anatomy that lack mechanistic information of disease. Because cellular and molecular events long precede anatomic derangement, detection beyond the scope of conventional MRI is required to recognize disease earlier in order to design more targeted biologic therapies. The synovium, a thin membrane that provides lubrication and nourishment to the joint, is a focus of inflammatory activity and rheumatoid arthritis. Contrast-enhanced MRI can be used to improve contrast in synovial tissues for delineation from tendon sheaths, cartilage, and effusion.[18] Low molecular weight metal-chelate contrast agents, such as Magnevist®, Omniscan®, or Dotarem®, have been used to enhance signal in interstitial fluid resulting from increased endothelial tissue permeability and blood flow caused by inflammatory

arthritis.[19] Specificity of these small Gd(III) contrast agents has some limited utility, though signal enhancement is often seen in both normal and inflammatory tissues. Using dynamic contrast-enhanced MRI, a modification of traditional techniques to help correlate the pathophysiology of synovial inflammation and response to treatment, acquisition of many sequential images immediately after administration of the contrast agent becomes possible and allows the analysis of synovial perfusion and capillary permeability.[16] While being able to give vascular detail of disease, the low molecular weight Gd(III)-chelate contrast agents are limited by their quick clearance from the blood and inability to sensitively label cellular and molecular markers for inflammation.

Molecular markers such as $\alpha v\beta 3$ integrins are expressed on synovial blood vessels in RA[20, 21] and regulate migration and proliferation of endothelial cells in the synovial tissue. Targeted induction of apoptosis in the synovial neovasculature has been demonstrated as a potent therapy for RA.[22] Using RGD peptides for integrin binding,[23, 24] murine collagen-induced arthritis can be suppressed by targeted apoptosis in cells of synovial neovasculature.[25] Integrin targeting is an example of a molecular marker that is desirable for use in diagnosis of neoangiogenesis seen in RA as well as other diseases. Unfortunately, currently available low molecular weight Gd(III)-chelates require concentrations orders of magnitude higher than available on overexpressed biomarkers on disease cell surfaces.[26] A potential solution for this concentration gap is the development of nanomaterials with higher MR sensitivity.

As MRI contrast nanomaterials with higher sensitivity are generated and optimized for targeted imaging, rapid uptake by the reticuloendothelial system (RES) is a major concern. Phagocytic cells, residing in the lymph nodes, spleen, and liver, clean blood by

uptake of particulate matter. This process is very fast, and often significantly interferes with targeted nanomaterials. Yet, these phagocytic cells also play an important role in the immune response, inflammation, and thus RA. Labeling phagocytic cells of the RES using inherent phagocytic activity toward particulate matter (i.e., contrast-enhancing nanoparticles) is an attractive alternative to helping image immunological responses in RA and subsequent soft tissue changes.

Recently, particular interest has surrounded monocytes and synovial macrophages as important mediators of tissue and bony destruction in inflammatory arthritis.[27-29] Activated macrophages are thought to play an important role in RA, and the total number of residing synovial macrophages correlates with RA disease activity (**Figure 2.3**).[30, 31] Generally a membrane of one to two layers, the synovium thickens due to infiltration by blood monocytes. The damage caused by these cells eventually cause irreversible destruction of the cartilage and bone. Particulate contrast agents, such as ultrasmall superparamagnetic iron oxide (USPIO), has been used in investigational studies in inflammatory disease responses as labels of hematopoetic phagocytic cells.[29, 32-34] USPIO are internalized by a variety of cells, but preferentially label monocytes/macrophages. In the collagen-induced arthritis (CIA)[34] and in the experimental antigen induced arthritis[29, 31] rodent models, USPIO particles showed a negative (dampened) signal intensity on MR images comparing arthritic to normal mouse joints. These studies support the feasibility of cellular tracking *in vivo* and suggest their potential application for monitoring inflammatory events and response to therapy. As cellular immunotherapies emerge,[35-37] where cells are used as therapeutic delivery vehicles, non-invasive cell *in vivo* imaging techniques are needed to monitor these therapies and track the fate of the administered cells.[38]

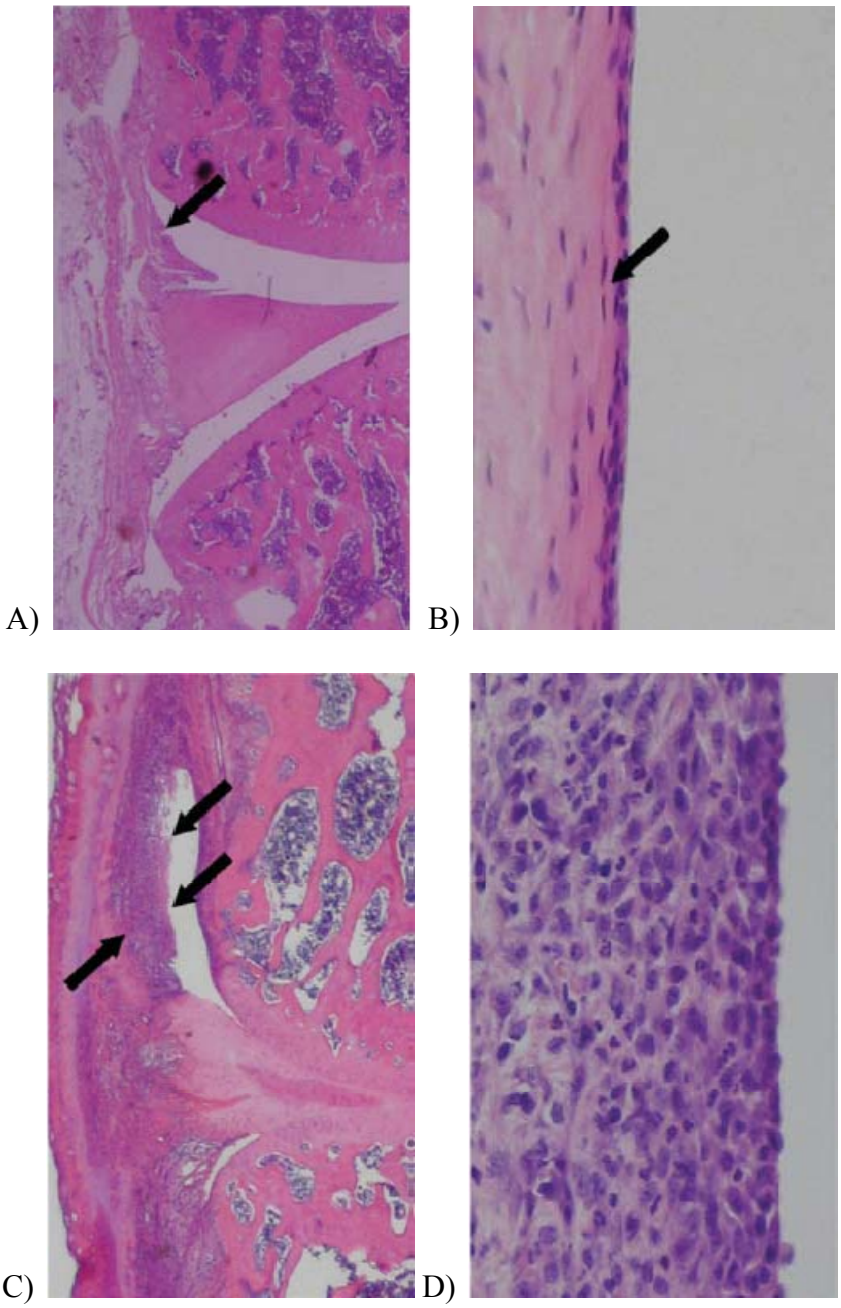

Figure 2.3 Hematoxylin and eosin (H&E) stains of histological stains of A) normal rat knee joint at 10X magnification, B) normal rat knee joint at 100X magnification, C) arthritic rat knee joint at 10X magnification, and D) arthritic rat knee joint at 100X magnification. Black arrows indicate the synovium, and hematoxylin stained cells (purple) show the infiltrating basophilic leukocytes.[31]

Our group has produced a new multimodal nanoparticle (MNP) contrast agent capable of *T1*- and *T2*- enhancement as well boasting relatively long fluorescence emission wavelengths[39]. MNP outperforms both Gd-DTPA and USPIO in T1-enhancement and is comparable to USPIO in T2-enhancement. This contrast agent has been shown to efficiently label monocytes for MRI and fluorescence without detriment to cell viability. It is our hypothesis that MNP contrast agents can eventually be used to noninvasively measure and guide treatment in inflammatory arthritis. Specifically, we will image animal models of inflammatory arthritis using multiple modalities to improve current MR imaging technologies (**Figure 2.4**). This transformational research aims to help develop advances to guide RA therapies and generate knowledge that cannot be obtained by our current methods of analysis.

A)

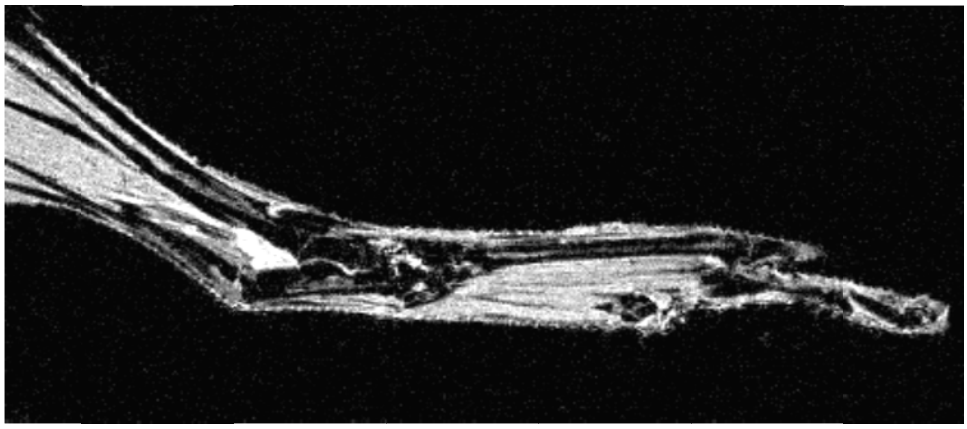

B)

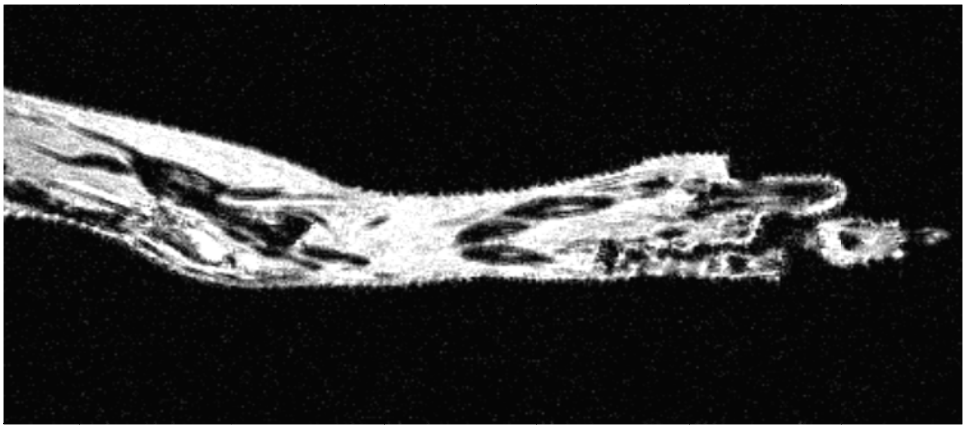

Figure 2.4 High resolution MR images from a 9.4T scanner of A) normal hind paw and B) inflamed hind paw of collagen-induced arthritis mouse model without the administration of any contrast agents.

2.2 Results and Discussion

2.2.1 Description of the multimodal nanoparticle (MNP) contrast agent

The multimodal nanoparticle contrast agent used in these studies is composed of a $Ru(bpy)_3Cl_2$ dye-doped silica nanoparticle with paramagnetic coating of a gadolinium(III)-diethylene triamine tetraacetic acid (DTTA)-silane (**Figure 2.5**). The Gd(III) chelate is structurally similar to the clinically used low molecular weight contrast agent Gd-DTPA. One of the acetate groups is replaced with a silane moiety for immobilization onto the surface of the silica nanoparticle. Thus, two water molecules can coordinate simultaneously to the paramagnetic metal center compared to the one water molecule that coordinates to Gd-DTPA potentially increasing proton relaxation efficiency. Gd(III) remains tightly bound to the chelator despite the loss of a coordinating acetate; loss of Gd(III) may result in increased toxicity due to interference with Ca(II) signaling.

The nanoparticles have a spherical morphology and are highly monodisperse with a 37 nm mean diameter. Characterization was performed by scanning electron microscopy (SEM), transmission electron microscopy (TEM), thermogravimetric analysis (TGA), and direct current plasma (DCP) elemental analysis. In a clinical 3.0 Tesla MR imaging scanner, the $r1$ and $r2$ were measured to be 2.0×10^5 and 6.1×10^5 s^{-1}, respectively. MNP has been validated for in vitro uptake by murine monocytes, demonstrating fluorescence and MR enhancement.[34]

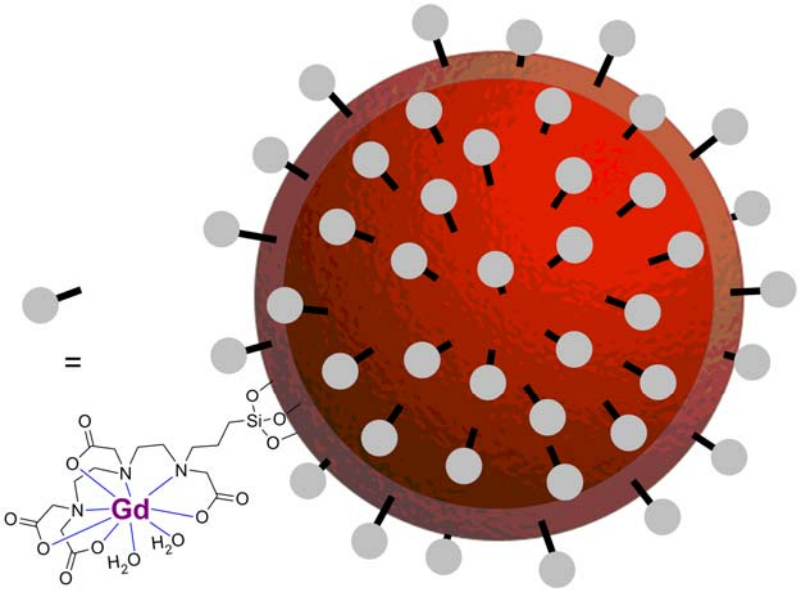

Figure 2.5 Schematic representation of the multimodal nanoparticle (MNP) contrast agent with luminescent $Ru(bpy)_3Cl_2$-doped core and Gd(DTTA) surface immobilized.

2.2.2 Monocytes and their role in inflammation

Monocytes are leukocytes that circulate in the bloodstream and can actively participate in immune responses toward pathogens. The main function of this type of cell is to mature into either macrophages for phagocytosis and digestion of undesirable material or to present antigens and trigger immune responses. Monocytes are produced from hematopoetic stem cells (hemocytoblasts) found in the bone marrow. The multipotency of these hemocytoblasts gives rise to a range of blood cell types: myeloid, lymphoid, and new stem cells. Monocytes are derived from myeloid origin, as hemocytoblasts first commit to the myeloid progenitor state, before becoming myeloblasts, and then monocytes. Approximately 400 million monocytes exist per liter of human blood, carefully guarding against infection.

Macrophages are monocytes that have left the bloodstream and have migrated into tissue actively undergoing inflammation. Foreign material is removed from the tissue by

endocytosis, specifically phagocytosis. During this process, macrophages can engulf particulate matter using its cell membrane to form an endosome, which can fuse with a lysosome to introduce superoxide (O^{2-}), hypochlorite (HOCl), and enzymes. These harsh conditions are suitable for breakdown of undesirable material, such as pathogenic microorganism or sensescent/dead/damaged cells.

Acute and chronic inflammation is an immune response that monocytes and their derivative macrophages are major participants. Inflammation is an essential healing process invoked by an organism toward tissue infection or damage. Monocytes respond to cellular signals, such as selectins or chemokines, to migrate from the bloodstream into the damaged tissue. Acting as macrophages within tissue, foreign debris is cleared and degraded to allow for regeneration of healthy tissue. While vital to the survival of the organism, this process can go awry resulting in autoimmune diseases such as RA.

In RA, monocytes have been implicated as a key contributor to dysfunctional immune response, specifically to joint tissue. Monocytes are known to infiltrate the synovial tissue during the unwanted inflammatory response.[33] Joints damage initially inflicted on the synovium eventually causes destruction to the cartilage and bone. Monocytes can become activated by endotoxins derived from pathogens[40] to release inflammatory mediators: tumor necrosis factor alpha (TNF-α)[41-43] and interleukins (IL) -1 and -6.[44] Upon activation, higher phagocytosis levels of particulate matter has also been demonstrated.[45] Since these immune cells play a critical role in regulating the inflammatory response, methods of tracking for studying is highly desirable.

The inherent phagocytic activities of live monocytes can act as a major hurdle for conventional labeling techniques. Common cell surface labeling techniques, such as

fluorescent antibodies, will be engulfed and digested. Also, antibodies labeled with Gd-DTPA generally do not have sufficient sensitivity for *in vivo* studies of pathogenesis. Instead, particulate uptake was used for labeling and tracking monocytes *in vitro* and *in vivo*. We found that murine monocytes could quickly uptake particulate aggregates of iron oxide nanoparticles (**Figure 2.6**). In this experiment, phagocytosis of large visible aggregates occurred within 45 minutes, with evidence of small vesicle formation for uptake of particles not visible by light microscopy at 100X magnification. Cells appeared viable by trypan blue examination up to approximately 2 weeks after uptake of iron oxide particulates. These observations were supported by literature reports of uptake of iron oxide by human monocytes.[46]

We hypothesized that monocytes could efficiently uptake MNP, by utilizing their inherent phagocytic activity, for labeling and tracking cell pathogenesis in disease models. Using the luminescent properties of MNP, we characterized monocytes movement using *in vitro* assays, histopathology, and *in vivo* optical imaging of low tissue depth joints. MR modalities were used to achieve further *in vivo* imaging of intricate joint structure and achieve greater resolution than what is available through optical imaging.

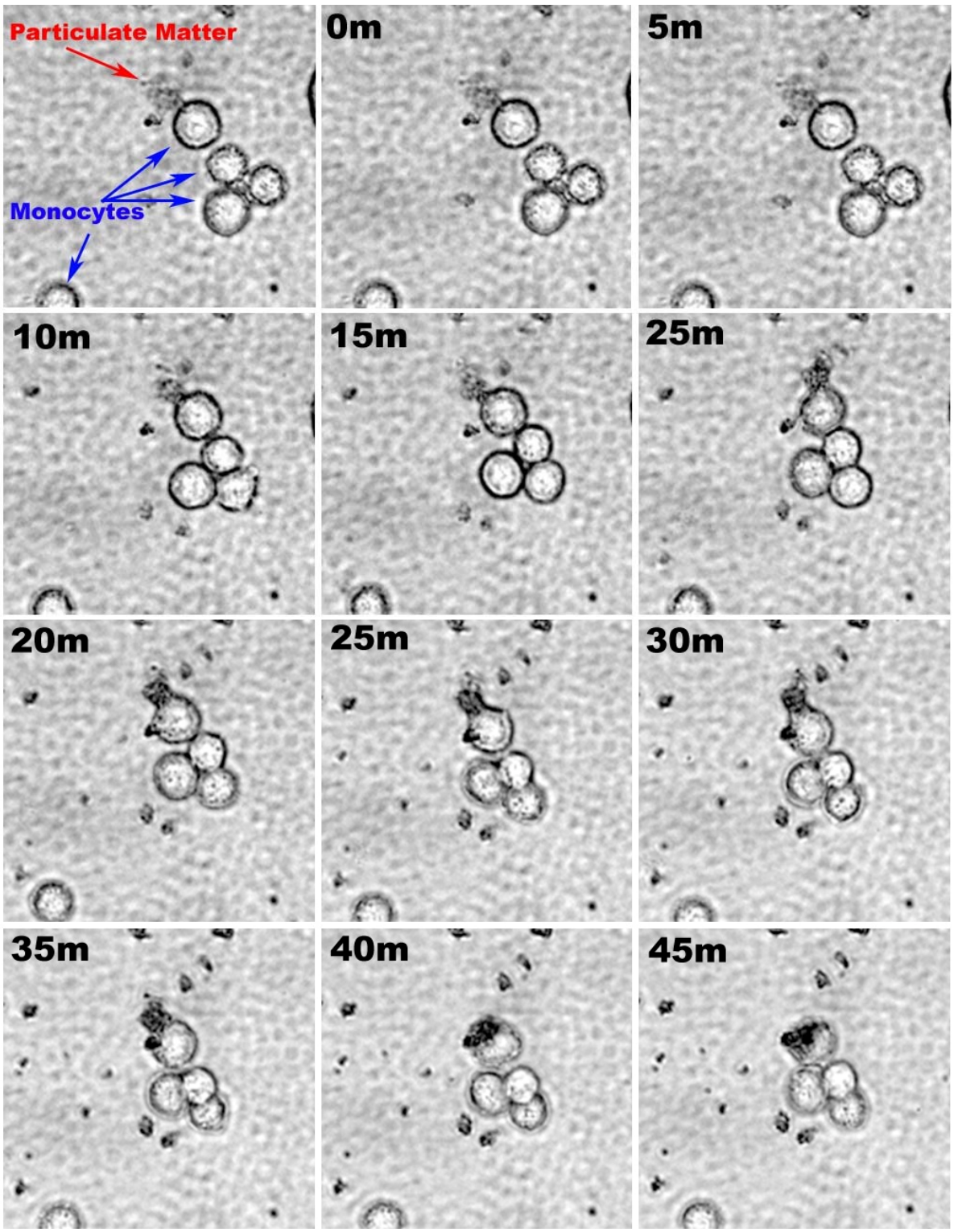

Figure 2.6 Monocytes can quickly engulf particulate matter (large aggregates of iron oxide nanoparticles) shown in these live cell bright field microscope images at 20X magnification.

2.2.3 The need for a robust system to track monocytes

As noted in the previous section, phagocytic cells, such as monocytes, have a primary function of digesting foreign material. In order to effectively track the action of monocytes in an active inflammatory process, we realized the need for a robust system able to withstand the harsh conditions of the endosome. Silica is known to be robust and biocompatible, having been used for industrial catalysis[47-50] but have also been used for cellular studies.[51-54] With reports of doping silica nanoparticles with fluorescent molecules,[55-57] we believed that coating luminescent silica nanoparticles with chelated metal centers could provide a robust contrast agent capable of withstanding harsh endosomal conditions. We found the resulting material, MNP, could be label monocytes without diminishing their viability to track monocytes movement within a disease model. MNP was monitored for over 4 weeks and found stable *in vitro* and *in vivo*.

2.2.4 Fluorescence confocal microscopy of labeled monocytes

To label monocytes *in vitro*, cells were incubated with MNP to allow for phagocytic uptake. Since MNP does not form large aggregates visible by light microscopy, confocal fluorescence was used to visualize nanoparticle uptake. Confocal laser scanning microscopy is a valuable *in vitro* imaging technique that has been used extensively to examine biological samples. Microscopy principles are similar to traditional fluorescence microscopy with the use of objective lens and a series of excitation/emission filters, but with a few key differences. Particularly, resolution in confocal microscopy is greatly enhanced over conventional fluorescence microscopy because an aperture or pinhole is used to block out-of-focus light. The result is sharper images from luminescence arriving directly from the focal

point of luminescence. Light can be detected at various z-axis planes, allowing visualization of a particular "slice" of a sample. Additionally, the "slices" can be stacked, generating three-dimensional composite images by software.

Imaging at z-axis planes is especially important for imaging monocytes with MNP uptake. While the 37 nm diameter MNP cannot be seen by confocal laser scanning microscopy (neither bright field nor fluorescence), the accumulation of MNP within the cells was apparent (**Figure 2.7**). By detecting fluorescence of a z-slice that cuts through the centers of the monocytes, MNP fluorescence within the cells was detected. Focal regions of fluorescence indicate concentration of the nanoparticles into endosomal vacuoles. Ring patterned fluorescence was not seen, which would be indicative of surface labeling of cells. Inspection of the representative images of MNP-labeled monocytes populations show high labeling efficiency that is also confirmed by flow cytometry.

A.

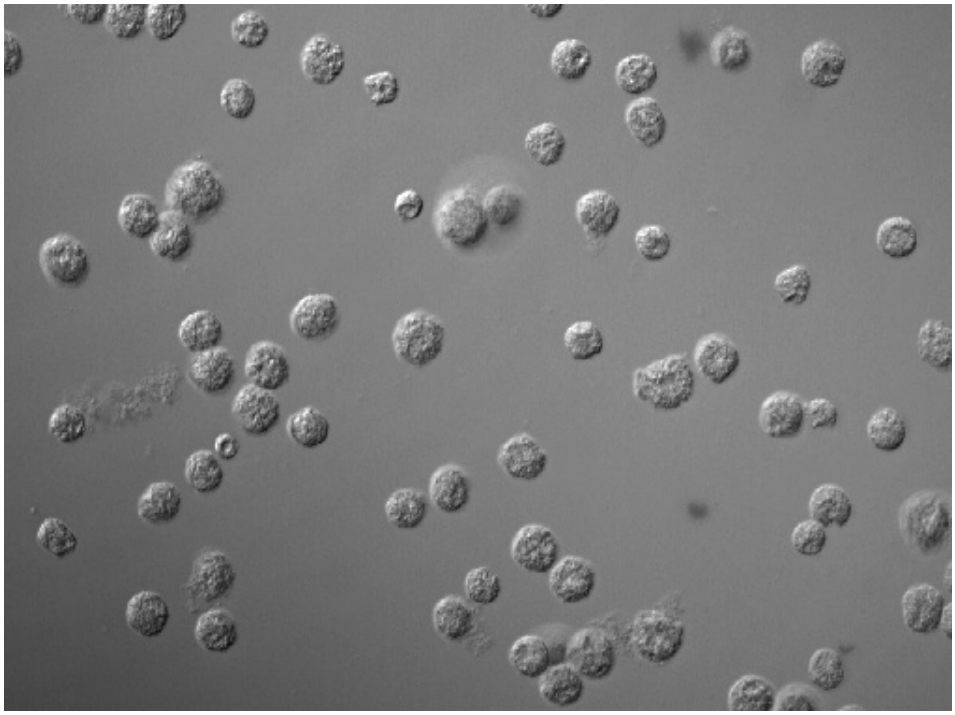

B.

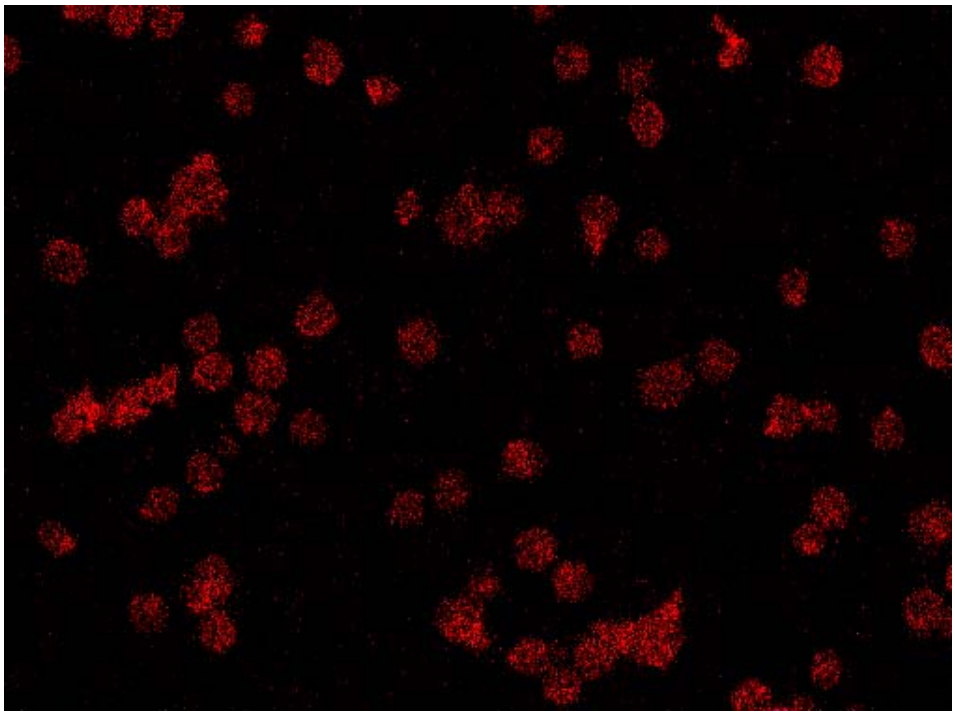

Figure 2.7 Laser scanning confocal microscopy images of murine monocytes incubated with MNP at 63X magnification under A) bright field and B) 433 nm excitation with 500-550 nm emission settings.

2.2.5 *In vitro* MRI of MNP labeled monocytes

To evaluate potential use for in vivo applications for tracking monocytes using MR-enhancing modalities of MNP, in vitro MRI was performed on labeled monocytes. After incubating monocytes with MNP, the cells are washed and pelleted into Eppendorf tubes before being placed in a 3.0T MR scanner. **Figure 2.8** demonstrates contrast enhancement in *T1*- and *T2*-weighted MR imaging when compared to unlabeled cells. *T1*-weighted images show a significant signal enhancement, while *T2*-weighted images show signal void of MNP-labeled cells. Both modalities may be useful in imaging disease and provide information regarding cellular pathogenesis.

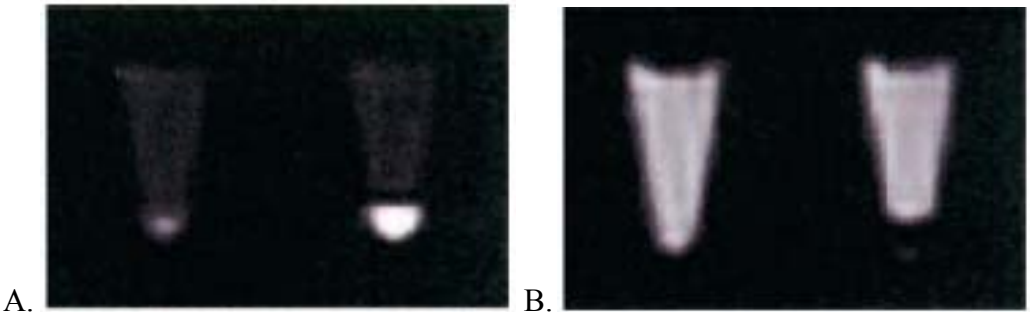

Figure 2.8 *In vitro* MR images of murine monocytes unlabeled (left) and MNP-labeled (right) showing clear contrast signal contrast enhancement in A) T1-weighted and B) T2-weighted modalities.

2.2.6 Flow cytometry of MNP labeled monocytes

Microfluidic advances have led to the development of the modern flow cytometer extensively used by immunologists and other scientists for studying populations of cells and microscale structures. A major technological challenge was the accurate measurement of single particle events as they pass through a detector. Typical manufacturing processes could not create microfluidic feature sizes that could effectively force particles to move

individually through channels. Hydrodynamic focusing using sheath fluid to surround particulate-containing fluid within a larger, manufactured tube was found ideal for narrowing the sample stream. Fluid dynamics allow two fluids that differ in velocity and density to resist mixing, enabling a stable two-layer flow, and thus producing the necessary stream diameter for single event detection.

Detectors for light scattering or fluorescence can be very useful for probing cellular samples in flow cytometry. Forward scattered (FS) light is measured through the sample stream, while side scattered (SS) light is measured orthogonal to the sample stream. Such scattered light is useful for measurements of cellular populations, as information about size and granularity of cells is generated. Larger cells result in higher FS signals than smaller cells. Cells of greater complexity, such as those with more granules or organelles, create higher amounts of SS light. Fluorescence, like SS light, is also measured by detectors perpendicular to the sample stream. In immunological assays, a wide range of fluorescently-tagged antibodies specific for cellular markers are extensively used for studying populations. This technique is much more powerful and absolute in counting and sorting populations than light scattering detection. Cells can be probed and sorted for functional characteristics labeled by fluorescent affinity molecules in conjunction to morphological characteristics provided by light scattering.

We used flow cytometry to measure the uptake efficiency of MNP by murine monocytes (**Figure 2.9**). Cells that were and were not incubated with MNP were probed in a flow cytometer using light scattering and fluorescence. A plot of SS versus FS light was used to determine healthy cells used for fluorescent measurement. The light scattering data of the inset in **Figure 2.9** shows "R2" as the region of interest encompassing the large

majority of cellular events, while those outside of the ellipse consist of dead cells and debris. Monocytes incubated with and without MNP had similar levels of events outside of the region of interest, indicating that the dead cells and debris are a result of the normal cell cycle rather than toxicity induced by MNP. Finally, fluorescence was used to count over $1x10^5$ MNP-labeled (blue curve) and unlabeled cells (red curve). Increasing concentrations of MNP used for incubating with monocytes were proportional to labeling efficiency. Presumably, the cells had an upper limit to MNP-labeling dependant on uptake capacity. Monocytes could be labeled in over 98% efficiency determined by increase in fluorescence intensity with little toxicity to cells. This corresponds with the qualitative level of labeling seen in confocal fluorescence imaging.

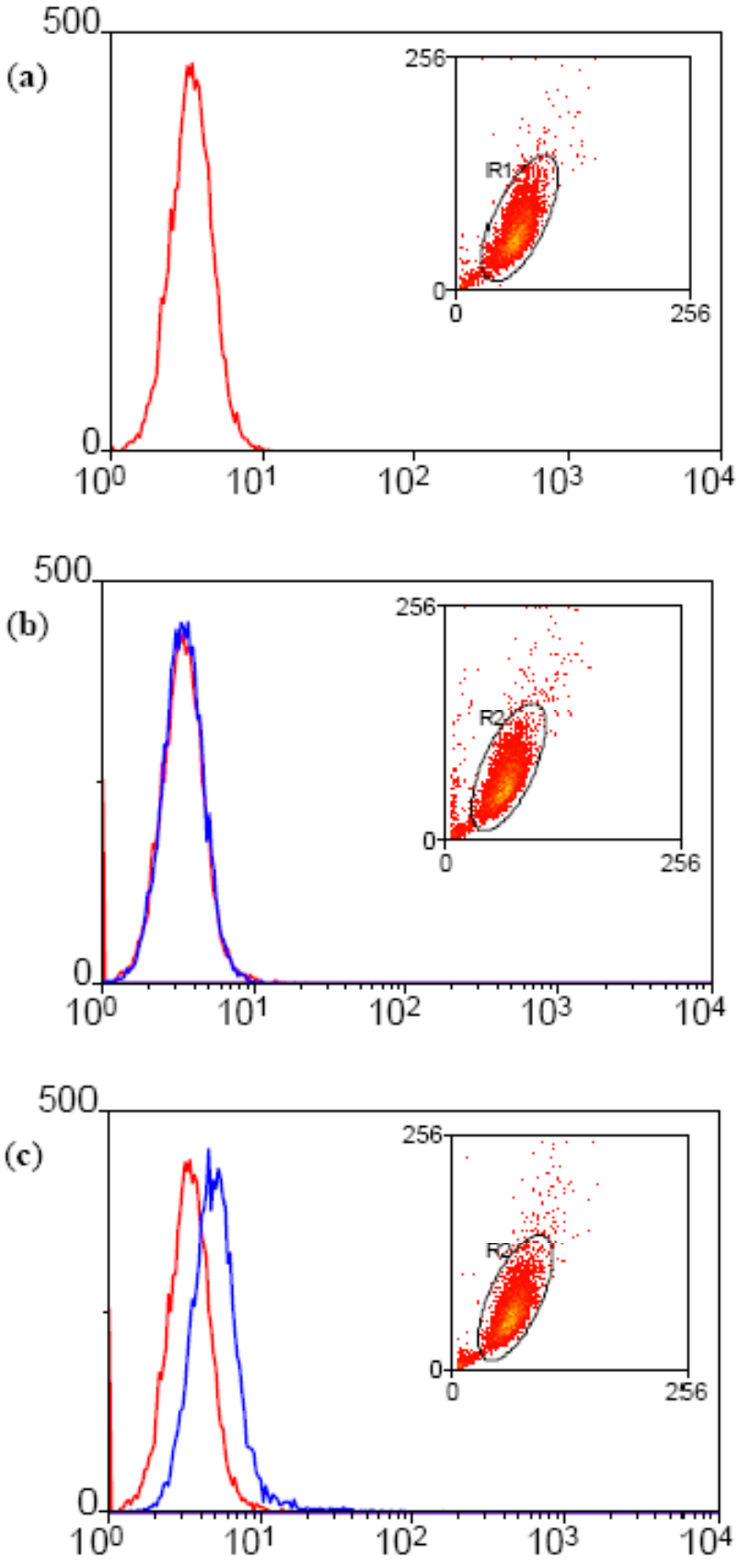
(a)
500
0
10^0
10^1
10^2
10^3
10^4
256
R1
0
0
256
(b)
500
0
10^0
10^1
10^2
10^3
10^4
256
R2
0
0
256
(c)
500
0
10^0
10^1
10^2
10^3
10^4
256
R2
0
0
256

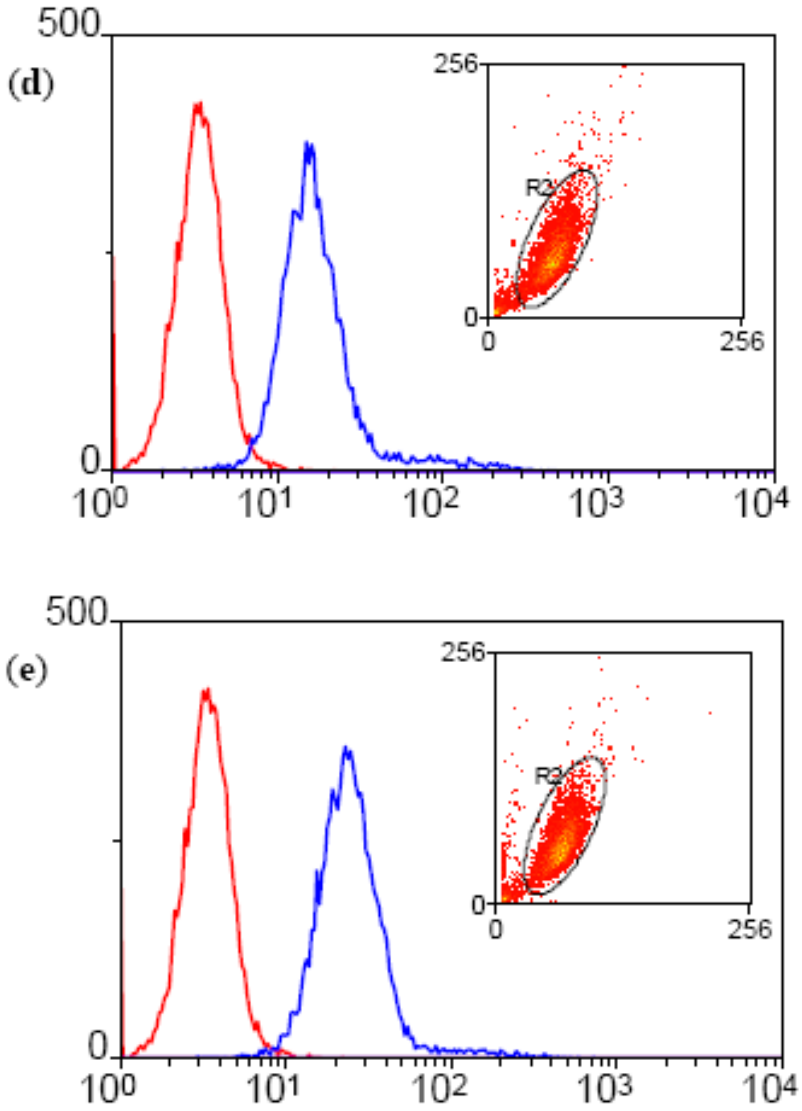

Figure 2.9 Flow cytometry analysis murine monocytes labeled with different MNP concentrations; plotted as cell counts (y-axis) versus luminescence intensity (x-axis). Insets show light scattering data to determine healthy cells sampled and counted in region of interest: R1, R2. of MNP labeled showing increased fluorescence intensity of labeled (blue curve) cells compared to unlabeled (red curve) cells. (a) 0 mg MNP per 1×10^6 cells in 2 mL media; R1 = 95.5% of total events; (b) 0.004 mg MNP per 1×10^6 in 2 mL media; 0.6% NP labeling efficiency, R2 =94.0% of total; (c) 0.042 mg MNP per 1×10^6 in 2 mL media; 10.8% NP labeling efficiency, R2 = 94.2% of total events; (d) 0.418 mg MNP per 1×10^6 in 2 mL media; 98.0% NP labeling efficiency, R2 = 90.9% of total events; (e) 2.140 mg MNP per 1×10^6 in 2 mL media; 99.4% NP labeling efficiency, R2 = 91.3% of total events.

2.2.7 Cell viability of monocytes incubated with MNP

MNP toxicity was measured using a commercially available colorimetric assay measuring enzymatic activity of the cells. (3-4,5-dimethylthiazol-2-yl)-5-(3-carboxymethoxyphenyl)-2-(4-sulfophenyl)-2H tetrazolium salt (MTS) is converted by cells to the derivative water-soluble formazan product that absorbs at 490 nm. Literature has reported MTS assay for measurement of cell viability and proliferation; formazan generation is time-dependent and proportional to the number of viable cells.[58, 59]

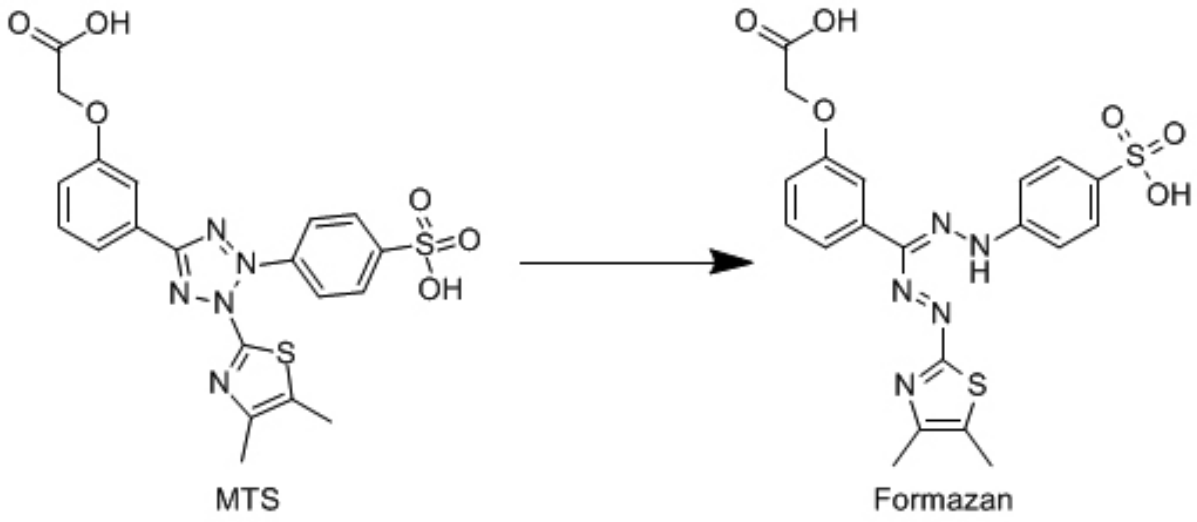

Figure 2.10 Structures of substrate and product used to measure cell viability of cells.

Upon incubation of murine monocytes with various concentrations of MNP, MTS assay showed monocytes are fully viable even at high concentrations of nanoparticle. Monocytes were incubated with MNP concentrations from 0.0123 μg up to 123 μg per 5000 cells in 120 μL media for 22 hours, and were found to be able to convert MTS as effectively as normal cells. This result indicates that the nanomaterial construct is not toxic to monocytes, which is expected because components are also known to have little toxicity.

Thus, nanoparticle labeling may be a useful method to track monocytes, as uptake of MNP does not seem to hinder viability or proliferation.

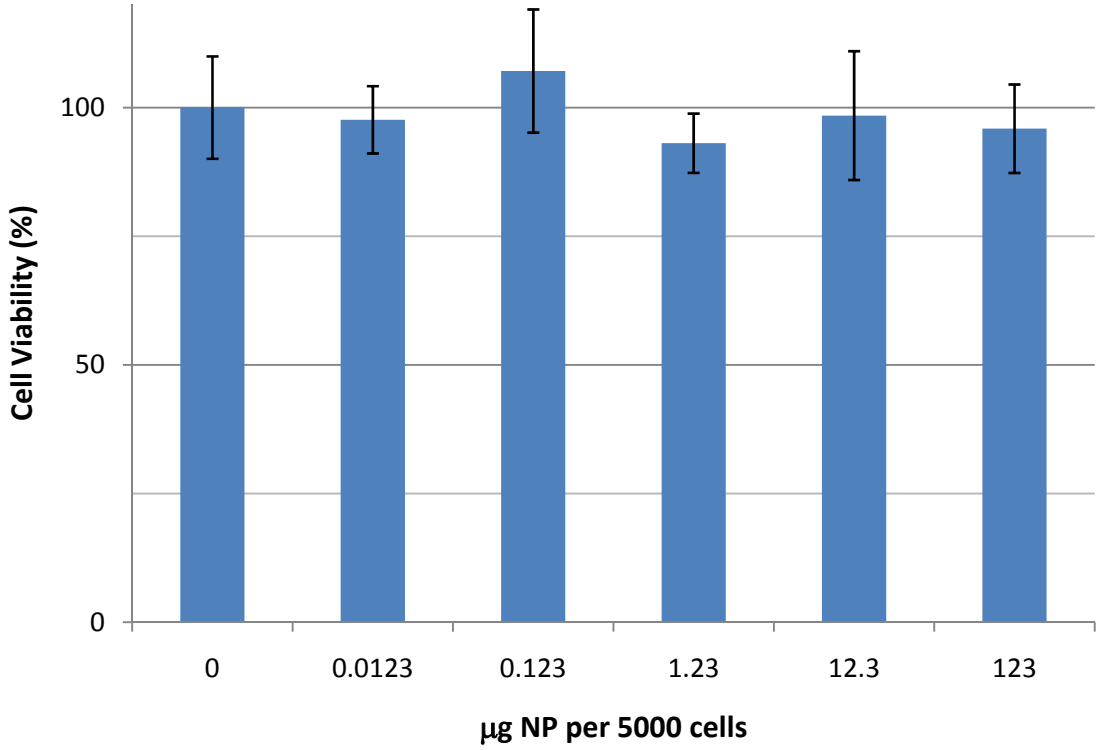

Figure 2.11 MTS assay results of murine monocytes incubated with 0, 0.0123, 0.123, 1.23, 12.3, and 123 μg MNP per 5000 cells showing no toxicity and high cell viability.

2.2.8 Determining background fluorescence in non-arthritic joints of control animals injected with and without MNP

At 12 hour time points following intravenous injection of MNP contrast agent, optical imaging was performed for fluorescence detection. **Figure 2.12** shows superimposed images of animals in both photographic (white light) and fluorescence (DsRed emission filter) channels. Control animals, vehicle-immunized without heterologous bovine collagen, are used to establish baseline fluorescence emission for animals injected with saline (or 0 mg MNP / kg animal), 125 mg MNP / kg animal, and 250 mg MNP / kg animal. These control animals injected with variable MNP dose demonstrate a slight increase in fluorescence background of the paws as MNP dose was increased. This small increase in fluorescence signal is presumably due to the vascular trapping of nanoparticle within the paw circulation.

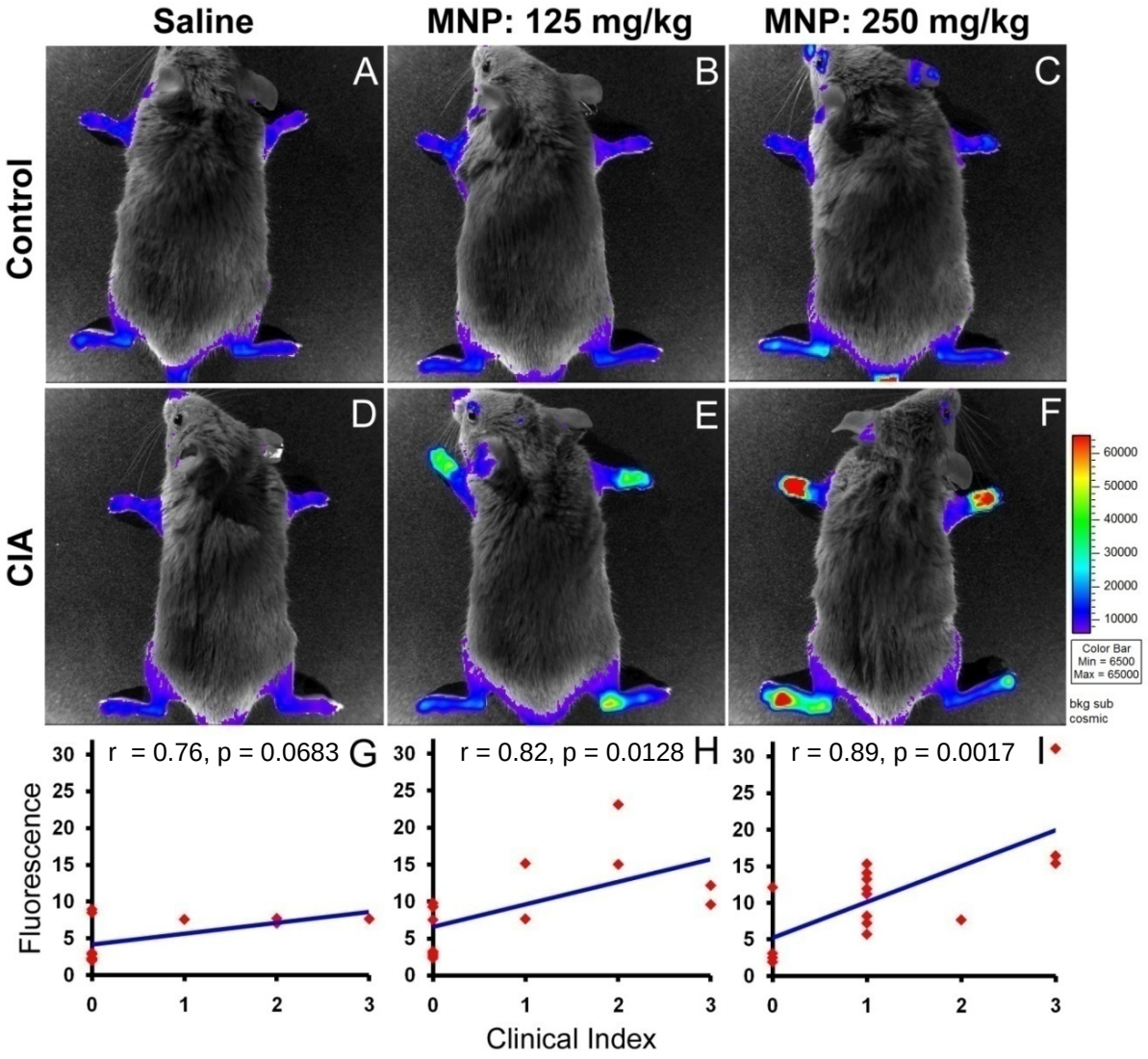

Figure 2.12 *In vivo* optical images of normal animals injected with A) saline, B) 125 mg/kg MNP, or C) 250 mg/kg MNP and collagen-induced arthritis (CIA) animals injected with D) saline, E) 125 mg/kg MNP, or F) 250 mg/kg MNP. Luminescence intensity in MNP-treated arthritic paws had strong positive correlation with the assigned clinical index score in animals that received either H) 125 mg MNP/kg ($r = 0.82$, $p = 0.01$) or I) 250 mg MNP/kg ($r = 0.89$, $p = 0.002$). Arthritis was not symmetric and varies for each animal.

2.2.9 Determining background fluorescence in arthritic joints of control animals injected with and without MNP

As compared to the non-arthritic group, animals with arthritis showed a dramatic increase in paw fluorescence. Arthritic animals given higher doses responded with greater paw fluorescence. The arthritic mouse injected with saline, shown in Figure 1, demonstrates little increase in fluorescence measured from the left hindlimb without arthritis (evaluated based on paw swelling) when compared to the right hindlimb with arthritis. This increase in fluorescence is due to the paw swelling of the arthritic hindlimb, which results in a greater amount of surface area from which tissue autofluorescence was generated. In the 125 mg / kg dosed arthritic animal shown, the left hindlimb (non-arthritic) clearly shows less fluorescence than the arthritic right hindlimb. The fluorescence of the arthritic right hindlimb is also significantly enhanced in contrast to the right arthritic hindlimb of arthritic animal dosed with saline (0 mg / kg). The fluorescence was further enhanced in the case of the arthritic animal dosed at 250 mg / kg.

2.2.10 Correlation of optical imaging and magnetic resonance imaging in arthritic paws

Using the MR-enhancing modality of MNP, animals with inflamed joints were imaged using a 9.4T small animal scanner. Animals were scanned before and 12 hours after 125 mg / kg MNP administration. The post-contrast image demonstrates a clear signal void compared to the pre-contrast image in the inflamed joints. Enhanced T2 relaxation as a result of MNP deposition in the inflamed tissue causes the signal void and correlates appropriately with the post-contrast *in vivo* fluorescent enhancement. The fluorescence images show a 30% enhancement of fluorescence in the circled toe ROIs.

2.2.11 Magnetic resonance imaging: Relaxation time (*T1, T2*) mapping

T1 and *T2* relaxation time mapping is an MR imaging technique that has been found to quickly detect cartilage changes and provide quantifiable data in healthy children, adolescents, and adults as well as patients with juvenile rheumatoid arthritis (JRA).[60-63] *T1* mapping with delayed administration of Gd-DTPA contrast agent has been shown to demonstrate loss of proteoglycan density in cartilage [63-65], but *T1* and *T2* mapping has yet to show changes as a result of cellular response. Our studies indicate an increased sensitivity by *T2* mapping MR imaging as compared to high resolution three-dimensional MR image.

Figure 2.13 compares arthritic animals with early arthritis (day 30) and late arthritis (day 50), pre- and post-injection of MNP. In early disease, the hind paws showed obvious enhancement of *T2* relaxation time, but little to no change in *T1* relaxation time. Unlike low molecular weight Gd(III) contrast agents, MNP has significant *T1*- and *T2*- effects. Often, parameters can be adjusted to weigh the effect in favor of *T1* or *T2*. In high concentrations, *T2*-effects dominate, outweighing *T1*-effects from being apparent even with parameter modification. In this animal, there was no obvious detectable change in the high resolution MR image, but the *T2* mapping image shows a marked enhancement of *T2* relaxation, demonstrating the promise of relaxation time mapping for sensitive early detection of disease.

Late arthritis did not detect significant *T1*- or *T2*-effects from MNP injection. Although this animal had heavy edema as result of inflammation, very little enhancement of *T2* relaxation time was shown. This is attributed to the lack of monocyte migration to the inflammation site. At late stage arthritis, the inflamed site may be saturated with monocytes

that had migrated earlier, such as in the day 30 results, preventing significant new infiltration. Additionally, these results potentially support the idea that monocytes trafficking, rather than vascular trapping of MNP causes MNP deposition in the synovial joints. An alternate mode of deposition may be the uptake of MNP by monocytes that have already infiltrated the joint, which indicate that monocytes in late stage arthritis may be less active. Both modes of MNP deposition working in concert is possible, though difficult to clearly prove.

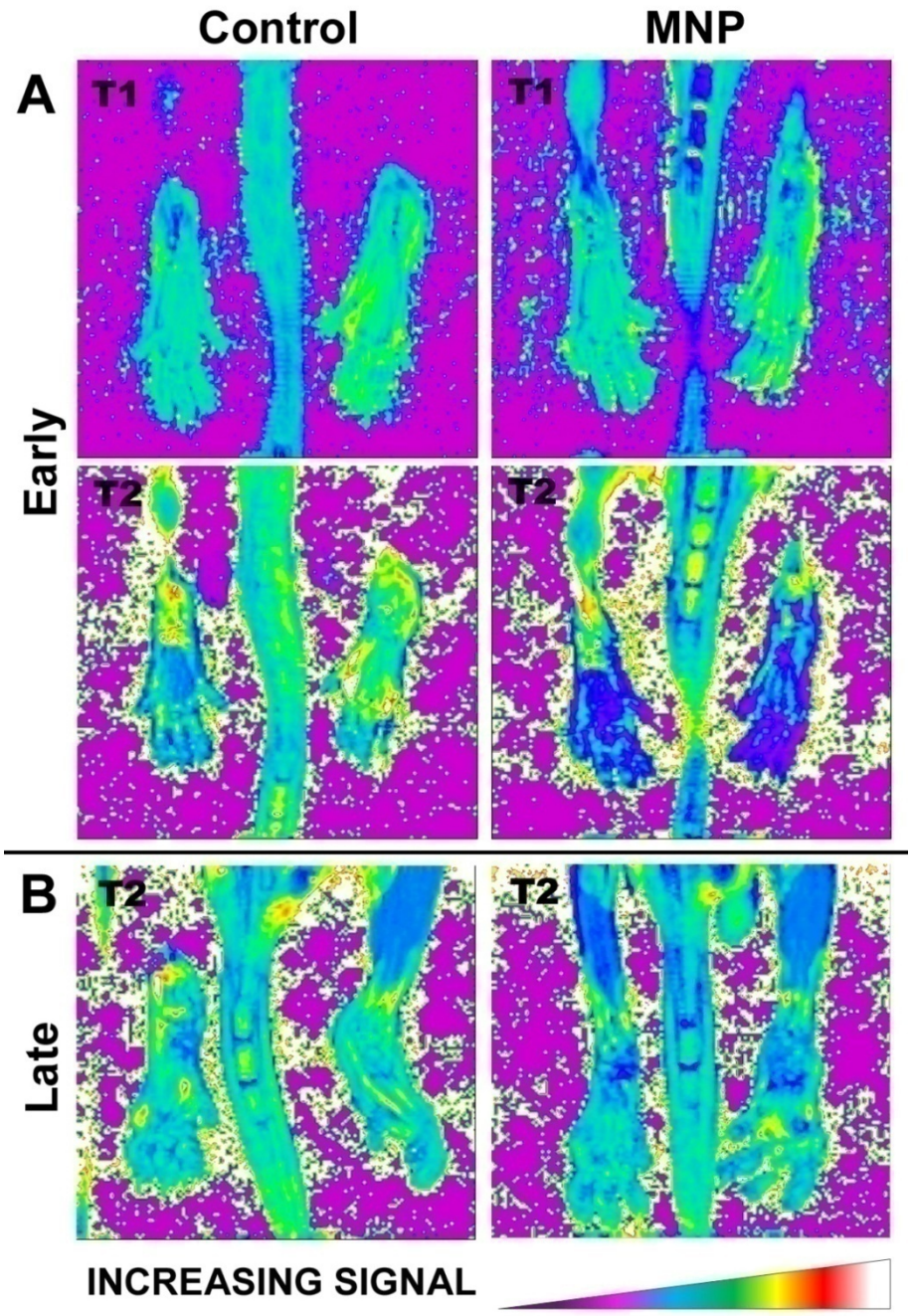

Figure 2.13 Representative *T1* and *T2* maps of arthritic animal hindlimbs showing pre- (day 35) and post-MNP (day 36) contrast injection in a mouse with active inflammation. The post-MNP contrast images were obtained 12 hours after injection with 2 separate doses of 125 MNP/kg. Changes in relaxation time are distinctly detected in *T2* maps after MNP injection.

2.2.12 High-resolution Magnetic resonance imaging

High-resolution MR images of collagen induced arthritis animals were scanned to show detailed anatomical structures not seen in *T1*- and *T2*- relaxation time maps and optical imaging. These results are representative scans that clinicians may commonly see when examining human patients. In **Figure 2.14**, an animal with arthritis is scanned by both high-resolution MR and optical imaging. The right hind paw of the animal post-injection of MNP shows luminescence enhancement when compared to the pre-injection optical image. This is represented by the elliptical ROIs showing an increase from 2.1×10^6 to 3.4×10^6 luminescent counts. This corresponded well to the MRI scans, showing signal void in the toes of the animal as a result of *T2*-effects of MNP. Slight signal void of toes in the left hind paw are also seen, which corresponds to the optical results. MR and optical cannot be directly correlated because of positioning factors. While MR can image slices of an anatomic structure, optical imaging will only provide data of the whole structure. In this sense, optical imaging is severely limited because of the dependency on excitation and emission light penetration into the tissue. For example, MNP accumulation closer to the skin surface will give greater luminescence than MNP accumulated further into the tissue. Also, positioning of the limb can also greatly affect the measurement of luminescence. Yet, optical imaging is an attractive potential diagnostic because it is inexpensive and less time consuming than MRI.

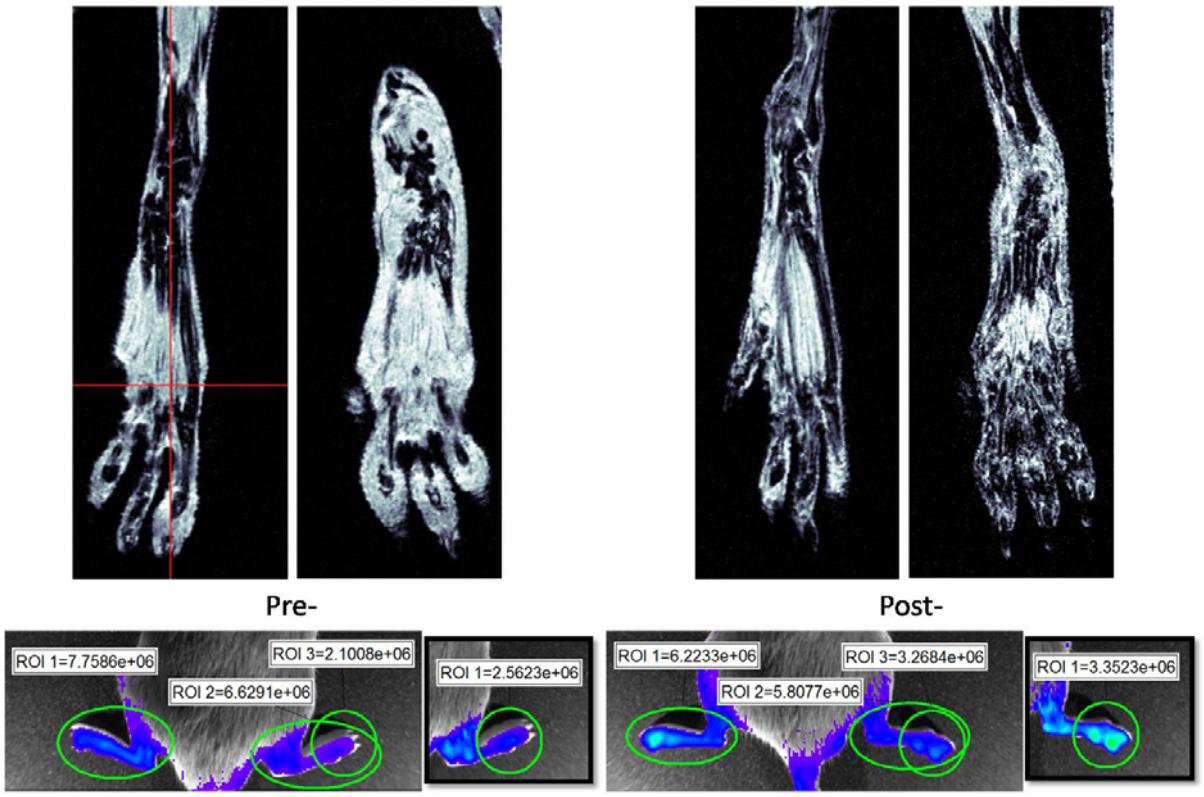

Figure 2.14 High resolution MRI and optical images of hind paws of collagen induced arthritis animals pre- and post- MNP injection. Right hind paw shows higher fluorescence intensity and *T2*-effect signal void after MNP injection.

2.2.13 Confocal fluorescence microscopy of arthritic joints

Tissue sections of arthritic hind paws were examined under light and confocal fluorescence microscopy. The characteristic fluorescence of $Ru(bpy)_3Cl_2$ retained in the MNP core was specifically found in the synovial tissue where active inflammatory disease was present. The nanoparticle contrast agent is hypothesized to *in vivo* label monocytes through phagocytosis. As previously demonstrated, monocytes phagocytically loaded with MNP have been shown to be completely viable by MTS assay, potentially allowing activated cells to migrate and infiltrate joints during inflammation. **Figure 2.15** shows MNP fluorescence specifically in the "crescent" shaped synovium surrounding the *calcaneus* (heel

bone) of the ankle joint at 10X magnification. Though a majority of MNP was localized in the synovial tissue surrounding the joint, some nanoparticle deposition was detected in the bone. This may be evidence of monocytes infiltrating the bony structure and causing permanent damage. Arthritic joints have apparent MNP deposition as measured by fluorescence, further magnification and immunofluorescence was necessary to examine cellular uptake and deposition.

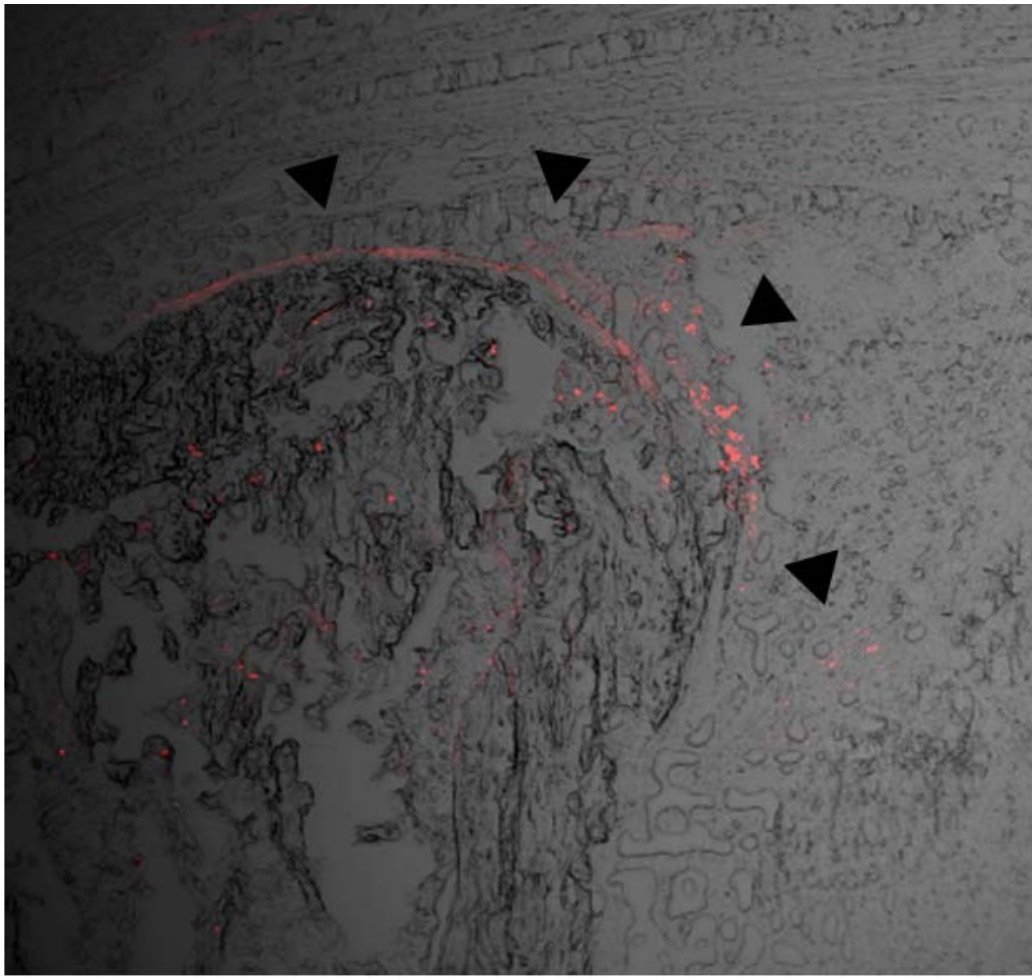

Figure 2.15 Overlay of 10X light and fluorescence images from hindlimbs of collagen-induced arthritis animals showed MNP localizes in the synovial tissue (indicated by black triangles).

2.2.14 Immunofluorescence of arthritic joints

Joint tissue slices stained for immune cells show that monocytes traffic nanoparticle to sites of inflammation under confocal fluorescence microscopy at 63X magnification. MNP contrast excites at 488 nm and emits at a 610 nm maximum wavelength, creating an ideal tandem stain with FITC-labeled antibodies. Monocytes, B-cells, and T-cells are all known to take active roles in the immune response, but also all are known to infiltrate synovial tissue in RA. As expected, monocytes, B-cells, and T-cells were present in the synovial tissue of the CIA mice, as shown by FITC fluorescence due to antibody stain. Only monocytes stained with the monocyte/macrophage marker MOMA2-FITC have overlapping fluorescence with the MNP, showed intracellular monocyte uptake. When stained with the T-cell marker anti-CD3-FITC, joint slices show little overlap with MNP fluorescence, due to low uptake by T-cells. B-cells stained with anti-B220-FITC within the joints show a similarly low overlap with MNP fluorescence, indicative of little to no uptake by B-cells present in the inflamed tissue. Overlap was indicated by the merging of fluorescence channels: FITC (green) + MNP (red) = overlay (yellow). The relevance of these results is the demonstration of monocytes or macrophages with specific MNP uptake. Although T-cells and B-cells also known to be present in sites of inflammation, they did not have nearly the same extent of MNP uptake.

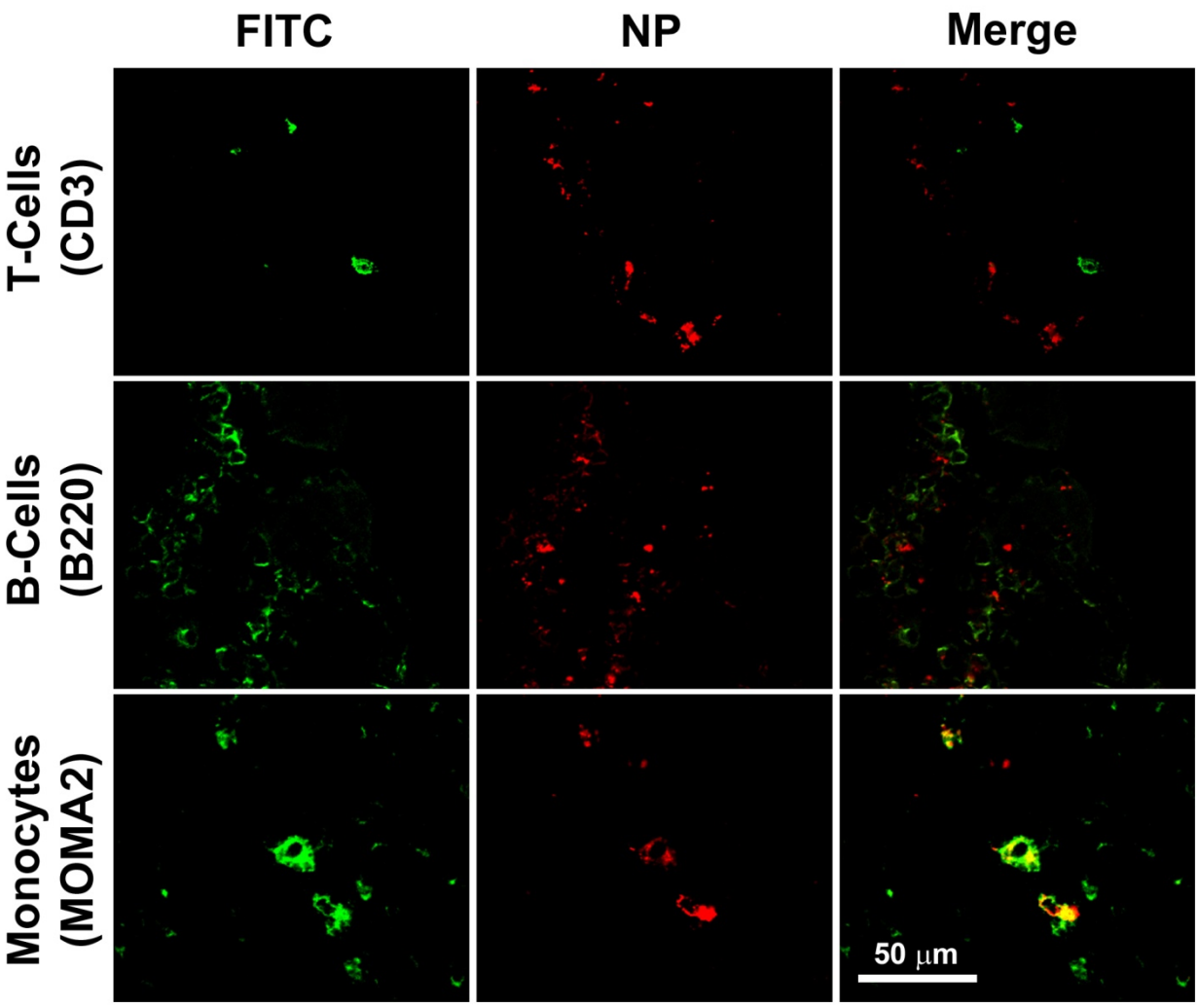

Figure 2.16 Immunofluorescence microscope images of cryopreserved joint histopathology from arthritic mice demonstrated that MNP contrast is intracellular and specific for macrophages. Tissue sections of the joints of the arthritic animals given MNP were stained and examined at 63X magnification. MNP fluorescence was concentrated within the synovial tissue. Macrophages stained with anti-MOMA2 had overlapping fluorescence with intracytoplasmic MNP, whereas lymphocytes (T-cells, B-cells) did not.

2.2.15 Tissue biodistribution of MNP in CIA mice

The tissue distribution of Gd(III) metal ions was measured by harvesting organs for direct current plasma elemental analysis. Gadolinium is not an endogenous element that is present in physiological systems, so there is no background signal from biological tissues. Organs that commonly collect particulate matter were selected for analysis: lung, spleen, and liver; but also organs which may elucidate clearance mechanism: kidney, small intestine, and colon. **Figure 2.17** shows the biodistribution of MNP as measured by Gd elemental analysis of a CIA animal injected with 2.5 mg MNP. Lung, kidney, and spleen demonstrated little to no detectable Gd(III).

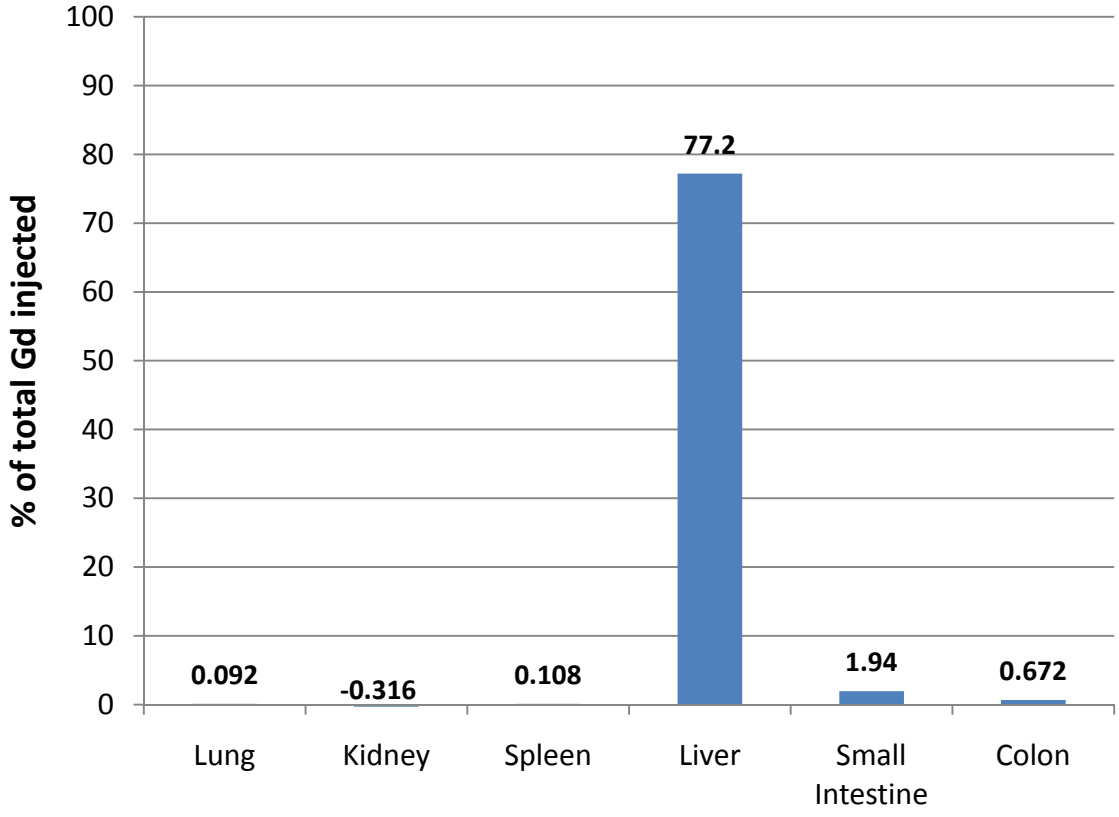

Figure 2.17 Biodistribution of MNP (2.5 mg injected dose, 4% Gd) in CIA mouse has been determined by DCP elemental analysis.

Another arthritic animal, injected with 5.0 mg MNP, demonstrated similar distribution of MNP within its tissues. Again, the clearance mechanism of the RES resulted in high levels of nanoparticle uptake. Gd(III) levels approximately doubled in the liver compared to the animal injected with 2.5 mg MNP **(Figure 2.18**). Liver uptake was, as expected, dose dependant to the amount of MNP injected (corresponding to the 4% Gd coverage of MNP as determined by DCP measurements).

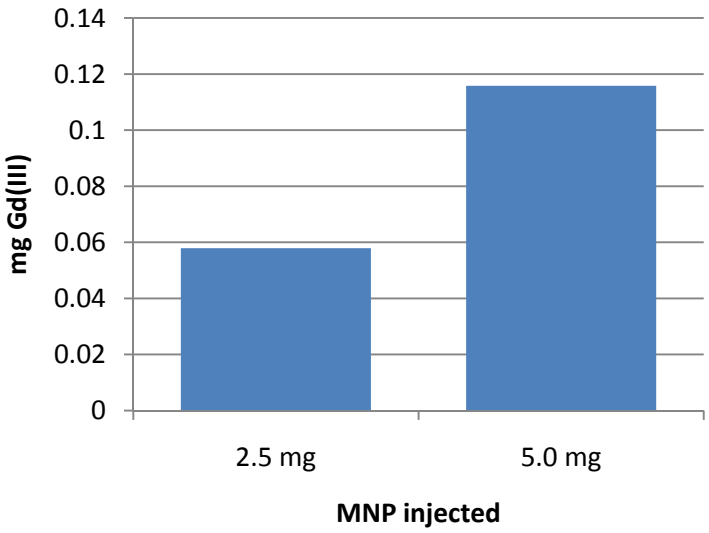

Figure 2.18 Gd levels measured in the livers of CIA animals injected with 2.5 mg MNP and 5.0 mg MNP. Elemental analysis of liver shows dose dependant uptake of MNP as correlated to milligrams of Gd in liver.

Arthritic, inflamed paws of this animal were analyzed for Gd content to demonstrate high levels of Gd within a small tissue volume. **Figure 2.19** shows Gd levels roughly correlated with optical measurements of the paws.

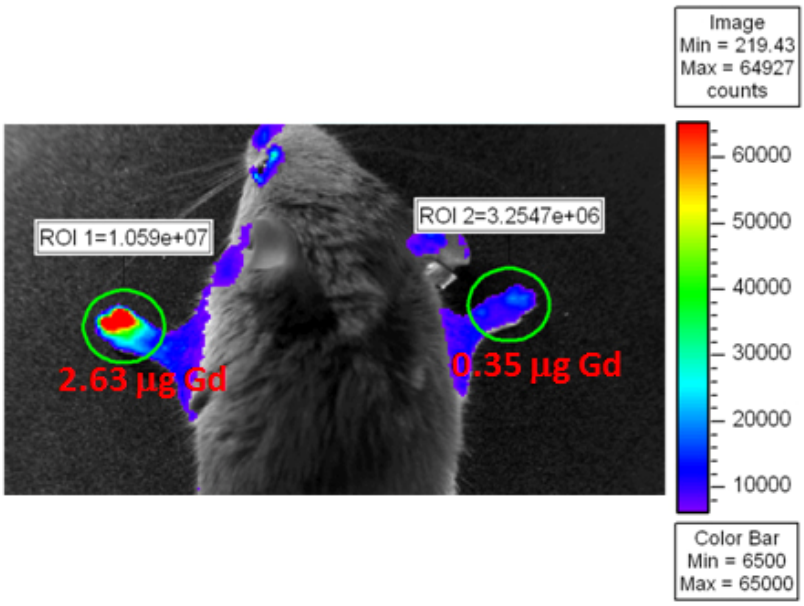

Figure 2.19 Gd levels measured in arthritic paws by elemental analysis were proportional to the increase in luminescence of MNP.

These results show that MNP retains Gd and luminescence after being injected and traveling to the disease site. CIA mice were also injected with a related MRI contrast enhancing nanomaterial reported by our group.[66] This nanoparticle is also silica based with Gd(III) immobilized onto its mesoporous surface using the DTTA ligand. Injecting 5.0 mg of these nanomaterials into CIA mice, the RES (liver and spleen) was found to contain a majority of the Gd(III), with the inflamed paws uptaking over 10% of the total Gd(III) injected. The inflamed forepaws contained 1.64% (right) and 1.73% (left) while the larger hindpaws contained 3.40% (right) and 3.75% (left) of the total Gd(III) (**Figure 2.20)**. This level of uptake is extraordinary considering the small volume of inflamed synovial tissue and demonstrates the high payload and labeling efficiency of the nanomaterials.

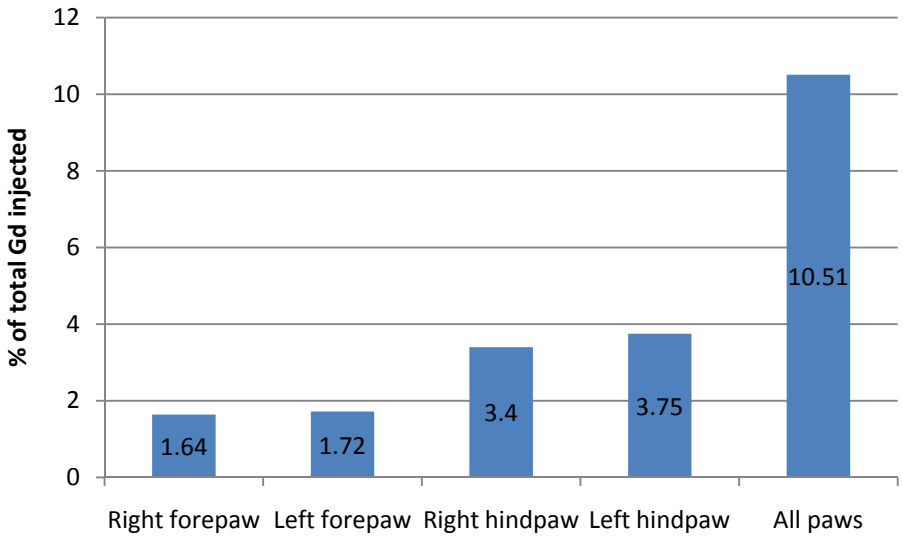

Figure 2.20 Gd levels measured in arthritic paws by elemental analysis of collagen-induced arthritis animals injected with mesoporous silica nanospheres.

The liver contained high levels of Gd(III) as a result of resident Kupffer cells (macrophages) quickly filtering particulate matter from the blood circulation. Small amounts of Gd(III) were detected in the small intestine and colon, potentially indicating slow clearance of the MNP by a biliary mechanism. Presumably, nanoparticles were filtered from the blood and collected by the liver, where they are slowly released with bile into the gastrointestinal system. Silica nanospheres labeled with fluorescent molecules injected into mice were also found in the liver and bile ducts (**Figure 2.21**).[66] Additionally, animals monitored over 4 weeks showed Gd(III) retained in the liver without detrimental effects to survival, demonstrating the robust nature of MNP while ensuring safe use.

A. 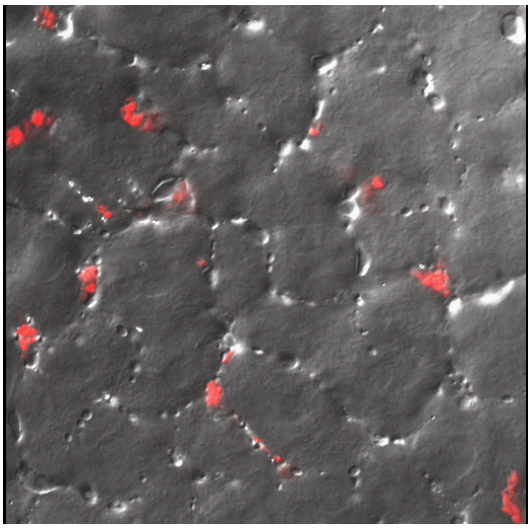 B. 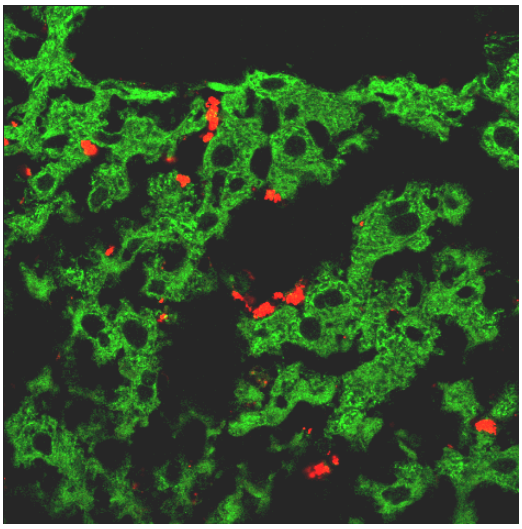

Figure 2.21 Silica nanospheres labeled with rhodamine injected into mice were found in the liver. A) Light microscopy overlay with rhodamine fluorescence shows presence of nanospheres in bile ducts near Kupffer cells. B) Immunofluorescence overlaying MOMA2-FITC stained macrophage Kupffer cells trapping rhodamine labeled nanospheres.

2.3 Concluding Remarks

Early diagnosis of subclinical inflammation is realized by harnessing nanoscience of newly developed multifunctional nanomaterials. These studies show that MNP contrast agent composed of a dye-doped silica nanoparticle with an enhanced paramagnetic coating of a Gd-DPTA silane derivative can deliver large payloads with enhanced relaxitives and thus be used as a highly sensitive noninvasive tool in inflammatory disease. Murine monocytes could uptake and become labeled by MNP. MNP-labeled cells were subsequently imaged *in vitro* by confocal and MRI, to show potential clinical application. Current clinical studies have shown that *T1* and *T2* relaxation time mapping can rapidly detect cartilage changes [60-63] and loss of proteoglycan density in cartilage. [63-65] Nanoscale materials can specifically label phagocytic cells because of these cells' inherent activity for uptake and clearance of particulate matter. Rather than avoiding the reticulo-endothelial system, we use the cellular mechanism to our advantage for diagnostic purposes using a robust hybrid nanomaterial. Our data provides evidence for high resolution *T2* MRI and *T2* relaxation time map changes at the cellular level in a model of autoimmune disease with dampening of the *T2* signal in inflamed joints of arthritic animals. Furthermore, multiple modalities of the MNP fluorescent core enabled us to demonstrate a strong positive correlation ($p < 0.01$) with clinical disease activity and determine the cellular target as infiltrating monocytes into the synovial tissue. The MNP found in the liver was dose dependent, like MNP luminescence in the paws, and showed evidence of clearance by a biliary mechanism. This novel technology has broad-reaching implications in guiding the diagnosis and treatment of autoimmune diseases such as rheumatoid arthritis in addition to other inflammatory disorders such as atherosclerosis and malignancy where targeted biologic therapy at the cellular level is

advancing. It also serves as a platform for validating future molecular and cellular targets with the multifunctionality of the silica-based core for carrying cargo such as luminophores or therapeutic drugs.

2.4 Materials and Methods

2.4.1 Multimodal nanoparticle contrast agent

The nanoparticle contrast agent was prepared by a synthetic procedure previously described.[39] Briefly, vigorously stirred luminophore-doped ($Ru(bpy)_3Cl_2$: excitation maxima 450 nm and emission maxima 595 nm) silicon dioxide nanoparticles prepared by water-in-oil reverse microemulsion are functionalized with Gd-(trimethoxysilylpropyl)-diethylenetriamine tetraacetate. After purification, the hybrid contrast agent is dispersed in sterile saline (0.9%) and ready for administration as a functional MNP contrast agent. In a clinical 3.0 Tesla MR imaging scanner, the $r1$ and $r2$ were measured to be 2.0×10^5 (mM Gd s)$^{-1}$ and 6.1×10^5 (mM Gd s)$^{-1}$, respectively.

2.4.2 Cell culture studies

Monocyte immortalized lines were generated using the previously described methods of Monner[67] and Walker[68] with minor modifications described by Lorenz et al[69]. Briefly, bone marrow progenitor cells from C57Bl/6 mice were harvested and grown in conditioned medium containing 10% heat-inactivated fetal calf serum, 1% l-glutamine, and 20% LADMAC (catalog no. CRL 2420; American Type Culture Collection) supernatant in Minimal Essential Medium. Once immortalized, cells were grown in the aforementioned conditioned medium, which provides the isolated monocytes with colony-stimulating factor-

1. Cell lines were matured over 9 months to achieve a homogeneous population expressing the macrophage/monocyte marker MOMA-2 with phagocytic capacity.

An alternate immortalized mononuclear cell line was cultured for viability and uptake experiments. These mouse monocyte-macrophages, adapted to culture from female BALB/c mouse tumor, were grown in conditioned DMEM/F12 medium containing 10% heat-inactivated fetal bovine serum and 1% Penicillin/Streptomycin at 37ºC with 5% CO_2. Subcultures were prepared by scraping to dislodge cells rather than trypsinization.

2.4.3 Monocyte cell viability assays

Cell viability of monocytes incubated in the presence of various nanoparticles was measured using the CellTiter 96® AQueous One Solution Cell Proliferation Assay purchased from Promega. This is a colorimetric assay based on the bioreduction of 3-(4,5-dimethylthiazol-2-yl)-5-(3-carboxymethoxyphenyl)-2-(4-sulfophenyl)-2H-tetrazolium salt (MTS) into a colored formazan product. Manufacturer's directions were followed for this assay with slight modifications for addition of nanoparticle incubation. Briefly, 5000 cells per well were placed in a 96-well plate with 100 μL of media per well. Nanoparticles were added in various concentrations in 20 μL volumes to each well. Variable concentration ranges were used, and each concentration was replicated five times. After addition of nanoparticles, cells are allowed to incubate and uptake nanoparticles for 20-24 hours at 37ºC with 5% CO_2. MTS reagent was subsequently thawed from 20ºC storage at 37ºC for 10 minutes before 20 μL per well and incubated for 4 hours. Absorbance at 490 nm was measured using a Bio-Rad 96-well plate reader. Data was processed through insertion of raw data into a spreadsheet.

2.4.4 *In vitro* MRI acquisition of MNP-labeled monocyte pellet

Monocyte cells were trypsinized for 5 minutes at 37 ºC and 5% CO_2 before collection, then concentration by low speed centrifugation. Cell concentration was determined by the trypan blue exclusion assay. Approximately 18.1 x 10^6 monocytes were placed in a culture dish with 1 mL of media and 0.433 mL of nanoparticle solution (24.6 mg/mL). After 1 hour of incubation, the cells were washed with fresh media twice and pelleted. A final layer of PBS (200 μL) was added on top, careful not to disturb the pellet, for MR imaging of the cells. *In vitro* MRI was acquired on a 3.0T clinical scanner using *T1*- and *T2*- weighted sequences. Upon completion of MR imaging, the cells were digested in 1.0 M HNO_3 for DCP measurements of the total Gd uptake by the cells.

2.4.5 Confocal fluorescence microscopy of MNP-labeled monocytes

Monocyte cells were incubated in media (2.0 mL) with nanoparticle suspension (17.0 μL, 24.6 mg/mL) for 30 minutes at 37 ºC with 5% CO_2. The cells were isolated from the media by centrifugation at 1000 RPM for 10 minutes at 4 ºC, and subsequently washed with fresh aliquots of media. The resulting isolated pellet was suspended in 100 μL of PBS and approximately 15 μL was placed onto a glass slide for imaging. Grease was used to create a protective barrier, to prevent crushing of cells and loss of buffer solution, before a glass cover slip was placed onto the slide. A Leica SP2 AOBS Upright laser scanning confocal fluorescence microscope at the UNC Michael Hooker Microscopy Facility was used with instrument settings of excitation at 488 nm and emission detected using a 530 long pass filter setting at 252X zoom (63X oil immersion optical + 4X digital).

2.4.6 Flow cytometry of MNP-labeled monocytes

One million monocyte cells were incubated in media (2.0 mL) with nanoparticle suspension (17.0 μL, 24.6 mg/mL) for 30 minutes at 37 ºC with 5% CO_2. The cells were isolated from the media by centrifugation at 1000 RPM for 10 minutes at 4 ºC, and subsequently washed with fresh aliquots of media. The resulting isolated pellet was suspended in 1 mL PBS before placing into flow cytometer. A Beckman-Coulter (Dako) CyAn ADP flow cytometer using 488 nm excitation and PE-Texas Red emission settings was used for acquisition and Summit software used for data analysis. Cells incubated without nanoparticles are used as a control and for gating purposes. Various concentrations of nanoparticle were incubated with monocytes to demonstrate uptake and labeling efficiency to trigger events via cell fluorescence.

2.4.7 Induction and evaluation of collagen induced arthritis (CIA) in animals

Collagen induced arthritis animal models are widely used and well characterized for studying rheumatoid arthritis.[70-73] First generated in rats, CIA in mouse models is most widely used, particularly for testing new anti-inflammatory and immune-specific therapeutics.[74] Genetically susceptible animals are immunized with type II collagen to induce T- and B-lymphocyte immunity. Also, major histocompatibility complex (MHC) class II, a large protein expressed on the surface of cells that displays antigens, is associated with both CIA and RA.[72] Further evidence of pathogenesis of this experimental disease has also been studied to draw parallels to RA for determining applicability to human disease.

Etiology of RA remains largely unknown, yet collagen II specific antibodies have been detected in RA patients, indicating the significance of this model.

Animals used in these experiments were DBA-1J mice either purchased from Jackson Laboratories (Bar Harbor, ME) or bred and cared for in Division of Laboratory Animal Medicine (DLAM) facilities under the University of North Carolina approved Institutional Animal Care and Use Committee (IACUC) protocol number 05-289.0 in pathogen free specific conditions. Eight week old DBA-1J mice were immunized with adjuvant (Complete Freund's on day 0 and incomplete Freund's on day 21) ± 100μg per mouse of heterologous bovine type II collagen. Using a 27 gauge needle, 0.1 mL of a 1:1 mixture of adjuvant + collagen or saline was injected subcutaneously into the base of the tail. Mice were assessed at baseline and from the onset of arthritis by a clinical scoring index. Clinical index was performed by a blinded observer with the following scoring system: 0 = normal paw; 1 = mild but definite swelling of either the ankle or digits; 2 = moderate redness and swelling of an ankle ± any number of digits; 3 = maximal redness and swelling of the entire paw and digits. The maximum score per paw obtainable was 3 with a total score obtainable of 12 per mouse. At experiment termination, hindlimbs were embedded in OCT and frozen in liquid nitrogen for immunofluorescence.

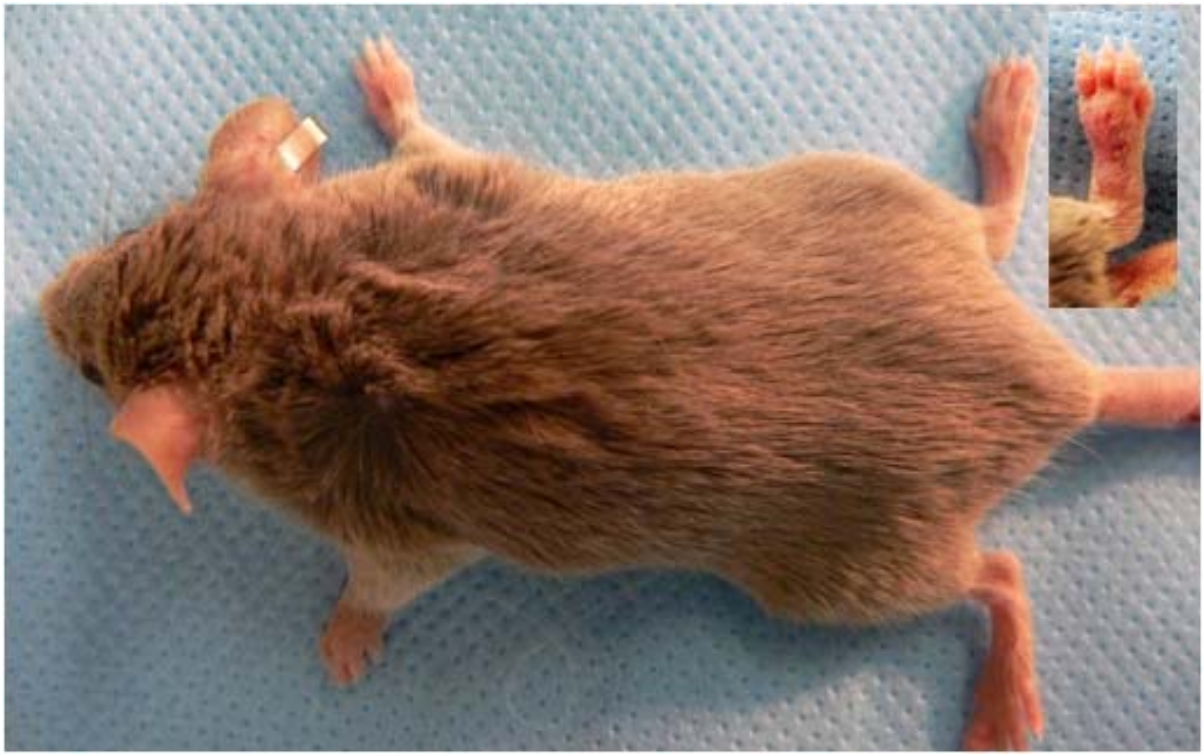

Figure 2.22 DBA-1J mouse was used for collagen-induced arthritis model. Upper right inset shows a visual comparison of the increased swelling resulting from hind paw inflammation.

2.4.8 Global assessment of disease

Paw swelling measurements consist of the mouse's fore- and hind-limbs in millimeters with a caliper. The change in paw thickness from the baseline (day 0) for each individual mouse is recorded. Results are reported as an average of change from baseline for each group. Clinical Index of disease is a clinical measurement of the degree of arthritis severity that has been validated in previous experiments.[75] The clinical index is based on scores assessed by a trained observer and takes into account arthritis that is present beyond the ankle swelling, such as individual toes or tenosynovium (**Table 2.1**). Each paw is assessed by a blinded observer; maximum score is 3 per paw for a total of 12 per mouse.

Table 2.1 Clinical Index of arthritis

Arthritis Score	Clinical Presentation
0	Normal paw, no arthritis
1	Mild, but definite swelling and/or redness of one major joint (wrist or ankle) or toe involvement (any number)
2	Moderate redness and swelling of wrist or ankle ± any number of toes
3	Maximal redness and swelling of entire paw including toes ± ankylosis

2.4.9 Administration of multimodal nanoparticle contrast agent

Twenty-four DBA-1J mice immunized with (n = 12) or without (n =12) type heterologous II bovine collagen were distributed randomly (n = 4 per group). Animals were warmed approximately 5 minutes using a heat lamp to increase blood flow and visualization of the vein. The animal was placed into a holding device before tail veil intravenous injection (0.05 mL) with saline or nanoparticle contrast agent (125mg/kg or 250mg/kg) in two doses separated by 12 hours on Day 35 or other specified time point. Intravenous injection was chosen over intraperitoneal or subcutaneous injection to insure direct delivery to the blood circulation.

2.4.10 *In vivo* optical imaging and imaging analysis

Fluorescence intensities of animals were collected using a Xenogen IVIS 100 series Optical/Fluorescence Scanner exciting with the GFP filter (445-490 nm) and collecting emission with the DsRed filter (575-650 nm). Animals had images taken under anesthesia with a carefully monitored inhaled isoflurane/oxygen gas mixture. Initially, animals are placed in an anesthesia chamber before transfer to the scanner. A continual flow of anesthesia was administered by the instrument's nose cone and the animal is positioned dorsal side up. Paws were positioned away from the body to obtain clear optical and luminescence images of the arthritis. Fluorescence images were taken 12 hours after the second injected dose of nanoparticle contrast agent. Additional images were obtained at 36, 60, and 84 hours after second injected dose. Igor Pro 4.06 Living Image®, version 2.20.1 was used to record images, normalize background, and select elliptical regions of interest (ROIs) for fluorescence quantification. For each animal measurement, four ROI ellipses are placed to include the inflamed wrist or ankle and associated digits, before requesting the software for a measurement. Scales are normalized at a minimum of 6500 counts and a maximum of 65000 counts, with background subtraction and cosmic correction. The obtained data was placed into an excel (.xls) spreadsheet with paw swelling measurements and clinical indices of arthritis.

2.4.11 *In situ* immunofluorescence

Tissue sections (5-7 μm) were cut from Tissue-Tek® O.C.T. embedded hindlimbs using a CryoJane Cryostat (at -20 ºC) and analyzed using a Zeiss LSM5 confocal laser scanning fluorescent microscope. Cold acetone was used for fixing tissue sections and

removing O.C.T. compound. Immunofluorescence was performed with monoclonal antibodies targeting the following FITC-labeled antigens; anti-B220 (B cell) (BD Biosciences, San Jose, CA), -CD3 (T cell) (BD Biosciences, San Jose, CA) , -MOMA-2 (monocytes/macrophages). After incubation of tissue section with labeled monoclonal antibodies, washing steps using 1X phosphate buffered saline occurred. Confocal laser scanning fluorescence microscopy images were taken using 488 nm excitation with emissions collected from 500-520 nm (FITC) and 575-625 nm (MNP). Data was processed with Leica LCS software to minimize background and generate overlay images.

2.4.12 MR Imaging and data analysis

MR imaging studies were acquired on a 9.4T Bruker BioSpec small animal scanner (Bruker Biospin, Ettlingen, Germany) with a 35 mm quadrature radiofrequency transmit and receive coil. Imaging of animals was performed under carefully monitored inhalational anesthesia of isoflurane/oxygen gas mixture. Two sets of images were obtained on 3 animals with CIA after the onset of clinical disease; one prior to MNP contrast injection and the second 12 hours after the last of 2 doses of contrast was administered intravenously. A 3D Fast Low Angle Shot (FLASH) gradient echo sequence was utilized to obtain high resolution anatomical images of both legs and paws of an animal. The imaging parameters were as follows, TR/TE=120/2.876 ms, flip angle = 30°, FOV = 32*32*12 mm^3, Matrix Size = 640*512*192, voxel size = 0.062 x 0.062 x 0.062 mm^3. Two-dimensional (2D) multiple echo spin echo sequence was used to estimate *T2* maps. In total, 32 echoes with an echo spacing of 3.7 ms were obtained. The first echo time was 3.7 ms. *TR* was 2000ms. FOV and matrix size were set to 35x30 mm^2 and 128 x 128. The slice thickness was 1 mm. *T1* maps

were obtained with a variable *TR* rapid acquisition relaxation enhanced (RARE) sequence with a *TE* = 5.14 ms. Twelve variable *TR*s (*TR* = 50, 100, 300, 600, 1000, 1500, 2000, 2500, 3000, 4000, 5000, 7000 ms) were used with a FOV of 35x30 mm^2 and a matrix size of 128 x 128. RARE factor was 3. Data was analyzed by the following software: Bruker TOPSPIN, MRIcro, and InsightSNAP.

2.4.13 Statistical data analysis

The relationship between fluorescence and clinical disease at day 36 was analyzed using linear mixed models with fixed clinical disease and random mouse effects. The methods of Lipsitz *et al.*[76] were used to calculate partial correlation coefficients adjusted for random mouse effects. Each mouse provides four data points derived from each inflamed paw, which is associated with the clinical assessment and the fluorescence counts measured from each ROI ellipse.

2.4.14 Sample preparation for biodistribution studies.

To quantify biodistribution of gadolinium associated with nanoparticles, 6-8 week old DBA/1J age / sex matched animals (Jackson Laboratory; Bar Harbor, ME) were injected intravenously with MNP. Studies were approved by the UNC institutional animal care and use committee and housed and maintained by DLAM veterinary staff. At desired timepoints, the animals were sacrificed by CO_2 chamber and cervical dislocation. Organs are harvested, and then cremated in a furnace at 500ºC for a minimum of 5 hours. The resulting ash is dissolved in 1M HNO_3 for elemental analysis.

2.5 References

1. Mount, C.; Featherstone, J., Rheumatoid arthritis market. *Nat Rev Drug Discov* **2005,** 4, (1), 11-2.

2. Gabriel, S. E., The epidemiology of rheumatoid arthritis. *Rheum Dis Clin North Am* **2001,** 27, (2), 269-81.

3. Pincus, T.; Brooks, R. H.; Callahan, L. F., Prediction of long-term mortality in patients with rheumatoid arthritis according to simple questionnaire and joint count measures. *Ann Intern Med* **1994,** 120, (1), 26-34.

4. Pugner, K. M.; Scott, D. I.; Holmes, J. W.; Hieke, K., The costs of rheumatoid arthritis: an international long-term view. *Semin Arthritis Rheum* **2000,** 29, (5), 305-20.

5. Arnett, F. C.; Edworthy, S. M.; Bloch, D. A.; McShane, D. J.; Fries, J. F.; Cooper, N. S.; Healey, L. A.; Kaplan, S. R.; Liang, M. H.; Luthra, H. S.; et al., The American Rheumatism Association 1987 revised criteria for the classification of rheumatoid arthritis. *Arthritis Rheum* **1988,** 31, (3), 315-24.

6. Persselin, J. E., Diagnosis of rheumatoid arthritis. Medical and laboratory aspects. *Clin Orthop Relat Res* **1991**, (265), 73-82.

7. Shiel, W. C., Rheumatoid Arthritis. *Medicinenet* **2007**.

8. Scutellari, P. N.; Orzincolo, C., Rheumatoid arthritis: sequences. *Eur J Radiol* **1998,** 27 Suppl 1, S31-8.

9. Scheel, A. K.; Hermann, K. G.; Ohrndorf, S.; Werner, C.; Schirmer, C.; Detert, J.; Bollow, M.; Hamm, B.; Muller, G. A.; Burmester, G. R.; Backhaus, M., Prospective 7 year follow up imaging study comparing radiography, ultrasonography, and magnetic resonance imaging in rheumatoid arthritis finger joints. *Ann Rheum Dis* **2006,** 65, (5), 595-600.

10. Gaffney, K.; Cookson, J.; Blake, D.; Coumbe, A.; Blades, S., Quantification of rheumatoid synovitis by magnetic resonance imaging. *Arthritis Rheum* **1995,** 38, (11), 1610-7.

11. Gandy, S. J.; Brett, A. D.; Dieppe, P. A.; Keen, M. C.; Maciewicz, R. A.; Taylor, C. J.; Waterton, J. C.; Watt, I., Measurement of cartilage volumes in rheumatoid arthritis using MRI. *Br J Radiol* **2005,** 78, (925), 39-45.

12. Ostergaard, M.; Stoltenberg, M.; Lovgreen-Nielsen, P.; Volck, B.; Jensen, C. H.; Lorenzen, I., Magnetic resonance imaging-determined synovial membrane and joint effusion volumes in rheumatoid arthritis and osteoarthritis: comparison with the macroscopic and microscopic appearance of the synovium. *Arthritis Rheum* **1997,** 40, (10), 1856-67.

13. Poleksic, L.; Musikic, P.; Zdravkovic, D.; Watt, I.; Bacic, G., MRI evaluation of the knee in rheumatoid arthritis. *Br J Rheumatol* **1996,** 35 Suppl 3, 36-9.

14. Tamai, K.; Yamato, M.; Yamaguchi, T.; Ohno, W., Dynamic magnetic resonance imaging for the evaluation of synovitis in patients with rheumatoid arthritis. *Arthritis Rheum* **1994,** 37, (8), 1151-7.

15. Hodgson, R. J.; Barnes, T.; Connolly, S.; Eyes, B.; Campbell, R. S.; Moots, R., Changes underlying the dynamic contrast-enhanced MRI response to treatment in rheumatoid arthritis. *Skeletal Radiol* **2008,** 37, (3), 201-7.

16. Hodgson, R. J.; O'Connor, P.; Moots, R., MRI of rheumatoid arthritis image quantitation for the assessment of disease activity, progression and response to therapy. *Rheumatology (Oxford)* **2008,** 47, (1), 13-21.

17. Brandser, E. A., Radiological evidence of Degenerative Joint Disease (DJD): Rheumatoid Arthritis Affecting the Hands. *University of Iowa Virtual Hospital* **2005**.

18. Rand, T.; Imhof, H.; Czerny, C.; Breitenseher, M.; Machold, K.; Turetschek, K.; Trattnig, S., Discrimination between fluid, synovium, and cartilage in patients with rheumatoid arthritis: contrast enhanced Spin Echo versus non-contrast-enhanced fat-suppressed Gradient Echo MR imaging. *Clin Radiol* **1999,** 54, (2), 107-10.

19. Demsar, F.; Van Dijke, C. F.; Kirk, B. A.; Kapila, S.; Peterfy, C. G.; Roberts, T. P.; Shames, D. M.; Tomazic, S.; Mann, J.; Brasch, R. C., Mapping abnormal synovial vascular permeability in temporomandibular joint arthritis in the rabbit using MRI. *Br J Rheumatol* **1996,** 35 Suppl 3, 23-5.

20. Johnson, B. A.; Haines, G. K.; Harlow, L. A.; Koch, A. E., Adhesion molecule expression in human synovial tissue. *Arthritis Rheum* **1993,** 36, (2), 137-46.

21. Storgard, C. M.; Stupack, D. G.; Jonczyk, A.; Goodman, S. L.; Fox, R. I.; Cheresh, D. A., Decreased angiogenesis and arthritic disease in rabbits treated with an alphavbeta3 antagonist. *J Clin Invest* **1999,** 103, (1), 47-54.

22. Firestein, G. S., Starving the synovium: angiogenesis and inflammation in rheumatoid arthritis. *J Clin Invest* **1999,** 103, (1), 3-4.

23. Arap, W.; Pasqualini, R.; Ruoslahti, E., Cancer treatment by targeted drug delivery to tumor vasculature in a mouse model. *Science* **1998,** 279, (5349), 377-80.

24. Koivunen, E.; Restel, B. H.; Rajotte, D.; Lahdenranta, J.; Hagedorn, M.; Arap, W.; Pasqualini, R., Integrin-binding peptides derived from phage display libraries. *Methods Mol Biol* **1999,** 129, 3-17.

25. Gerlag, D. M.; Borges, E.; Tak, P. P.; Ellerby, H. M.; Bredesen, D. E.; Pasqualini, R.; Ruoslahti, E.; Firestein, G. S., Suppression of murine collagen-induced arthritis by targeted apoptosis of synovial neovasculature. *Arthritis Res* **2001,** 3, (6), 357-61.

26. Caravan, P.; Ellison, J. J.; McMurry, T. J.; Lauffer, R. B., Gadolinium(III) Chelates as MRI Contrast Agents: Structure, Dynamics, and Applications. *Chem Rev* **1999,** 99, (9), 2293-352.

27. Koch, A. E.; Kunkel, S. L.; Strieter, R. M., Cytokines in rheumatoid arthritis. *J Investig Med* **1995,** 43, (1), 28-38.

28. Brennan, F. M.; Maini, R. N.; Feldmann, M., Role of pro-inflammatory cytokines in rheumatoid arthritis. *Springer Semin Immunopathol* **1998,** 20, (1-2), 133-47.

29. Lutz, A. M.; Gopfert, K.; Jochum, W.; Nanz, D.; Frohlich, J. M.; Weishaupt, D., USPIO-enhanced MR imaging for visualization of synovial hyperperfusion and detection of synovial macrophages: preliminary results in an experimental model of antigen-induced arthritis. *J Magn Reson Imaging* **2006,** 24, (3), 657-66.

30. Mulherin, D.; Fitzgerald, O.; Bresnihan, B., Synovial tissue macrophage populations and articular damage in rheumatoid arthritis. *Arthritis Rheum* **1996,** 39, (1), 115-24.

31. Simon, G. H.; von Vopelius-Feldt, J.; Wendland, M. F.; Fu, Y.; Piontek, G.; Schlegel, J.; Chen, M. H.; Daldrup-Link, H. E., MRI of arthritis: comparison of ultrasmall superparamagnetic iron oxide vs. Gd-DTPA. *J Magn Reson Imaging* **2006,** 23, (5), 720-7.

32. Wu, Y. L.; Ye, Q.; Foley, L. M.; Hitchens, T. K.; Sato, K.; Williams, J. B.; Ho, C., In situ labeling of immune cells with iron oxide particles: an approach to detect organ rejection by cellular MRI. *Proc Natl Acad Sci U S A* **2006,** 103, (6), 1852-7.

33. Lutz, A. M.; Seemayer, C.; Corot, C.; Gay, R. E.; Goepfert, K.; Michel, B. A.; Marincek, B.; Gay, S.; Weishaupt, D., Detection of synovial macrophages in an experimental rabbit model of antigen-induced arthritis: ultrasmall superparamagnetic iron oxide-enhanced MR imaging. *Radiology* **2004,** 233, (1), 149-57.

34. Dardzinski, B. J.; Schmithorst, V. J.; Holland, S. K.; Boivin, G. P.; Imagawa, T.; Watanabe, S.; Lewis, J. M.; Hirsch, R., MR imaging of murine arthritis using ultrasmall superparamagnetic iron oxide particles. *Magn Reson Imaging* **2001,** 19, (9), 1209-16.

35. Hercend, T.; Farace, F.; Baume, D.; Charpentier, F.; Droz, J. P.; Triebel, F.; Escudier, B., Immunotherapy with lymphokine-activated natural killer cells and recombinant interleukin-2: a feasibility trial in metastatic renal cell carcinoma. *J Biol Response Mod* **1990,** 9, (6), 546-55.

36. Sykes, M.; Nikolic, B., Treatment of severe autoimmune disease by stem-cell transplantation. *Nature* **2005,** 435, (7042), 620-7.

37. Radbruch, A.; Thiel, A., Cell therapy for autoimmune diseases: does it have a future? *Ann Rheum Dis* **2004,** 63 Suppl 2, ii96-ii101.

38. Lang, P.; Yeow, K.; Nichols, A.; Scheer, A., Cellular imaging in drug discovery. *Nat Rev Drug Discov* **2006,** 5, (4), 343-56.

39. Rieter, W. J.; Kim, J. S.; Taylor, K. M.; An, H.; Lin, W.; Tarrant, T.; Lin, W., Hybrid Silica Nanoparticles for Multimodal Imaging. *Angew Chem Int Ed Engl* **2007**.

40. Rittig, M. G.; Kaufmann, A.; Robins, A.; Shaw, B.; Sprenger, H.; Gemsa, D.; Foulongne, V.; Rouot, B.; Dornand, J., Smooth and rough lipopolysaccharide phenotypes of Brucella induce different intracellular trafficking and cytokine/chemokine release in human monocytes. *J Leukoc Biol* **2003,** 74, (6), 1045-55.

41. Pennica, D.; Nedwin, G. E.; Hayflick, J. S.; Seeburg, P. H.; Derynck, R.; Palladino, M. A.; Kohr, W. J.; Aggarwal, B. B.; Goeddel, D. V., Human tumour necrosis factor: precursor structure, expression and homology to lymphotoxin. *Nature* **1984,** 312, (5996), 724-9.

42. Itaya, H.; Imaizumi, T.; Yoshida, H.; Koyama, M.; Suzuki, S.; Satoh, K., Expression of vascular endothelial growth factor in human monocyte/macrophages stimulated with lipopolysaccharide. *Thromb Haemost* **2001,** 85, (1), 171-6.

43. Kermarrec, N.; Selloum, S.; Plantefeve, G.; Chosidow, D.; Paoletti, X.; Lopez, A.; Mantz, J.; Desmonts, J. M.; Gougerot-Pocidalo, M. A.; Chollet-Martin, S., Regulation of peritoneal and systemic neutrophil-derived tumor necrosis factor-alpha release in patients with severe peritonitis: role of tumor necrosis factor-alpha converting enzyme cleavage. *Crit Care Med* **2005,** 33, (6), 1359-64.

44. Chen, Y.; Kam, C. S.; Liu, F. Q.; Liu, Y.; Lui, V. C.; Lamb, J. R.; Tam, P. K., LPS-induced up-regulation of TGF-{beta} receptor 1 is associated with TNF-{alpha} expression in human monocyte-derived macrophages. *J Leukoc Biol* **2008**.

45. Hetland, G.; Namork, E.; Schwarze, P. E.; Aase, A., Mechanism for uptake of silica particles by monocytic U937 cells. *Hum Exp Toxicol* **2000,** 19, (7), 412-9.

46. Metz, S.; Bonaterra, G.; Rudelius, M.; Settles, M.; Rummeny, E. J.; Daldrup-Link, H. E., Capacity of human monocytes to phagocytose approved iron oxide MR contrast agents in vitro. *Eur Radiol* **2004,** 14, (10), 1851-8.

47. McMorn, P.; Hutchings, G. J., Heterogeneous enantioselective catalysts: strategies for the immobilisation of homogeneous catalysts. *Chem Soc Rev* **2004,** 33, (2), 108-22.

48. Wan, Y.; Zhao, D., On the controllable soft-templating approach to mesoporous silicates. *Chem Rev* **2007,** 107, (7), 2821-60.

49. Grela, K.; Michrowska, A.; Bieniek, M., Catalysts for new tasks: preparation and applications of tunable ruthenium catalysts for olefin metathesis. *Chem Rec* **2006,** 6, (3), 144-56.

50. Huh, S.; Chen, H. T.; Wiench, J. W.; Pruski, M.; Lin, V. S., Cooperative catalysis by general acid and base bifunctionalized mesoporous silica nanospheres. *Angew Chem Int Ed Engl* **2005,** 44, (12), 1826-30.

51. Senarath-Yapa, M. D.; Phimphivong, S.; Coym, J. W.; Wirth, M. J.; Aspinwall, C. A.; Saavedra, S. S., Preparation and characterization of poly(lipid)-coated, fluorophore-doped silica nanoparticles for biolabeling and cellular imaging. *Langmuir* **2007,** 23, (25), 12624-33.

52. Slowing, I.; Trewyn, B. G.; Lin, V. S., Effect of surface functionalization of MCM-41-type mesoporous silica nanoparticles on the endocytosis by human cancer cells. *J Am Chem Soc* **2006,** 128, (46), 14792-3.

53. Radu, D. R.; Lai, C. Y.; Jeftinija, K.; Rowe, E. W.; Jeftinija, S.; Lin, V. S., A polyamidoamine dendrimer-capped mesoporous silica nanosphere-based gene transfection reagent. *J Am Chem Soc* **2004,** 126, (41), 13216-7.

54. Radu, D. R.; Lai, C. Y.; Wiench, J. W.; Pruski, M.; Lin, V. S., Gatekeeping layer effect: a poly(lactic acid)-coated mesoporous silica nanosphere-based fluorescence probe for detection of amino-containing neurotransmitters. *J Am Chem Soc* **2004,** 126, (6), 1640-1.

55. Santra, S.; Xu, J.; Wang, K.; Tan, W., Luminescent nanoparticle probes for bioimaging. *J Nanosci Nanotechnol* **2004,** 4, (6), 590-9.

56. Tapec, R.; Zhao, X. J.; Tan, W., Development of organic dye-doped silica nanoparticles for bioanalysis and biosensors. *J Nanosci Nanotechnol* **2002,** 2, (3-4), 405-9.

57. Xing, X.; He, X.; Peng, J.; Wang, K.; Tan, W., Uptake of silica-coated nanoparticles by HeLa cells. *J Nanosci Nanotechnol* **2005,** 5, (10), 1688-93.

58. Buttke, T. M.; McCubrey, J. A.; Owen, T. C., Use of an aqueous soluble tetrazolium/formazan assay to measure viability and proliferation of lymphokine-dependent cell lines. *J Immunol Methods* **1993,** 157, (1-2), 233-40.

59. Cory, A. H.; Owen, T. C.; Barltrop, J. A.; Cory, J. G., Use of an aqueous soluble tetrazolium/formazan assay for cell growth assays in culture. *Cancer Commun* **1991,** 3, (7), 207-12.

60. Dardzinski, B. J.; Laor, T.; Schmithorst, V. J.; Klosterman, L.; Graham, T. B., Mapping T2 relaxation time in the pediatric knee: feasibility with a clinical 1.5-T MR imaging system. *Radiology* **2002,** 225, (1), 233-9.

61. Kight, A. C.; Dardzinski, B. J.; Laor, T.; Graham, T. B., Magnetic resonance imaging evaluation of the effects of juvenile rheumatoid arthritis on distal femoral weight-bearing cartilage. *Arthritis Rheum* **2004,** 50, (3), 901-5.

62. Van Breuseghem, I.; Bosmans, H. T.; Elst, L. V.; Maes, F.; Pans, S. D.; Brys, P. P.; Geusens, E. A.; Marchal, G. J., T2 mapping of human femorotibial cartilage with turbo mixed MR imaging at 1.5 T: feasibility. *Radiology* **2004,** 233, (2), 609-14.

63. Van Breuseghem, I.; Palmieri, F.; Peeters, R. R.; Maes, F.; Bosmans, H. T.; Marchal, G. J., Combined T1-T2 mapping of human femoro-tibial cartilage with turbo-mixed imaging at 1.5T. *J Magn Reson Imaging* **2005,** 22, (3), 368-72.

64. Bashir, A.; Gray, M. L.; Boutin, R. D.; Burstein, D., Glycosaminoglycan in articular cartilage: in vivo assessment with delayed Gd(DTPA)(2-)-enhanced MR imaging. *Radiology* **1997,** 205, (2), 551-8.

65. Trattnig, S.; Mlynarik, V.; Breitenseher, M.; Huber, M.; Zembsch, A.; Rand, T.; Imhof, H., MRI visualization of proteoglycan depletion in articular cartilage via intravenous administration of Gd-DTPA. *Magn Reson Imaging* **1999,** 17, (4), 577-83.

66. Taylor, K. M.; Kim, J. S.; Rieter, W. J.; An, H.; Lin, W.; Lin, W., Mesoporous silica nanospheres as highly efficient MRI contrast agents. *J Am Chem Soc* **2008,** 130, (7), 2154-5.

67. Monner, D. A.; Denker, B., Characterization of clonally derived, spontaneously transformed bone marrow macrophage cell lines from lipopolysaccharide hyporesponsive LPS(d) and normal LPS(n) mice. *J Leukoc Biol* **1997,** 61, (4), 469-80.

68. Walker, W. S., Establishment of mononuclear phagocyte cell lines. *J Immunol Methods* **1994,** 174, (1-2), 25-31.

69. Lorenz, E.; Patel, D. D.; Hartung, T.; Schwartz, D. A., Toll-like receptor 4 (TLR4)-deficient murine macrophage cell line as an in vitro assay system to show TLR4-independent signaling of Bacteroides fragilis lipopolysaccharide. *Infect Immun* **2002,** 70, (9), 4892-6.

70. Ichim, T. E.; Zheng, X.; Suzuki, M.; Kubo, N.; Zhang, X.; Min, L. R.; Beduhn, M. E.; Riordan, N. H.; Inman, R. D.; Min, W. P., Antigen-specific therapy of rheumatoid arthritis. *Expert Opin Biol Ther* **2008,** 8, (2), 191-9.

71. Cho, Y. G.; Cho, M. L.; Min, S. Y.; Kim, H. Y., Type II collagen autoimmunity in a mouse model of human rheumatoid arthritis. *Autoimmun Rev* **2007,** 7, (1), 65-70.

72. Brand, D. D.; Kang, A. H.; Rosloniec, E. F., Immunopathogenesis of collagen arthritis. *Springer Semin Immunopathol* **2003,** 25, (1), 3-18.

73. Vierboom, M. P.; Jonker, M.; Tak, P. P.; t Hart, B. A., Preclinical models of arthritic disease in non-human primates. *Drug Discov Today* **2007,** 12, (7-8), 327-35.

74. Trentham, D. E.; Townes, A. S.; Kang, A. H., Autoimmunity to type II collagen an experimental model of arthritis. *J Exp Med* **1977,** 146, (3), 857-68.

75. Tarrant, T. K.; Patel, D. D., Chemokines and leukocyte trafficking in rheumatoid arthritis. *Pathophysiology* **2006,** 13, (1), 1-14.

76. Lipsitz, S. R.; Leong, T.; Ibrahim, S.; Lipshultz, S., A partial correlation coefficient and coefficient of determination for multivariate normal repeated measures data. *The Statistician* **2001,** 50, (1), 87-95.

CHAPTER 3

SELF-ASSEMBLED HYBRID NANOPARTICLES FOR CANCER-SPECIFIC MULTIMODAL IMAGING

3.1 Introduction

In the previous chapter, a new nanomaterials with surfaced immobilized Gd(III) was presented for *in vitro* and *in vivo* imaging applications. Large payloads of paramagnetic metal centers were immobilized onto the surface of the nanoparticle to take advantage of its high surface area. As a comparison, we prepared nanoparticles with both a monolayer and multilayer of silane-derivatized Gd(III) chelates (**Figure 3.1**). The two derivative nanoparticles produced excellent relaxivities, though the monolayer system produced the higher relaxivities per Gd(III) than the multilayer system. [199] Although the multilayer approach increased the payload of Gd(III) chelates, their MR relaxivities on a per Gd(III) basis diminished, presumably as a result of reduced water accessibility of the Gd(III) chelates buried in the interior of the multilayer. This chapter presents a new electrostatic layer-by-layer self-assembled nanoparticle platform for cancer-specific multimodal imaging.

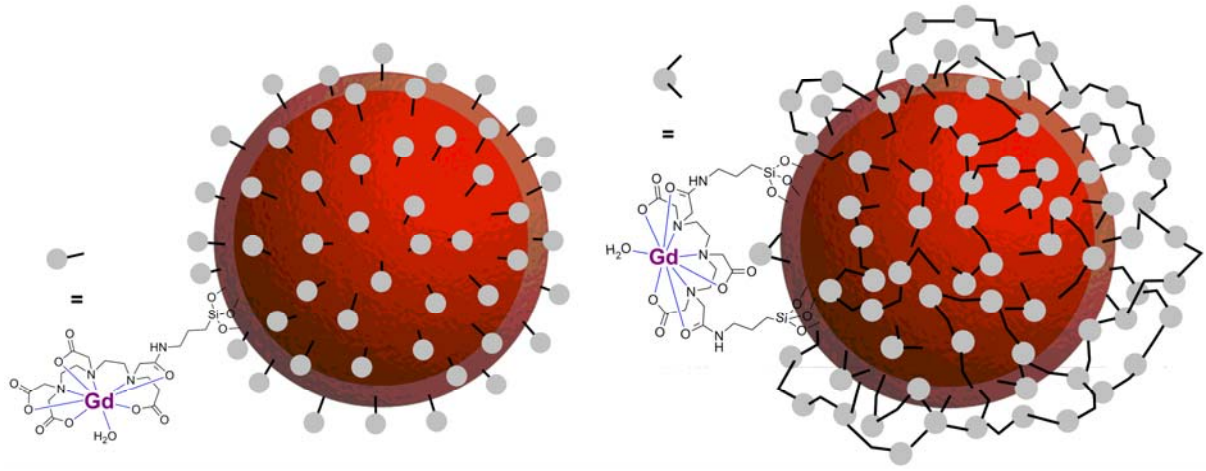

Figure 3.1 Hybrid silica nanoparticles for multimodal imaging with luminescent core and monolayer (left) or multilayer (right) surface coating of Gd(III) chelates.

3.1.1 Electrostatic layer-by-layer self-assembly

Assembly of multilayer films on solid surfaces has been studied for over 70 years to allow for fabrication of multifunctional architecture assemblies. Initially, Langmuir-Blodgett (LB) films were thoroughly explored to for the deposition of organic molecules onto surfaces by immersion into liquids. Multiple layers of aliphatic molecules could be formed with accurate control of thicknesses. LB films, however, suffer from dependence on specific classes of molecules and specialized equipment. Alternatives to LB films have since been developed,[200, 201] one of the most well-studied being layer-by-layer (LbL) self-assembly.

Nuzzo and Allara first reported LbL self-assembly with the adsorption of thiols on gold substrates.[202] LbL self-assembly has since been further developed to utilize interactions of varying strength: covalent bonds,[203] metal-ligand coordination,[204] and electrostatic attraction of charged polyelectrolytes.[115] First conceived as a method for developing layered films onto planar surfaces, electrostatic LbL self-assembly has been recently reported in core-shell nanostructures[116, 205, 206] and nanoshells.[207-210]

Building multilayer films using oppositely charge polyelectrolytes has created many opportunities for new biofunctional coatings. Multilayer architectures can be created using synthetic (organic polymers, colloidal particles, inorganic complexes) or natural polyelectrolytes (proteins, polysaccharides, DNA. Electrostatic LbL self assembly has found applications in thin film coating,[211] micropatterning,[212, 213] nanobioreactors,[208, 214] artificial cells,[215] drug delivery,[216, 217] and electronic devices.[218, 219] Polyelectrolyte LbL adsorption is a general and versatile tool for creating multifunctional surface coatings using flexible macromolecules which can form defined superlattice architectures without crystallinity.[115] Polyelectrolyte LbL self-assembly continues to remain an interesting method for development of new applications as the field expands toward nanomaterials.

Gero Decher has used the well-characterized gold nanoparticle system to show the preparation of core-shell nanostructures with polyelectrolyte LbL self-assembly.[205] Subsequently, these core-shell structures could be converted to nanoshells. Furthermore, fluorescent polyelectrolytes were used to characterize the LbL-gold nanoparticle system using fluorescence resonance energy transfer.[116] Parameters, such as length and concentration of polyelectrolytes as well as ionic strength of the suspending solution, were investigated to optimize parameters for control of nanoparticle flocculation, aggregation, and stability.[206] We hope to continue the development of functional polyelectrolyte LbL self-assembly nanomaterial systems.

By electrostatic layer-by-layer self-assembly, multilayers of Gd(III) containing polymer are formed and retain active magnetic centers for MR relaxation. The disordered polyelectrolyte network allows for sufficient water molecule access to the Gd(III) centers. The network is built upon the previously mentioned fluorescent nanoparticle with a

monolayer of chelated Gd(III) (designated as MNP in Chapter 2). Based upon the net negative surface charge of the MNP system, a newly developed Gd(III)-chelated polymer (positively-charged) and poly(styrene sulfonate) (PSS; widely used for LbL architectures as a negatively-charged polyelectrolyte) are used to assemble multiple layer pairs onto the nanoparticle surface.

3.1.2 Targeting integrins

Integrins are a family of cell surface receptors that attach cells to the extracellular matrix (ECM) to mediate the mechanical and chemical signals.[220] The ECM is the protein network that provides structural support and regulates intercellular communication. Intimately linked to the architectural assembly of the actin filaments composing the cytoskeleton, multivalent integrin binding of the cell to the ECM causes integrin clustering,[221] inducing changes in morphology and adhesion properties of the cell.

Signaling mediated by integrins is fundamentally shared by virtually all tissues of multicellular animals.[222] Binding of extracellular proteins to integrins can create a signal to the cell or the cell can create a signal to the integrin to bind extracellular proteins.[223-226] Cells can use integrins to interact with the surrounding ECM to determine ideal conditions for survival.[227] Interactions with the ECM may allow the cell to determine suitable conditions for growth, regardless of other exogenous signals for apoptosis. Conversely, trauma to tissue may result in ECM damage, unsuitable conditions, to cue cell death. Endothelial cells use integrins are the primary receptors for interacting with the ECM angiogenesis, or growth of new blood vessels. During this process, integrins can signal endothelial cells to become more proliferative and invasive.[228]

Twenty-five years ago, Erkki Ruoslahti discovered the arginine-glycine-aspartic acid (RGD) sequence within fibronectin to be the essential recognition site for cell adhesion.[229] Later, it was realized that the three amino acid sequence was present in other adhesive proteins, such as laminin,[230] fibrinogen,[231] and vitronectin.[232] The discovery of a conserved sequence contained within many adhesive proteins in conjunction with the study of integrins has led to significant advances in the understanding of cell signaling by surface receptors. Integrins contain two subunits of 15 α and 8 β that combine to form over 20 heterodimers for a variety of specificity and signaling toward such ECM and blood plasma proteins.

RGD peptides can be designed to mimic specific adhesion proteins, thus binding the desired integrin target. The RGD peptide sequence will bind non-selectively to more than one integrin receptor. Affinity of the RGD sequence can be much lower than those specifically designed to target specific integrins. For example, the GRGDSP sequence found in fibronectin binds 1000 times more effectively than RGD peptide.[233] However, the RGD sequence alone can be very effective for targeting of many integrins.

In tumor cell proliferation and growth, ligation of different integrins on tumor cells can modulate proliferation or apoptosis via the Bcl-2 cell survival pathway.[234] The αvβ3 integrin has been one of the most widely studied receptors in cancer cells, particularly for its role in angiogenesis. On vascular cells of human tumors, these integrins are highly overexpressed.[235, 236] Anti-αvβ3 monoclonal antibodies and RGD peptides could reduce growth of blood vessels in tumors in animal models, while antibodies specific for other integrins and scrambled peptides could not.[236] Specifically, this study and others[237] found that αvβ3 antagonists prevented growth of new blood vessels with no effect on pre-existing mature blood vessels.

The following work describes a RGD peptide with oligomeric lysine residues is electrostatically deposited onto the surface of the nanoparticle for the purpose of general targeting toward integrin receptors. The positive charges of the consecutive lysine sequence interact with the anionic polymer layer on the nanoparticle to display the RGD sequence. The adsorption of many RGD peptides onto the surface of the nanoparticle generated a multivalency effect, well known throughout nanoparticle functionalization literature.[238, 239] The displayed RGD peptides targeted all integrins, but should preferentially target cancer cells due to the high overexpression of αvβ3 integrins.

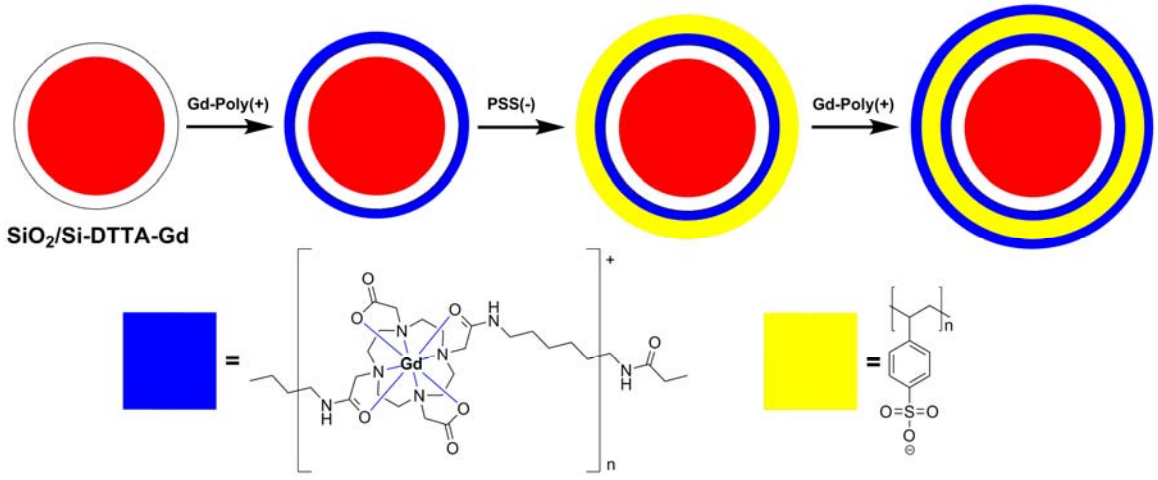

Figure 3.2 Two-dimensional cross-sectional schematic representation of polyelectrolyte layer-by-layer self assembly strategy using nanoparticle platform with anionic surface (MNP) to alternate deposition of Gd(III)-DOTA oligomer (blue) and PSS (yellow).

3.2 Results and Discussion

3.2.1 Rationale

Silica nanoparticles doped with $Ru(bpy)_3Cl_2$ and monolayer coated with Gd(III)-DTTA (**MNP**) was used as the platform for multilayer self-assembly. The DTTA ligand has three tertiary amines and four carboxy groups to provide seven sites of coordination with a Gd(III) ion. Two coordination sites remain open on the chelated Gd(III) ion for interaction with water. As a result of the three positive charges of the Gd(III) and the four negative charges of the DTTA ligand, the net complex is anionic, rendering the surface of the nanoparticle as anionic (**Figure 3.3**). The MNP particles thus provide an interesting starting point for depositing multilayers of cationic polymers of Gd(III) chelates to enhance the Gd(III) payload of each nanoparticle. The versatility of the electrostatic LbL method also allows for the addition of charged oligomeric peptide sequences that can target cancer cells.

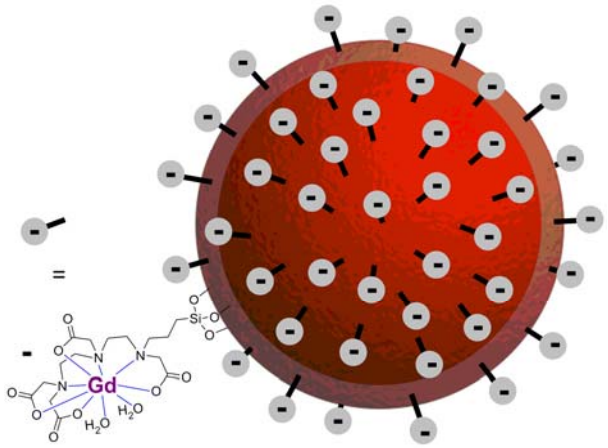

Figure 3.3 Anionic net surface charge of MNP due to immobilization of anionic Gd(III)-DTTA ligand onto the nanomaterials surface.

Using the resulting anionic surface of the nanoparticle, cationic Gd(III)-DOTA polymer was deposited onto the surface via electrostatic interactions. Anionic polystyrene sulfonate (PSS) was subsequently deposited in order to provide a substrate for further polycation layers. In a typical deposition step, MNP was treated with cationic Gd(III) oligomer before washing steps to remove weakly interacting oligomers. The resulting cationic layer was followed with the interaction of anionic PSS, which was also washed to remove any weakly bound polyelectrolytes. These alternating deposition steps were repeated to build up to seven bilayers of Gd(III) oligomer and PSS. **Figure 3.4** illustrates the LbL self-assembly strategy for building polyelectrolyte multilayer architectures. These nanoparticles are designated **NP*n*A** or **NP*n*B** with ***n*** denoting surface termination with Gd(III)-DOTA oligomer and PSS, respectively.

A) Addition of cationic Gd(III)-DOTA oligomer to **NP0**

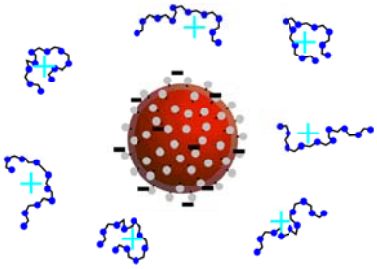

B) Single polyelectrolyte self-assembly on **NP0**

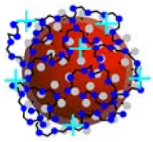

C) Addition of anionic polystyrene sulfonate to **NP1A**

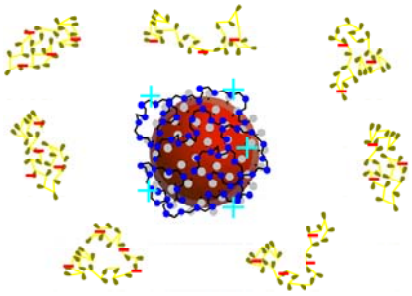

D) Polyelectrolyte bilayer self-assembly forming **NP1B**

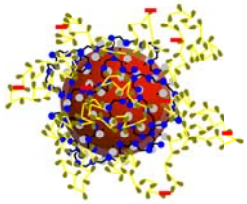

E) Stepwise growth of *n* bilayers forming **NP*n*B**

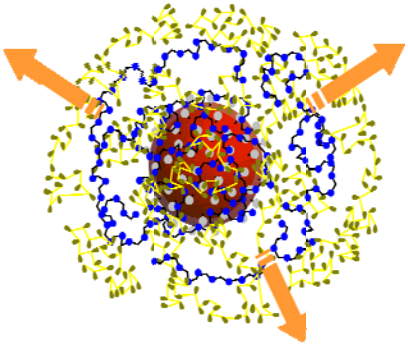

Figure 3.4 Proposed stepwise growth of multilayer architectures by LbL self-assembly. A) Addition of cationic Gd(III)-DOTA oligomer. B) Formation of single cationic monolayer. C) Addition of anionic polystyrene sulfonate. D) Formation of single polyelectrolyte bilayer. E) Continued stepwise growth of multilayers.

3.2.2 Measurement of LbL multilayer growth

A variety of methods were used to demonstrate the multilayer growth of alternating polyelectrolytes on the nanoparticle surface. These included the measurement of size, relaxivities, and fluorescence of the self-assembled multilayer growth. Size was measured by TEM. MR measurements served to directly correlate Gd(III) levels on the nanoparticle to water proton relaxation efficiency. Fluorescence derived from increasing layers of tagged Gd(III)-DOTA oligomer was also used to quantify growth and Gd(III) levels. The multiple techniques convincingly demonstrated LbL self-assembly on nanoparticles.

3.2.2.1 Measurement of nanoparticle diameters by transmission electron microscopy

TEM images indicated alternate deposition of Gd(III)-DOTA oligomer and PSS onto the nanoparticles by growth of average diameters from no layers to seven layers of polyelectrolytes (**Figure 3.5**).

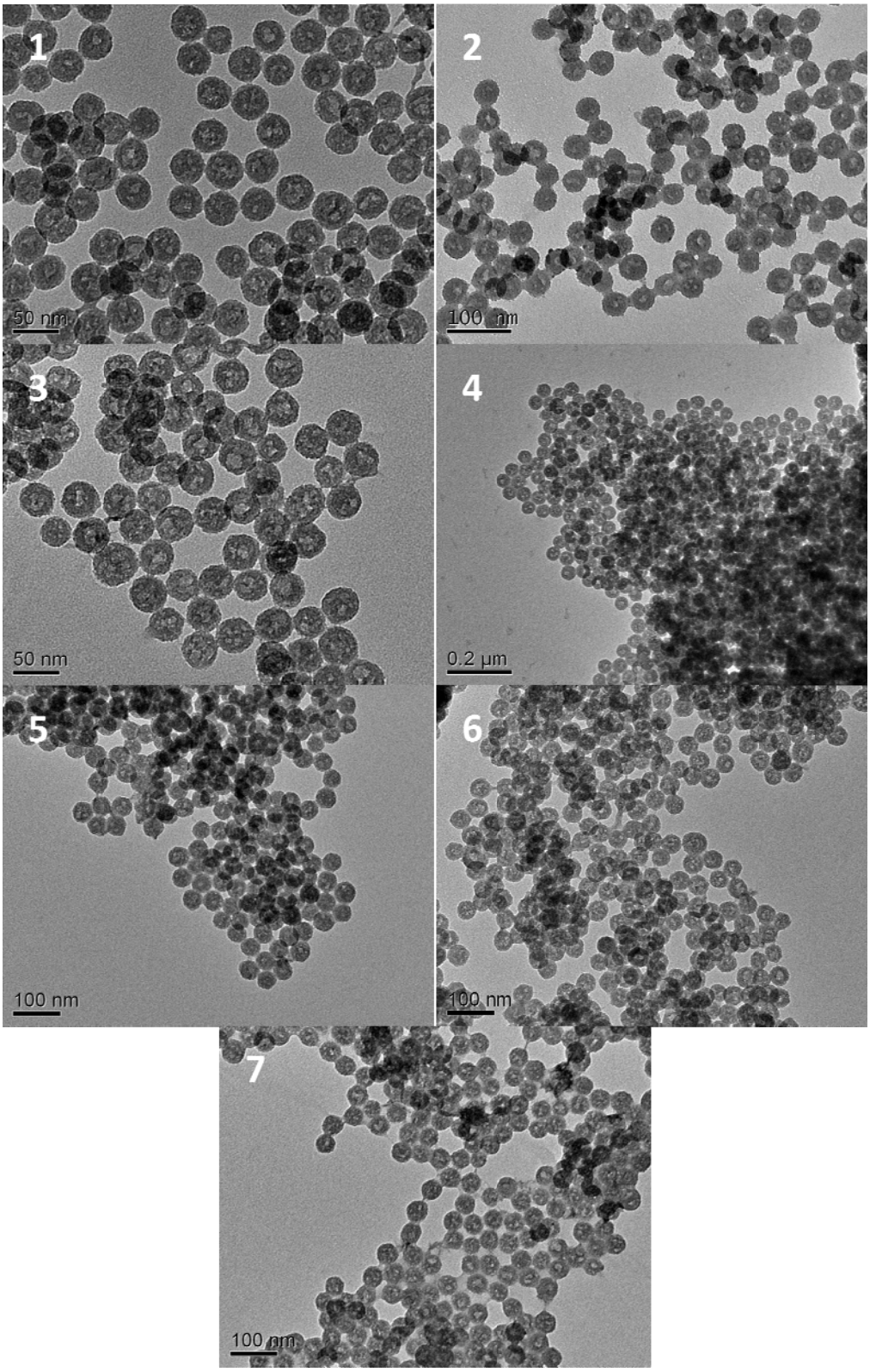

Figure 3.6 TEM images of MFNPs with increasing numbers of deposited layers of Gd-DOTA oligomer **1** (1 layer to 7 layers).

Populations of nanoparticles were measured to determine average diameters for each layer. A linear increase nanoparticle diameter was determined, rising from 37 ± 1 nm to 44.5 ± 1 nm (**Figure 3.6**). With increasing layers, TEM showed electrostatic cross-linking between nanoparticles. These particles remained dispersible in water, though higher concentrations could lead to aggregation due to interactions between polyelectrolyte layers. The TEM images show particles as they are concentrated in populations during dehydration.

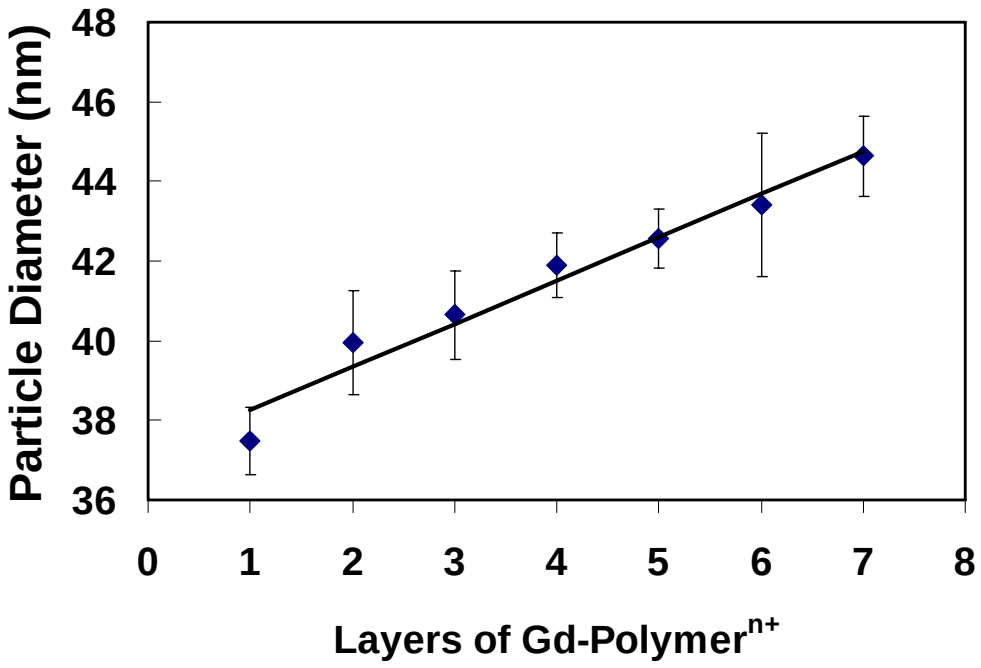

Figure 3.6 Particle diameter plotted against increasing layers of Gd(III)-DOTA oligomer.

3.2.2.2 Measurement of fluorescein-tagged multilayer growth

A fluorescein isothiocyanate (FITC)-tagged Gd(III)-chelate polymer was synthesized in order to probe layer growth using fluorescence spectroscopy. Upon excitation at 488 nm, the large Stokes' shift of the $Ru(bpy)_3Cl_2$-doped nanoparticle produced emission at 615 nm

and did not overlap with the fluorescein emission at 515 nm. Since the luminescence intensity at 615 nm is proportional to the nanoparticle concentration, the ratio of the 515 nm emission intensity to the 615 nm emission intensity is proportional to the number of FITC molecules on each nanoparticle. The 515 nm channel was used to monitor washes following deposition steps to ensure removal of excess FITC-tagged Gd(III)-DOTA oligomer. **Figure 3.7** shows that the ratio between 515 nm emission and 615 nm emission increases quadratically as more layers of Gd(III)-DOTA oligomer and PSS are deposited. Since the surface area of the spherical nanoparticle scales quadratically to the particle diameter, this result is consistent to the linear increase in diameter.

Decher and coworkers noted a non-linear increase in UV (225 nm) absorption for polyelectrolyte deposition of PSS onto colloidal gold nanoparticles. The manuscript attributes the non-linear, vaguely exponential, growth of PSS absorbance to the increasing diameter and thus surface area.[205] Our spherical nanoparticle also experiences a similar increase in diameter and surface area. As Decher has shown in another recent publication,[116] fluorescent tagging of the polyelectrolyte yields higher sensitivity to clearly demonstrate exponential growth, much like the growth experienced in our system.

Interlayer diffusion, the phenomenon in which species of a polyelectrolyte LbL system vertically diffuse through films during the assembly process, may partially explain the LbL assembly growth described by the polynomial curve. Exponential layer growth is behavior characteristic of systems exhibiting interlayer diffusion, previously evidenced through fluorescence-labeled[240] and radiolabeled[241] polyelectrolytes. As the polyelectrolyte interactions equilibrate through interlayer diffusion, the interactions may become weaker and more easily stripped by polyelectrolyte solutions used for deposition. The interlayer

diffusion in our polyelectrolyte architecture may occur, though TEM and relaxivity measurements support linear diameter growth. .

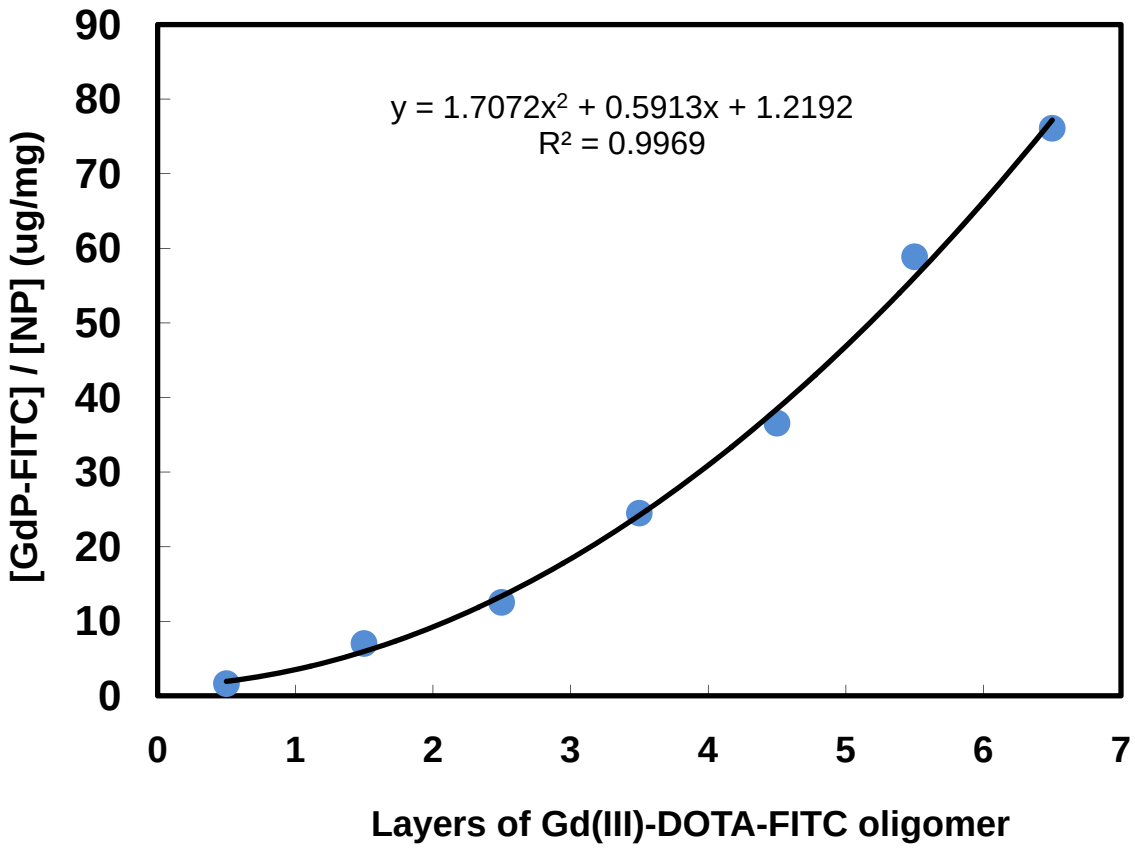

Figure 3.7 Gd(III)-DOTA-FITC oligomer concentrations, measured by fluorescence, increases exponentially with multilayer growth.

3.2.2.3 MR relaxivities of layer-by-layer self-assembled nanoparticles

Longitudinal (*r1*) and transverse (*r2*) MR relaxivities for LbL nanoparticles were determined with up to seven layers of Gd(III)-DOTA oligomer. Interestingly, relaxivity values for NPnA on a per Gd(III) basis remained essentially constant at *r1* = 19.0 ± 1.7 $mM^{-1}s^{-1}$ and *r2* = 55.0 ± 5.0 $mM^{-1}s^{-1}$ regardless of the number of deposited layers of Gd(III)-

DOTA oligomer. This contrasted starkly with the previously reported covalently attached multilayer system using bis(silylated)-Gd(III)-DTPA, which exhibited diminished relaxivities on a per Gd(III) basis.[199] The highly disordered and hydrophilic nature of Gd(III)-DOTA oligomer and PSS allows ready access of water molecules to the metal centers for efficient water proton relaxation. On the basis of the size of the LbL particles, we further estimated *r1* and *r2* relaxivities of **NP*n*A** on a per particle basis, which increased linearly as more layers of Gd(III)-DOTA oligomer were deposited **(Figure 3.9** and **Table 3.1).** LbL self-assembly offers a superb strategy for increasing nanoparticle MR relaxivities.

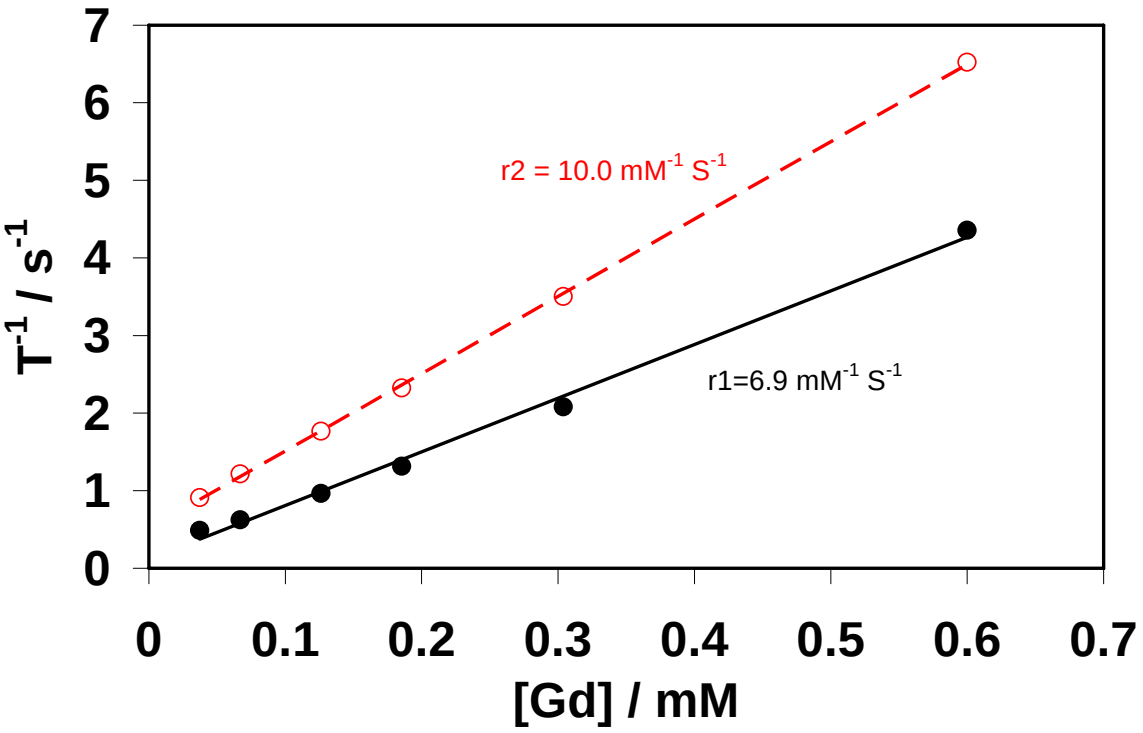

Figure 3.8 MR relaxivities, r1 and r2, per Gd(III) for cationic Gd(III)-DOTA oligomer.

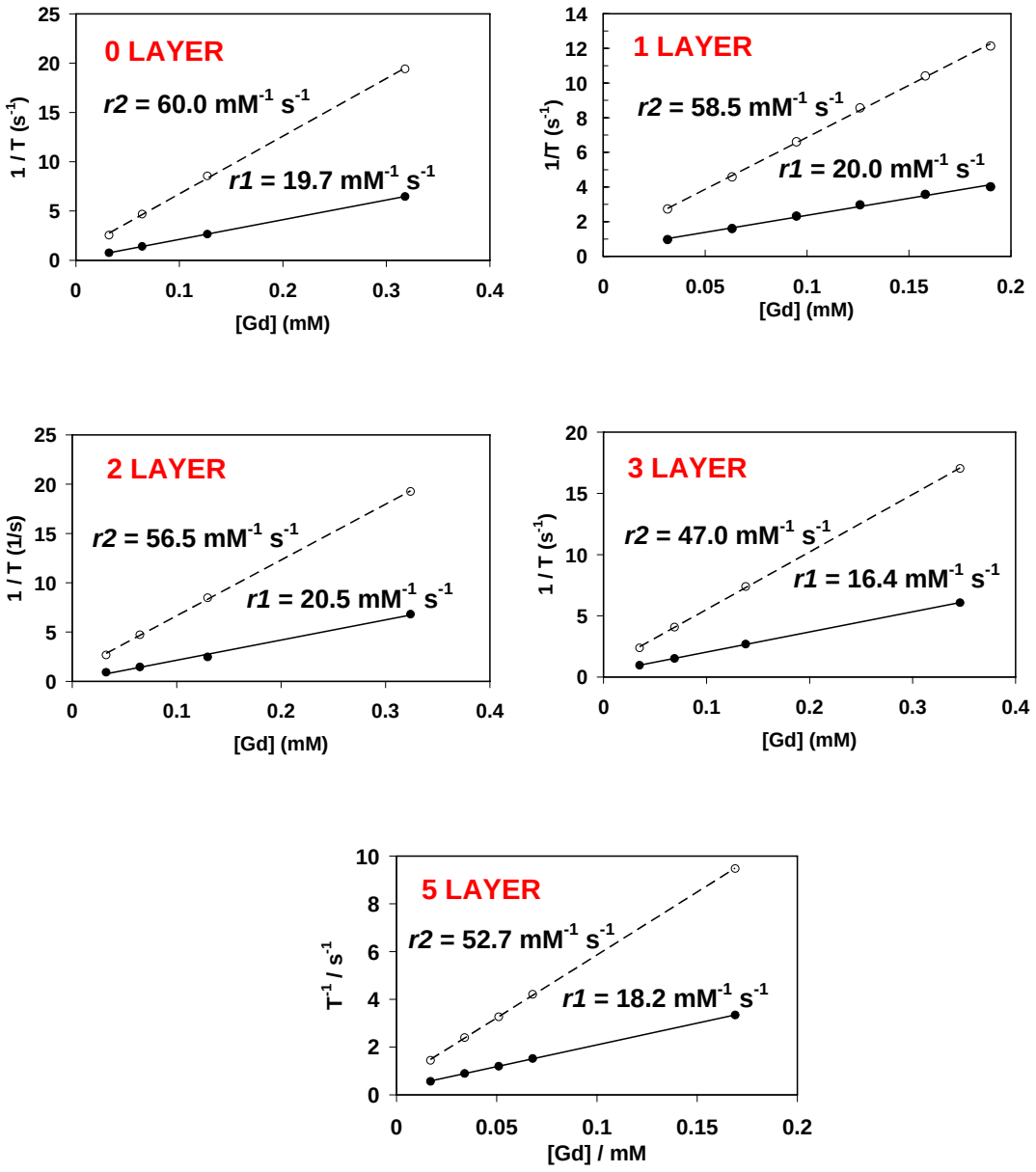

Figure 3.9 MR relaxivities, *r1* and *r2*, per Gd(III) for LbL self-assembled nanoparticles.

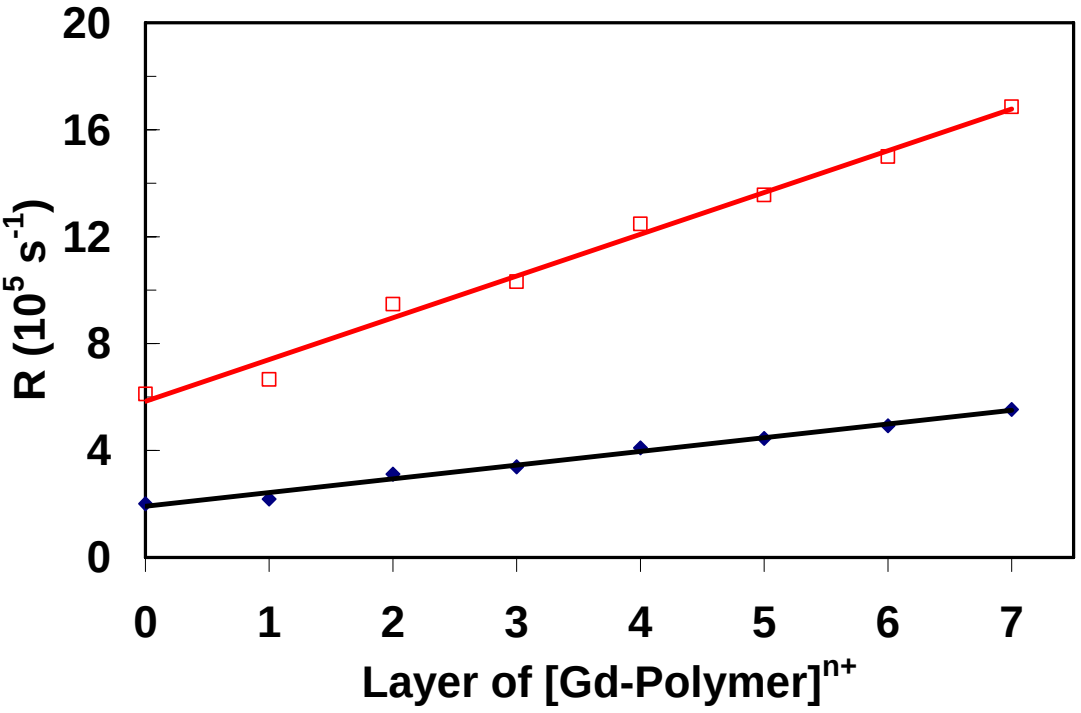

Figure 3.10 Linear increase of *r1* (black) and *r2* (red) as layers of Gd(III)-containing oligomer are increased.

3.2.3 Using electrostatic interactions to attach targeting moieties

3.2.3.1 Description of the method

Since the LbL self-assembled nanoparticles were terminated with anionic PSS polymers, we hypothesized that the particles could be functionalized with targeting peptides that carry positive charges under physiological conditions. The arginine-glycine-aspartate peptide sequence with seven consecutive lysine residues (K_7RGD) was chosen for this study, with a glycine-arginine-aspartate derivative (K_7GRD) serving as the scrambled control. The negatively charged PSS layer could electrostatically interact with positively-charged lysine residues of the K_7RGD sequence to display RGD peptides onto the surface of the PSS-capped multilayer surface of the nanoparticles. The RGD peptide is known to bind strongly

(with a K*d* in the micromolar range) to all integrin cell surface receptors that are upregulated in cells implicated in angiogenesis and cancer.

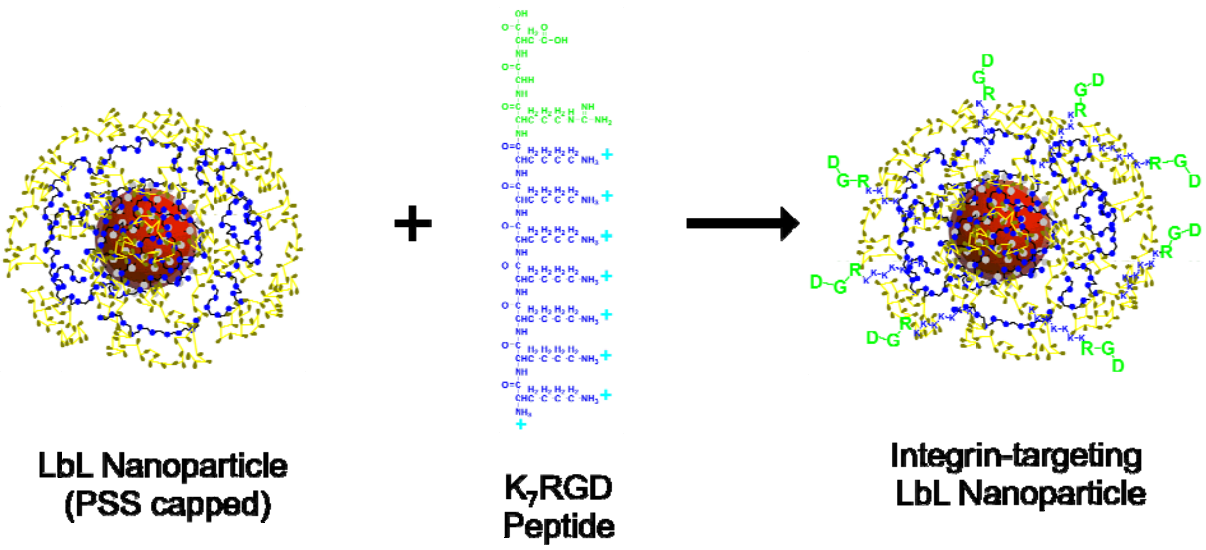

Figure 3.11 RGD peptide functionalization for Integrin-targeting by nanoparticles with polyelectrolyte self-assembled multilayers.

3.2.3.2 Zeta potentials measurements to measure surface changes of self-assembly nanoparticles

The electrokinetic potential of colloidal systems dispersed in solution is measured by zeta potentials.[242] The surface charge, depending on the medium the colloid is suspended, can carry an electric charge. Beyond the charged surface of the colloid, a Stern layer of strongly associated ions of opposing charge exists. A diffuse layer forms an outer region of less firmly associated ion. A boundary within the diffuse layer forms a stable entity and when a voltage is applied to the sample solution, particles are attracted to the electrode of opposite polarity. The potential at the boundary front is ultimately the zeta potential.

Measurement of zeta potentials was performed to monitor changes in surface properties of the nanoparticles at various stages of multilayer growth and functionalization. **Figure 3.12** shows that bare silica nanoparticles have negatively charged surfaces, as demonstrated with a zeta potential of -35.81 mV. With the addition of the Gd(III)-DTTA monolayer coating, the zeta potential became more anionic to -42.45 mV. Nanoparticles with three bilayers of Gd(III)-DOTA oligomer and PSS became more neutrally charged, -25.83 mV. Functionalization with the RGD or GRD peptides with lysine tail further shifted the zeta potential toward a cationic surface with zeta potential values of -18.98 and -17.79 mV, respectively. The oligomeric lysine tail interacts with the PSS surface, to create a more positive surface.

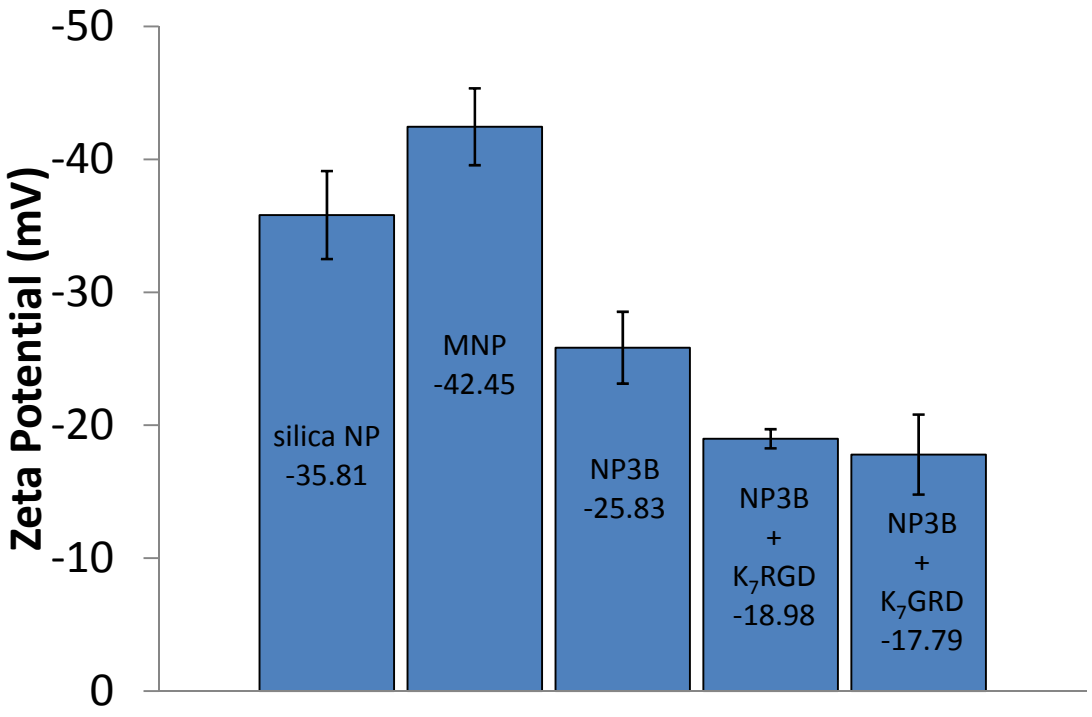

Figure 3.12 Zeta potential (mV) measurements of bare silica nanoparticles, Gd(III)-DTTA monolayer covalent coated nanoparticles (MNP), MNP with 3 bilayers, MNP with 3 bilayers and K_7RGD functionalization, and MNP with 3 bilayers and K_7GRD functionalization.

3.2.3.3 Targeting endothelial cells

Angiogenesis, the process of new blood vessel formation, has been widely researched for its involvement in tumor growth and metastasis. Malignant tumor expansion and metastasis requires the neovasculature to supply nutrients, oxygen, and waste disposal. Endothelial cells line the interior of blood vessels for the circulatory system and play an obviously important role in angiogenesis. Integrins, the primary receptors for endothelial cells in initiating proliferation and invasion, can be targeted through RGD peptides.

Cow pulmonary artery endothelial (CPAE) cells have high expression of these integrin receptors.[243] Luminescent imaging and targeting capability of LbL nanoparticles were confirmed by laser scanning confocal fluorescence microscopy. As shown in **Figure 3.13**, significant luminescence signal was observed for CPAE cells incubated with NP5B particles that were non-covalently functionalized with K_7RGD sequence. Little to no luminescent signal was observed for control CPAE: incubated without nanoparticles, incubated with unfunctionalized nanoparticles, and incubated with a scrambled binding site (K_7GRD). The resulting images correlate with the membrane flow model of cell migration.[244] Cellular projections, lamellipodia and filopodia, extend from the cell's migrating edge and have an abundance of integrins. Serving as adhesion points and directing movement, integrins are closely linked to the actin network that shapes the cytoskeleton.[244] Thus, the RGD-labeled nanoparticles are localized at cellular projections and edges that display increased levels of integrins.

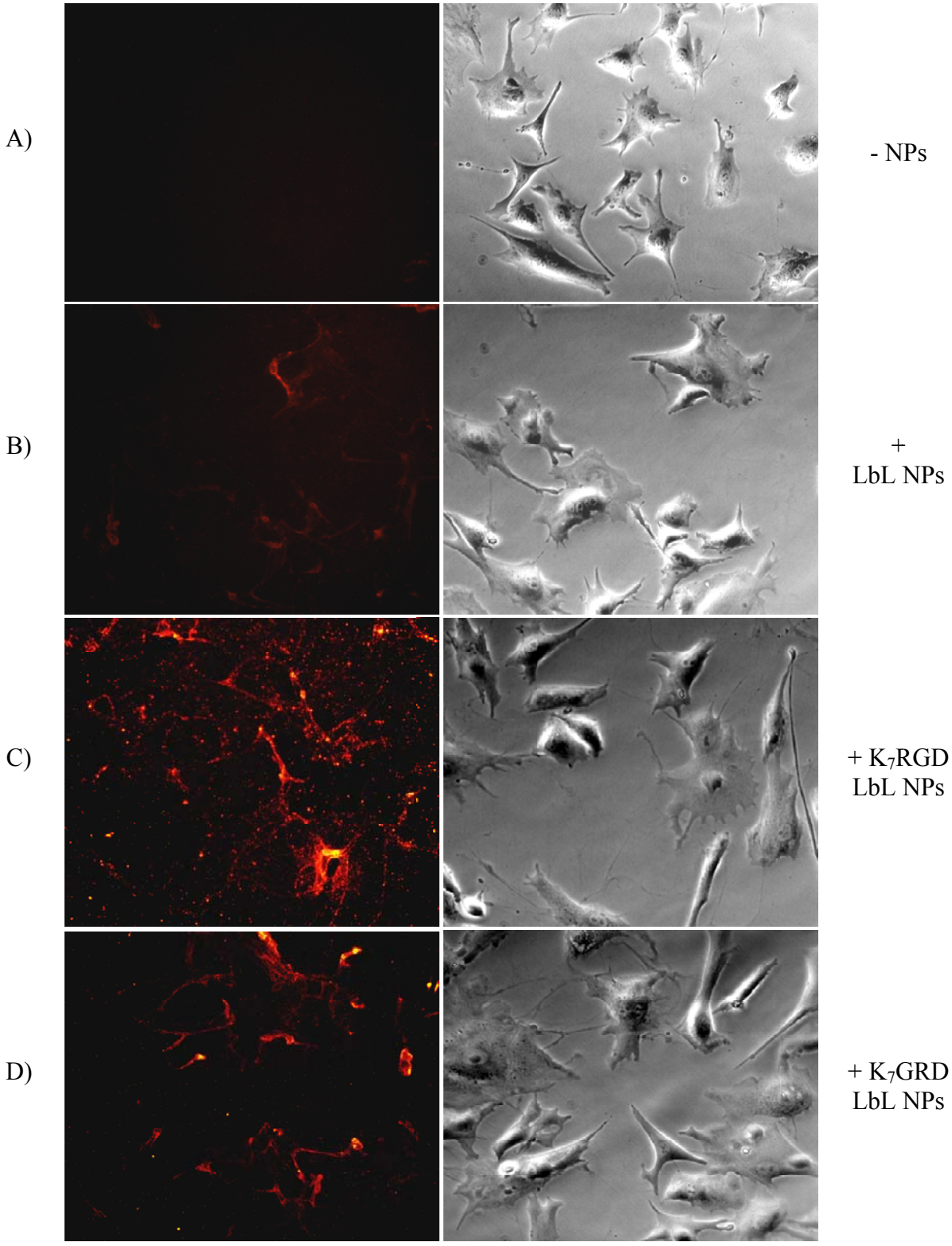

Figure 3.14 Fluorescence (left) and DIC (right) confocal microscopy images of endothelial (CPAE) cells: A) without nanoparticle incubation, B) incubated with multilayer nanoparticles, C) incubated with RGD-peptide decorated multilayer nanoparticles, and D) incubated with GRD-peptide decorated nanoparticles.

3.2.3.4 Targeting cancer cells

Integrin receptors have been found to be overexpressed in HT-29 human colon cancer cells.[245, 246] Previously, fluorescent albumin microspheres were labeled with K_7RGD were reported to show integrin mediated uptake by HT-29 cells.[247] Targeting capability of our LbL nanoparticles was initially determined by laser scanning confocal fluorescence microscopy. As shown in **Figure 3.14**, significant luminescence signal was observed in HT-29 cells incubated with NP5B particles that have been non-covalently functionalized with K_7RGD sequence, indicating efficient targeting of HT-29 cells. In comparison, little to no luminescent signal was observed for control HT-29 cells without nanoparticles and for cells that have been incubated with NP5B particles without functionalization or functionalized with K_7GRD.

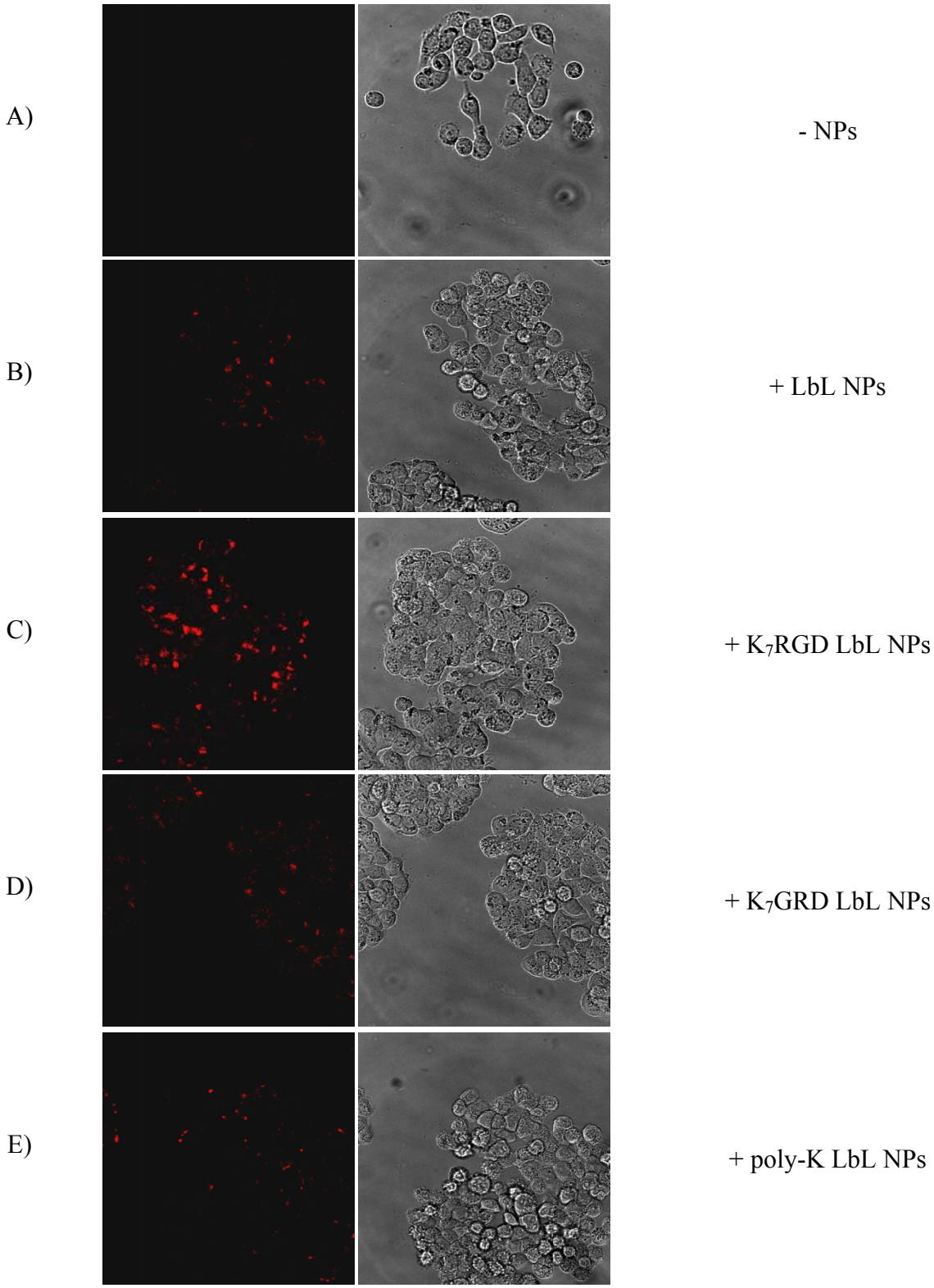

Figure 3.14 Fluorescence (left) and DIC (right) confocal microscopy images of colon carcinoma (HT-29): A) without nanoparticle, B) incubated with multilayer nanoparticles, C) incubated with RGD-peptide decorated multilayer nanoparticles, D) incubated with GRD-peptide decorated nanoparticles, and E) incubated with poly-lysine decorated nanoparticles.

T1-weighted MR images of HT-29 cells after incubation with various nanoparticles are shown in **Figure 3.15**. Significant signal enhancement in the *T1*-weighted image was observed only for HT-29 cells incubated with **NP3B** particles that have been non-covalently functionalized with the K_7RGD sequence. In contrast, no signal enhancement was observed for the HT-29 cells incubated with either **NP3B** particles with K_7GRD or no functionalization. In vitro MR imaging studies demonstrated efficient targeting of cancer cells by the LbL particles with non-covalently attached RGD peptides.

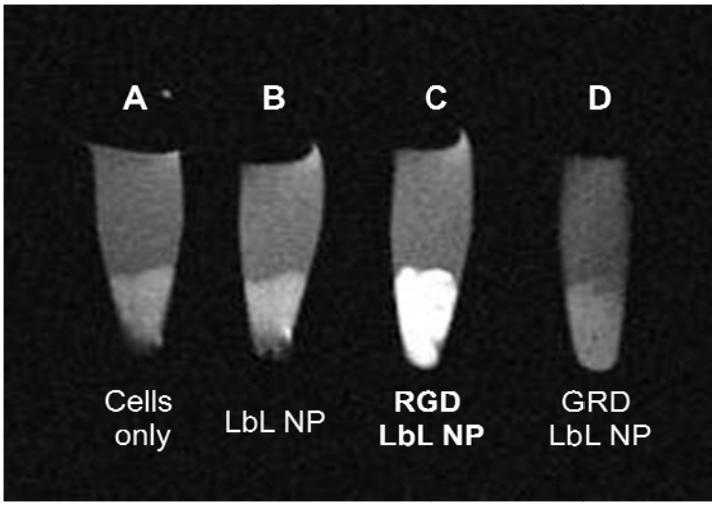

Figure 3.15 *In vitro* MRI of colon carcinoma cell (HT-29) pellets: A) unlabeled, B) incubated with unfunctionalized multilayer nanoparticles, C) incubated with RGD-peptide multilayer nanoparticles, and D) incubated with GRD-peptide multilayer nanoparticles.

3.3 Concluding remarks

In summary, we have utilized electrostatic LbL self-assembly to prepare targeted multifunctional nanoparticles with both MR and optical imaging capabilities. Electrostatic LbL self-assembly enabled increased loading of Gd(III) payloads and the preservation of efficient water proton relaxation by Gd(III) metal centers. Multilayer growth was confirmed by electron microscope measurement of nanoparticle diameters, demonstration of increasing MR relaxivities, as well as increasing fluorescence. The LbL self-assembly strategy not only affords nanoparticles with extraordinarily high MR relaxivities but also provides an efficient means for non-covalent functionalization with affinity molecules. Specifically, a cationic tail was used to display an integrin specific targeting peptide sequence that could label cancer cells (HT-29) and cells that participate in angiogenesis (CPAE). The generality of the polyelectrolyte LbL self-assembly should allow the design of imaging and/or therapeutic multifunctional nanoparticles that can specifically target a wide range of diseased cells.

3.4 Materials and Methods

3.4.1 General

All of the chemicals were obtained from commercial sources and used without further purification. Solvents used in all the reactions were dried by standard procedures.[248] Multimodal nanoparticles were prepared as described previously.[199] Poly(sodium-4-styrenesulfonate) (PSS) MW = 70 kDa (Sigma-Aldrich) was used without further purification. Poly-*L*-lysine was purchased from MP Biomedicals and used without further purification. The water (dH_2O) used in all experiments was prepared by a Millipore NanoPure purification system (resistivity higher than 18.2 MΩ cm^{-1}) and autoclaved before use. KKKKKKKRGD peptide was purchased from EZ Biolabs whereas KKKKKKKGRD peptide was prepared with an Applied Biosystems Pioneer peptide synthesizer using Applied Biosystems PEG-PAL amide resin. Thermogravimetric analysis (TGA) was performed using a Shimadzu TGA-50 equipped with a platinum pan and heated at a rate of 3°C / min under air. Gd(III) ion concentration was measured on an Applied Research Laboratories SpectraSpan7 Direct Current Plasma (DCP) Spectrometer. T1 and T2 values were determined on a Bruker 3.0 Tesla full body Magnetic Resonance Imaging (MRI) Scanner. Confocal laser scanning microscope images were taken with a Zeiss LSM5 (488 nm excitation, 550-650 nm emission) at the University of North Carolina Michael Hooker Microscopy Facility. Fluorescence microscope images were taken at the University of North Carolina Pharmacy School with a Zeiss Axiovert 100 TV Fluorescence Microscopy using a long pass FITC filter. A JEM 100CX-II Transmission Electron Microscope (TEM) was used to determine particle size and morphology.

3.4.2 Cationic Gd(III)-DOTA oligomer and FITC-labeled Gd(III)-DOTA oligomer

The synthesis of cationic Gd(III) containing oligomer (**1**) was presented in a previous manuscript.[249] Briefly, oxidative coupling of the prepared cyclen-1,7-bis(butylacetate)-4,12-bis(*N*-propargyl acetamide, serving as the cross-linker, and prepared cyclen-1,4,7-tris(butylacetate)-12-(*N*-propargyl acetamide) serving as the terminator yielded the protected oligomeric backbone. The crude product was hydrogenated, then deprotected with trifluoroacetic acid before complexing with Gd(III) ions. Purification was accomplished by dialysis against de-ionized water over many days. FITC-labeled oligomer (**1a**) was similarly synthesized.

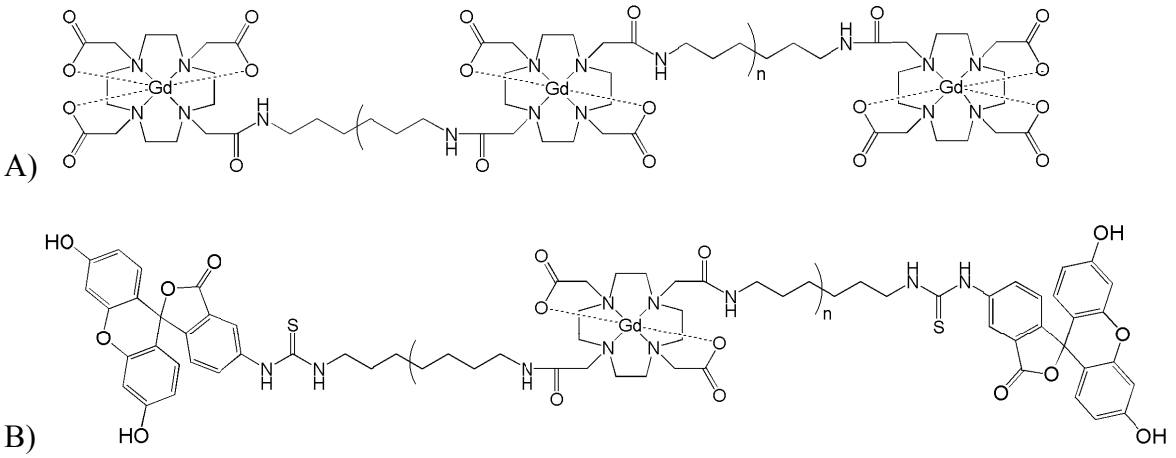

Figure 3.16 Cationic Gd(III) oligomers used for multilayer formation on nanoparticles: A) **1** without fluorescent terminating label and B) **1a** with fluorescent terminating label.

3.4.3 Polyelectrolyte layer-by-layer deposition onto nanoparticles (MNP)

A 250 μL aliquot of the paramagnetic fluorescent-labeled nanoparticles **MNP** or **NP0** (24.6 mg/mL) was placed in a 1.5 mL polypropylene Eppendorf tube with 250 μL dH_2O and 500 μL of **1** or **1a** (1 mg/mL dH_2O). The tube was placed in an ultrasonic bath for 15

minutes before centrifugation at 14000 RPM for 20 minutes. The supernatant was removed (Flow Through = FT), and the nanoparticle pellet was re-suspended in 1 mL of dH_2O. Centrifugation/re-suspension was repeated twice (Wash 1 = W1, Wash 2 = W2) before the washed nanoparticle pellet was re-suspended into the original volume (250 μL). The collected supernatant fractions and re-suspended nanoparticle suspension were measured for fluorescence (515 nm and 610 nm) to ensure that the nanoparticles were free from excess unbound materials. To deposit the negatively charged PSS layer, 250 μL of the previously layered nanoparticle was placed into 250 μL and 500 μL PSS (1 mg/mL dH_2O). The previous process was repeated to obtain the desired stage of layer deposition using constant concentrations of PSS and **1** or **1a**. This LbL deposition was repeated for depositing more layers of **1** (**1a**) and PSS.

3.4.4 Functionalization of layer-by-layer nanoparticles

A 50 μL aliquot of 3 or 5 bilayer nanoparticle (**NP3B** or **NP5B**) was placed in a 1.5 mL polypropylene Eppendorf tube and 2 μL of KKKKKKKRGD, KKKKKKKGRD, or poly-lysine (1mg / μL) was added. The tube was placed in a sonicator for 20 minutes before being centrifuged for 20 minutes at 14000 RPM. The supernatant was removed and the nanoparticles were re-dispersed in 50 μL of dH_2O. The centrifugation / re-dispersion step was repeated once more before being re-dispersed in 50 μL of dH_2O for use as labeling agent.

3.4.5 Endothelial cell culture

Cow pulmonary artery endothelial (CPAE) cells were maintained at 37°C in a 5% CO_2 incubator with EMEM containing 20% FBS and 1% Penicillin/Streptomycin. All cells were passed and overgrowth maintained by trypsinization for detachment of adherent cells from the surface of the flasks. Fresh media was added to flasks for continued growth of culture.

3.4.6 Colon carcinoma cell culture

Human colon carcinoma (HT-29) cells were maintained at 37°C in a 5% CO_2 incubator with McCoy's 5A containing 10% FBS and 1% Penicillin/Streptomycin. Cells were passed and overgrowth maintained by trypsinization to detach adherent cells from the surface of the flasks before aspiration and refreshing of media.

3.4.7 *In vitro* labeling and fluorescence imaging of live endothelial and cancer cells

CPAE and HT-29 cells were grown on 6-well plates with sterile glass coverslips at 37°C in a 5% CO_2 incubator with EMEM containing 20% FBS and 1% P/S, and McCoy's 5A containing 10% FBS and 1% P/S, respectively. Cells were incubated with functionalized and unfunctionalized nanoparticle concentration of 11 μg/mL for 15-60 minutes. The cells were then washed extensively with Hank's Balanced buffered Saline Solution (HBSS) before being immediately imaged by scanning laser confocal fluorescence microscopy.

3.4.8 *In vitro* MRI of nanoparticle-labeled cancer cells

HT-29 cells were cultured in large dishes with McCoy's 5A media containing 10% FBS and 1% P/S at 37°C with 5% CO_2 until approximately 70% confluency was observed. Cells were incubated with and without KKKKKKKRGD-functionalized, KKKKKKKGRD-functionalized, and unfunctionalized 3-layer nanoparticles (11 μg/mL) for 60 minutes. The cells were extensively washed with HBSS before trypsinization. Free floating cells were counted using trypan blue exclusion (~10 million cells per dish), before collection and centrifugation at 1000 RPM for 10 minutes. The cell pellets were placed into small PCR tubes with 100 μL of HBSS on top for MR imaging.

3.4.9. Zeta potential measurements

Zeta potentials of these materials were measured using a Brookhaven Instruments Corporation ZetaPlus Zeta Potential Analyzer. Each sample was suspended in a 1 mM KCl aqueous solution (pH 7.0) to achieve ~0.1 mg/mL concentration. Measurements were conducted at 25ºC and run a minimum of ten times. The average values for various samples are determined and standard deviations are reported using error bars.

3.4.10 Determination of relaxivities per layer

Nanoparticles with 3 layers of cationic Gd(III)-DOTA polymer was used to determine the Gd(III) amounts for layer relaxivity calculations.

1) Mass % Gd for 3 layers of cationic polymer:

2.96% Gd (as determined by TGA)

2) Diameter of silica nanoparticle:

37 nm (as determined by TEM)

3) Calculated volume of silica nanoparticle (SiNP):

$$(4/3)\times\pi\times(\text{radius})^3 = (4/3)\times\pi\times(37\text{ nm}/2)^3 = 2.65\times10^{-17}\text{ cm}^3$$

4) SiO_2 density:

$$2.0\text{ g cm}^{-3}$$

5) Calculated mass of silica nanoparticle:

$$2.65\times10^{-17}\text{ cm}^3 \times 2.0\text{ g cm}^{-3} = 5.30\times10^{-17}\text{ g SiNP}^{-1}$$

6) Gd atoms per nanoparticle:

$$(Y\times m_{Gd}) / (m_{SiNP} + Y\times m_{oligomer\,+\,PSS}) = \text{mass \% Gd}$$

$$\frac{(Y\times 157.25\text{ g mol}^{-1})}{(5.30\times10^{-17}\text{ g SiNP}^{-1} \times 6.022\times10^{23}\text{ SiNP mol}^{-1}) + (Y\times 669.3\text{ g mol}^{-1})} = 2.96\ \%$$

$$Y\times 137.45 = 9.44\times10^5$$

$$Y = 6870\text{ Gd per SiNP}$$

NP0 was previously determined to have ~10200 Gd(III) ions immobilized onto its surface.[199] Using TGA to determine weight loss of organics (from polymers), the number of Gd(III) ions of each layer was approximated. Given the calculated number of Gd(III) ions within 3 layers of cationic polymer on the surface of Gd-DTTA functionalized nanoparticles we could determine the approximate number of Gd(III) ions per volume to be 0.822 taking into account the change in particle diameter found by TEM measurements. Gd(III) relaxivities of each successive layer deposition did not show appreciable change in relaxivities. Thus, we could average the relaxivities and multiply the number of Gd(III) per particle by the average relaxivities on a per Gd(III) basis to obtain relaxivities on a per particle basis.

For **NP3A**,

$r1$ = (10200 + 6870) Gd(III) ions per NP3A × 19 mM Gd s^{-1} = 3.24 × 10^5 (mM^{-1} s^{-1})

$r2$ = (10200 + 6870) Gd(III) ions per NP3A × 55 mM Gd s^{-1} = 9.39 × 10^5 (mM^{-1} s^{-1})

Table 3.1 Estimated MR relaxivities on a per particle basis (10^5 mM^{-1} s^{-1})

	NP0	NP1A	NP2A	NP3A	NP4A	NP5A	NP6A	NP7A
r1	1.94	2.11	3.00	3.24	3.95	4.29	4.75	5.34
r2	5.61	6.11	8.69	9.46	11.4	12.4	13.8	15.5

3.5 References

1. Rieter, W. J.; Kim, J. S.; Taylor, K. M.; An, H.; Lin, W.; Tarrant, T.; Lin, W., Hybrid silica nanoparticles for multimodal imaging. *Angew Chem Int Ed Engl* **2007,** 46, (20), 3680-2.

2. Netzer, L.; Sagiv, J., A new approach to construction of artificial monolayer assemblies. *J. Am. Chem. Soc.* **1983,** 105, (3), 674-676.

3. Lee, H.; Lynch, V. M.; Cao, G.; Mallouk, T. E., Structure of [Mg(HO3PCH(C6H5)2)2].8H2O, a layered phosphonate salt. *Acta Crystallogr C* **1988,** 44 (Pt 2), 365-7.

4. Nuzzo, R. G.; Allara, D. L., Adsorption of bifunctional organic disulfides on gold surfaces. *J. Am. Chem. Soc.* **1983,** 105, (13), 4481-4483.

5. Love, J. C.; Estroff, L. A.; Kriebel, J. K.; Nuzzo, R. G.; Whitesides, G. M., Self-assembled monolayers of thiolates on metals as a form of nanotechnology. *Chem Rev* **2005,** 105, (4), 1103-69.

6. Lin, W.; Lin, W.; Wong, G. K.; Marks, T. J., Supramolecular Approaches to Second-Order Nonlinear Optical Materials. Self-Assembly and Microstructural Characterization of Intrinsically Acentric [(Aminophenyl)azo]pyridinium Superlattices. *J. Am. Chem. Soc.* **1996,** 118, (34), 8034-8042.

7. Decher, G., Fuzzy Nanoassemblies: Toward Layered Polymeric Multicomposites. *Science* **1997,** 277, (5330), 1232-1237.

8. Schneider, G.; Decher, G., From Functional Core/Shell Nanoparticles Prepared via Layer-by-Layer Deposition to Empty Nanospheres. *Nano Lett.* **2004,** 4, (10), 1833-1839.

9. Schneider, G.; Decher, G., Functional Core/Shell Nanoparticles via Layer-by-Layer Assembly. Investigation of the Experimental Parameters for Controlling Particle Aggregation and for Enhancing Dispersion Stability. *Langmuir* **2008,** 24, (5), 1778-89.

10. Schneider, G.; Decher, G.; Nerambourg, N.; Praho, R.; Werts, M. H.; Blanchard-Desce, M., Distance-dependent fluorescence quenching on gold nanoparticles ensheathed with layer-by-layer assembled polyelectrolytes. *Nano Lett* **2006,** 6, (3), 530-6.

11. Caruso, F.; Caruso, R. A.; Mohwald, H., Nanoengineering of inorganic and hybrid hollow spheres by colloidal templating. *Science* **1998,** 282, (5391), 1111-4.

12. Fang, M.; Grant, P. S.; McShane, M. J.; Sukhorukov, G. B.; Golub, V. O.; Lvov, Y. M., Magnetic Bio/Nanoreactor with Multilayer Shells of Glucose Oxidase and Inorganic Nanoparticles. *Langmuir* **2002,** 18, (16), 6338-6344.

13. Edwin Donath, G. B. S. F. C. S. A. D. H. M., Novel Hollow Polymer Shells by Colloid-Templated Assembly of Polyelectrolytes. *Angewandte Chemie International Edition* **1998,** 37, (16), 2201-2205.

14. Dmitry G. Shchukin, G. B. S. H. M., Smart Inorganic/Organic Nanocomposite Hollow Microcapsules. *Angewandte Chemie International Edition* **2003,** 42, (37), 4472-4475.

15. Dubas, S. T.; Farhat, T. R.; Schlenoff, J. B., Multiple membranes from "true" polyelectrolyte multilayers. *J Am Chem Soc* **2001,** 123, (22), 5368-9.

16. Hua, F.; Lvov, Y.; Cui, T., Spatial patterning of colloidal nanoparticle-based thin film by a combinative technique of layer-by-layer self-assembly and lithography. *J Nanosci Nanotechnol* **2002,** 2, (3-4), 357-61.

17. Zheng, H.; Berg, M. C.; Rubner, M. F.; Hammond, P. T., Controlling cell attachment selectively onto biological polymer-colloid templates using polymer-on-polymer stamping. *Langmuir* **2004,** 20, (17), 7215-22.

18. Lvov, Y.; Caruso, F., Biocolloids with ordered urease multilayer shells as enzymatic reactors. *Anal Chem* **2001,** 73, (17), 4212-7.

19. Ai, H.; Fang, M.; Jones, S. A.; Lvov, Y. M., Electrostatic layer-by-layer nanoassembly on biological microtemplates: platelets. *Biomacromolecules* **2002,** 3, (3), 560-4.

20. Ai, H.; Jones, S. A.; de Villiers, M. M.; Lvov, Y. M., Nano-encapsulation of furosemide microcrystals for controlled drug release. *J Control Release* **2003,** 86, (1), 59-68.

21. Qiu, X.; Leporatti, S.; Donath, E.; Mohwald, H., Studies on the Drug Release Properties of Polysaccharide Multilayers Encapsulated Ibuprofen Microparticles. *Langmuir* **2001,** 17, (17), 5375-5380.

22. Ho, P. K.; Kim, J. S.; Burroughes, J. H.; Becker, H.; Li, S. F.; Brown, T. M.; Cacialli, F.; Friend, R. H., Molecular-scale interface engineering for polymer light-emitting diodes. *Nature* **2000,** 404, (6777), 481-4.

23. Mingyuan Gao, B. R. S. K., White-light electroluminescence from self-assembled Q-CdSe/PPV multilayer structures. *Advanced Materials* **1997,** 9, (10), 802-805.

24. Giancotti, F. G.; Ruoslahti, E., Integrin signaling. *Science* **1999,** 285, (5430), 1028-32.

25. Gumbiner, B. M., Cell adhesion: the molecular basis of tissue architecture and morphogenesis. *Cell* **1996,** 84, (3), 345-57.

26. Gilcrease, M. Z., Integrin signaling in epithelial cells. *Cancer Lett* **2007,** 247, (1), 1-25.

27. Williams, M. J.; Hughes, P. E.; O'Toole, T. E.; Ginsberg, M. H., The inner world of cell adhesion: integrin cytoplasmic domains. *Trends Cell Biol* **1994,** 4, (4), 109-12.

28. Clark, E. A.; Brugge, J. S., Integrins and signal transduction pathways: the road taken. *Science* **1995,** 268, (5208), 233-9.

29. Aplin, A. E.; Howe, A.; Alahari, S. K.; Juliano, R. L., Signal transduction and signal modulation by cell adhesion receptors: the role of integrins, cadherins, immunoglobulin-cell adhesion molecules, and selectins. *Pharmacol Rev* **1998,** 50, (2), 197-263.

30. Juliano, R. L.; Reddig, P.; Alahari, S.; Edin, M.; Howe, A.; Aplin, A., Integrin regulation of cell signalling and motility. *Biochem Soc Trans* **2004,** 32, (Pt3), 443-6.

31. Stupack, D. G.; Cheresh, D. A., Get a ligand, get a life: integrins, signaling and cell survival. *J Cell Sci* **2002,** 115, (Pt 19), 3729-38.

32. Stupack, D. G.; Cheresh, D. A., Integrins and angiogenesis. *Curr Top Dev Biol* **2004,** 64, 207-38.

33. Pierschbacher, M. D.; Ruoslahti, E., Cell attachment activity of fibronectin can be duplicated by small synthetic fragments of the molecule. *Nature* **1984,** 309, (5963), 30-3.

34. Yamada, K. M.; Kennedy, D. W., Dualistic nature of adhesive protein function: fibronectin and its biologically active peptide fragments can autoinhibit fibronectin function. *J Cell Biol* **1984,** 99, (1 Pt 1), 29-36.

35. Gartner, T. K.; Bennett, J. S., The tetrapeptide analogue of the cell attachment site of fibronectin inhibits platelet aggregation and fibrinogen binding to activated platelets. *J Biol Chem* **1985,** 260, (22), 11891-4.

36. Suzuki, S.; Pierschbacher, M. D.; Hayman, E. G.; Nguyen, K.; Ohgren, Y.; Ruoslahti, E., Domain structure of vitronectin. Alignment of active sites. *J Biol Chem* **1984,** 259, (24), 15307-14.

37. Hautanen, A.; Gailit, J.; Mann, D. M.; Ruoslahti, E., Effects of modifications of the RGD sequence and its context on recognition by the fibronectin receptor. *J Biol Chem* **1989,** 264, (3), 1437-42.

38. Varner, J. A.; Cheresh, D. A., Integrins and cancer. *Curr Opin Cell Biol* **1996,** 8, (5), 724-30.

39. Brooks, P. C.; Montgomery, A. M.; Rosenfeld, M.; Reisfeld, R. A.; Hu, T.; Klier, G.; Cheresh, D. A., Integrin alpha v beta 3 antagonists promote tumor regression by inducing apoptosis of angiogenic blood vessels. *Cell* **1994,** 79, (7), 1157-64.

40. Brooks, P. C.; Clark, R. A.; Cheresh, D. A., Requirement of vascular integrin alpha v beta 3 for angiogenesis. *Science* **1994,** 264, (5158), 569-71.

41. Drake, C. J.; Cheresh, D. A.; Little, C. D., An antagonist of integrin alpha v beta 3 prevents maturation of blood vessels during embryonic neovascularization. *J Cell Sci* **1995,** 108 (Pt 7), 2655-61.

42. Carlson, C. B.; Mowery, P.; Owen, R. M.; Dykhuizen, E. C.; Kiessling, L. L., Selective tumor cell targeting using low-affinity, multivalent interactions. *ACS Chem Biol* **2007,** 2, (2), 119-27.

43. Puffer, E. B.; Pontrello, J. K.; Hollenbeck, J. J.; Kink, J. A.; Kiessling, L. L., Activating B cell signaling with defined multivalent ligands. *ACS Chem Biol* **2007,** 2, (4), 252-62.

44. Armarego, W. L. F.; Perrin, D. D., *Purification of Laboratory Chemicals*. 4 ed.; Reed Educational and Professional Publishing Ltd.: 1996.

45. Kim, J. S.; Rieter, W. J.; Taylor, K. M.; An, H.; Lin, W.; Lin, W., Self-assembled hybrid nanoparticles for cancer-specific multimodal imaging. *J Am Chem Soc* **2007,** 129, (29), 8962-3.

46. Picart, C.; Mutterer, J.; Richert, L.; Luo, Y.; Prestwich, G. D.; Schaaf, P.; Voegel, J. C.; Lavalle, P., Molecular basis for the explanation of the exponential growth of polyelectrolyte multilayers. *Proc Natl Acad Sci U S A* **2002,** 99, (20), 12531-5.

47. Wood, K. C.; Chuang, H. F.; Batten, R. D.; Lynn, D. M.; Hammond, P. T., Controlling interlayer diffusion to achieve sustained, multiagent delivery from layer-by-layer thin films. *Proc Natl Acad Sci U S A* **2006,** 103, (27), 10207-12.

48. Delgado, A. V.; Gonzalez-Caballero, F.; Hunter, R. J.; Koopal, L. K.; Lyklema, J., Measurement and interpretation of electrokinetic phenomena. *J Colloid Interface Sci* **2007,** 309, (2), 194-224.

49. Su, G.; Hodnett, M.; Wu, N.; Atakilit, A.; Kosinski, C.; Godzich, M.; Huang, X. Z.; Kim, J. K.; Frank, J. A.; Matthay, M. A.; Sheppard, D.; Pittet, J. F., Integrin alphavbeta5 regulates lung vascular permeability and pulmonary endothelial barrier function. *Am J Respir Cell Mol Biol* **2007,** 36, (3), 377-86.

50. Bretscher, M. S., Getting membrane flow and the cytoskeleton to cooperate in moving cells. *Cell* **1996,** 87, (4), 601-6.

51. Reinmuth, N.; Liu, W.; Ahmad, S. A.; Fan, F.; Stoeltzing, O.; Parikh, A. A.; Bucana, C. D.; Gallick, G. E.; Nickols, M. A.; Westlin, W. F.; Ellis, L. M., Alphavbeta3 integrin antagonist S247 decreases colon cancer metastasis and angiogenesis and improves survival in mice. *Cancer Res* **2003,** 63, (9), 2079-87.

52. Lee, J. W.; Juliano, R. L., alpha5beta1 integrin protects intestinal epithelial cells from apoptosis through a phosphatidylinositol 3-kinase and protein kinase B-dependent pathway. *Mol Biol Cell* **2000,** 11, (6), 1973-87.

53. Toublan, F. J.; Boppart, S.; Suslick, K. S., Tumor targeting by surface-modified protein microspheres. *J Am Chem Soc* **2006,** 128, (11), 3472-3.

CHAPTER 4

HIGHLY-EFFICIENT PURIFICATION OF NATIVE HEXAHISTIDINE-TAGGED RECOMBINANT PROTEINS BY MULTIVALENT NITRILOTRIACETIC ACID-MODIFIED MAGNETIC NANOPARTICLES

4.1 Introduction

Therapeutic proteins are undergoing rapid growth in pharmaceutical use in recent years. Proteins are of primary importance to enzymatic and structural biochemical functions and control cell signaling, cell adhesion, and immune responses. These abilities make proteins topics of great interest for therapy and treatment of diseases. Additionally, the development of recombinant protein technology[1] has allowed the production of many proteins of interest in large-scales. Recombinant versions of proteins, such as human growth factor, human insulin, insulin-like growth factor, and interferon, have replaced therapeutics previously harvested from human and animal organs.

As the demand for protein therapeutics increases, an emerging need exists for more efficient protein purification techniques allowing for direct isolation of proteins from cell lysates.[2] Among many currently used protein purification strategies,[3] immobilized metal affinity chromatography (IMAC) has emerged as one of the most powerful techniques for the purification of recombinant proteins.[4] In the most common IMAC implementation, a hexahistidine (His×6) tag, comprised of six consecutively placed histidine residues, is incorporated into the C- or N-terminus of a recombinant protein. The His×6 tag binds strongly to a divalent metal chelate, such as the Ni(II) nitrilotriacetate complex (Ni-NTA),

which is immobilized on a convenient commercial resin. Four of the six coordination sites on the octahedral Ni(II) center are occupied by the NTA ligand and the remaining coordination sites are occupied by two of the six imidazole moieties available in the His×6 tag.[5]

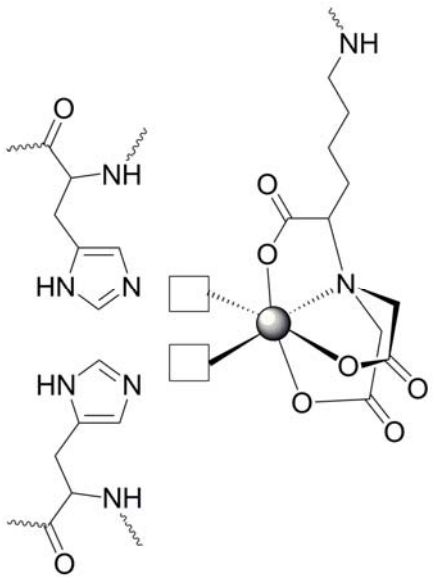

Figure 4.1 Open sites of Ni(II) center open for imidazole (histidine) coordination.

This basic IMAC strategy allows the purification of recombinant His×6-tagged proteins in one or two steps to achieve a moderate degree of purity. Moreover, the His×6 tag is relatively small and generally does not interfere with the native structure or function of the protein and, is thus commonly used without cleavage of the tag. Since its discovery in late 1980's, Ni-NTA based IMAC has been widely used for purifying recombinant proteins and many His×6-tagged proteins are now commercially available. While this strategy has proven to be fairly successful, a significant percentage of recombinant proteins remain difficult to purify by IMAC.[6] Low protein expression is a key contributor to difficulties in protein isolation. The target protein concentration may be less than 0.1% of the cleared crude lysate

when overexpressed in *E. coli*, and much lower when overexpressed in mammalian cells. Numerous functionally active proteins can only be expressed in mammalian cells and this imposes new challenges to protein purification techniques. The target protein structure may also add to purification difficulties by blocking the His×6-tag from the Ni-NTA moiety on the surface of commonly used commercially available microbeads. Consequently, a large number of His×6-tagged proteins cannot be captured by commercial Ni-NTA resin under native conditions. To overcome this problem, purification under denaturing conditions has been used to gain full access to the His×6-tag, but the overall protein purification efficacy significantly decreases because of the unreliability and inefficiency of *in vitro* protein re-folding to their native functional conformations.

Significant efforts have been devoted to gaining a better understanding of the Ni-NTA/His×6-tag interactions and thus improving the IMAC protein purification efficiency over the past few years. Recently, the strength of the Ni-NTA interaction to histidine-tagged peptides was probed and assessed using scanning force microscopic techniques.[7] Here, the benefit of tags with increased histidine residues was examined, and showed that His×6-tag created a significantly more stable interaction than His×2-tag (two histidine residues). Others have used His×10-tags to attempt to achieve higher affinity with a variety of designed Ni-NTA molecules.[8] These studies appear to indicate the histidine tag affinity to Ni-NTA does not benefit from redundancy greater than His×6 due to increased loss of entropy.

In an alternate viewpoint, Ebright *et al.* has elegantly demonstrated enhanced binding of the His×6-tag to a bivalent Ni-NTA system over a monovalent Ni-NTA control using fluorescence anisotropy and fluorescence resonance energy transfer measurements. [9] Tampé, Piehler, and coworkers have further studied the enhanced affinity of multivalent Ni-NTA-

derived molecules toward the histidine tag in great detail with fluorescence quenching experiments. [8, 10-12] Mono-, bis-, tris-, and tetra-Ni-NTA fluorescent probes were used to determine dissociation constants by fluorescence and isothermal titration calorimetry. The extensive characterization of the Ni-NTA/His×6 interaction has expanded its use to drug delivery[13] and designing fluorescent imaging probe of protein localization in live cells.[14] Yet, there is an unmet need for purification systems with multivalent Ni-NTA moieties, which can be competitive with commercial products.

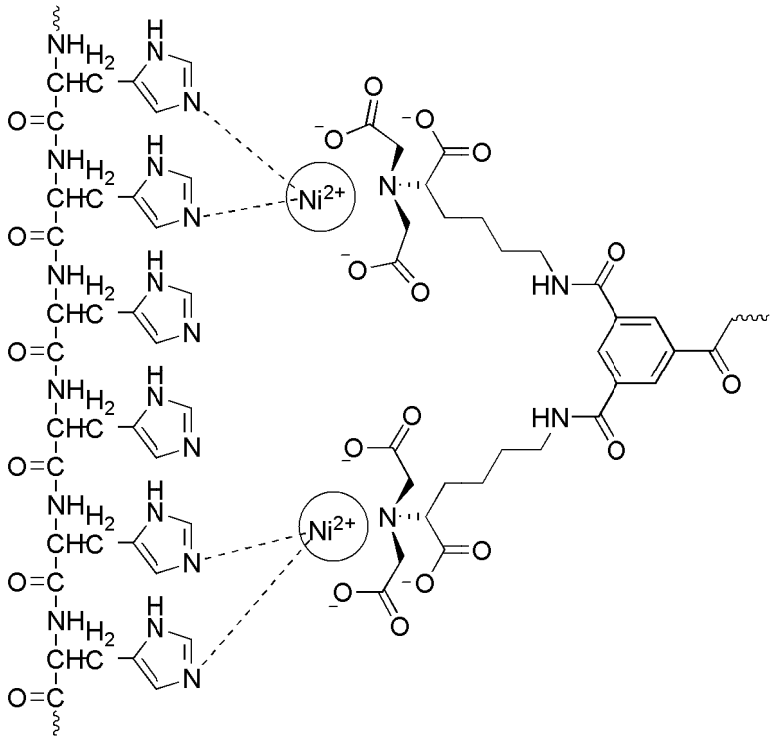

Figure 4.2 Multivalent binding strategy for His×6-tag proteins.

Various biocompatible resins exist commercially for immobilizing and separating proteins in affinity chromatography, such as cross-linked dextran, agarose, and magnetic

micron-sized particles coated with these materials. To utilize the increased surface area of nanomaterials, a variety of nanometer-scale platforms are available. Katzenellenbogen and coworkers have recently used fluorescent silica nanoparticles modified with Ni-NTA derivatives for protein purification.[15] Xu *et al.* reported the use of dopamine to immobilize Ni-NTA onto an iron oxide shell of a magnetic nanoparticle to isolate His×6-GFP from *E. coli* lysate.[16] The use of dopamine to chelate surface Fe metal centers for Ni-NTA immobilization is an elegant method that can be designed to merge with Ni-NTA multivalency to create a more effective protein purification system.

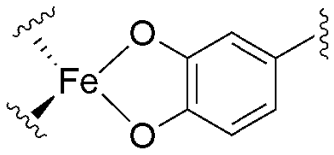

Figure 4.3 Catechol moiety of dopamine can chelate Fe metal centers on iron oxide surfaces.

In the work presented in this chapter, we demonstrated the design of a superparamagnetic iron oxide nanoparticle immobilized bivalent Ni(II)-NTA chelate system with the aim of improving IMAC purification of His×6-tagged proteins by strengthening the interactions between the His×6-tag and a bivalent Ni-NTA chelate. The bis-Ni-NTA-immobilized nanoparticles were shown to be capable of binding His×6-tagged proteins in their native, folded conformations that failed to bind commercial microbeads under identical conditions. The present system is superior to commercial magnetic beads in binding to His×6-tagged proteins and is useful for isolating target proteins that are overexpressed at low levels in the mammalian cells. Control experiments with a mono-NTA chelate immobilized

on iron oxide nanoparticles indicated a similarly high affinity for His×6-tagged proteins, suggesting that the very high density of the mono-NTA chelate presented by the nanoparticles allows the binding of the His×6-tag to more than one NTA moiety on the surface. This work thus demonstrates that the multivalency strategy can be utilized to enhance the binding of his-tagged proteins in their native, folded conformations.

4.2 Results and Discussion

4.2.1 Surface Modification of Iron Oxide Nanoparticles with Bis-NTA and Mono-NTA Ni(II) Chelates

The iron oxide magnetic nanoparticles were synthesized using protocols previously described.[19-21] The nanoparticles were washed in ethanol and transferred into *n*-hexanes and used without further purification. The concentration of the nanoparticles was estimated based on the dry mass after the removal of the solvents. Iron oxide nanoparticles prepared by different routes gave similar results for protein binding and purification experiments.

Although a number of functional groups have been immobilized on iron oxide nanoparticles, their binding strength and their ease of surface immobilization vary significantly. Since Xu and co-workers recently demonstrated the efficient immobilization of dopamine derivatives on iron oxide nanoparticles,[16] we have decided to use this strategy to immobilize bis-NTA Ni(II) chelate for protein purifications. The new bis-NTA ligand with a catechol group (**4**) was synthesized according to the procedures outlined in the previous section. Compound **4** was synthesized in 22% overall yield in 4 steps starting from known benzyl-protected dopamine trifluoroacetate salt and benzene-1,3,5-tricarbonyltrichloride. New compounds **1**-**4** were characterized by ^{1}H and $^{13}C\{^{1}H\}$ NMR spectroscopy and mass spectrometry.

In order to determine the effects of multivalency on protein binding, we have also prepared a new mono-NTA ligand with two catechol groups (**8**) by using a 1:1 ratio of dopamine hydrochloride and benzene-1,3,5-tricarbonyltrichloride as shown in Scheme 2. Compound **8** was synthesized in an overall yield of 28% in 4 steps. New compounds **5**-**8** were characterized by ^{1}H and $^{13}C\{^{1}H\}$ NMR spectroscopy and mass spectrometry.

Surface modification of iron oxide nanoparticles with new NTA-derived ligands was accomplished by simply stirring a biphasic mixture of the ligand in water and iron oxide nanoparticles in hexanes. The NTA-ligand-immobilized nanoparticles were charged with Ni(II) ions by ultrasonic mixing in 2M $NiCl_2$. The iron oxide nanoparticles with different coatings were characterized by transmission electron microscopy (TEM). TEM images of ~10 nm monodisperse iron oxide nanoparticles (prepared by thermal decomposition) before and after surface modifications illustrate the retention of nanoparticle size and shape, and monodispersity throughout monovalent and bivalent NTA-ligand surface modification and Ni(II)-loading. Slight aggregation of Ni(II)-loaded nanoparticles was however observed in the TEM images (**Figure 4.4**).

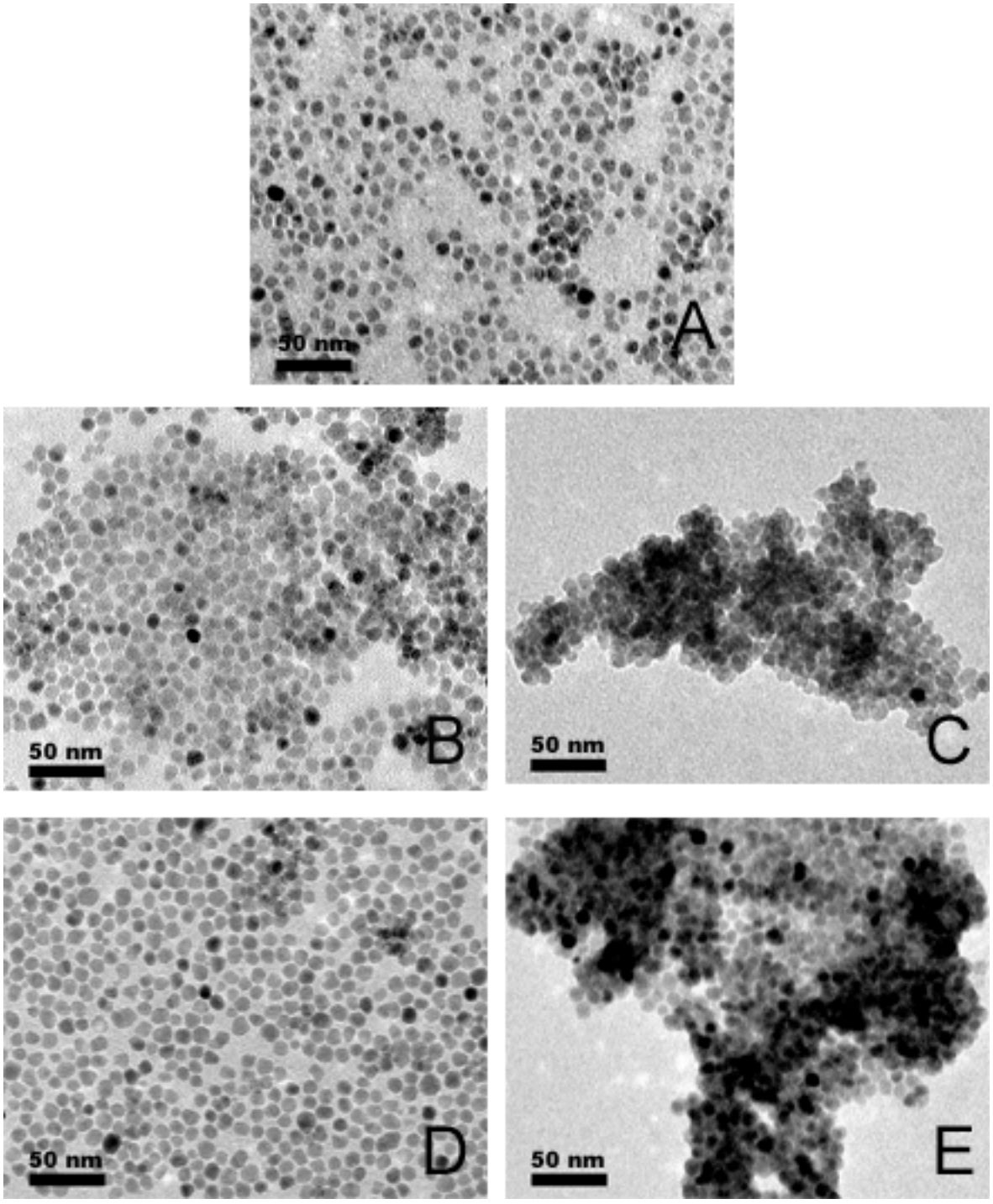

Figure 4.4 TEM images of monodisperse iron oxide nanoparticles (10 nm in diameter): (A) Prepared by thermal decomposition and stabilized with oleic acid. (B) Modified with bis-NTA ligand. (C) Ni(II)-loaded bis-NTA nanoparticle. (D) Modified with mono-NTA ligand. (E) Ni(II)-loaded mono-NTA nanoparticle. The scale bar is 50 nm.

4.2.2 Binding of His×6-tagged Proteins Labeled with [^{35}S]-Methionine

Immobilization of proteins onto the nanoparticles and subsequent elution were initially demonstrated with His×6-tagged, [^{35}S]-methionine-labeled GMAP-210 protein synthesized via coupled *in vitro* transcription and translation. In a typical binding-elution experiment, the direct lysate (DL) signal is equal to the sum of the flow through (FT), washes (W1, W2, W3), elutions (E1, E2), and residual resin signals. The signal from each fraction was measured using liquid scintillation counting (**Figure 4.5, Table 4.1**).

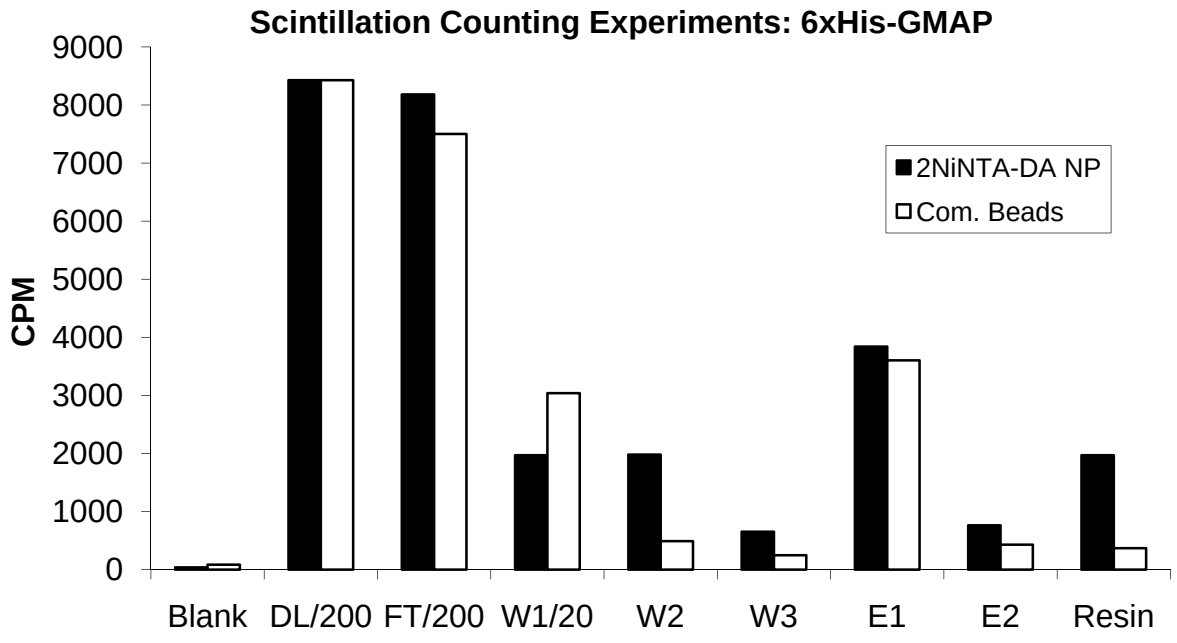

Figure 4.5 Graphical representation the results of an [^{35}S]-labeled HisX6-GMAP-210 binding radioactive scintillation counting assay for bis-Ni-NTA nanoparticles (solid bars) and commercial Ni-NTA agarose beads (open bars). Fractions collected and radioactivity quantified in counts per minute (CPM). DL = direct lysate, FT = flow through, W1 = wash 1, W2 = wash 2, W3 = wash 3, E1 = elution 1, E2 = elution 2.

Table 4.1 Raw counts per minutes (CPM) data from [^{35}S]-labeled HisX6-GMAP-210 binding radioactive scintillation counting assay for bis-Ni-NTA nanoparticles and commercial Ni-NTA agarose beads (DL = direct lysate, FT = flow through, W1 = wash 1, W2 = wash 2, W3 = wash 3, E1 = elution 1, E2 = elution 2).

	Blank (CPM)	DL (CPM)	FT (CPM)	W1 (CPM)	W2 (CPM)	W3 (CPM)	E1 (CPM)	E2 (CPM)	Resin (CPM)
Bis-Ni-NTA Nanoparticles	**38**	**1685170**	**1636552**	**39410**	**1980**	**653**	**3840**	**764**	**1971**
Commercial Beads	**85**	**1685170**	**1500000**	**60783**	**490**	**248**	**3602**	**430**	**269**

Since only a small percentage of [^{35}S]-methionine was incorporated into the recombinant protein in the TNT reaction, a majority of the radioactivity in both the commercial beads and nanoparticle systems came from unbound free [^{35}S]-methionine in the FT (**Figure 4.5 and Table 4.1**). Following the removal of FT, the resin was washed three times until low background was reached and subsequently eluted with imidazole. This scintillation counting assay demonstrates that the NTA-modified nanoparticles can specifically capture His×6-tagged proteins followed by efficient elution with imidazole. We also examined the relative protein binding capacity of nanoparticles as compared to the commercial beads. It was found that the 10 μL (0.32% v/v suspension, assuming Fe_3O_4 density of 5.15 g/cm^3) of nanoparticle (16.3 mg/mL) had a similar binding capacity to 10 μL (5% v/v suspension) of commercial magnetic agarose beads. It appears that the un-optimized nanoparticles used in this work have higher residual radioactivity after elutions when compared to the commercial beads, presumably due to relatively strong nonspecific binding. This result was within expectation, since the commercial beads were coated with agarose, which has low non-specific binding to proteins. We think that the non-specific binding of the nanoparticle could be minimized if its surface is modified with hydrophilic molecules such as PEG that are known to resist nonspecific protein binding.[22]

4.2.3 Binding of Overexpressed His×6-tagged Proteins

We next carried out protein binding studies of several commercially available recombinant His×6-tagged proteins. One of the major problems in using Ni-NTA in protein purification is that numerous His×6-tagged proteins can only be purified under denaturing conditions. Consequently, a complicated refolding process is needed that often results in low yield of the active protein. In this work, we focus on examining whether the NTA-modified nanoparticles can be used under native conditions to purify His×6-tagged proteins that require denaturing conditions when commercial NTA beads are used. We used recombinant murine His×6-endostatin as an example. Endostatin is a potent angiogenesis inhibitor that has shown therapeutic suppression of tumor-induced angiogenesis in mice implanted with tumors.[23] O'Reilly *et al.* reported that recombinant murine endostatin with His×6 tag could be expressed in *E. coli* as insoluble inclusion bodies and purified using Ni-NTA resin under denaturing conditions. Endostatin thus purified underwent an inefficient refolding process before it could be used in xenograft mouse studies. We found that the already folded endostatin could not be captured when commercial Ni(II)-NTA beads were used. As shown in Figure 3, approximately 90% of His×6-rmES was present in the FT, and almost no protein was detected in the elutions, indicating that commercial beads failed to capture His×6-rmES under native conditions. Significantly, Ni(II)-loaded nanoparticles readily bound His×6-rmES without the use of denaturing conditions. A 10 μL volume of Ni(II)-loaded nanoparticles (163 μg) is found to have a binding capacity of 5.6 μg under un-optimized conditions. The bound His×6-rmES was readily eluted by imidazole. This result indicates that milligrams of a native protein can be purified using approximately 30 mg of Ni(II)-loaded nanoparticles (**Figure 4.6 and Table 4.2**).

A)

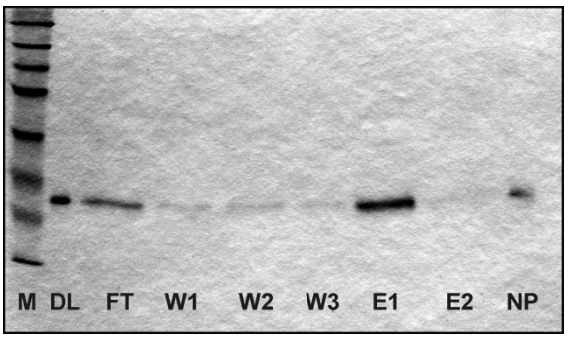

B)

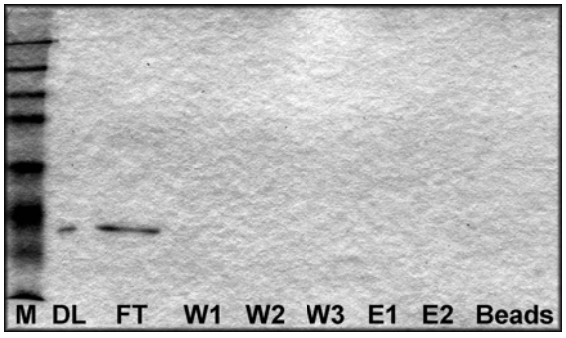

Figure 4.6 SDS-PAGE analysis of mouse Hisx6-rmES protein binding assay using (A) bis-Ni-NTA nanoparticles and (B) commercially available magnetic agarose beads.

We have also successfully recycled and reused the modified nanoparticles in His×6-rmES binding without Ni(II) reloading. The recycled nanoparticle appears to have a similar binding capacity to the pristine sample based on SDS-PAGE analysis (**Figure 4.7**).

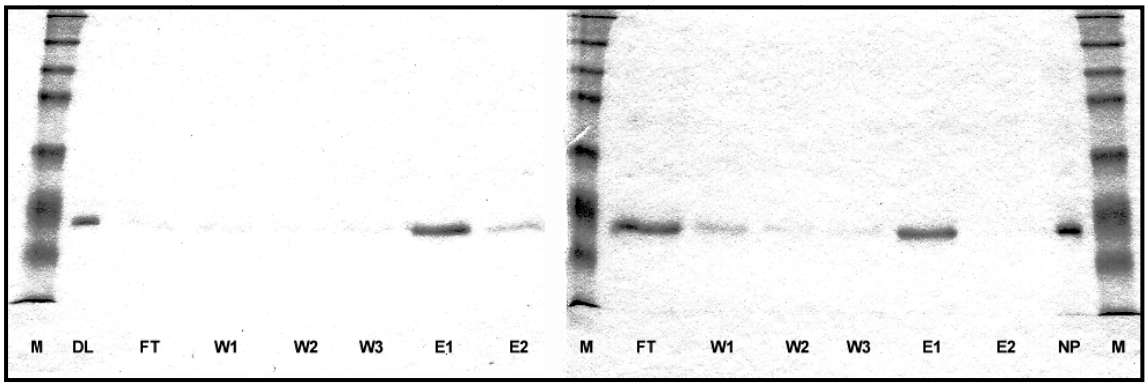

Figure 4.7. SDS-PAGE analysis of Hisx6-rmES binding assay with Ni(II)-loaded nanoparticles, first, with pristine nanoparticles, then with recycled nanoparticles. The two merged gels show similar binding capacities by eluted protein (E1).

His×6-Endostatin bound and eluted from bis-Ni-NTA loaded nanoparticles was used to show that the native, active conformation of the protein was maintained and protein activity was preserved. Cow pulmonary artery endothelial (CPAE) cells were treated with bis-Ni-NTA nanoparticle eluted His×6-rmES to induce apoptosis. The apoptosis was confirmed by confocal fluorescence microscopy of the CPAE cells stained with the apoptosis marker Annexin-V PE (**Figure 4.8**). Cells without treatment of the eluted protein did not show evidence of apoptosis induction.

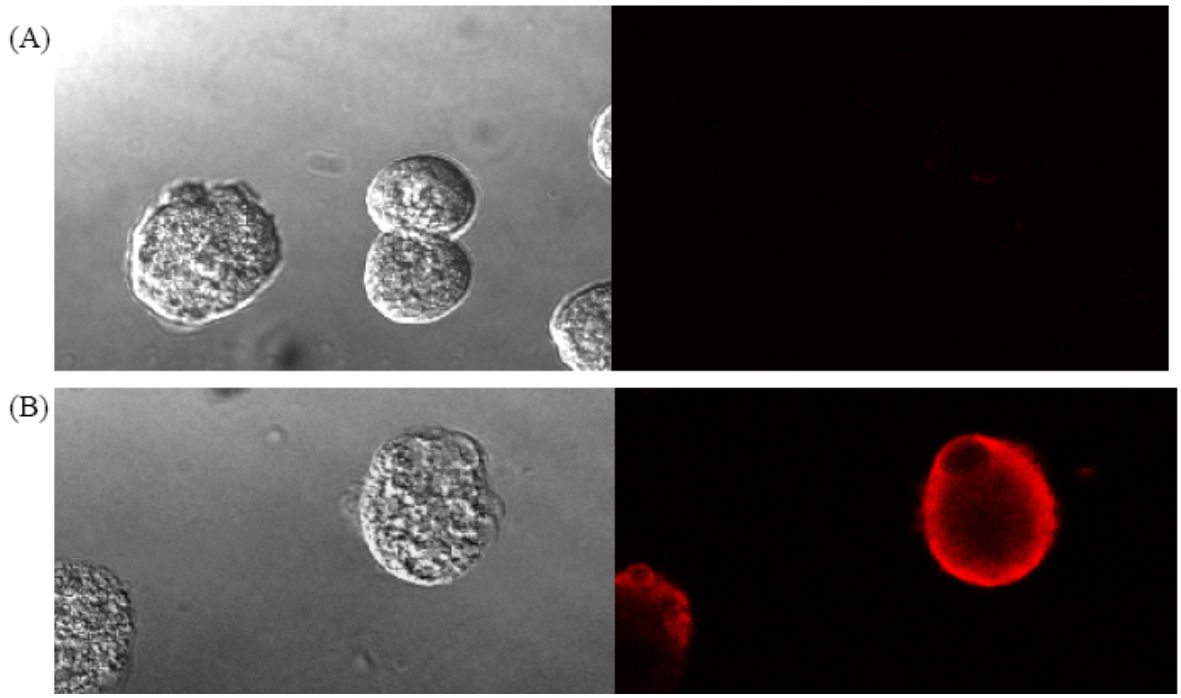

Figure 4.8 (A) Bright field (left) and corresponding confocal fluorescence microcopy (right) images of normal cow pulmonary artery endothelial (CPAE) cells (without 6×His-rmES treatment). (B) Bright field (left) and corresponding confocal fluorescence microcopy (right) images of apoptotic CPAE cells labeled with Annexin V-PE. Apoptosis was induced over 24 hours using 6×His-rmES (10 μg/mL) eluted from bis-Ni-NTA nanoparticles.

Additionally, bis-Ni-NTA nanoparticles were used to bind His×6-caspase 3, the key mediator of apoptosis in mammalian cells, and demonstrate retention of activity after elution. After typical binding/elution of the His×6-caspase 3, the resulting fractions were used for an activity assay of a fluorogenic substrate containing the caspase 3-specific sequence (**Figure 4.9**). Activity was shown in the untreated protein (DL) and the unbound protein (FT). Little activity was found in the final wash before elution (W3), suggesting that unbound protein has been washed away. The first elution showed an apparent fluorescence due to activity of the caspase 3. The second elution showed little fluorescence, suggesting that most of the

elutable protein was release in the first elution fraction. The nanoparticle resin also showed activity, demonstrating that protein immobilized onto the surface of the nanoparticle retains activity.

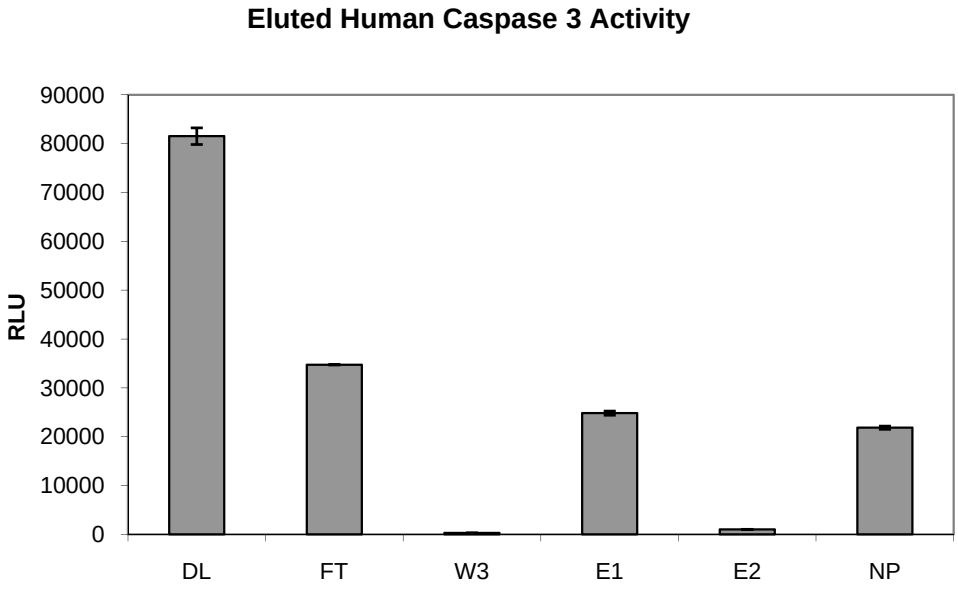

Figure 4.9 His×6-caspase 3 activity of fractions from binding/elution experiment with bis-Ni-NTA nanoparticles. RLU was measured from the fluorescence resulting from the cleavage of the DEVD-APC substrate.

We also compared the binding of other His×6-tagged proteins that do not require denaturing conditions for Ni-NTA based purifications. Ubiquitin is a protein found throughout all eukaryotic cells and plays key roles in highly specific protein degradation. The small His×6-tagged ubiquitin (9.3 kDa) is expected to have an affinity for both the commercial beads as well as the surface modified nanoparticles. SDS-PAGE analysis confirms the affinity of the commercial beads and the Ni(II)-loaded nanoparticle (**Figure 4.10 and Table 4.2**).

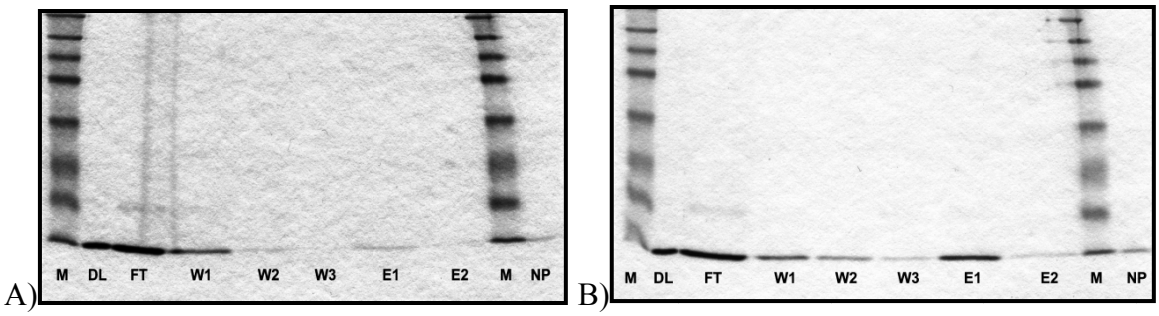

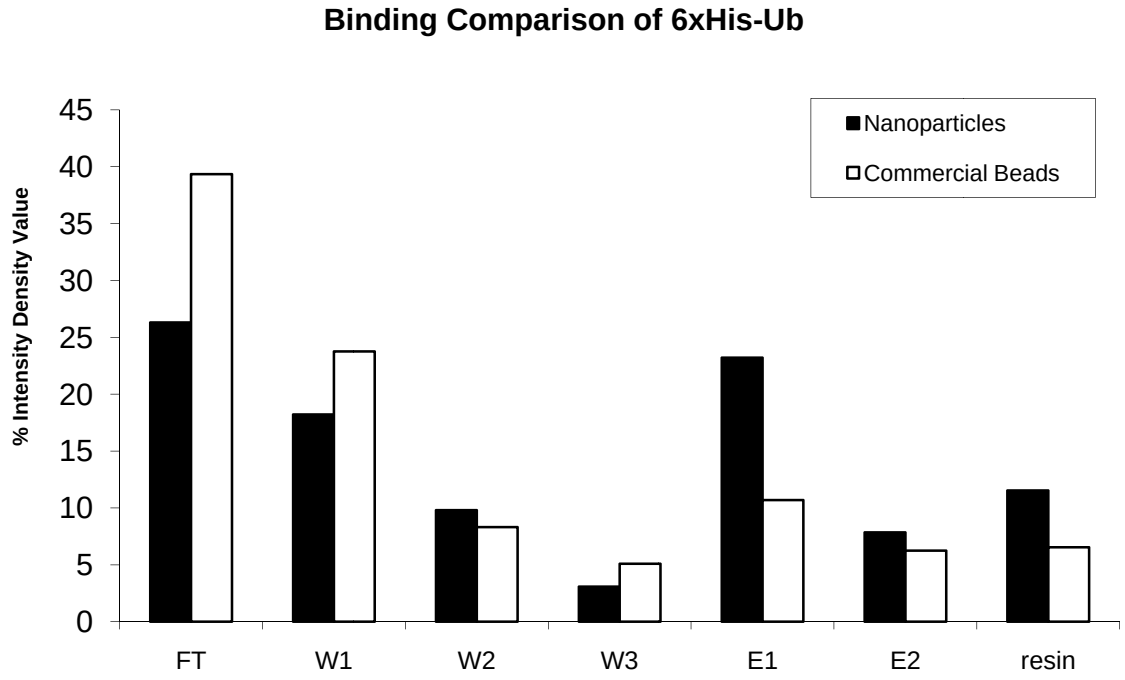

Figure 4.10 Binding assay of Hisx6-Ub. A) Commercial magnetic agarose beads (Qiagen): no protein is bound to the bead or eluted by imidazole. Most of the protein is washed away unbound in the FT. B) Bis-Ni-NTA NPs: His-tag protein is bound and a majority is eluted from the nanoparticles by imidazole. C) Graphical representation of densitometry quantification of SDS-PAGE gels.

Densitometry analysis shows the binding capacity of 20 μL (5% v/v suspension) of commercial beads is 1.1 μg His×6-Ub, while that of 10 μL (0.32% v/v suspension) of bis-NTA-Ni(II)-loaded nanoparticle is 2.3 μg. In comparing the binding of 10 μL (0.32% v/v suspension) of nanoparticle for His×6-rmES (21.3 kDa , 5.6 μg) and 6xHis-Ub (9.3 kDa , 2.3 μg), it is estimated that the binding capacity of the Ni(II)-loaded nanoparticles is approximate 25 pmol of proteins/μL.

Table 4.2 Intensity Density Values (%IDV) compiled from densitometry quantification of SDS-PAGE results for collected fractions comparing Bis-Ni-NTA-modified nanoparticles and commercial Ni-NTA agarose beads in HisX6-tagged protein binding experiments (10 μg total protein).

	FT	W1	W2	W3	E1	E2	NP/resin
6xHis-rmES + 2NiNTA-NP	30.48	1.05	1.70	0.67	56.20	1.21	8.70
6xHis-rmES + Com. Beads	89.58	6.06	0.44	0.44	0.54	0.18	2.74
6xHis-Ub + 2NiNTA-NP	26.30	6.06	0.44	0.44	0.54	0.18	11.54
6xHis-Ub + Com. Beads	39.35	18.22	9.80	3.07	23.21	7.85	6.54
6xHis-UCH-L1 + 2NiNTA NP	31.80	12.38	1.25	1.16	34.78	3.30	15.33
6xHis-UCH-L1 + Com. Beads	83.16	6.19	0.89	0.89	0.58	0.03	8.27

Binding studies on His×6-UCH-L1 (~25 kDa) were also used to demonstrate the nanoparticle's ability to capture His×6-enzymes (**Figure 4.11 and Table 4.2**). Binding capacities of 40 μL (5% v/v suspension) of commercial beads and 10 μL (0.32% v/v suspension) of nanoparticle are 0.06 μg and 3.48 μg His×6-UCH-L1, respectively. This

method provides the possibility of using His×6-enzymes displayed on the surface of magnetic nanoparticles to catalyze various biochemical reactions.

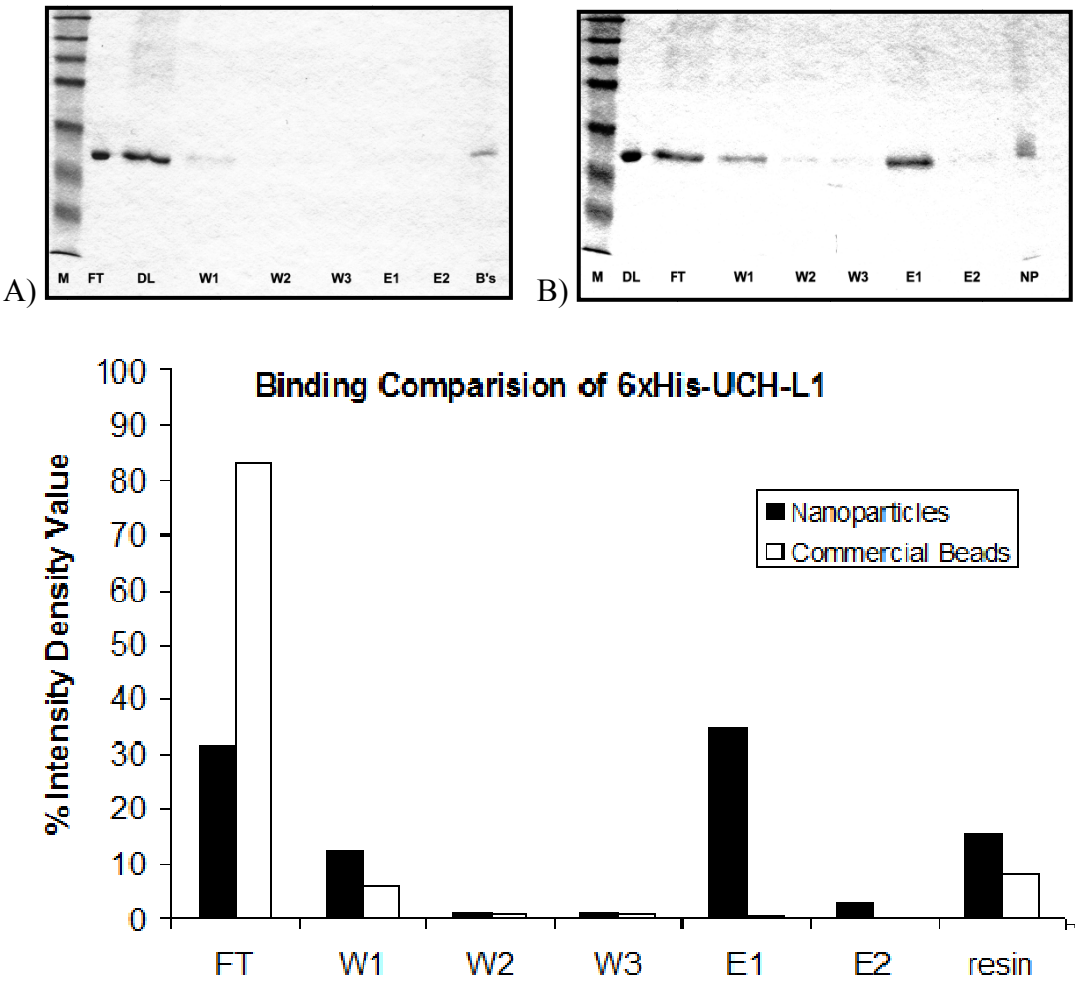

Figure 4.11 Binding assay experiments of his-tag enzymes comparing commercially available beads and surface modified nanoparticles. A) Hisx6-UCH-L1/commercial beads B) Hisx6-UCH-L1/divalent Ni(II)-loaded nanoparticles.

One major concern in NTA microbeads based protein purification is the large elution volume that requires additional concentration steps before being used in the subsequent experiments. While lyophilization can be used to concentrate most proteins, the process reduces the biological activity of many other proteins. Ultra-filtration is another widely used

method in volume reduction. However, the loss of purified proteins could be significant, presumably due to nonspecific interactions with the membrane. Our Ni(II)-loaded nanoparticles disperse well in aqueous solution, and therefore significantly smaller elution volume can be used. This advantage eliminates the need of volume reduction and makes it possible to directly use the proteins after purification.

Our magnetic, recyclable nanoparticles are able to bind important His×6-proteins in native conformations with a high capacity. It is worth mentioning that our Ni(II)-loaded nanoparticles were able to efficiently capture all the proteins we randomly chose for this study. Although we have only tested a small number of proteins, our success rate is much higher than that of previous research, which has shown an approximately 60% success rate.[5]

4.2.4 Purification of Recombinant His×6-tagged Proteins from Crude Mammalian Cell Lysate

Proteins expressed in mammalian cells are usually soluble and active, and therefore extremely useful in studying their physiological significances. The biggest drawback is that their expression levels are very low, making the purification challenging. The nanoparticle platform was previously used for protein purification from *E. Coli* cell lysate,[15] in which proteins are much more easily overexpressed. We investigated whether our NTA-loaded nanoparticles could be used to purify recombinant proteins expressed in mammalian cells. 293T cells were used to express a recombinant His×6-UGT protein. The lysate was prepared for purification of 6xHis-UGT protein by the bis-Ni(II)-NTA modified nanoparticles. **Figure 4.12** shows the staining of DL, FT, W3, E1, E2, and nanoparticle fractions and clearly indicates the purification of desired His×6-tagged protein from the mammalian crude lysate.

The elution E1 is significantly cleaner than the direct lysate, with few impurities. These nonspecifically bound impurities are probably due to proteins with many amino acid residues that can coordinate to the immobilized metal ion. Nonetheless, the present nanoparticle system has shown great promise in the purification of His×6-tagged proteins from crude mammalian cell lysates.

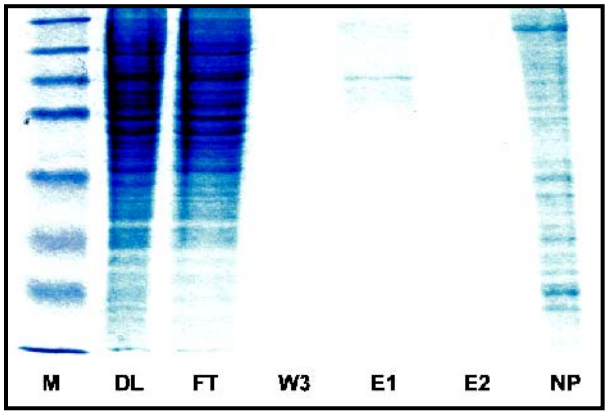

Figure 4.12 Mammalian Cell Lysate Fractionation. SDS-PAGE (12.5% separation gel) results of flag-6xHis-UGT prepared from 293T cells showing marker (M). direct lysate (DL, 10% dilution), flow through (FT, 10%), 3rd wash (W3), elution 1 (E1), elution 2 (E2), and protein residue on nanoparticle (NP).

4.2.5 Nonspecific Interactions

Nonspecific interactions between the protein and nanoparticles do not appear to be significant when the NTA nanoparticles are chelated with N(II). Table 1 shows approximately 8.7% of His×6-rmES remained on the Ni(II) loaded bis-NTA-modified nanoparticles after elution, slightly higher than that on commercial microbeads. Without the chelation of Ni(II), His×6-rmES was found to have a high affinity for the bis-NTA-modified nanoparticle (**Figure 4.6**). Densitometry measurements show that more than 45% of the

6xHis-rmES was present in the sum of the washes and elutions, while 39% of the protein remained on the bis-NTA-modified nanoparticles.

On the other hand, freshly prepared iron oxide nanoparticles (without surface modifications) had little interaction with His×6-rmES. Over 70% of the 10 μg of loaded protein was detected in the FT and over 90% was detected in the sum of the FT and washes. The nanoparticles retained approximately 7% of the His×6-rmES after elution, a significant reduction from the 39% retention of Ni(II)-free bis-NTA-modified nanoparticles. The nonspecific interaction of the rmES to the nanoparticle is thus a result of the surface modifications. To rule out the potential role of residual oleic acid on the nanoparticle surface, we carried out a binding experiment using particles without oleic acid stabilization. Nonspecific interaction was observed for the oleic acid-free nanoparticles as well.

As the ratio of His×6-rmES (μg) to bis-Ni(II)-loaded NTA nanoparticle (mg) is increased from 10.2 to 61.3, the amount of non-specifically bound protein appears to remain constant (**Figure 4.13**). The specific his-tag binding to Ni(II)-NTA occurs after the full capacity of the nonspecific interaction is reached at a 6×His-rmES (μg) to bis-Ni(II)-loaded NTA nanoparticle (mg) ratio between 10.2 and 15.3. Maximum binding capacity of the nanoparticle via the His×6-tag appears to have been reached with a His×6-rmES (μg) to bis-Ni(II)-loaded NTA nanoparticle (mg) ratio of 61.3 since some 6xHis-rmES is detectable in the FT.

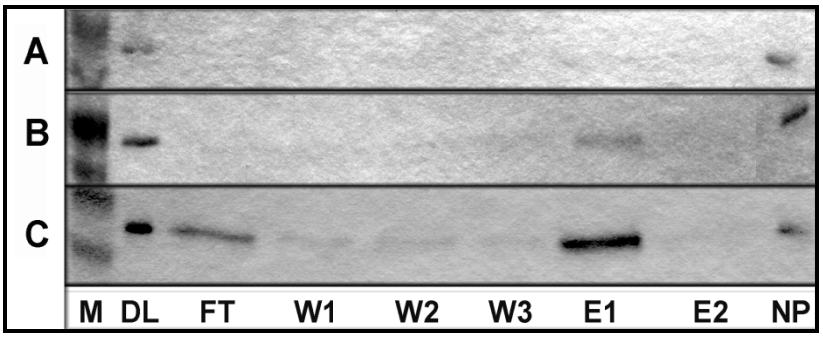

Figure 4.13 Preference toward nonspecific interaction before his-tag—Ni-NTA interaction demonstrated through increasing ratios of 6xHis-rmES protein (μg) to bis-Ni-NTA nanoparticle (mg) A: 10.2, B: 15.3, C: 61.3. (M = Marker, FT = Flow Through, W1 = Wash 1, W2= Wash 2, Wash 3 = W3, E1 = Elution 1, E2 = Elution 2, NP = protein bound nonspecifically to nanoparticle.)

Various attempts were made to block the nonspecific interaction of the target protein (**Figure 4.14**). We first attempted to block the nonspecific binding with BSA. The surface modified nanoparticles were pre-incubated with BSA before the His×6-rmES binding experiment was performed. Unfortunately, BSA did not effectively block the His×6-rmES nonspecific binding. An attempt of blocking the His×6-rmES nonspecific interaction of the nanoparticle with a smaller protein (His×6-Ub) did not seem to result in any noticeable improvement by SDS-PAGE analysis.

A)

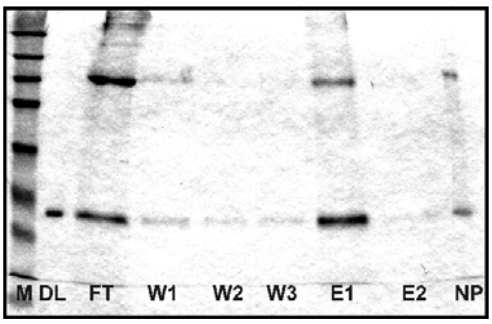

B)

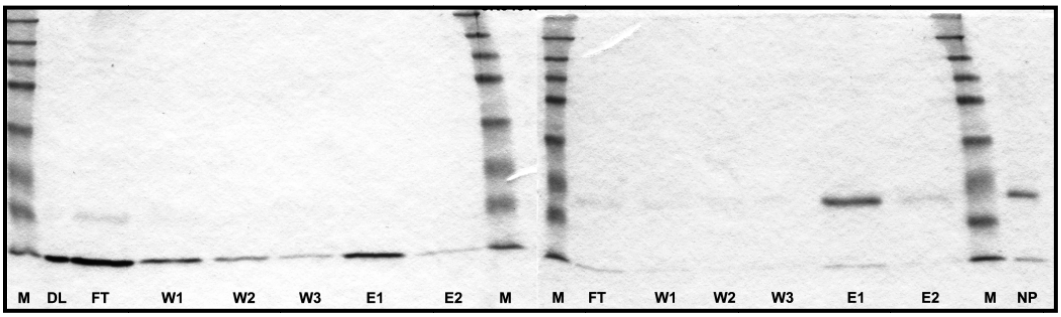

Figure 4.14 Attempts at blocking nonspecific interaction occurring in Hisx6-rmES binding assay. A) Ineffective blocking shown in SDS-PAGE analysis after overnight pre-incubation of nanoparticles with 1% BSA. B) Ineffective blocking shown in SDS-PAGE analysis after recycling nanoparticles used in 6xHis-Ub binding assay for a Hisx6-rmES binding assay.

4.2.6 Surface Density of the Ni-NTA Chelates

The mono-NTA ligand with two dopamine anchors was synthesized to present monovalency of the Ni(II)-NTA moiety onto the nanoparticle surface. Interestingly, an SDS-PAGE binding assay of the mono-Ni(II)-NTA-modified nanoparticle showed a similarly effective binding with His×6-rmES (**Figure 4.14**).

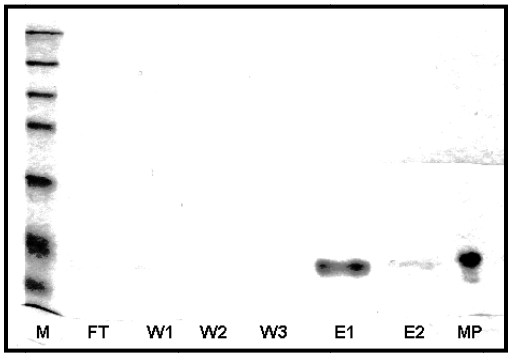

Figure 4.15 Hisx6-rmES binding assay using Ni(II)-NTA conjugated microparticles demonstrating similar binding capacity as bis-Ni-NTA nanoparticles by high surface coverage.

Furthermore, we compared the mono- and bis-Ni(II)-NTA ligand modified nanoparticles by elution with variable imidazole concentrations, and no significant difference was observed. Unlike commercial Ni-NTA beads, the His×6-rmES could not be eluted from the mono- and bis-Ni(II)-NTA-modified nanoparticles at a pH as low as 4.0 (without the use of imidazole; **Figure 4.15**). These results are suggestive of similar binding affinity of mono- and bis-Ni(II)-NTA-modified nanoparticles, probably a result of high surface coverage of mono-Ni(II)-NTA moieties.

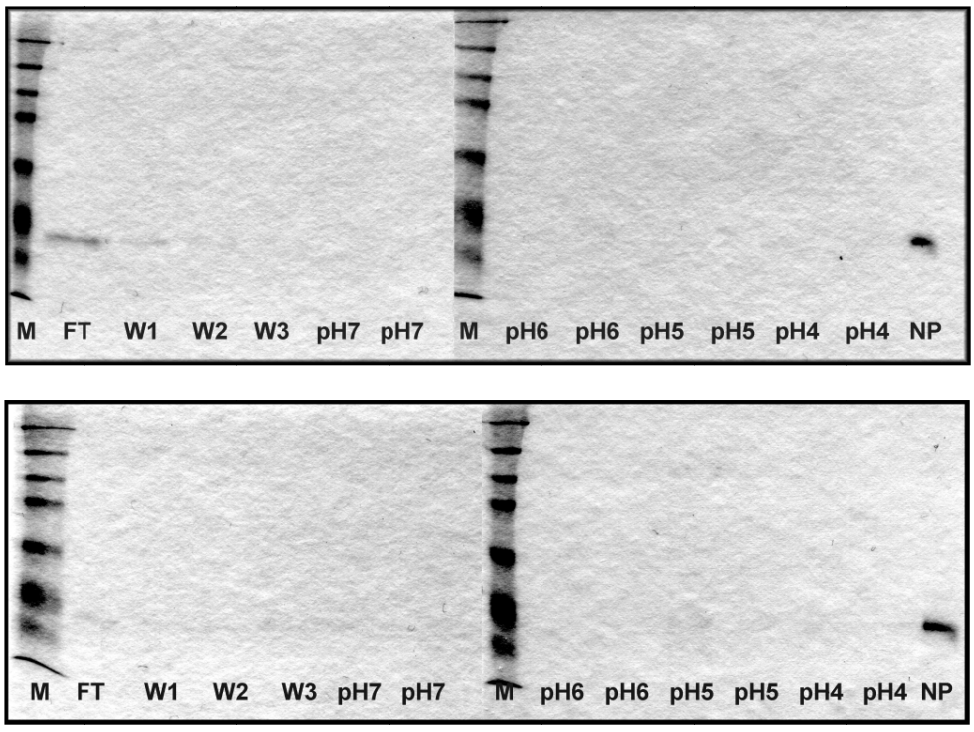

Figure 4.16 Attempt toward pH elution in Hisx6-rmES binding assay for A) bis-Ni-NTA nanoparticles and B) mono-Ni-NTA nanoparticles showing no elution of protein at pH of 7, 6, 5, and 4 (washed twice at each pH) without the presence of imidazole.

To demonstrate the importance of high surface coverage, we conjugated Ni(II)-NTA to micrometer-sized, carboxy-terminated commercial beads (~1.5 μm diameter). NTA-lysine was conjugated to the beads via the amide bond using the DCC/NHS coupling protocol. Upon loading with Ni(II), these beads were found to bind His×6-rmES as effectively as mono- and bis-Ni(II)-NTA modified nanoparticles (**Figure 4.16**). This experiment unambiguously supports the notion that enhanced binding of His×6-tagged protein can be achieved by taking advantage of the multivalency effect (**Figure 4.17**).

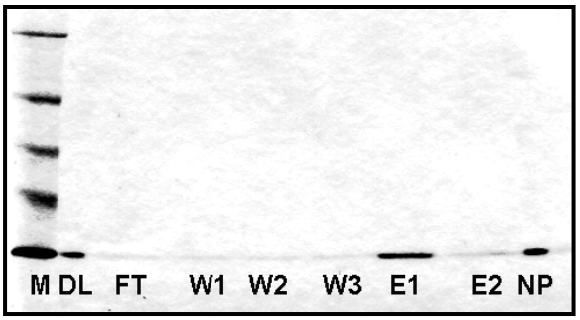

Figure 4.17 Similar His×6-rmES binding and elution from mono-Ni-NTA nanoparticles demonstrating a multivalent effect as a result of high surface density.

4.3 Concluding Remarks

New bis-nitrilotriacetic acid (NTA) chelates with catechol anchors were synthesized and immobilized on superparamagnetic iron oxide nanoparticles. When loaded with Ni(II), these NTA-immobilized nanoparticles were shown to bind His×6-tagged proteins in their native, folded conformations that commercial microbeads fail to bind under identical conditions. An extensive series of control experiments suggest that the multivalency strategy can be utilized to enhance the binding of His×6-tagged proteins in their native, folded conformations. Additionally, proteins were confirmed for activity after binding and release by a fluorometric assay for enzymatic cleavage of a caspase 3-specific peptide sequence and induction of apoptosis of endothelial cells. We further demonstrated the selective purification of His×6-tagged proteins from direct cell lysates by using the Ni(II)-loaded magnetic nanoparticles. The present platform is capable of efficient purification of His×6-tagged proteins that are expressed at low levels in mammalian cells. This work thus presents a novel nanoparticle-based high-capacity protein purification system with shorter incubation times, proportionally large washes, and significantly smaller elution volumes compared to currently available microbeads.

4.4 Materials and Methods

4.4.1 General

N_α,N_α-bis(carboxymethyl)-*L*-lysine was purchased from Fluka. All other chemicals were purchased from Sigma-Aldrich and used as received unless otherwise noted. Carboxy-terminated magnetic microparticles were purchased from Bangs Laboratories, Inc. Purified recombinant His×6-endostatin (His×6-rmES) was purchased from Calbiochem. Recombinant human His×6-ubiquitin (His×6-Ub) and mouse His×6-ubiquitin C-terminal hydrolase L-1 (His×6-UCH-L1) were from Boston Biochem. ^{1}H and $^{13}C\{^{1}H\}$ NMR spectra were obtained on a Bruker 400MHz AVANCE or Bruker 400MHz DRX. Mass spectra were obtained from Voyager DE-Pro MALDI-MS or HP/Agilent LC/Ion-trap MS in the Department of Chemistry at Duke University. Liquid scintillation counting experiments are performed on a Tri-Carb 2900TR Liquid Scintillation Analyzer. SDS-PAGE gels were quantified using the AlphaEaseFC program. Transmission Electron Microscopy (TEM) images were taken with a JEM-100CXII transmission electron microscope at 100 KV.

4.4.2 Synthesis of 2-(3,4-Bis-benzyloxy-phenyl)-ethylamine-trifluoroacetate-salt (Bn-DA-TFA)

2-(3,4-Bis-benzyloxy-phenyl)-ethylamine-trifluoroacetate-salt (Bn-DA-TFA) was prepared from literature procedures.[16] Briefly, dopamine hydrochloride was neutralized by stirring with NaOH in dioxane. *Tert*-butyl dicarbonate dioxane solution was dropped into the stirring solution while solution was cooled in an ice bath. The solution was allowed to stir for under inert atmosphere and allowed to warm to room temperature. The solution was acidified with an HCl solution and subsequently washed with ethyl acetate. The tert-butyl

carbonate (tBOC) protected product was concentrated, purified by column chromatography, and confirmed using ^{1}H NMR spectroscopy. The tBOC-dopamine was dissolved in anhydrous DMF and stirred vigorously with K_2CO_3. Excess benzyl bromide was added dropwise and allowed to stir overnight. The reaction mixture was filtered and washed with ether, dH_2O, and brine. The benzyl protected tBOC-dopamine was purified by recrystallization and confirmed by ^{1}H NMR spectroscopy. The tBOC deprotection was removed by stirring the fully protected compound in 5% trifluoroacetic acid (TFA) in dichloromethane. The solvents were evaporated under reduced pressure to yield the benzyl protected dopamine TFA salt, which was confirmed by ^{1}H NMR spectroscopy.

Scheme 4.1 2-(3,4-Bis-benzyloxy-phenyl)-ethylamine-trifluoroacetate-salt (Bn-DA-TFA) synthesis.

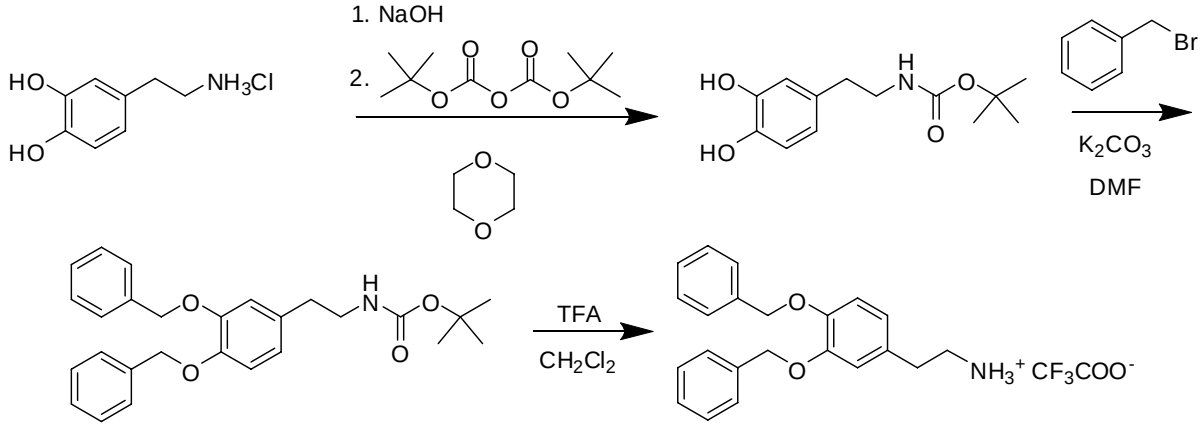

4.4.3 Synthesis of N_α,N_α-bis(carboxymethyl)-*L*-lysine tribenzyl ester-trifluoroacetate-salt (Bn-NTA-lys-TFA)

N_α,N_α-bis(carboxymethyl)-*L*-lysine tribenzyl ester-trifluoroacetate-salt (Bn-NTA-lys-TFA) prepared from literature procedures.[17] Briefly, N_α,N_α-bis(carboxymethyl)-*L*-lysine and Cs_2CO_3 were stirred vigorously in H_2O and dioxane. *Tert*-butyl dicarbonate dioxane solution

was dropped into the stirring solution while solution was cooled in an ice bath. The completion of the reaction was checked using thin layer chromatography (TLC) and ninhydrin. The tBOC-protected lysine derivative cesium salt was filtered dried under reduced pressure to remove solvent. The intermediate protected cesium salt product was dissolved in DMF before excess benzyl bromide was slowly dropped into solution. The final protected product was extracted using chloroform and washed with water before column chromatography and ^{1}H NMR confirmation. The tBOC protection group was removed by TFA in dichloromethane to from the benzyl protected lysine derivative TFA salt, which was confirmed by ^{1}H NMR spectroscopy.

Scheme 4.2 Nα,Nα-bis(carboxymethyl)-L-lysine tribenzyl ester-trifluoroacetate-salt (Bn-NTA-lys-TFA) synthesis.

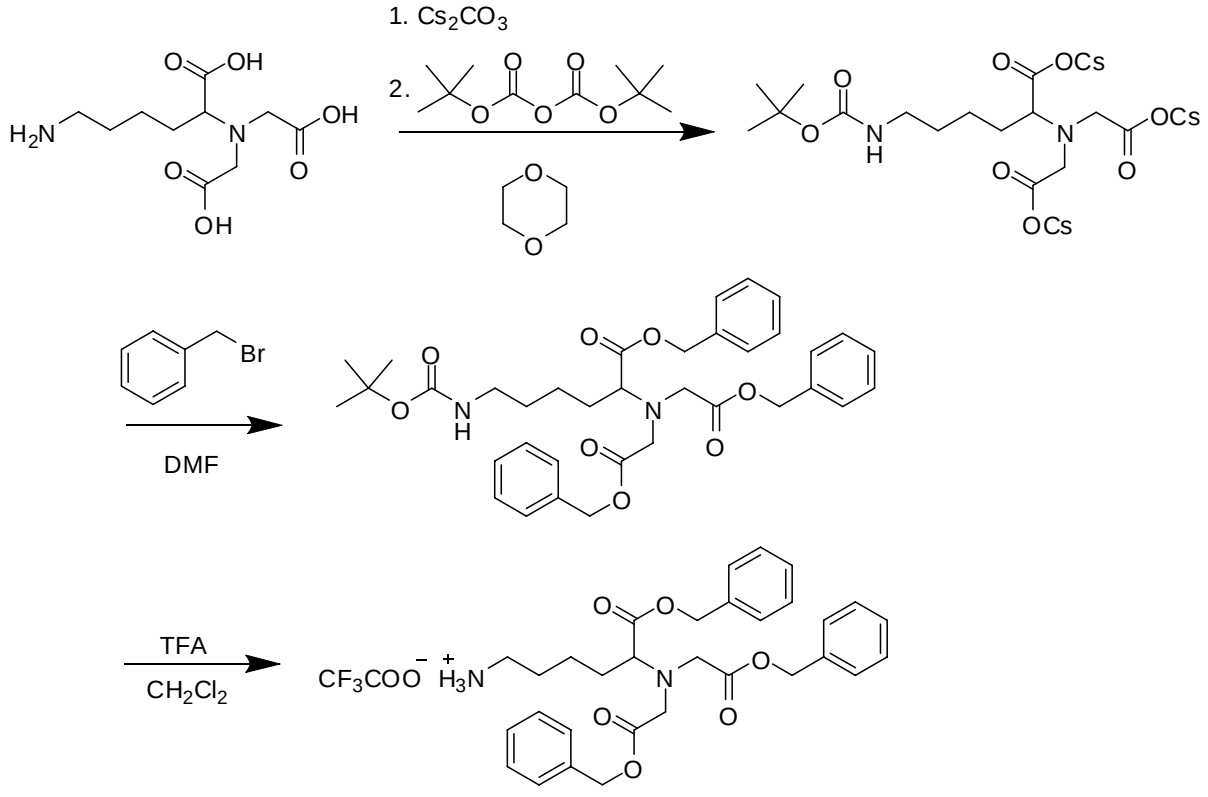

4.4.4 Synthesis of dimethyl 5-(3,4-bis(benzyloxy)phenethylcarbamoyl)benzene-1,3-dioate (1).

To a stirring solution of benzene-1,3,5-tricarbonyltrichloride (1.7 g, 6.40 mmol) in dry CH_2Cl_2 (170 mL) at 0°C was added Bn-DA-TFA (0.536 g, 1.20 mmol) in dry CH_2Cl_2 (100 mL) dropwise over 5 hours. The solution was allowed to warm to room temperature. The solvent was removed under reduced pressure to produce a white residue. Methanol was added and stirred for a few hours. The excess methanol was removed under reduced pressure to produce a white solid. The product was isolated using flash column chromatography (ethyl acetate/hexanes, 2:3 v/v; R_f = 0.4). The solvents were removed under reduced pressure to yield a white solid of **1** (0.225 g, 0.408 mmol, 34.0% yield). ^{1}H NMR (400MHz, $CDCl_3$): 8.75 (s, 1H), 8.52 (s, 2H), 7.40 (d, 4H), 7.29 (m, 6H), 6.90 (d, 1H), 6.81 (s, 1H), 6.72 (d, 1H), 5.11 (s, 2H), 5.01 (s, 2H), 3.92 (s, 6H), 3.64 (q, 2H), 2.83 (t, 2H); ^{13}C NMR ($CDCl_3$, 100 MHz) δ 165.4, 165.3, 149.0, 147.6, 137.2, 137.0, 135.4, 132.9, 132.0, 131.9, 130.9, 128.3, 127.7, 127.2, 121.5, 115.5, 115.3, 71.3, 71.2, 52.4, 41.4, 34.9, 31.5; MALDI-MS: $[M+H]^+$ *m/z* 554.0 (calcd 554.6); $[M+Na]^+$, m/z 577.2 (calcd 576.6); $[M+K]^+$ m/z 592.8 (calcd 592.7).

Scheme 4.3 Dimethyl 5-(3,4-bis(benzyloxy)phenethylcarbamoyl)benzene-1,3-dioate (**1**) synthesis.

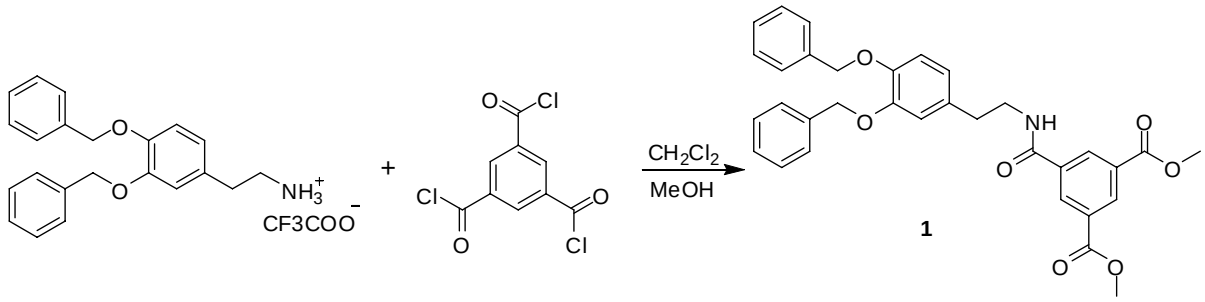

4.4.5 Synthesis of 5-(3,4-bis(benzyloxy)phenethylcarbamoyl)benzene-1,3-dioic acid (2)

To a stirring solution of **1** (0.160, 0.289 mmol) in acetone (6 mL) was added 1N NaOH (4 mL). After 3 hours, complete deprotection was confirmed by TLC. The solution was acidified to pH 3 using 1N HCl. The solvent was removed and the product was stirred in H_2O. The precipitate of **2** was collected by suction filtration and recrystallized in acetone (0.145 g, 0.276 mmol, 95.5% yield). ^{1}H NMR (400MHz, MeOD): 8.42 (s, 1H), 8.21 (s, 2H), 7.15-6.90 (m, 10H), 6.67 (s, 1H), 6.62 (d, 1H), 6.49 (d, 1H), 4.73 (s, 4H), 3.28 (t, 2H), 2.54 (t, 2H); ^{13}C NMR (DMSO, 100 MHz) δ 166.4, 164.6, 148.3, 146.8, 137.5, 137.4, 135.5, 132.7, 132.2, 132.0, 131.8, 128.4, 127.8, 127.7, 127.6, 127.5, 121.2, 115.2, 114.8, 70.3, 70.2, 41.1, 34.4; MALDI-MS: $[M+H]^+$ *m/z* 525.9 (calcd 526.6).

Scheme 4.4 5-(3,4-bis(benzyloxy)phenethylcarbamoyl)benzene-1,3-dioic acid (**2**) synthesis.

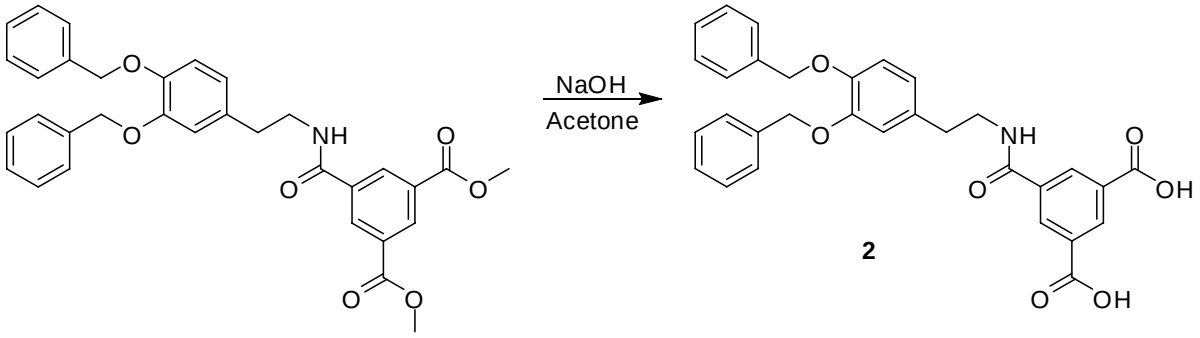

4.4.6 Synthesis of 5-(3,4-bis(benzyloxy)phenethylcarbamoyl)benzene-1,3-benzyl-NTA-lysine (3)

The diacid **2** (0.140 g, 0.266 mmol) was stirred in dry CH_2Cl_2 (13 mL) to form a cloudy suspension. 0.40 mL of $SOCl_2$ was slowly added and stirring continued at 50 °C for 6 hours to form a clear solution. The solvent was removed under reduced pressure to give the

5-(3,4-bis(benzyloxy)phenethylcarbamoyl)benzene-1,3-dioyl dichloride intermediate which was used without further purification.

To a stirring mixture of Bn-NTA-lys-TFA (0.408 g, 0.632 mmol), TEA (0.5 mL), and $CHCl_3$ (5 mL) was added a solution of 5-(3,4-bis(benzyloxy)phenethylcarbamoyl)benzene-1,3-dioyl dichloride in $CHCl_3$ (10 mL) dropwise at 0 °C. The reaction was allowed to warm to room temperature and stir overnight. After removal of solvents under reduced pressure, column chromatography (ethyl acetate/hexanes, 3:2 v/v; $R_f = 0.5$) was used to isolate a pure white solid of **3** (0.281 g, 0.181 mmol, 67.9% yield). ^{1}H NMR ($CDCl_3$, 400 MHz) δ 8.33 (s, 3H), 7.41-7.25 (m, 35H), 6.95 (t), 6.86 (d, 2H), 6.80 (s, 2H), 6.69 (d, 2H), 5.10 (s, 8H), 5.06 (s, 2H), 4.98 (s, 4H), 3.68 (s, 4H), 3.59 (t, 4H), 3.46 (t, 1H), 3.32 (t, 2H) 2.75 (t, 4H), 1,69-1.24 (m, 6H); ^{13}C NMR ($CDCl_3$, 100 MHz) δ 172.8, 171.7, 166.3, 149.3, 148.0, 137.6, 137.5, 135.9, 135.8, 135.6, 135.4, 132.4, 128.8, 128.7, 128.6, 128.5, 128.0, 127.7, 121.7, 116.2, 115.9, 71.6, 66.8, 66.7, 64.5, 53.1, 40.2, 35.4, 29.9, 28.5, 23.1; MALDI-MS: $[M+H]^+$ *m/z* 1556.3 (calcd 1555.8); $[M+Na]^+$, m/z 1577.5 (calcd 1577.8); [M+K]+, m/z 1593.1 (calcd 1593.9).

Scheme 4.5 5-(3,4-bis(benzyloxy)phenethylcarbamoyl)benzene-1,3-benzyl-NTA-lysine (**3**) synthesis.

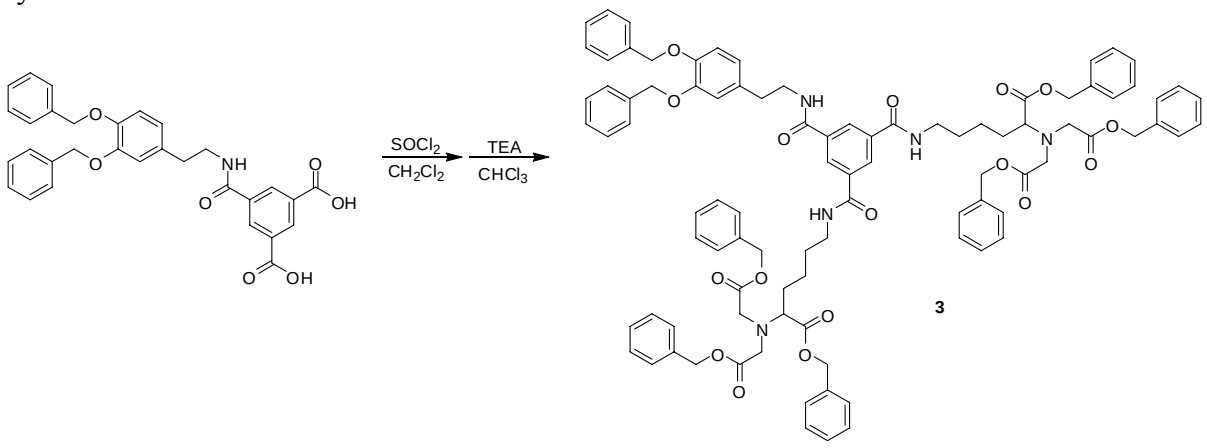

4.4.7 Synthesis of 5-(3,4-bis(hydroxy)phenethylcarbamoyl)benzene-1,3-NTA-lysine (4)

Product **3** (0.043 g, 0.052 mmol) was dissolved in 1.5 mL of $CHCl_3$ and 6 mL of MeOH and placed in a Parr flask with 15 mg Pd/C (10%). The mixture was shaken in a Parr reactor for 24 hours under H_2 (60 psi). Upon complete deprotection, the palladium catalyst was filtered off using Celite and solvent removed under reduced pressure. The product was purified by recrystallization in MeOH/CH_2Cl_2 to give **4** in a quantitative yield. ^{1}H NMR (MeOD, 400 MHz) δ; 8.29 (s, 3H), 6.60 (s, 1H), 6.59 (s, 1H), 6.47 (d, 2H), 3.71-3.21 (m, 16H), 2.68 (t, 2H), 1.63-1.45 (m, 8H), 1.18 (m, 4H); ^{13}C NMR ($CDCl_3$, 100 MHz) δ; 174.1, 173.0, 168.6, 146.7, 144.7, 136.6, 132.0, 130.0, 121.1, 117.0, 116.4, 66.9, 54.3, 43.1, 40.7, 35.9, 29.8, 29.8, 24.4; MALDI-MS: $[M]^+$, *m/z* 833 (calcd 833.8); $[M+Na]^+$, m/z 856 (calcd 856.8).

Scheme 4.6 5-(3,4-bis(hydroxy)phenethylcarbamoyl)benzene-1,3-NTA-lysine (**4**) synthesis.

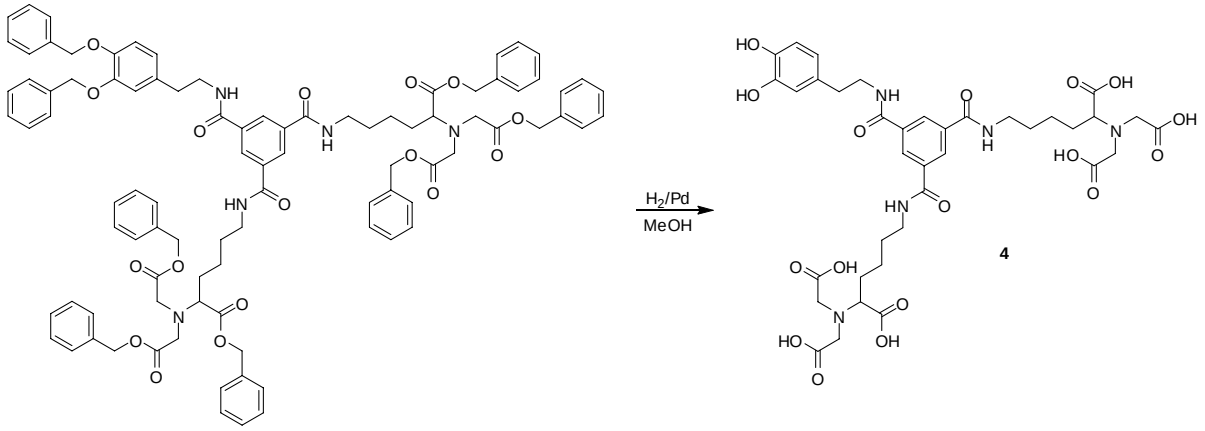

4.4.8 Synthesis of methyl 3,5-bis(3,4-bis(benzyloxy)phenethylcarbamoyl)benzoate (5)

To a stirring solution of benzene-1,3,5-tricarbonyltrichloride (0.320 g, 1.20 mmol) in dry CH_2Cl_2 (170 mL) at 0 °C was added Bn-DA-TFA (0.536 g, 1.20 mmol) in dry CH_2Cl_2 (100 mL) dropwise over 5 hours. The solution was allowed to warm to room temperature. The solvent was removed under reduced pressure to produce a white residue. Methanol was added and allowed to stir for a few hours. The excess methanol was removed under reduced pressure to produce a white solid. The product was isolated using silica flash column chromatography (ethyl acetate/hexanes, 1:1 v/v; $R_f = 0.4$). The solvents were removed under reduced pressure to yield a white solid of **5** (0.298 g, 0.349 mmol, 29.0% yield). ^{1}H NMR ($CDCl_3$, 400 MHz) δ 8.44 (s, 2H), 8.28 (s, 1H), 7.45-7.25 (m, 20H), 6.88 (d, 2H), 6.81 (s, 2H), 6.71 (d, 2H), 6.56 (t, 2H), 5.10, (s, 8H), 3.88 (s, 3H), 3.60 (q, 4H), 2.80 (t, 4H); ^{13}C NMR ($CDCl_3$, 100 MHz) δ 165.6, 165.3, 148.7, 147.4, 136.9, 136.8, 135.1, 131.9, 130.5, 130.3, 129.6, 128.2, 127.6, 127.2, 127.1, 121.4, 115.4, 115.0, 71.1, 52.2, 41.3, 34.7; MALDI-MS: $[M+Na]^+$, *m/z* 877.0 (calcd 878.0); $[M+K]^+$, m/z 893.0 (calcd 894.1).

Scheme 4.7 Methyl 3,5-bis(3,4-bis(benzyloxy)phenethylcarbamoyl)benzoate (**5**) synthesis.

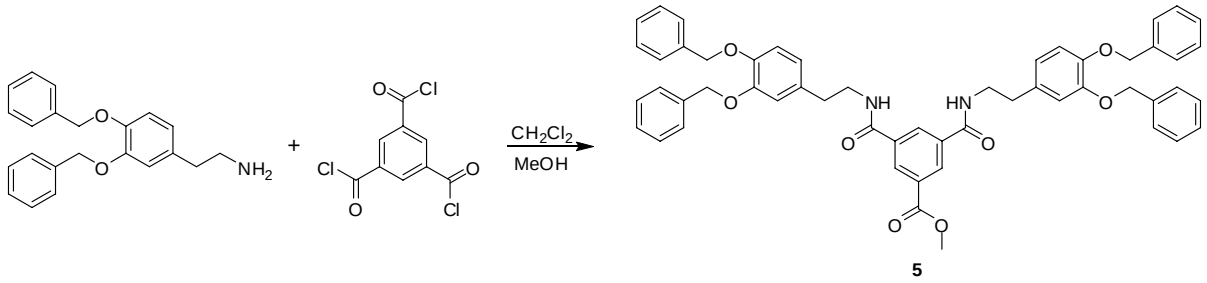

4.4.9 Synthesis of 3,5-bis(3,4-bis(benzyloxy)phenethylcarbamoyl)benzoic acid (6)

Compound **5** (0.250 g, 0.292 mmol) was stirred in a solution of 3 mL of acetone and 1 mL of 1M NaOH overnight. The solution was acidified to pH 3 using 1N HCl, added dropwise. The solvent was removed and the product was stirred in H_2O. The precipitate was collected by vacuum filtration to give **6** in quantitative yield. ^{1}H NMR (MeOD, 400 MHz) δ 8.53 (s, 2H), 8.37 (s, 1H), 7.40-7.20 (m, 20H), 6.93 (s, 2H), 6.91 (s, 2H), 6.76 (d, 2H), 5.03 (s, 8H), 3.54 (t, 4H), 2.81 (t, 4H); ^{13}C NMR ($CDCl_3$, 100 MHz) δ 169.2, 164.9, 150.4, 148.9, 138.9, 138.8, 136.3, 134.3, 131.9, 129.8, 129.5, 128.9 128.8, 123.1, 117.2, 116.9, 72.7, 72.5, 42.8, 37.0; MALDI-MS: $[M+Na]^+$, *m/z* 863.4 (calcd 864.0).

Scheme. 4.8 3,5-bis(3,4-bis(benzyloxy)phenethylcarbamoyl)benzoic acid (**6**) synthesis.

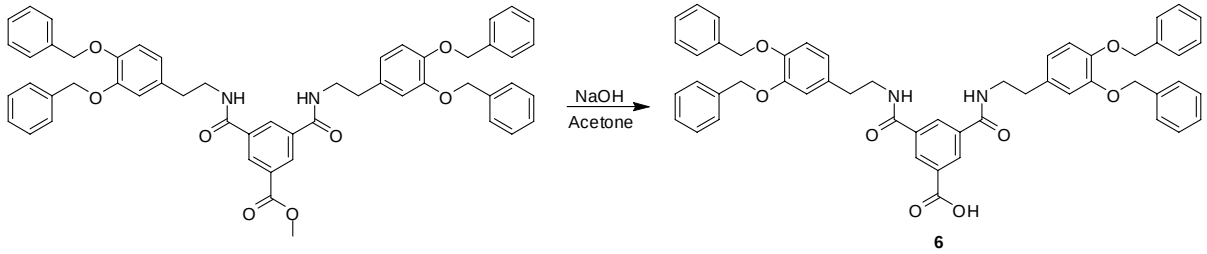

4.4.10 Synthesis of benzyl 6-(N^3,N^5-bis(3,4-bis(benzyloxy)phenethyl)benzene-1,3,5-tricarboxamido)-2-(bis(((benzyloxy)carbonyl)methyl)amino)hexanoate (7)

A mixture of Bn-NTA-lys-TFA (0.060 g, 0.071 mmol), 6 (0.075 g, 0.142 mmol), and HOBt (0.010 g, 0.074 mmol) was stirred in 3 mL anhydrous DMF for 5 minutes. Dicyclohexylcarbodiimide (0.015 g, 0.073 mmol) was added and the mixture was allowed to stir overnight. The solvents were removed under reduced pressure. The product 7 was isolated with silica gel flash column chromatography (ethyl acetate/hexanes, 3/2 v/v; R_f = 0.4). Yield: 0.094 g (97.7%). ^{1}H NMR ($CDCl_3$, 400 MHz) δ 8.43 (s, 1H), 8.41 (s, 2H), 7.50-7.26 (m, 40H), 7.04 (s, 3H), 6.87 (s, 1H), 6.85 (d, 1H), 6.72 (d, 1H), 5.12 (s, 8H), 5.07 (s, 8H), 3.74 (s, 8H), 3.59 (t, 2H), 3.51 (t, 2H), 3.35 (t, 4H), 2.79 (t, 2H), 1.75-1.28 (m, 12H); ^{13}C NMR ($CDCl_3$, 100 MHz) δ 172.5, 171.5, 165.9, 148.9, 147.6, 137.2, 137.1, 135.3, 132.0, 128.5, 128.4, 128.3, 128.2, 128.1, 127.7, 127.4, 127.3, 121.5, 115.7, 115.2, 71.3, 66.5, 66.4, 64.0, 52.8, 41.5, 39.9, 35.0, 27.9, 25.5, 24.8; MALDI-MS: $[M+H]^+$, *m/z* 1356.4 (calcd 1355.6); $[M+Na]^+$, m/z 1378.0 (calcd 1378.6); $[M+K]^+$, m/z 1393.9 (calcd 1394.7).

Scheme 4.9 Benzyl 6-(N^3,N^5-bis(3,4-bis(benzyloxy)phenethyl)benzene-1,3,5-tricarboxamido)-2-(bis(((benzyloxy)carbonyl)methyl)amino)hexanoate (7) synthesis.

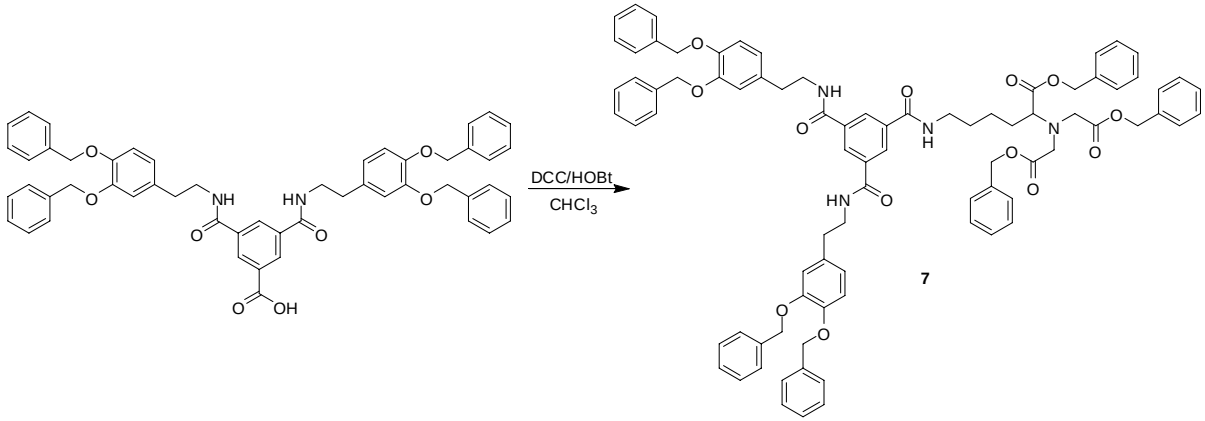

4.4.11 Synthesis of 6-(N^3,N^5-bis(3,4-dihydroxyphenethyl)benzene-1,3,5-tricarboxamido)-2-(bis(carboxymethyl)amino)hexanoic acid (8)

To a solution **7** (0.094 g, 0.069 mmol) in of 5 mL of MeOH and 10 mL of $CHCl_3$ was added 20 mg Pd/C (10%). The mixture was placed in a Parr reactor bottle and rocked for 24 hours at 60 psi H_2. Upon complete deprotection, the catalyst was filtered off using Celite and the solvents were removed under reduced pressure. **8** was purified by recrystallization in MeOH/CH_2Cl_2 in a quantitative yield. ^{1}H NMR (MeOD, 400 MHz) δ 8.34 (s, 3H), 6.69 (s, 2H), 6.67 (s, 2H), 6.56 (d, 2H), 3.64 (t, 4H), 3.60 (t, 1H), 3.33 (s, 4H), 3.29 (t, 2H), 2.77 (t, 4H), 1.90-1.50 (m, 4H), 1.27 (p, 2H); ^{13}C NMR ($CDCl_3$, 100 MHz) δ; 175.3, 174.1, 168.5, 146.1, 144.7, 136.6, 132.0, 129.4, 121.1, 117.0, 116.4, 68.2, 55.1, 43.1, 40.3, 35.9, 26.4, 25.9, 23.6. MALDI-MS: $[M+H]^+$, *m/z* 724.8 (calcd 725.7); $[M+Na]^+$, m/z 746.8 (calcd 747.7).

Scheme 4.10 6-(N^3,N^5-bis(3,4-dihydroxyphenethyl)benzene-1,3,5-tricarboxamido)-2-(bis(carboxymethyl)amino)hexanoic acid (**8**) synthesis.

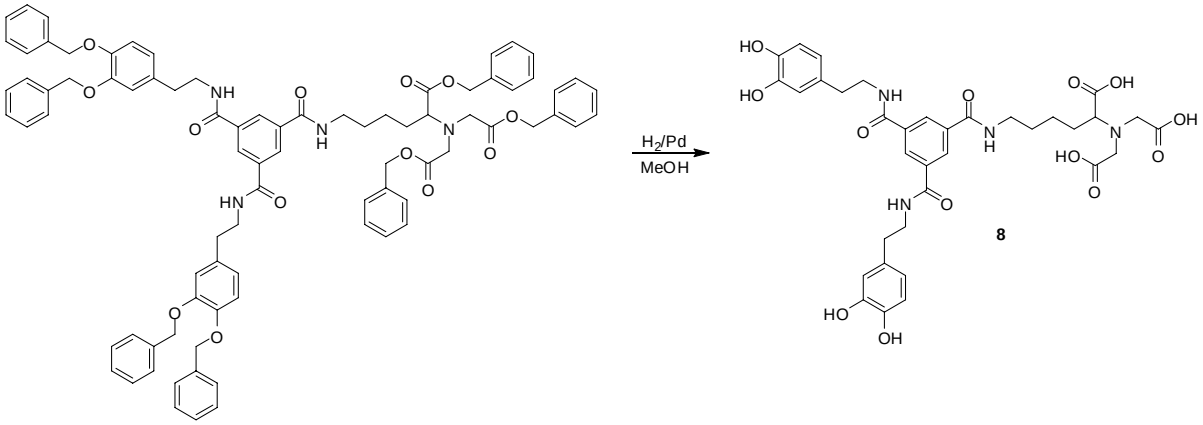

4.4.12 Surface modification of iron oxide nanoparticles with bis-NTA-derived Ni(II) chelate and mono-NTA-derived Ni(II) chelate

The ligand **4** (0.5 mL of a 10 mg/mL MeOH solution) was placed in 1.25 mL dH_2O of pH 4. To this aqueous solution was added 1 mL of iron oxide nanoparticles in *n*-hexanes (16.3 mg/mL). The two layers were sonicated for 1 hour, and repeatedly washed with *n*-hexanes, then methanol until the nanoparticles were readily dispersed in dH_2O. Using a magnet, the nanoparticles were collected and placed in 2 mL of dH_2O. The bis-NTA-pendant ligand-immobilized nanoparticles (0.5 mL) were placed in 2M $NiCl_2$ solution and sonicated for 1 hour. The Ni(II)-loaded nanoparticles were stored in the $NiCl_2$ solution before use. Iron oxide nanoparticle modified with mono-NTA Ni(II)-loaded nanoparticles were similarly prepared.

Scheme 4.11 Surface modification of iron oxide nanoparticles with bis-NTA-derived Ni(II) chelate.

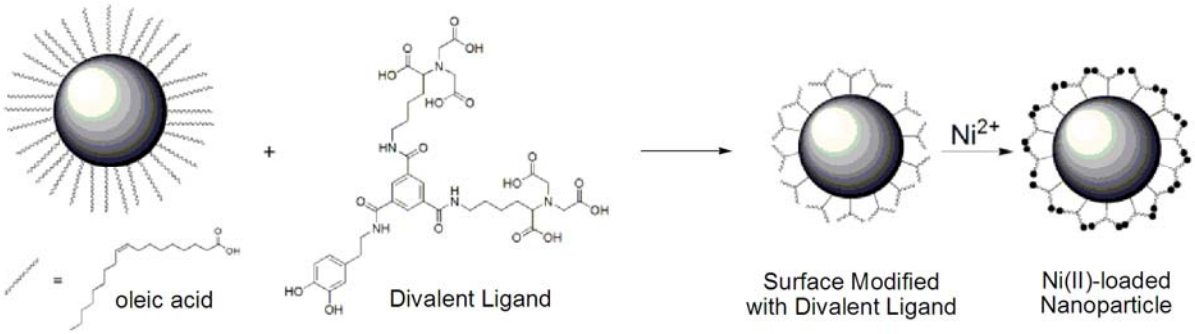

4.4.13 Preparation of Ni(II)-loaded magnetic microparticles

An aliquot of 0.5 mL (2.4 μmol carboxyl) BioMag Carboxyl magnetic iron oxide microparticles (~1.5 μm mean diameter, ~20 mg/mL particle concentration, ~4.8 μmol/mL carboxy-surface titration, Bang's Lab) was washed with dH_2O (3×500 μL), then with acetone (3×500 μL). Aliquots of *N*-hydroxysuccinimide (NHS) (25 μL, 30 mg/mL acetone) and dicyclohexylcarbodiimide (50 μL, 50 mg/mL acetone) were added and incubated overnight. The NHS-activated particles were washed with acetone and used without further purification.

A 240 μM solution of N_α,N_α-bis(carboxymethyl)-L-lysine was prepared by dissolving 0.629 mg N_α,N_α-bis(carboxymethyl)-L-lysine in 35 μL of triethylamine, 500 μL of acetone, and 500 μL of dH_2O. The NHS-activated microparticles were washed with dH_2O, then placed in 100 μL of the N_α,N_α-bis(carboxymethyl)-L-lysine solution. After overnight incubation, the particles were washed with dH_2O. The particles were placed in a 1M $NiCl_2$ solution for 1 hour before use.

4.4.14 Isolation of recombinant mouse His×6-Endostatin (His×6-rmES) with Ni(II)-loaded nanoparticles

The Ni(II)-loaded nanoparticles (7-10 μL; 16.3 mg/mL) were washed in dH_2O (3×50 μL) and a binding buffer (3×50 μL; 50 mM phosphate buffer system, 300 mM NaCl, 10 mM imidazole, pH 8.0). The washed nanoparticles were incubated with 10 μg of His×6-rmES in 40 μL of binding buffer for 5-60 minutes at 4 °C. Using a centrifuge and magnet, the supernatant was collected and nanoparticles washed in 50 μL aliquots of binding buffer (FT: Flow Through, W1: Wash 1, W2: Wash 2, W3: Wash 3). After the third wash, 50 μL of the

elution buffer (50 mM phosphate buffer system, 300 mM NaCl, 250 mM imidazole, pH 8.0) was added and the mixture tumbled for 10 minutes at 4 °C. The eluents were similarly collected by centrifugation and magnetic immobilization (E1: Elution 1, E2: Elution 2). Non-specifically bound protein was released from the nanoparticles by boiling at 95 °C for 4 minutes in a Laemmli SDS-PAGE gel loading buffer. The volumes of the aliquots were reduced in a Speedvac before loading to an SDS-PAGE (12.5%, 180V, 50 min). After separation, the SDS-PAGE gel was stained in a Coomassie Blue solution (0.1% Coomassie blue, 10% acetic acid, 40% methanol) overnight. Recombinant human His×6-ubiquitin (His×6-Ub) and recombinant mouse His×6-ubiquitin C-terminal hydrolase L-1 (His×6-UCH-L1) were isolated with Ni(II)-loaded nanoparticles in the same fashion. Protein isolation by commercial magnetic agarose beads was performed according to the manufacturer's instructions (Qiagen).

Scheme 4.12 General scheme for bis-NTA nanoparticle protein purification system

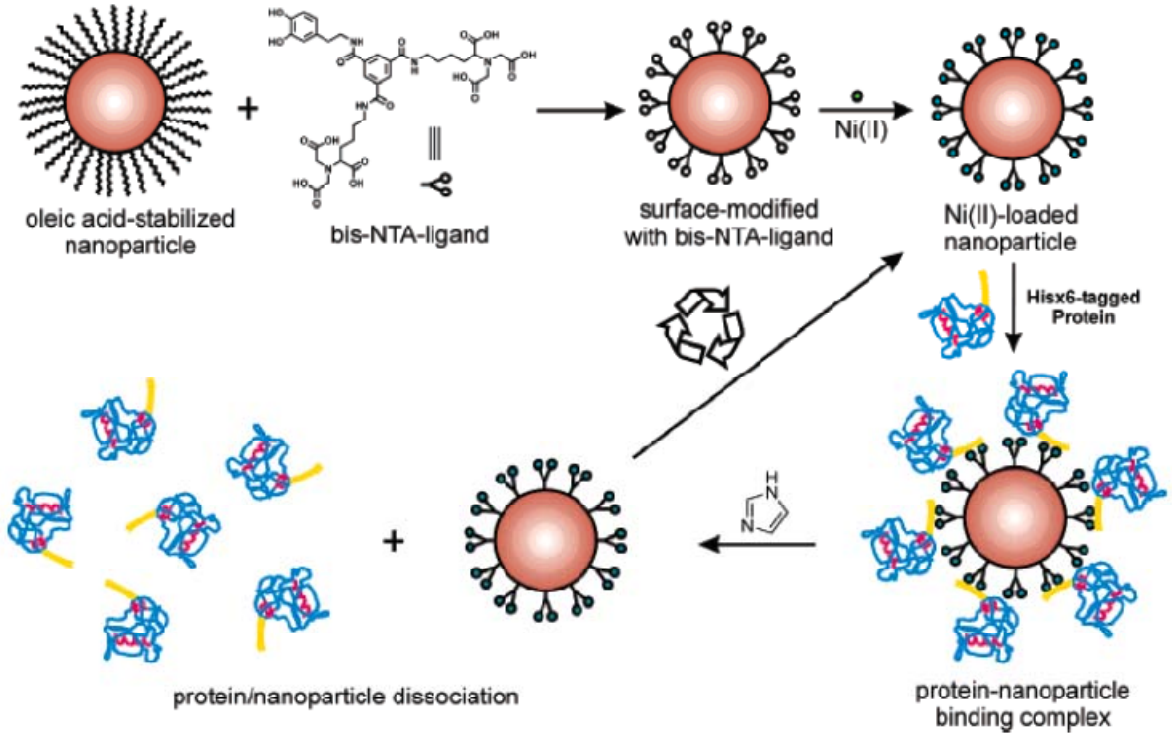

4.4.15 Isolation of His×6-rmES by Ni(II)-loaded microparticles

The Ni(II)-loaded microparticles (10 µL, 20mg/mL) were washed in dH_2O (3x50 µL) and binding buffer (3 x 50 µL). The washed microparticles were incubated with 10 µg of His×6-rmES in 40 µL of binding buffer for 60 minutes at 4 °C. The beads were washed and the bound protein eluted similarly. All the fractions were loaded to an SDS-PAGE for analysis as previously described.

4.4.16 Expression of [^{35}S]-methionine-labeled His×6-GMAP-210

The gene coding a 70 kDa fragment of GMAP-210 (Golgi-associated microtubule-binding protein) was PCR-amplified from a human total RNA library (Stratagene). After

introducing the T7 promoter and TMV 5'-UTR by second PCR, the cDNA was used as template for a coupled *in vitro* transcription/translation (TNT) reaction in the presence of 10 μCi [^{35}S]-methionine (Perkin-Elmer) in a total volume of 25 μL for 90 minutes at 30 °C. Protein synthesis was confirmed by SDS-PAGE and autoradiography. The protein was stored at –80 °C until used.

Hisx6-GMAP-210 Properties:

Protein Sequence:

```
10          20          30          40          50
MQLLFTITME  KGEIEAELCW  AKKRLLEEAN  KYEKTIEELS  NARNLNTSAL
60          70          80          90          100
QLEHEHLIKL  NQKKDMEIAE  LKKNIEQMDT  DHKETKDVLS  SSLEEQKQLT
110         120         130         140         150
QLINKKEIFI  EKLKERSSKL  QEELDKYSQA  LRKNEILRQT  IEEKDRSLGS
160         170         180         190         200
MKEENNHLQE  ELERLREEQS  RTAPVADPKT  LDSVTELASE  VSQLNTIKEH
210         220         230         240         250
LEEEIKHHQK  IIEDQNQSKM  QLLQSLQEQK  KEMDEFRYQH  EQMNATHTQL
260         270         280         290         300
FLEKDEEIKS  LQKTIEQIKT  QLHEERQDIQ  TDNSDIFQET  KVQSLNIENG
310         320         330         340         350
SEKHDLSKAE  TERLVKGIKE  RELEIKLLNE  KNISLTKQID  QLSKDEVGKL
360         370         380         390         400
TQIIQQKDLE  IQALHARISS  TSHTQDVVYL  QQQLQAYAME  REKVFAVLNE
410         420         430         440         450
KTRENSHLKT  EYHKMMDIVA  AKEAALIKLQ  DENKKLSTRF  ESSGQDMFRE
460         470         480         490         500
TIQNLSRIIR  EKDIEIDALS  QKCQTLLAVL  QTSSTGNEAG  GVNSHQFEEL
510         520         530         540         550
LQERDKLKQQ  VKKMEEWKQQ  VMTTVQNMQH  ESAQLQEELH  QLQAQVLVDS
560         570         580         590         600
DNNSKLQVDY  TGLIQSYEQN  ETKLKNFGQE  LAQVQHSIGQ  LCNTKDLLLG
610         620         630         640
KLDIISPQLS  SASLLTPQSA  ECLRASKSEV  LSEHHHHHH_
```

Number of amino acids: 639

Molecular weight: 74406.8

Theoretical pI: 5.43

4.4.17 Isolation of [^{35}S]-methionine-labeled His×6-GMAP-210 with Ni(II)-loaded nanoparticles

The Ni(II)-loaded nanoparticles (10 μL; 16.3 mg/mL) were washed in dH_2O (3×50 μL) and binding buffer (3×50 μL). The washed nanoparticles were incubated with 5 μL of TNT reaction mixture in 100 μL of binding buffer for 60 minutes at 4 °C. The nanoparticles were washed and the bound protein eluted according to the procedures detailed above. All the fractions including the remaining nanoparticles were transferred to scintillation vials for radioactivity measurements using a liquid scintillation counter. Protein isolation using commercial magnetic agarose beads (Qiagen) was performed according to the manufacturer's instructions, and scintillation counts were measured as mentioned above.

4.4.18 Expression of His×6-UGT from cultured 293T cells

The cDNA corresponding to the open reading frame of *C. elegans* UGT was amplified from a *C. elegans* cDNA library (Invitrogen) using high fidelity Platinum *Pfx* DNA polymerase (Invitrogen) and sequence-specific primers with CACC at the 5' end of the forward primer. The full-length cDNA was gel purified and subcloned into the pcDNA3.1D/V5-His TOPO vector (Invitrogen) according to the manufacturer's instructions. The resulting gene-containing plasmid was confirmed by PCR and sequence analysis.

293T cells were cultured in Dulbecco's Minimal Essential Media (DMEM, Gibco) supplemented with 10% Fetal Bovine Serum (FBS, Sigma), 1% L-glutamate (Gibco), and 1% Penicillin/Streptomycin. Cell culture was maintained at 37 °C with 5% CO_2. On the day of transfection, the pre-formed UGT plasmid DNA-Lipofectamine complex (500 μL) was added directly to each well. Cells were incubated at 37 °C in 5% CO_2 for 4 hours.

Afterwards, the media was changed and 2 mL of fresh DMEM (with 10% FBS and 1% L-glutamate) was added. After incubation at 37 °C in a 5% CO_2 incubator for a total of 24 hours to allow protein expression, cells were harvested and lysed using a commercial extraction buffer (Biovision). Intact cells were removed by centrifugation and the supernatants were cleared at 21,000×g for 15 minutes at 4 °C. Levels of protein expression were assessed by separation on SDS-PAGE gels, followed by Western blotting onto nitrocellulose membranes (Amersham Pharmacia), and probing with anti-V5 antibody (Invitrogen). The lysates that were prepared were used for binding studies.

C. elegans UGT (C-HisX6-tagged) properties:

10	20	30	40	50
MLLRILTFLA	VCQVTTSHKI	LMFSPTASKS	HMISQGRIAD	ELANAGHEVV
60	70	80	90	100
NFEPDFLNLT	DKFVPCKKCR	RWPVTGLNNY	KFKKIQNGLS	GDVFQQSSIW
110	120	130	140	150
SKIFNTDSDP	YQDEYTNMCE	EMVTNKELIE	KLKKEKFDAY	FGEQIHLCGM
160	170	180	190	200
GLAHLIGIKH	RFWIASCTMS	VSMRDSLGIP	TPSSLIPFMS	TLDATPAPFW
210	220	230	240	250
QRAKNFVLQM	AHIRDEYRDV	VLTNDMFKKN	FGSDFPCVEF	LAKTSDLIFV
260	270	280	290	300
STDELLEIQA	PTLSNVVHIG	GLGLSSEGGG	LDEKFVKIME	KGKGVILFSL
310	320	330	340	350
GTIANTTNLP	PTIMENLMKI	TQKFKDYEFI	IKVDKFDRRS	FDLAEGLSNV
360	370	380	390	400
LVVDWVPQTA	VLAHPRLKAF	ITHAGYNSLM	ESAYAGVPVI	LIPFMFDQPR
410	420	430	440	450
NGRSVERKGW	GILRDRFQLI	KDPDAIEGAI	KEILVNPTYQ	EKANRLKKLM
460	470	480	490	500
RSKPQSASER	LVKMTNWVLE	NDGVEELQYE	GKHMDFFTFY	NLDIIITAAS
510	520	530	540	550
IPVLIFIVLR	ISNISIITSS	PKNKKDKGQD	NSADIQHSGG	RSSLEGPRFE
560	570			
GKPIPNPLLG	LDSTRTGHHH	HHH		

Molecular weight: 64722.7 daltons

Theoretical PI: 8.03

4.4.19 Isolation of His×6-UGT from cultured 293T cells using Ni(II)-loaded nanoparticles

To purify the His×6-UGT expressed in 293T cells, the pre-washed, Ni(II)-loaded nanoparticles (10 μL; 16.3 mg/mL) were incubated with 50 μL of cleared crude cell lysate (~4 μg/μL total protein) in 50 μL of binding buffer for 15 minutes at 4 °C. After washing nanoparticles three times using 50 μL of binding buffer, the bound proteins were eluted using 15 μL of elution buffer. Aliquots of each fraction were loaded to an SDS-PAGE for separation. The protein was detected by Coomassie blue staining.

4.4.20 Iron oxide nanoparticle surface modification with mono-NTA Ni(II) chelate

One mL of iron oxide magnetic nanoparticles suspension (16.3 mg/mL) was added to ligand **8** (0.5 mL of a 10 mg/mL MeOH solution diluted by 1.25 mL dH_2O of pH 4). The two layers were sonicated for 1 hour, and repeatedly washed with *n*-hexanes, then methanol until the nanoparticles were readily dispersed in dH_2O. Using a magnet, the nanoparticles were collected and placed in 2 mL of dH_2O. The mono-NTA modified nanoparticles (0.5 mL) were placed in 1M $NiCl_2$ solution and sonicated for 1 hour. The divalent Ni(II)-loaded nanoparticles were stored in the $NiCl_2$ solution before use.

4.4.21 Isolation of His-Ubiquitin C-terminal Hydrolase L-1, *mouse recombinant* (6xHis-UCH-L1) with Ni(II)-loaded nanoparticles

The Ni(II)-loaded nanoparticles (10 μL; 16.3 mg/mL) were washed in dH_2O (3×50 μL) and wash buffer (3×50 μL; 50 mM phosphate buffer system, 300 mM NaCl, 10 mM imidazole, pH 8.0). The washed nanoparticles were placed in 40 μL of wash buffer and 10

μL of 6xHis-UCH-L1 (1 μg 6xHis-UCH-L1/1 μL dH_2O) and incubated for 60 minutes at 4 °C. Using a centrifuge and magnet, the supernatant was collected and nanoparticles washed in 50 μL aliquots (FT, W1, W2, W3). After W3, 50 μL of elution buffer (50 mM phosphate buffer system, 300 mM NaCl, 250 mM imidazole, pH 8.0) was added and rotated for 10 minutes at 4 °C. Nanoparticles were collected in 50 μL aliquots (E1, E2). Nonspecifically bound protein was released from the nanoparticles by boiling at 95 °C for 4 minutes. The volumes of the aliquots were reduced for analysis by SDS-PAGE (12.5% separation gel, 180V, 50 min). The SDS-PAGE gel was stained using Coomassie Blue overnight.

4.4.22 Isolation of His-Ubiquitin, *human recombinant* (6xHis-Ub) with Ni(II)-loaded nanoparticles

The Ni(II)-loaded nanoparticles (10 μL; 16.3 mg/mL) were washed in dH_2O (3×50 μL) and wash buffer (3×50 μL; 50 mM phosphate buffer system, 300 mM NaCl, 10 mM imidazole, pH 8.0). The washed nanoparticles were placed in 40 uL of wash buffer and 10 uL of 6xHis-Ub (1 μg 6xHis-Ub/1 μL dH_2O) and incubated for 60 minutes at 4 °C. Using a centrifuge and magnet, the supernatant was collected and nanoparticles washed in 50 μL aliquots (FT, W1, W2, W3). After W3, 50 μL of elution buffer (50 mM phosphate buffer system, 300 mM NaCl, 250 mM imidazole, pH 8.0) was added and rotated for 10 minutes at 4 °C. Nanoparticles were collected in 50 μL aliquots (E1, E2). Non-specifically bound protein was released from the nanoparticles by boiling at 95 °C for 4 minutes. The volumes of the aliquots were reduced for analysis by SDS-PAGE (12.5% separation gel, 180V, 50 min). The SDS-PAGE gel was stained using Coomassie Blue overnight.

4.4.23 Isolation of Endoproteinase GluC, (6xHis-EndoGluC) with Ni(II)-loaded nanoparticles

The Ni(II)-loaded nanoparticles (10 μL; 16.3 mg/mL) were washed in dH_2O (3×50 μL) and wash buffer (3×50 μL; 50 mM phosphate buffer system, 300 mM NaCl, 10 mM imidazole, pH 8.0). The washed nanoparticles were placed in 40 μL of wash buffer and 20 μL of 6xHis-EndoGluC (1 μg 6xHis-EndoGluC/2 μL dH_2O) and incubated for 60 minutes at 4°C. Using a centrifuge and magnet, the supernatant was collected and nanoparticles washed in 50 μL aliquots (FT, W1, W2, W3). After W3, 50 μL of elution buffer (50 mM phosphate buffer system, 300 mM NaCl, 250 mM imidazole, pH 8.0) was added and rotated for 10 minutes at 4 °C. Nanoparticles were collected 50 μL aliquots (E1, E2). Non-specifically bound protein was released from the nanoparticles by boiling at 95 °C for 4 minutes. The volumes of the aliquots were reduced for analysis by SDS-PAGE (12.5% separation gel, 180V, 50 min). The SDS-PAGE gel was stained using Coomassie Blue overnight.

4.4.24 Isolation of *human recombinant* His×6-caspase 3 (His×6-huCsp3) with Ni(II)-loaded nanoparticles

The Ni(II)-loaded nanoparticles (1 μL; 16.3 mg/mL) were washed in dH_2O (3×50 μL) and wash buffer (3×50 μL; 50 mM phosphate buffer system, 300 mM NaCl, 10 mM imidazole, pH 8.0). The washed nanoparticles were placed in 45 uL of wash buffer and 5 uL of 6xHis-huCsp3 (1X) and incubated for 60 minutes at 4 °C. Using a centrifuge and magnet, the supernatant was collected and nanoparticles washed in 50 μL aliquots (FT, W1, W2, W3). After W3, 50 μL of elution buffer (50 mM phosphate buffer system, 300 mM NaCl, 250 mM imidazole, pH 8.0) was added and rotated for 10 minutes at 4°C. Nanoparticles

were collected in 50 μL aliquots (E1, E2). Non-specifically bound protein was released from the nanoparticles by boiling at 95 °C for 4 minutes. Aliquots are analyzed by SDS-PAGE (12.5% separation gel, 180V, 50 min). The SDS-PAGE gel was stained by silver staining.

4.4.25 Activity Assay of *human recombinant* His×6-caspase 3 (His×6-huCsp3) eluted from Ni(II)-loaded nanoparticles

Eluted protein activity was measured using a commercially available (Biovision) caspase 3 fluorometric substrate. Nanoparticle eluted His×6-caspase 3 (10 μL from 50 μL eluted volume) was incubated with 50 μM DEVD-AFC (Asp-Glu-Val-Asp-AFC) substrate in provided reaction buffer (50 μL) containing 10 mM DTT. Multi-well fluorescence plate reader was set for excitation at 400 nm and emission at 505 nm and incubation temperature of 37ºC.

4.4.26 Activity Assay of recombinant mouse His×6-Endostatin (His×6-rmES) eluted from Ni(II)-loaded nanoparticles

A previously published protocol is used to determine apoptotic activity of eluted Hisx6-rmES.[18] Briefly, cow pulmonary artery endothelial (C-PAE) cells are maintained in DMEM containing 2% FCS and 3 ng/mL bFGF. Cells are treated with Hisx6-rmES directly eluted from Ni(II)-loaded nanoparticles (10 μg/mL). As a negative control, cells are treated with an equivalent volume of elution buffer. Cells are collected by trypsinization and washed twice with cold phosphate buffered saline (pH 7.4) before resuspension in binding buffer (10 mM HEPES, pH 7.4, 140 mM NaCl, 2.5 mM $CaCl_2$). Cells are incubated with

Annexin V-PE per manufacturer's protocol. Stained cells are analyzed using confocal fluorescence microscopy.

4.5 References

1. Cohen, S. N.; Chang, A. C.; Boyer, H. W.; Helling, R. B., Construction of biologically functional bacterial plasmids in vitro. *Proc Natl Acad Sci U S A* **1973,** 70, (11), 3240-4.

2. Porath, J.; Olin, B., Immobilized metal ion affinity adsorption and immobilized metal ion affinity chromatography of biomaterials. Serum protein affinities for gel-immobilized iron and nickel ions. *Biochemistry* **1983,** 22, (7), 1621-30.

3. Garrett, R.; Grisham, C. M., *Biochemistry*. 3rd ed.; Thomson Brooks/Cole: Belmont, CA, 2005; p 1 v. (various pagings).

4. Scopes, R. K., *Protein purification : principles and practice*. 3rd ed.; Springer-Verlag: New York, 1994; p xix, 380 p.

5. Hochuli, E.; Dobeli, H.; Schacher, A., New metal chelate adsorbent selective for proteins and peptides containing neighbouring histidine residues. *J Chromatogr* **1987,** 411, 177-84.

6. Braun, P.; Hu, Y.; Shen, B.; Halleck, A.; Koundinya, M.; Harlow, E.; LaBaer, J., Proteome-scale purification of human proteins from bacteria. *Proc Natl Acad Sci U S A* **2002,** 99, (5), 2654-9.

7. Conti, M.; Falini, G.; Samori, B., How Strong Is the Coordination Bond between a Histidine Tag and Ni - Nitrilotriacetate? An Experiment of Mechanochemistry on Single Molecules. *Angew Chem Int Ed Engl* **2000,** 39, (1), 215-218.

8. Lata, S.; Reichel, A.; Brock, R.; Tampe, R.; Piehler, J., High-affinity adaptors for switchable recognition of histidine-tagged proteins. *J Am Chem Soc* **2005,** 127, (29), 10205-15.

9. Kapanidis, A. N.; Ebright, Y. W.; Ebright, R. H., Site-specific incorporation of fluorescent probes into protein: hexahistidine-tag-mediated fluorescent labeling with (Ni(2+):nitrilotriacetic Acid (n)-fluorochrome conjugates. *J Am Chem Soc* **2001,** 123, (48), 12123-5.

10. Lata, S.; Gavutis, M.; Tampe, R.; Piehler, J., Specific and stable fluorescence labeling of histidine-tagged proteins for dissecting multi-protein complex formation. *J Am Chem Soc* **2006,** 128, (7), 2365-72.

11. Lata, S.; Piehler, J., Synthesis of a multivalent chelator lipid for stably tethering histidine-tagged proteins onto membranes. *Nat Protoc* **2006,** 1, (4), 2104-9.

12. Hutschenreiter, S.; Neumann, L.; Radler, U.; Schmitt, L.; Tampe, R., Metal-chelating amino acids as building blocks for synthetic receptors sensing metal ions and histidine-tagged proteins. *Chembiochem* **2003,** 4, (12), 1340-4.

13. Huang, Z.; Park, J. I.; Watson, D. S.; Hwang, P.; Szoka, F. C., Jr., Facile synthesis of multivalent nitrilotriacetic acid (NTA) and NTA conjugates for analytical and drug delivery applications. *Bioconjug Chem* **2006,** 17, (6), 1592-600.

14. Hauser, C. T.; Tsien, R. Y., A hexahistidine-Zn2+-dye label reveals STIM1 surface exposure. *Proc Natl Acad Sci U S A* **2007,** 104, (10), 3693-7.

15. Kim, S. H.; Jeyakumar, M.; Katzenellenbogen, J. A., Dual-mode fluorophore-doped nickel nitrilotriacetic acid-modified silica nanoparticles combine histidine-tagged protein purification with site-specific fluorophore labeling. *J Am Chem Soc* **2007,** 129, (43), 13254-64.

16. Xu, C.; Xu, K.; Gu, H.; Zheng, R.; Liu, H.; Zhang, X.; Guo, Z.; Xu, B., Dopamine as a robust anchor to immobilize functional molecules on the iron oxide shell of magnetic nanoparticles. *J Am Chem Soc* **2004,** 126, (32), 9938-9.

17. Brook, M. A.; Stan, R. S. Chelating silicone polymers. CA2274040, 2000.

18. Dhanabal, M.; Ramchandran, R.; Waterman, M. J.; Lu, H.; Knebelmann, B.; Segal, M.; Sukhatme, V. P., Endostatin induces endothelial cell apoptosis. *J Biol Chem* **1999,** 274, (17), 11721-6.

19. Sahoo, Y.; Pizem, H.; Fried, T.; Golodnitsky, D.; Burstein, L.; Sukenik, C. N.; Markovich, G., Alkyl Phosphonate/Phosphate Coating on Magnetite Nanoparticles: A Comparison with Fatty Acids. *Langmuir* **2001,** 17, (25), 7907-7911.

20. Sun, S.; Murray, C. B.; Weller, D.; Folks, L.; Moser, A., Monodisperse FePt nanoparticles and ferromagnetic FePt nanocrystal superlattices. *Science* **2000,** 287, (5460), 1989-92.

21. Park, J.; An, K.; Hwang, Y.; Park, J. G.; Noh, H. J.; Kim, J. Y.; Park, J. H.; Hwang, N. M.; Hyeon, T., Ultra-large-scale syntheses of monodisperse nanocrystals. *Nat Mater* **2004,** 3, (12), 891-5.

22. Bentzen, E. L.; Tomlinson, I. D.; Mason, J.; Gresch, P.; Warnement, M. R.; Wright, D.; Sanders-Bush, E.; Blakely, R.; Rosenthal, S. J., Surface modification to reduce nonspecific binding of quantum dots in live cell assays. *Bioconjug Chem* **2005,** 16, (6), 1488-94.

23. O'Reilly, M. S.; Boehm, T.; Shing, Y.; Fukai, N.; Vasios, G.; Lane, W. S.; Flynn, E.; Birkhead, J. R.; Olsen, B. R.; Folkman, J., Endostatin: an endogenous inhibitor of angiogenesis and tumor growth. *Cell* **1997,** 88, (2), 277-85.